Constraining Subduction Zone Processes Through Local, Regional, and Global Chemical Systematics

Constraining subduction zone processes through local, regional, and global chemical systematics

A dissertation presented

by

Stephen Judson Turner

to

The Department of Earth and Planetary Sciences

In partial fulfillment of the requirements

for the degree of

Doctor of Philosophy

in the subject of

Earth and Planetary Sciences

Harvard University

Cambridge, Massachusetts

April, 2015

Dissertation Advisor: Professor Charles Langmuir Stephen Judson Turner

Constraining subduction zone processes through local, regional,

and global chemical systematics

Abstract

Subduction zones recycle material from Earth's surface into the mantle, and are an important means of continent building. The subduction system serves as a stamp, imprinting the distinct chemical characteristics of our planet's geological reservoirs, and distinguishing it within the solar system. As such, the elemental exchanges mediated by this system are a long-standing focus of geochemical and geophysical research. Advances in geochemical techniques and improved geophysical models of subduction have illuminated the processes which give rise to arc volcanism. Great strides have been made in answering the question of what goes down, and what comes back up, though much remains unknown. Arc volcanoes provide a valuable window into the complex subduction environment, and so a comprehensive understanding of arc magma petrogenesis provides a means to resolve significant outstanding questions.

The processes that regulate the compositions of erupted arc magmas are complicated, however. In order to use arc magmas as a tool for constraining elemental fluxes across large-scale geochemical reservoirs, we must trace the path of lavas sampled on Earth's surface back down through the lithosphere. Once we reach the asthenosphere, we require constraints on the conditions from which the magma was generated – a mantle source, fluxed by some hydrous material originating from the

subducting plate. We can determine which elements have been added to the mantle at this point only if we know the composition of the mantle before the hydrous addition. None of these processes are likely to be identical from one volcano to the next (or, indeed, at a single volcano over time). Instead, these processes will vary dependent on the physical conditions present. Thus, this work requires an understanding of the physical conditions across the earth, as well as their effects of physical processes on elemental transfer within the system.

Chapter 1 of this dissertation addresses the question of how magma ascent through the crust can vary on short timescales (~50 years) at a single location, specifically at Bezymianny Volcano, in Kamchatka, Russia. This project was conducted following two field seasons at Bezymianny. Field experience provided an on-the-ground understanding of this volcano's unique magma system, and fostered multi-disciplinary interactions with geophysicists and seismologists that informed the interpretation of its geochemistry. Bezymianny often erupts multiple times per year. The sample set used in this study was collected by several different volcanologists over five decades, and provides unprecedented temporal resolution of sampling for this time period. The compositions of Bezymianny magmas varied regularly throughout the eruptive cycle. Using whole rock trace element compositions and thermobarometry from amphiboles, it was possible to characterize magma mixing at Bezymianny that varied in proportions from three separate crustal reservoirs -- each positioned at a different depth within the crust. A comparison is then drawn between the magma plumbing systems of Bezymianny and other volcanoes with similar surface features. This analysis

demonstrates that the form of a volcano on the surface does not necessarily reflect the structure of its roots.

Chapters 2 and 3 were motivated by Chapter 4, rather than the other way around. Chapter 4 is a regional investigation of chemical variability along the Chilean Southern Volcanic Zone (SVZ). The SVZ is a classic study area for igneous chemistry, in which the compositions of erupted magmas vary along and across the strike of the volcanic arc. Along with magma chemistry, multiple physical parameters that may influence the subduction system (or simply, "subduction parameters"), also vary along-strike. From south to north within the SVZ the crust becomes thicker, while the depth of the slab increases significantly. In addition, there is a decrease in the angle of the slab beneath the arc front. To resolve whether the magma variability in the SVZ is due to variation of subduction parameters within the overriding plate or the subducting slab (or both) is non-trivial. In part, this is because variations in the flux from the slab, the melting processes, and in intra-crustal processing, can have similar chemical consequences.

This ambiguity motivated a re-examination of the relationships between subduction parameters and global magma chemistry. In many ways this project builds upon the study of Plank and Langmuir (1988), but also utilizes the extensive literature database that has been developed in the interim. The new data enable assessment of not only major elemental variation, but also trace elements and isotopes. Chapter 2 presents the systematics of a global dataset, which includes several new observations of global correlations between trace elements and trace element ratios. The global

correlations with magma chemistry also extend to correlations with crustal thickness. There are strong correlations among incompatible elements that are typically separated into groups. The ratio Dy/Yb also correlates with incompatible elements, suggesting involvement of garnet.

In Chapter 2, this dataset is used to investigate whether the global trends might arise from intra-crustal processes. This possibility is supported by the correlations between chemical parameters and the thickness of the crust. The main crustal processes considered are high-pressure crystal fractionation and mixing between primary magmas and an enriched crustal component. High-pressure fractionation trends are not found to be more abundant at arcs with thick crust, however, and the composition of the hypothetical global contaminant is unlikely to exist in nature. The global magma variation is therefore most plausibly primary in nature, arising from processes in the slab or mantle, rather than the crust.

Chapter 3 investigates whether variable slab fluxes or melting processes are responsible for the global correlations in magma chemistry. The correlations with crustal thickness, if not produced by processes within the crust itself, are suggestive of a melting process. The chemical parameters also correlate, however, with the slab "thermal parameter," implicating processes within the downgoing plate. In addition to the arc front chemical systematics, it is shown that rear-arc volcanic compositions, after filtration to minimize the effects of slab input, have strong correlations between Sr and Nd isotopes. Rear-arc Nd isotopes also correlate well with the Nd isotope values of the arc front. To constrain the potential effects of slab and mantle processes, quantitative

models are developed for two different scenarios: In one scenario, global chemical diversity is produced by a variable slab flux, while the mantle thermal structure is held constant. In a second scenario, global chemical diversity is produced by a variable mantle thermal structure, while slab flux is relatively constant. Both models are able to reproduce the global trends, though the observed correlations between filtered rear-arc and arc front Nd isotopes are difficult to reconcile with potentially large fluxes of slab material to the mantle wedge. Both models have implications as well for the flux of H_2O, both from the slab to the mantle, and from the mantle back to the exosphere.

Finally, in Chapter 4, we apply this global modeling framework back to the problem of the SVZ. It is demonstrated that the systematics of the SVZ mimic those of the global system in a remarkable way. The correlations between elements within the global dataset are also present in the SVZ, and these trends overlap. An extensive dataset of rear arc SVZ samples is used to demonstrate control of Nd isotopes and other compositional features by variable mantle heterogeneity, rather than variable slab flux. The along-strike chemical trends of the SVZ are consistent with the scenario of variable mantle thermal structure, but not with the scenario of variable slab flux. This conclusion is quantitatively tested using a model in which both mantle heterogeneity and mantle thermal structure are varied along the arc. The model is successful in reproducing the observed chemical variations. Because the SVZ and global systematics are so similar, it is likely that conclusions drawn from this region can be extrapolated back to the global framework.

Table of Contents

List of Figures

Chapter 1: The magma plumbing system of Bezymianny Volcano: Insights from a 54 year time series of trace element whole rock geochemistry and amphibole compositions

Chapter 2: The global chemical systematics of arc front stratovolcanoes: Evaluating the role of crustal processes

Chapter 3: What processes control the chemical compositions of arc front stratovolcanoes?

Chapter 4: Global and regional implications of the chemical systematics along Chile's Southern Volcanic Zone

Appendices

List of Tables

Chapter 1: The magma plumbing system of Bezymianny Volcano: Insights from a 54 year time series of trace element whole rock geochemistry and amphibole compositions

Appendices

Acknowledgments

Above all, I would like to acknowledge the ever-present support of my wife, Lauren. She is my rock, my sounding board, and my life – without her, this wouldn't have been possible. The same is of course true for my wonderful parents, and family. I couldn't imagine better. And of course, I would like to acknowledge the support of my adviser, Charlie, who taught me igneous geochemistry, and patience. Finally I would like to acknowledge the support of Allie Gale, my geochem sis for life.

Chapter 1: The magma plumbing system of Bezymianny Volcano: Insights from a 54 year time series of trace element whole rock geochemistry and amphibole compositions

[Turner, S.J., Izbekov, P., Langmuir, C., 2013. The magma plumbing system of Bezymianny Volcano: Insights from a 54 year time series of trace element whole-rock geochemistry and amphibole compositions. Journal of Volcanology and Geothermal Research 263, 108-121.]

Abstract

Samples from 33 individual eruptions of Bezymianny volcano between 1956 and 2010 provide an opportunity to study in detail the temporal evolution of an arc volcano. Major element and ICP-MS trace element analyses show that the eruptive products shifted progressively from relatively silicic magma in 1956 (~ 60.4% SiO2) to more mafic compositions (e.g., 56.8% SiO_2 in 2010). Amphibole compositions changed concurrently from low-Al_2O_3 to high-Al_2O_3. Whole rock element-element variation diagrams show tight compositional arrays, some with a distinct kink in the late 1970s, which cannot be reproduced by fractionation of a single magma along a liquid line of descent. Amphibole thermobarometry indicates amphibole crystallization in two separate reservoirs, one between 200 and 300 MPa, and another between 500 and 750 MPa. Liquid compositions calculated from the amphibole analyses show that liquids stored in each reservoir become increasingly mafic from 1956 to 2010, suggesting that each reservoir received magma inputs from more mafic sources throughout the eruptive cycle.

End member mixing analysis of the dataset allows calculation of three end member compositions that can be combined in varying proportions to reproduce major and trace element whole rock compositions. The end-member mixing proportions vary systematically between 1956 and 2010, with maxima for end-members A, B and C during 1956, 1977, and 2010, respectively. Major element compositions of phenocrysts, combined with published trace

element partition coefficients, show that each end member may have evolved from a common parental magma by fractionation of three different mineral assemblages, possibly due to different pressures of crystallization and volatile contents. The petrologic data are consistent with three magma reservoirs at different depths. Magmas from the shallowest reservoir erupted first, with increasing proportions of deeper reservoirs over time. Past studies have demonstrated similarities in eruptive style between Bezymianny and both Mount St. Helens and Soufrière Hills volcanoes. Contrasting time series data show that the magma plumbing systems of Mount St. Helens and Bezymianny have little in common, while Soufrière Hills may be a better analog. Similar eruptive styles at the surface do not necessarily reflect similar systems of magma supply and evolution at depth.

1.1 Introduction

The composition of a magma erupted at an arc volcano is a function of the source composition, the extent of melting, the pressure and temperature conditions in which the magma undergoes fractional crystallization, and the extent to which that magma has mixed with crustal material and other batches of magma and crystals during its ascent from the mantle. Regional and global studies have advanced our understanding of the physical mechanisms that control the source composition, extent of melting, and extent of crustal assimilation at volcanic arcs (e.g., Class et al., 2000; Elliot et al., 1997; Plank and Langmuir, 1998; Hildreth and Moorbath, 1988). Polybaric crystal fractionation and magma mixing are more difficult to detect in regional studies, which have large spatial coverage, but poor spatial and temporal resolution. Evidence for these processes primarily comes from detailed studies of individual volcanic centers (e.g., Grove et al., 2005), though it is probable that such processes affect a large portion of erupted arc magmas (Sparks et al., 1977; Eichelberger et al., 2006; Kent et al., 2010). A complete understanding of volcanic arcs, therefore, must include careful examinations of the magma supply systems of individual volcanoes. Frequently erupting volcanoes, such as Bezymianny, are valuable natural laboratories in which these processes can be investigated.

This study provides an extensive, high-quality dataset on a series of samples for which the time of eruption is known precisely, within the course of 54 years of eruptions at Bezymianny volcano. The primary goal of this work is to understand the processes responsible for such short term compositional variations. The duration of the eruptive activity at Bezymianny coupled with the high temporal resolution of sampling are unprecedented, allowing new insights to be drawn from analyses of both whole rock and amphibole compositions. Continuous variations in erupted whole rock compositions at Bezymianny clearly demonstrate multi-component magma mixing. These whole rock compositional variations, augmented by

thermobarometric and chemometric constraints from amphibole compositions, enable quantitative modeling of the compositions of mixing components as well as the pressure and temperature conditions of the reservoirs that contain them. The dense temporal sampling of the eruptive products of Bezymianny provide a unique opportunity to understand how the relative proportions of mixing components have varied through time, from which a robust physical model of the volcano's plumbing system can be constructed.

Similar case studies have been conducted at a few other volcanoes. At Arenal Volcano in Costa Rica, mineral analysis indicates multiple episodes of basaltic replenishment have occurred over the course of 30 years, despite nearly constant bulk rock compositions (Streck et al., 2002). Eruptive products from the beginning of the 1996 eruption of Karymsky Volcano, in Kamchatka, have a basaltic signature in both glass and mineral chemistry. Within a few months after the initial eruption, however, the basaltic signature diminished, and the composition of erupted material remained nearly constant for the following three years (Izbekov et al., 2004). At Mount St. Helens, bulk rock compositions have varied somewhat among recent eruptions, but there is no evidence for an influx of new mafic magma (Pallister et al., 2008). Bezymianny provides an additional case study that contributes to our understanding of the diversity of time-series data from active volcanoes.

1.2 Geological background and recent eruptive history of Bezymianny Volcano

Bezymianny volcano is a member of the Kliuchevskoi group of volcanoes, situated within the Central Kamchatka Depression (CKD). The volcano is located on the southern flank of the older and presumably extinct Kamen volcano, which in turn is immediately south of Kliuchevskoi volcano, the largest and most active volcanic center in the CKD. Bezymianny began growing approximately 10,000-11,000 yr. BP, with extended repose periods from 6900-4700 BP, 2750-

2100 BP, 1550-1200 BP, and most recently from 1000 BP-1955 AD (Braitseva et al., 1991). The pre-historic eruptive activity at Bezymianny formed extensive pyroclastic flow deposits, lava flows, and extrusive domes (Braitseva et al., 1991), with magma compositions varying from basaltic to andesitic (e.g., Malyshev, 2000; Bogoyavlenskaya et al., 1991). Basalts are the most common eruptive products of the Kliuchevskoi group of volcanoes, and dacites are rare. In the Holocene, dacites erupted almost exclusively at Bezymianny volcano as well as at several extrusive domes situated along a narrow, longitudinally-oriented fault zone extending from Bezymianny to the south (Timerbaeva, 1967; Melekestsev et al., 1991).

The current eruptive cycle of Bezymianny volcano began in late 1955, when moderate explosive activity and dome growth ended a ca. 1000 year dormancy. On March 30, 1956, within six months of the initial intermittent eruptive activity at the central vent, the eastern flank of Bezymianny suddenly collapsed, generating a massive directed blast followed by four hours of vigorous explosive activity. During this event, the eruptive cloud reached an elevation of 35-40 km, pyroclastic flows devastated an area of ca. 40 km^2, and melting of snow generated lahars as long as 100 km. The climactic eruption destroyed the summit of Bezymianny and formed a 1.3-km-wide crater. Within weeks, the volcano started rebuilding its edifice via extrusion of a dome in the middle of the crater, periodic dome collapses, and associated block-and-ash flows. This type of activity continued until the mid 1970s, at which point the extrusive dome growth continued, complemented by short explosive events generating ash clouds as well as pyroclastic flows and surges, which were often followed by effusions of lava flows. Between 2000 and 2010, Bezymianny typically erupted twice per year.

1.3 Samples and analytical techniques

The sample suite consists of 55 fragments of volcanic bombs, juvenile clasts from pyroclastic flows, lava flows, and two samples of volcanic ash. The collection spans the entire 1955-2010 period of the eruptive activity at Bezymianny and includes samples from 33 individual eruptions. Samples of the most recent eruptions were collected during 2005-2010 summer field work as part of the NSF-funded PIRE project. Samples from earlier periods were provided by Genrietta E. Bogoyavlenskaya, Boris V. Ivanov, Alexander P. Maximov, Alexander and Marina Belousovs, Olga A. Girina, and Phillip Kyle. Extreme care was taken in the identification of juvenile material in pyroclastic deposits. The majority of our samples were collected soon after the cessation of individual eruptive episodes, when the deposits were still hot and could be identified unequivocally. The juvenile blocks in the deposits of pyroclastic density currents were identified based on evidence of their cooling and expansion *in situ*. A detailed description of samples can be found in Supplementary Dataset A1.1.

The eruptive products of Bezymianny are remarkably homogenous and rarely contain enclaves or xenoliths. A few mafic enclaves have been found in the juvenile material of the 1997 and 2007 eruptions, two of which are included in this study. The juvenile products of the December 2009 and June 2010 eruptions are notable, as they contain abundant light-colored amphibole-bearing enclaves, four of which are included in this study as well. All enclaves appear texturally and compositionally homogenous.

1.3.2 Analysis of whole rock major and trace element composition

For whole rock analysis, samples were crushed to small chips using a geologic hammer and then pulverized by either an agate mortar or a shatter box with alumina ceramic crucible. Major elements were analyzed by X-ray fluorescence analysis using a PANalytical Axios

wavelength dispersive spectrometer at the Advanced Instrumentation Laboratory of the University of Alaska Fairbanks. The instrument was calibrated at the beginning of analytical session using AGV-1 BHVO-1, BIR-1, JB-2, JGb-1, JP-1, and JR-1 standard reference materials, prepared as glass disks following the same procedure used for samples with unknown concentrations. Trace elements were analyzed by solution nebulized inductively coupled plasma mass spectrometry (SN-ICP-MS) at Harvard University, following digestion in an HF:HNO_3 mixture. Measurements were obtained using Thermo X Series quadruple mass spectrometer. Standard powders BHVO-2, DNC-1, JB-2, W-2, and BCR-2 were used to generate calibration curves. The full description of sample preparation, analytical conditions, and uncertainties of measurements can be found in the Appendix A1.1.

1.3.3 Electron microprobe analysis of amphiboles

For electron probe microanalysis, all rock samples were prepared as standard petrographic thin sections, polished, and carbon-coated to a thickness of ca. 250 Å. Amphiboles were analyzed for major elements at the University of Alaska Fairbanks using a Cameca SX-50 electron microprobe, which is equipped with four wavelength-dispersive and one energy-dispersive spectrometers. The electron probe is fully automated with Probe for Windows software (Donovan et al., 2007). A 15 keV, 10 nA, 1-3- µm-diameter focused electron beam was used for all analyses. Major oxides are reported in wt.% with Fe_2O_3 calculated using Probe Amph v.3 (Tindle and Webb, 1994) following stoichiometric considerations of Rock and Leake (1984). Details about counting times, standards, and typical analytical errors calculated using the methods of Scott et al. (1995) can be found in the Appendix A1.1.

1.4 Results

Bezymianny magmas that erupted during the pre-climactic period in late 1955 and early 1956, as well as magmas of the March 30, 1956 climactic eruption contain (in order of decreasing abundance) phenocrysts of plagioclase, amphibole, orthopyroxene, magnetite, ilmenite, and clinopyroxene, as well as subordinate amounts of quartz and apatite. The erupted material typically contains 35% to 45% phenocrysts and 32% to 42% glass by volume, estimated on a vesicle-free basis.

Plagioclase phenocrysts comprise 35-40 vol. % of Bezymianny andesites and are strongly zoned. A typical plagioclase core-to-rim compositional profile is comprised of (sequentially): An50-60 oscillatory zoning, a dissolution boundary, an abrupt jump in An content up to 70-75 mol. %, and a gradual return to An50-60. Less commonly, the dissolution boundary is followed by a resorption zone made of An80-85 plagioclase and abundant melt inclusions. Individual plagioclase phenocrysts often contain multiple iterations of this sequence (Shcherbakov et al., 2011).

The abundance of amphibole decreased rapidly after the climactic March 30, 1956 eruption, diminishing from about 25-30 % of all phenocrysts in 1956, to trace quantities in the 1970s. Amphibole can still be found in later eruptive products as resorbed cores in opacitic microcrystalline aggregates of pyroxenes, magnetite, and plagioclase. The relative abundance of clinopyroxene gradually increased through time. Pyroxenes are euhedral and occur as phenocrysts, microphenocrysts, and microlites. The other crystalline phases remained relatively constant across all samples. Titanomagnetites are typically subhedral and occur as microphenocrysts and microlites.

The mafic enclaves from the 1997 and 2007 eruptive products vary in size from a few to tens of centimeters. They are characterized by a rounded shape and concentric textural zoning

with vesicular interiors and massive, fine-grained rims. The mafic enclaves are phenocryst-poor, but contain abundant acicular microphenocrysts and microlites of plagioclase, orthopyroxene, clinopyroxene, high-Al amphiboles, and occasional resorbed grains of olivine.

The light-colored enclaves from the 2009 and 2010 eruptive products vary in size from tens of centimeters to 0.5 meters. They are irregularly shaped and typically have straight, sharp margins. Their mineral assemblage is similar to that of the host andesite, though they contain a larger proportion of amphibole.

1.4.1 Range and temporal variation of whole rock compositions

Key major and trace element concentrations are shown in Figures 1.1 and 1.2, with representative analyses in Table 1.1 (full data tables can be found in Supplementary Dataset A1.2). The samples are all andesitic in composition, and have become increasingly mafic through time, shifting from ~61 wt% SiO_2 and ~2.5 wt% MgO in 1956 to ~57% SiO_2 and ~4 wt% MgO in 2010. All samples have subduction zone trace element patterns, with enrichments in fluid mobile elements (Rb, Ba, Sr, U, Pb) relative to rare earth elements (REE) and relative depletions in high field strength elements (HFSE). Incompatible element concentrations have decreased almost continuously since 1956 (e.g.,, Figure 1.3c). Enrichments of light rare earth elements (LREE) over heavy rare earth elements (HREE) also decreased between 1956 and 2010, with La/Yb dropping from an average of 4.57 to 3.64 (Figure 1.3d). While most of the moderately compatible and compatible elements have either increased in concentration or remained constant since 1956, Cr and Ni exhibit more complex behavior. Cr and Ni concentrations increased from an average of 12.6 ppm and 6.7 ppm, respectively, in 1956 to over 2 times these

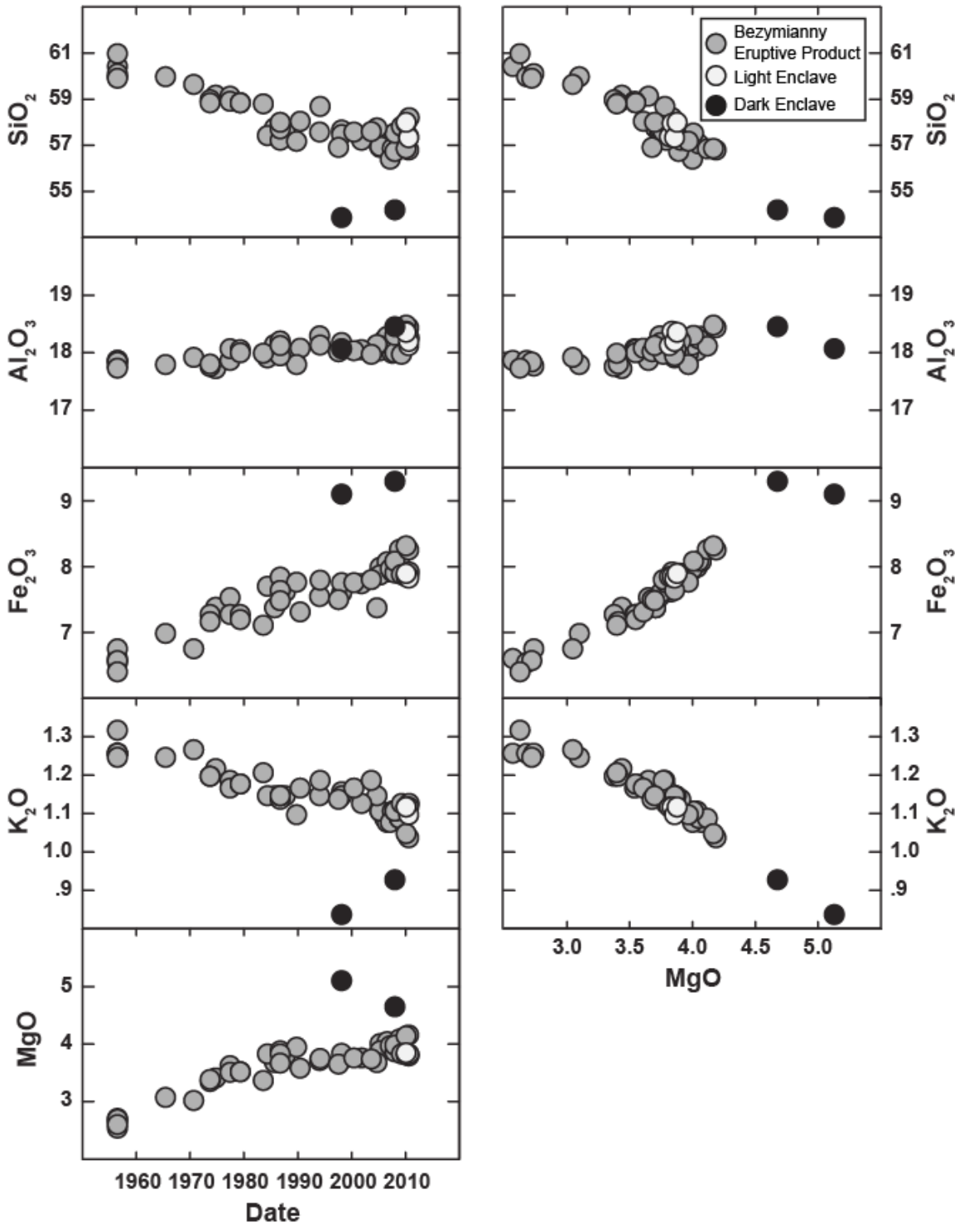

Figure 1.1: Whole rock concentrations of Bezymianny eruptive products are andesitic in concentration, and became increasingly mafic between 1956 and 2010.

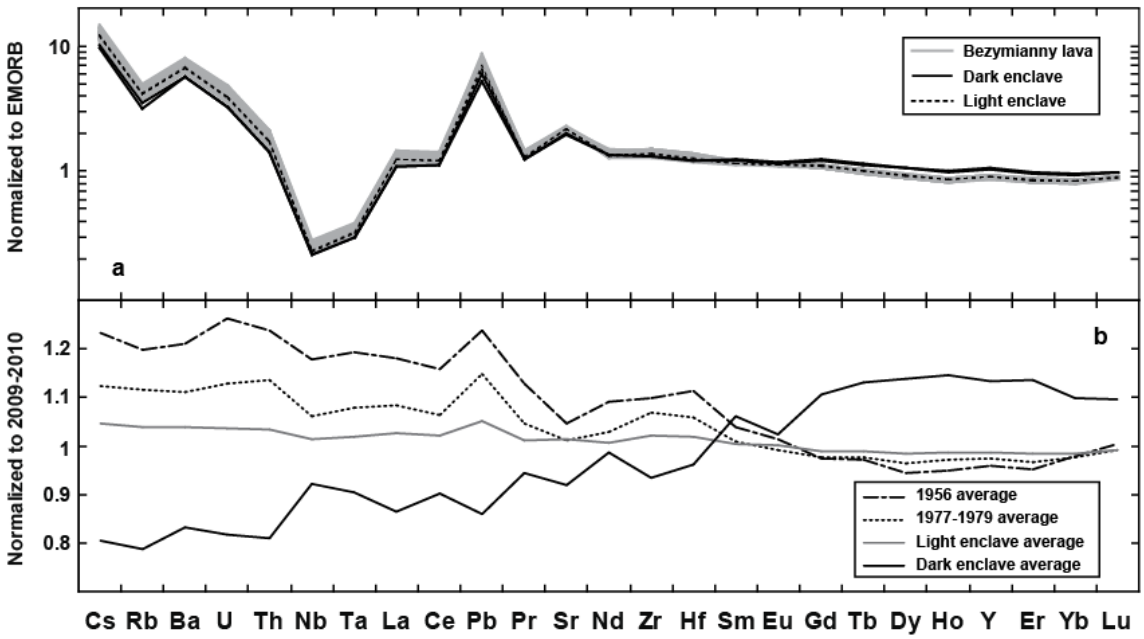

Figure 1.2: (a) Spidergram normalized to EMORB (Sun and McDonough, 1989). All samples exhibit characteristic arc lava signatures. (b) Average compositions of samples from 1956 and 1977-1979 as well as average compositions of samples of light and dark enclaves, normalized to the average compositions of samples from 2009-2010. Note the increasing abundance of incompatible elements through time, as well as the concave HREE patterns.

Table 1.1 Representative whole rock analyses

Sample	05IPE23a	B-65	B-77	B-1987	BZ1997PF1	10IPE1a
Eruption	1956/3/30	1965/3/10	1977/3/25	1987/6/15	1997/12/5	2010/6/1
Material	Bomb	Pyroclastic	Pyroclastic	Lava Flow	Pyroclastic	Pyroclastic
SiO_2	60.03	60.02	59.18	57.61	57.72	56.85
TiO_2	0.59	0.63	0.71	0.72	0.72	0.80
Al_2O_3	17.88	17.81	17.88	17.98	18.20	18.45
Fe_2O_3	6.56	7.00	7.55	7.63	7.62	8.27
MnO	0.14	0.14	0.15	0.14	0.14	0.15
MgO	2.67	3.09	3.64	3.82	3.74	4.18
CaO	6.63	6.85	7.32	7.54	7.52	8.10
Na_2O	3.51	3.32	2.99	3.43	3.39	2.89
K_2O	1.26	1.25	1.19	1.15	1.16	1.04
P_2O_5	0.18	0.18	0.18	0.18	0.18	0.17
TiO_2	0.59	0.62	0.68	0.69	0.71	0.79
Na_2O	3.6	3.5	3.5	3.5	3.5	3.5
MnO	0.130	0.131	0.135	0.129	0.131	0.140
Li	19.4	19.0	18.0	16.9	17.1	15.4
Be	0.96	0.92	0.87	0.88	0.84	0.79
Sc	13.2	14.8	19.2	19.0	20.0	23.8
V	119	138	161	168	174	206
Cr	13.6	21.2	25.5	20.1	18.9	16.4
Co	14.3	16.5	21.6	20.7	22.6	24.1
Ni	7.9	10.8	14.1	16.1	15.1	15.6
Cu	22.9	32.7	37.7	43.8	44.1	46.1
Zn	72.3	74.5	73.9	70.0	71.7	74.8
Ga	17.5	17.4	17.1	17.5	17.6	17.6
Rb	23.4	23.2	22.2	21.3	21.8	19.2
Sr	349	342	335	340	341	332
Y	19.4	19.2	20.1	19.5	19.6	20.6
Zr	109	111	104	102	102	96
Nb	2.23	2.17	2.00	1.96	1.96	1.83
Cs	0.89	0.88	0.82	0.77	0.77	0.69
Ba	439	434	407	390	390	351
La	8.88	8.55	8.32	7.88	7.94	7.39
Ce	20.5	19.8	19.2	18.4	18.3	17.3
Pr	2.91	2.84	2.78	2.67	2.67	2.57
Nd	12.9	12.6	12.6	12.1	12.0	11.8
Sm	3.08	3.03	3.04	3.03	3.01	2.97
Eu	1.03	1.02	1.03	1.02	1.03	1.02
Gd	3.23	3.20	3.33	3.22	3.20	3.34
Tb	0.52	0.51	0.53	0.53	0.52	0.54
Dy	3.12	3.11	3.26	3.23	3.19	3.36
Ho	0.65	0.65	0.67	0.68	0.67	0.69
Er	1.89	1.88	1.95	1.94	1.92	2.03
Yb	1.97	1.95	2.02	1.97	1.93	2.03
Lu	0.32	0.32	0.32	0.31	0.32	0.32
Hf	2.78	2.79	2.62	2.60	2.59	2.44
Ta	0.18	0.17	0.16	0.15	0.16	0.14
Pb	4.63	*	4.33	4.01	4.10	3.65
Th	1.22	1.20	1.13	1.04	1.07	0.95
U	0.85	0.83	0.76	0.74	0.72	0.63

*Sample B-65 became contaminated in Pb during storage

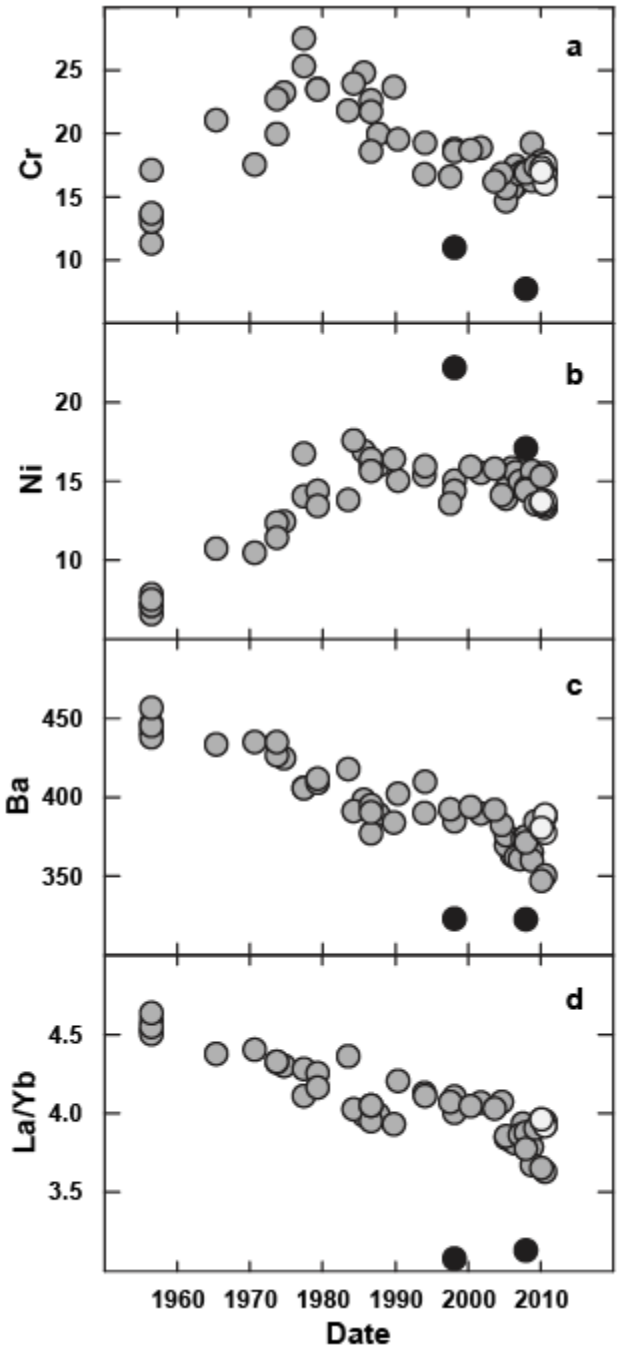

Figure 1.3: (a-b) Concentrations of Cr and Ni in Bezymianny eruptive products and enclaves through time. Note the kinks in the late 1970s. (c-d) Concentrations of Ba and the ratio La/Yb decrease from 1956-2010.

concentrations in 1977 (Figures 1.3a-b). From 1977 to 2010, however, Cr concentrations decreased while Ni concentrations remained constant.

The trace element compositions of the light enclaves, which were erupted in 2009 and 2010, are tightly clustered (Figure 1.2a). They are enriched in incompatible elements relative to their host magmas and are similar in all trace element concentrations to magmas erupted approximately 10 to 20 years earlier (Figure 1.3). The two dark enclaves, which were erupted in 1997 and 2007, are significantly more mafic (basaltic andesite) and have lower concentrations of highly incompatible elements than their host magmas, but higher concentrations of HREE. The average La/Yb ratio of the dark enclaves is 3.1 (Figure 1.2b).

The sample compositions form linear arrays on most element-element variation diagrams (Figure 1.4d). On some element-element or element-ratio plots, however, there is a "kink" in the arrays that consistently occurs around the points representing the eruptive products of 1977 (Figure 1.4a-c). On the linear plots, dark enclaves are generally co-linear with the rest of the samples. On the diagrams showing kinked arrays, the dark enclaves are close to co-linear with samples from the eruptions between 1979 and 2010, though one of the two dark enclaves (09IPE67/1) is slightly offset from this line for some elements.

If the compositional trends at Bezymianny are a fractionation trend, or liquid line of descent (LLD), then the kinks could be generated by the onset of crystallization of some phase at about 3.5 wt% MgO. It is also possible that the compositional trends are the result of mixing between distinct end-member compositions. In this case, an abrupt change in mixing end members would be necessary in 1977, in order to explain why the compositional arrays kink at this point.

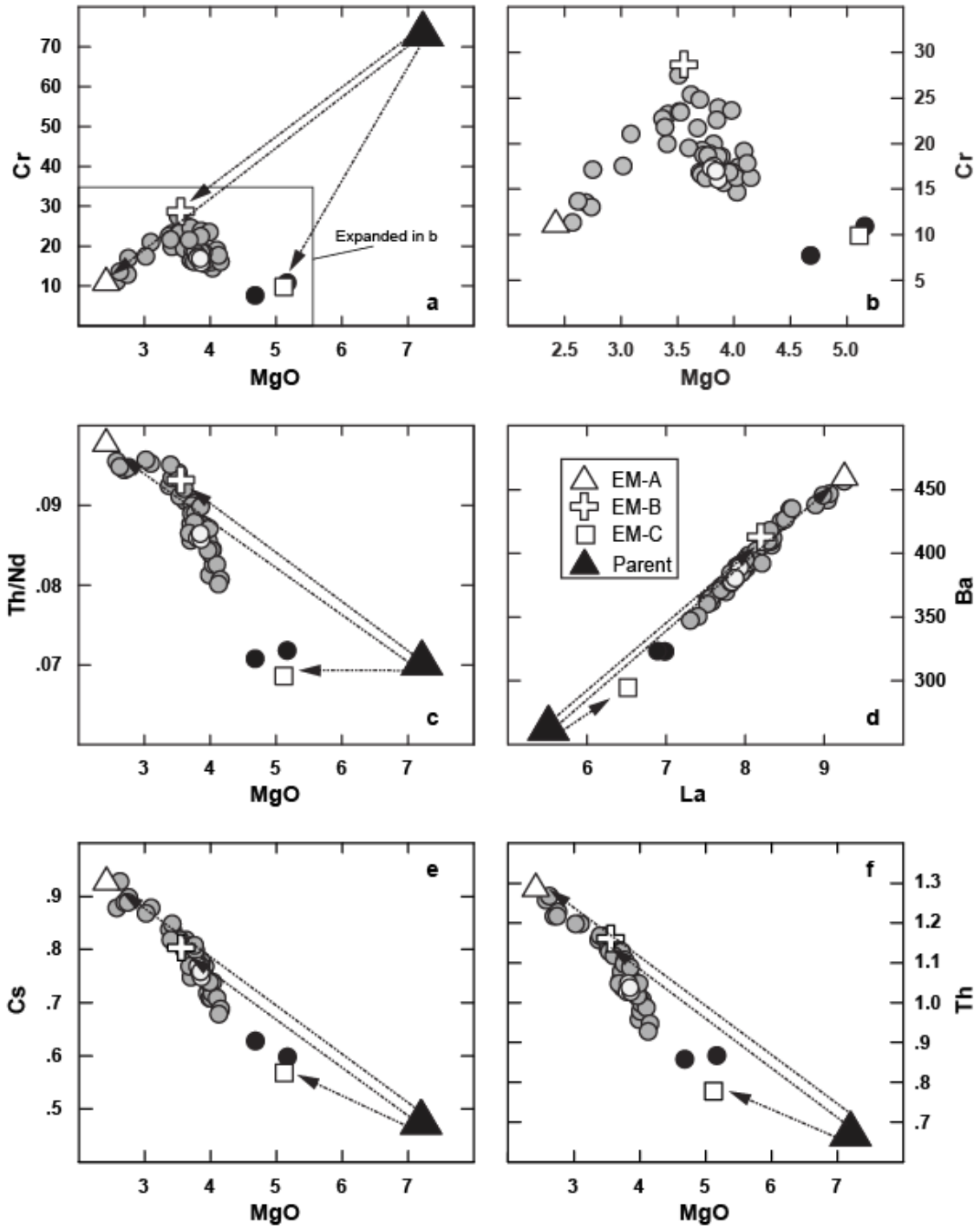

Figure 1.4: (a-c) Plots of Cr and Th/Nd vs MgO produce kinked arrays, which cannot be produced by simple fractional crystallization or two component mixing. The arrays can be reproduced by three component mixing between the end-members EM-A, EM-B, and EM-C. These end-members can be modeled as the products of fractional crystallization of a single parental composition via the removal of different mineral assemblages, presumably caused by fractionation at varying pressures. (d) On this plot of Ba vs La, as well as many other element-element plots, the sample compositions form simple linear arrays.

1.4.2 Range and temporal variation of amphibole compositions

Amphibole comprises up to 30% of all phenocrysts in the pre-climactic ash of Bezymianny and in the andesites of the March 30, 1956 eruption. Amphibole occurs as euhedral prismatic phenocrysts and micro-phenocrysts surrounded by microcrystalline opacitic rims, with widths varying from a few to nearly 50 microns (Plechov et. al., 2008). The majority of amphiboles in the pre-climactic ash are texturally and compositionally homogeneous. Their Al_2O_3 content is unimodal and ranges from 8 to 12.4 wt.% (Figure 1.5a). In contrast, amphiboles from the climactic eruption show wider compositional variations and vary from 9% to 15% Al_2O_3. High-Al amphiboles are often darker and occur as anhedral cores surrounded by light-colored, low-Al rims (Figure 1.6). The boundary between high-Al cores and low-Al rims is sharp, exhibiting a distinctive compositional discontinuity.

The abundance of amphiboles in Bezymianny magmas rapidly declined after the 1956 climactic event. Nevertheless, they can still be found in almost all juvenile products, including the most recent ones. In these recent samples, amphiboles occur as rare resorbed cores in 1-2 mm long opacitic aggregates of plagioclase, pyroxenes, and magnetite microlites. Although the range of compositional variations in the post-climactic amphiboles remained nearly the same as in the March 30, 1956 magma, high-Al amphiboles became more abundant with time (Figure 1.5b-c).

Our amphibole analyses confirm the results of previous studies for the 1956 magma, which report compositions predominantly within the ranges of magnesio-hastingite and tschermakite (Plechov et al. 2008, Al'meev at al. 2002). The addition of amphibole data for the post-1956 period, however, indicates a somewhat broader range of compositions in addition to systematic

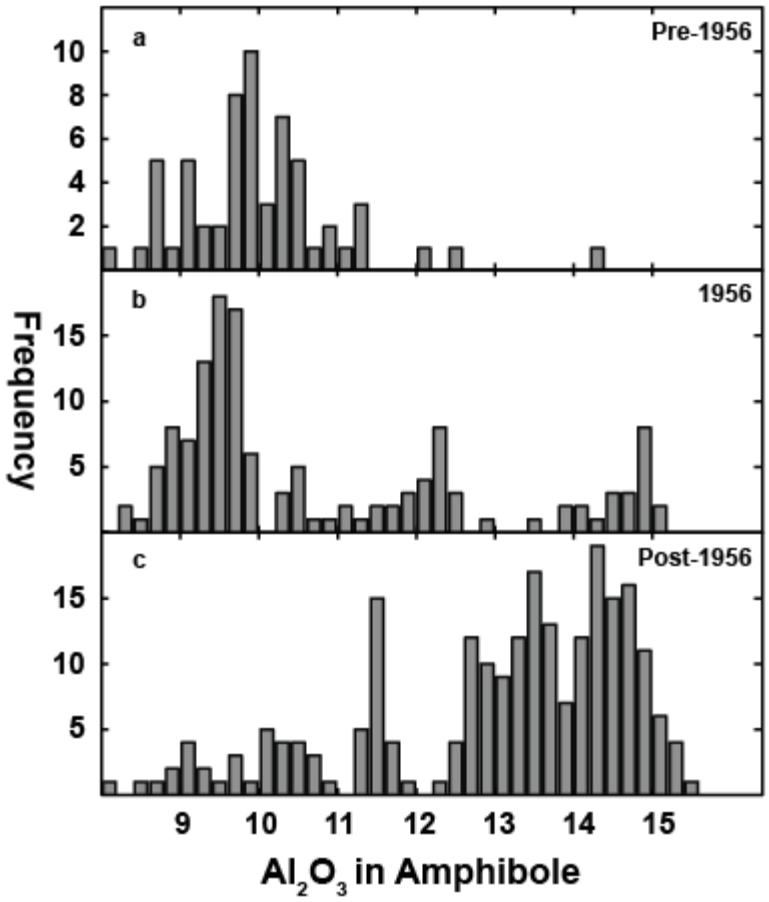

Figure 1.5: The concentration of Al_2O_3 in amphibole phenocrysts forms a bimodal distribution. (a) In the pre-climatic ash, Al_2O_3 content is unimodal and ranges from 8 to 12.4 wt.% (b) Amphiboles from the climactic eruption show wider compositional variations with Al_2O_3 content as high as 14-15 wt. %. (c) Though rare, amphiboles erupted after 1956 cluster around 13 to 15 wt.% Al_2O_3.

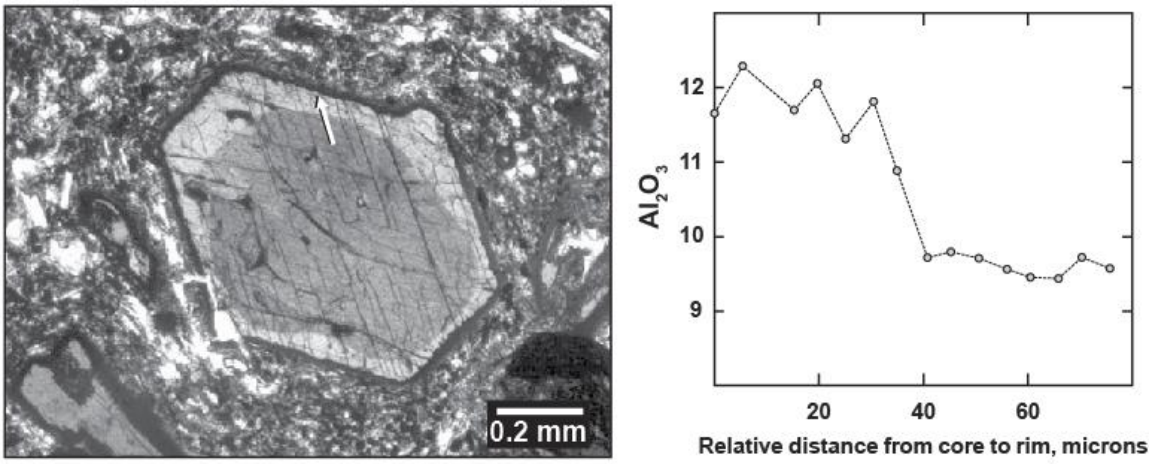

Figure 1.6: Photomicrograph showing amphibole phenocrysts with high-Al core and low-Al rim from the Bezymianny andesite erupted on March 30, 1956. The white arrow indicates the location of the electron microprobe profile shown on the right.

temporal variation. Al_2O_3 concentrations, for example, vary from 8.47 wt. % to 14.65 wt. %, while Na_2O compositions vary from 1.5 wt % to 2.75 wt %. Lower Al_2O_3 amphiboles are more abundant in the earlier eruptive products and are scarce in all eruptive products after the 1970s. The amphibole compositions also appear to vary bimodally, with one cluster around 9 to 10 wt % Al_2O_3 and another around 13 to 14 wt % Al_2O_3.

1.4.3 Amphibole thermobarometry and estimates of liquid compositions

The pressure and temperature conditions of amphibole crystallization, as well as the liquid compositions from which the amphiboles likely crystallized, can be calculated from amphibole compositions using the method described in Ridolfi and Renzulli (2012) (hereafter referred to as RR12). We used averaged compositions of transects taken within unaltered amphibole cores for thermobarometric and chemometric calculations. As can be seen in Figure 1.7a, thermobarometric results indicate that the amphiboles originated in two distinct zones of pressure and temperature. Zone one falls between 200 and 300 MPa with a temperature of 900 ± 50 °C. Zone two falls between 500 and 750 MPa with a temperature of 975 ± 25 °C. These two

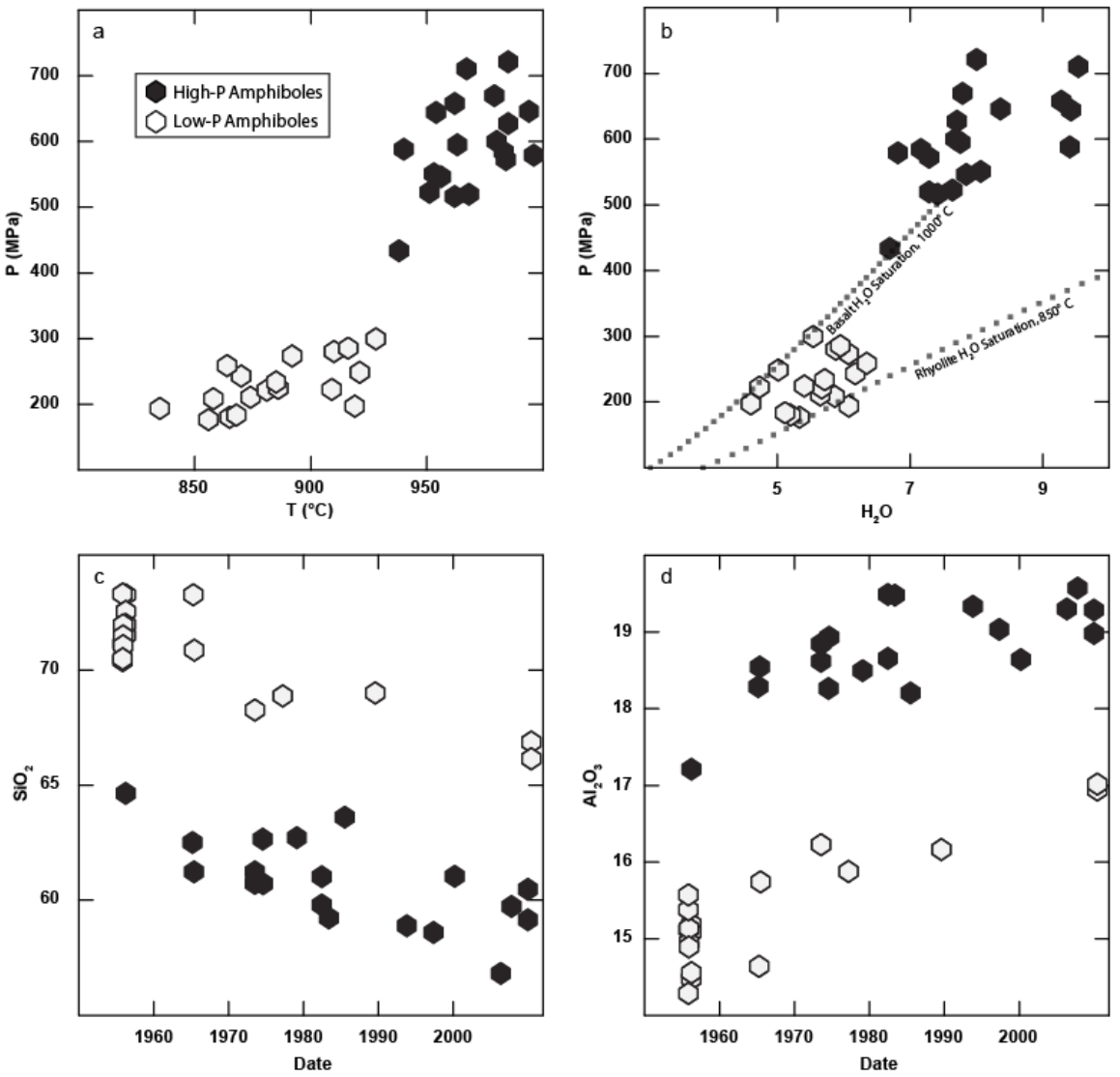

Figure 1.7: Results of amphibole thermometric, barometric, and chemometric equations from Ridolfi and Renzulli (2012). (a) The amphiboles reflect equilibration temperatures from two distinct zones in P and T space. (b) The high-P amphiboles are in equilibrium with a liquid that is >7% H_2O, while the low-P amphiboles reflect liquids of <7%. The H_2O saturation lines were calculated with VolatileCalc, using default Rhyolite composition and a basalt with 49% SiO_2. As the high-P liquids are transferred to the low-P reservoir, the liquids most likely cross their H_2O saturation surface and de-gas significantly. (c) Amphibole concentrations reflect more mafic liquids in the high-P chamber than in the low-P chamber. Both liquids become increasingly mafic from the onset of volcanic activity to present day. (d) The offset in Al_2O_3 concentrations is probably due to different phenocryst assemblages in the two magma reservoirs. The Low-P chamber most likely has a larger proportion of plagioclase phenocrysts, resulting in lower Al_2O_3 concentrations in the low-P liquid.

ranges of pressure correspond well to the depths of local crustal storage reservoirs of 7 km (Thelan et al., 2010) and 18 km (Fedotov et al., 2010). It should be noted that following the exact protocol described in RR12 is impractical for the high pressure (high-P) range of compositions, as the pressure range under examination crosses the threshold between two of RR12's recommended equations, creating an artificial discontinuity in the results. Given these circumstances, it is desirable to apply a single barometric method to all of the high-P samples under consideration. The barometric results shown in Figure 1.7 are considered optimal for this study, and were calculated as the average of RR12 equations P1b, P1c, and P1e (Filippo Ridolfi, personal communication).

Chemometric results indicate that H_2O contents of the liquids in equilibrium with high-P amphiboles were between 7 and 9 wt%, while results for low pressure (low-P) amphiboles fall mostly between 4 and 6 wt% H_2O. As shown on Figure 1.7b, the high-P liquids, which are nearly rhylotic in composition, are undersaturated with respect to H_2O, while the low-P liquid H_2O contents sit very near the rhyolitic saturation surface calculated using the VolatileCalc macro of Newman and Lowenstern (2002). Notably, the major element compositions all liquids (calculated using RR12) are slightly less rhyolitic than the experimental compositions used to calibrate VolatileCalc. As a result, the relevant saturation surface should be shifted slightly away from the rhyolitic curve towards the basaltic curve. The relevant saturation surface for our calculated liquids likely falls within error of the calculated water contents of low-P samples. Therefore, if high-P reservoir liquids (which appear to be mostly H_2O undersaturated) were transferred to the low-P reservoir, they would likely become H_2O saturated and de-gas significantly during their ascent.

The amphibole-calculated major element compositions of liquids are somewhat more felsic for the low-P group than the high-P group, though both low-P and high-P amphiboles

indicate increasingly mafic liquid compositions from 1956 to 2010. This offset between the two groups, combined with the trends toward more mafic compositions within each group, creates parallel trends in plots of liquid composition vs date (e.g., Figure 1.7c). The calculated liquid compositions for the low-P group overlap considerably with and follow the same trend as the compositions of melt inclusions from the outermost rims of plagioclase phenocrysts (Owen Neill and Vasily Shcherbakov, in prep). Calculated liquid Al_2O_3 concentrations are greater in the high-P group, and tend to increase over time within each group, though this increase in Al_2O_3 is larger in the low-P group (Figure 1.7d).

1.5 Discussion

The simplest mechanism capable of producing whole rock compositional variation within a continuously erupting volcano is magma derived from a cooling, homogenous, closed system chamber, where ongoing crystal fractionation will drive the magma towards increasingly felsic compositions. At Bezymianny, however, this is not possible, given that the eruptive products have become increasingly mafic through time (Figure 1.1). It follows that the magma system at Bezymianny is either not a closed system, is not homogeneous, or is neither a closed system nor homogenous.

Intermittent eruption of a closed system, compositionally zoned magma chamber, such as those proposed by Hildreth (1983) or Bacon and Druitt (1988), might instead be responsible for the compositional trends at Bezymianny. The simplest compositional variation within a magma chamber is produced by fractional crystallization of a single parent magma prior to the initial eruption. Magma that has undergone a greater amount of fractional crystallization becomes more felsic and decreases in density. The most felsic, least dense, magmas reside at the top of the reservoir, while denser mafic magmas are confined to the bottom. A temporal trend of increasingly mafic products may form as buoyant, felsic magmas are removed from the

top of the reservoir by an eruption, leaving deeper, mafic layers of the reservoir to be erupted subsequently (Kadik et. al., 1986).

If the compositional variation of a volcano's eruptive products is produced by varying degrees of fractional crystallization, as proposed above, then it will be possible to generate any erupted felsic lava composition by removing some combination of crystallizing phases from any of the more mafic lavas. As can be seen on Figure 1.4b, the Cr contents of the Bezymianny eruptive products increase from about 15 ppm to about 30 ppm, a factor of 2, as MgO decreases from 4.2 wt% to 3.5 wt%. Over this same range of MgO, highly incompatible elements, such as Th and Cs (Figure 1.4e and 1.4f), increase by a factor of 1.2. This range of variation is well resolved for all elements given the analytical uncertainties in Appendix A1.1. There are no potential crystallizing phases in which Cr has a lower partition coefficient than Th and Cs, therefore these trace element variations could not have been produced via crystal fractionation alone.

Convective self-mixing is another process that has been proposed to create compositional diversity among mineral populations, and potentially among whole rock compositions, within a single magma chamber that is heated from below and cooled from above (e.g., Couch et al, 2001; Ridolfi et al, 2008). Magma at different temperatures will crystallize minerals of different compositions, with cooler portions of the magma chamber crystallizing to greater degrees. If contrasting mineral and liquid populations are then partially remixed by convection within the magma chamber, a range of whole rock compositions could be produced. It is unclear, however, how such a process could produce the trend towards increasingly mafic whole rock compositions over the course of 54 years of activity at Bezymianny. Furthermore, plagioclase textures and compositional zoning patterns in Bezymianny eruptive products appear to rule out convective self-mixing in favor of conventional magma mixing (Shcherbakov et al.,

2011). Mixing between two magma bodies would have resulted in a perfectly linear array on Figure 1.4a-b, and a nearly linear array on Figure 1.4c. Because the compositional arrays on both of these diagrams are kinked, a simple mixing model between two compositional end members is also not consistent with the data.

1.5.1 A three component mixing model for Bezymianny

A three component magma mixing system can account for the compositional arrays seen in the eruptive products of Bezymianny. As noted earlier, such a mixing model requires an abrupt change in mixing components around 1977 in order to account for the shifts in trajectories seen in Figure 1.3a and 1.3b. It is likely that the 1977 kink is a result of either the addition or removal of a mixing component at this point in time. For a straightforward three component mixing model, two of the components are fairly well constrained on the plot of Cr vs MgO (Figure 1.4b). As shown on Figure 1.4b, the samples with both the highest and lowest MgO concentrations have 10 ppm Cr or lower, while samples with intermediate MgO contents trend towards higher Cr. In order to encompass the entire range of compositions on Figure 1.4b, one of the mixing components must have low MgO (<~2.5 wt% MgO) and low Cr, while another must have >~5 wt% MgO with similarly low Cr. If two out of three mixing components have low Cr concentrations, then the third mixing component must have higher Cr concentrations. Qualitatively, three component mixing appears to be a plausible mechanism for producing the compositional diversity of the eruptive products of Bezymianny. A quantitative evaluation is presented in section 1.5.2.

Amphibole themobarometry and chemometry results are also consistent with a three component mixing model for Bezymianny. As discussed above, amphibole crystallization appears to have occurred in two distinct zones of pressure and temperature, which presumably

correspond to two distinct magma reservoirs. In some cases, amphiboles from each of the two regions appear in a single sample, which indicates that the whole rock assemblages are produced via mixing between magmas derived from at least two reservoirs. Also, as shown in Figure 1.6, in some cases the high Al_2O_3, high pressure amphibole compositions are surrounded by low Al_2O_3 rims, indicating that the individual amphibole crystal initially crystallized in the high-P reservoir, and was later transferred to the low-P reservoir, where it continued to grow. The offsets in calculated liquid compositional trends (Figures 1.7c and 1.7d) indicate that two reservoirs contain liquids with unique compositions, and that the liquid compositions of each reservoir individually become more mafic over time.

The offset in liquid compositions could result from either different whole rock compositions in the reservoirs, or different proportions of crystallized minerals and liquids. The trends towards increasingly mafic compositions over time indicate that each reservoir was injected with a continuous input of a liquid that was more mafic than the initial liquid composition of that reservoir. The composition of the low pressure reservoir was likely modified by injection of liquid from the high pressure reservoir, causing the low-P liquids to become more similar to the initial high-P liquids over the course of the eruptive cycle. The high-P reservoir also became more mafic, however, indicating that it was injected with a third, even more mafic liquid. This third, most mafic, liquid is presumably derived from a third reservoir which did not itself contribute amphiboles to the erupted material.

1.5.2 Solving for mixing end-members

In order to quantitatively assess whether a three end-member mixing model can account for the complete range of compositions, end-member-mixing-analysis was undertaken, following Weltje (1997). This method is preferable to standard principle component analysis or

factor analysis because it ensures that each measurement of the individual samples can be reproduced within error from nonnegative end-members and mixing proportions. Elements that became contaminated during storage in multiple samples (Zn, Pb) and elements for which measured compositions for some samples approached analytical limits (Co, Ni, Cu) were not included in the mixing analysis.

End-member-mixing-analysis consists of two main stages. First, a linear approximation of the composition matrix (the set of elemental compositions measured in each sample) must be constructed based on an assumed number of components. In this stage, the compositions of all elements can be scaled following a variety of different methods (Meisch, 1980). For our model it is desirable for the linear approximation of the data to be close to the actual measured data on average. However, it is also desirable to minimize the maximum discrepancy between any measurement and its associated approximation. In order to meet these goals, scaling coefficients were selected by a weighted least squares minimization of both the average difference and maximum single difference between the actual and approximated data.

If the dark enclaves are not included in the model, the maximum difference between any observation and its model approximation is 6%, with an average difference of only 1.2%. For major and minor elements, the maximum differences are 4.6% and 4.2% and the average differences are 0.8% and 1.4%. If the dark enclave 09IPE65b is included in the model, the maximum and average differences between the model and measured trace elements are 8% and 1.4% (direct comparison in Figure 1.8). For major and minor elements, the maximum differences are 5.1% and 7.4% with average differences of 0.9% and 1.5%. The discrepancies between the model output and actual measurements are small considering the analytical uncertainty and heterogeneity within sampled material likely to exist in a natural system.

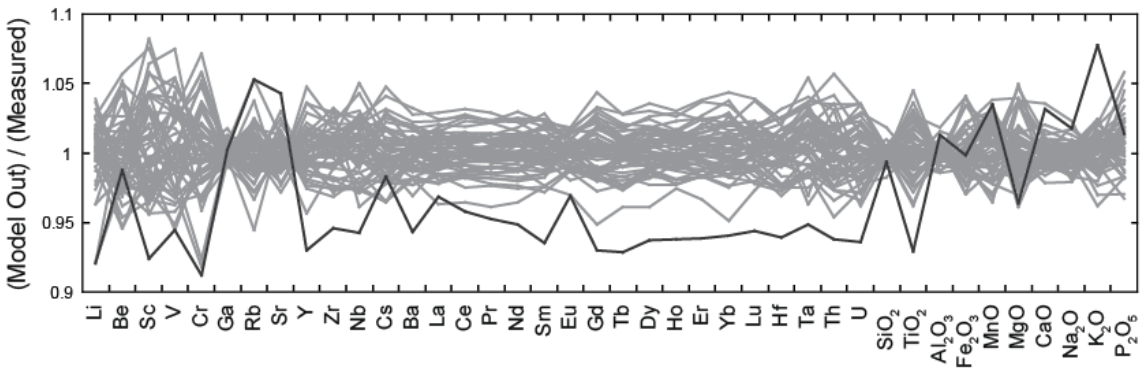

Figure 1.8: Comparison between measured whole rock compositions and mixing model results.

1.5.3 Temporal variation in end-member mixing proportions

Once the approximated composition matrix has been calculated, it is possible to solve for end-member compositions. The end-member compositions are whole rock values, since the aim is to account for the total lava compositions. A weighted least squares procedure was used to obtain non-negative end-member compositions and the corresponding nonnegative mixing proportions for each sample that perfectly reproduced the approximated composition matrix. As outlined in Weltje (1997), the algorithm searches for a scaled loading matrix that, in combination with the approximated composition matrix and its associated reference vectors described in the previous section, can be used to compute end-member compositions that are non-negative and a set of mixing proportions that are both non-negative and sum to one for each sample. Our procedure utilizes MATLAB's active-set algorithm rather than the specific iterative algorithm described by Weltje (1997), though improvements in processing power enable quick calculations using either method.

As discussed in section 1.5.1, the compositions of two of the mixing end-members (EM-A and EM-C) are fairly well constrained. Best-fit solutions for these end-members are similar to the compositions of the 1956 lavas and the mafic enclaves. Any end-member solutions that are

more distant from the compositions of the 1956 lavas and enclaves will either approach negative Cr concentrations or produce mixing proportions that do not sum exactly to one. The third mixing end-member (EM-B) can be assigned a range of compositions constrained to a compositional vector that is roughly defined by a line connecting the compositions of the 1956 and 1977 eruptives. The minimum MgO contents of EM-B are similar to those of the eruptive products of 1977. The maximum MgO is not constrained mathematically, but if higher MgO is assigned to EM-B, larger proportions of EM-A are necessary to produce the 1977 compositions. Varying MgO in EM-B causes the proportions of mixing end-members with time to vary, and determines whether EM-A can go to near zero after 1977. Two possible solutions, to be discussed further in the following section, are presented in Supplementary Dataset A1.3.

In scenario one, EM-B is as similar as possible to the eruptive products of 1977. Figure 1.9 shows how the three end-members would then vary between 1956 and 2010. The volcano begins to erupt in 1956 with a composition of almost pure EM-A. The proportion of EM-A decreases continuously between 1956 and 1977, possibly undergoing a minor resurgence in the 1990s. By 1977, EM-A contributes negligibly to the erupted material (considering model error and the constraint that mixing proportions be >1), at which point EM-B begins to dominate erupted compositions. EM-C, the most mafic end-member, first appears significantly in 1977, reaching over 50% in 2010.

In scenario two, EM-B is calculated assuming 5 wt% MgO (as opposed to 3.56 wt % in scenario 1). As in scenario 1, the initial composition is almost entirely EM-A. As of 1977, the proportion of EM-A levels off to about 50% of the erupted material, with EM-B contributing the other 50%. If EM-B had still higher MgO concentrations, the maximum contributed proportion of EM-B would be still lower, and the minimum contribution of EM-A still higher. EM-C increases progressively in significance after 1977. Therefore, the key difference in the two scenarios is

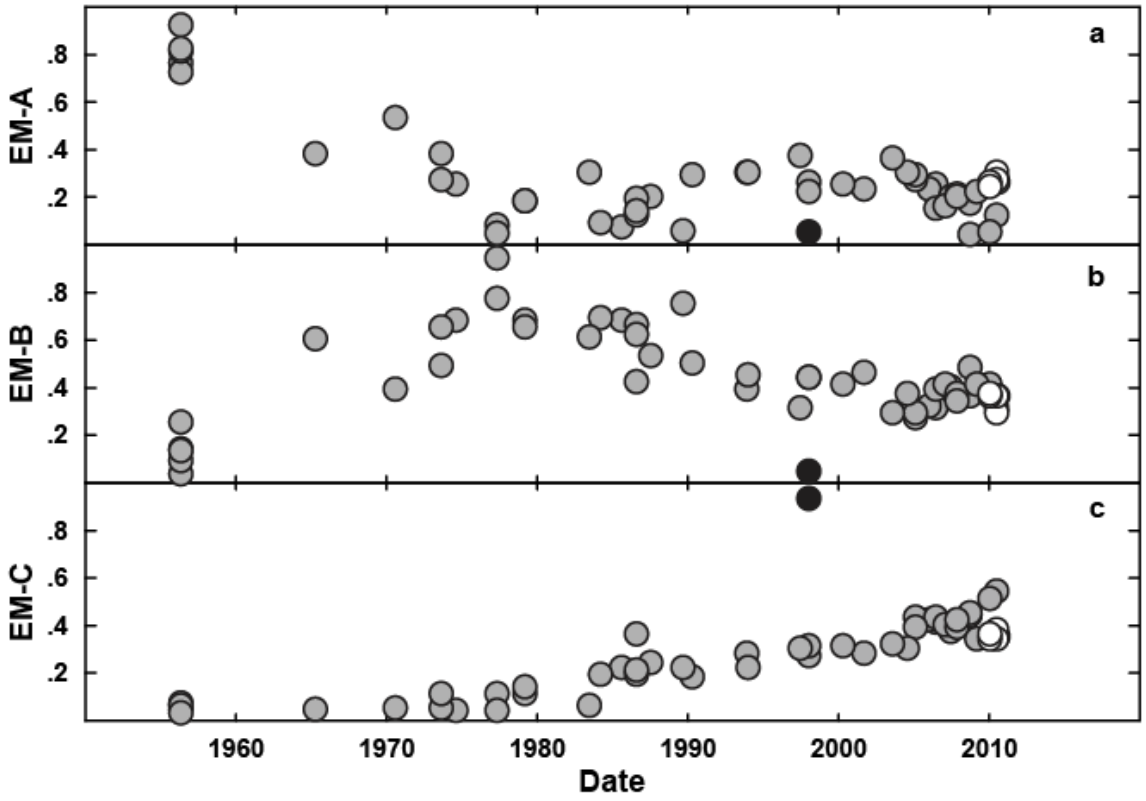

Figure 1.9: Mixing proportions of the three calculated mixing end-members for each sample from 1956-2010. See text for details.

whether EM-A becomes negligible after 1977, or continues as an important mixing end-member. In Scenario 2, all three mixing end-members contribute significantly to the eruptive products following 1977, while in Scenario 1, the eruptive products after 1977 are primarily a mixture of EM-B and EM-C.

While the details of the end-member analysis are non-unique, we prefer scenario 1. First, this scenario uses end-members that correspond with erupted compositions, rather than inferring an alternative end-member for which there is no independent evidence. Second, there are sound mineralogical arguments that EM-A becomes negligible after 1977. As discussed previously, low aluminum, low pressure amphiboles dominate the phenocryst population of the eruptive products from 1956-1965, but are rare in all material erupted since that time. It is logical that these low pressure amphiboles are a component of EM-A, which dominates the

eruptive products of 1956. The scarcity of low pressure amphiboles in later eruptions suggests that the proportion of EM-A in erupted material most likely diminished rapidly after the initial eruptions. This petrologic constraint favors scenario one over scenario two, because scenario two requires that significant contributions from EM-A persisted from 1956 up to 2010. Model results from scenario one will for this reason be the basis for the discussion in the following section.

1.5.4 Origin of the diversity of end-member compositions

It is worth considering whether the three end-member compositions might be related by isobaric fractionation from a common parental magma, along a single liquid line of descent (LLD). The possibility that the end-member compositions are produced by a single fractionation sequence can be ruled out, however, for the same reason that this relationship was discounted within the individual samples. As shown in Figure 1.4b, if the mixing end-members were related by a LLD, the Cr contents must have increased from about 10 ppm to about 30 ppm between EM-C and EM-B, a factor of 3. The highly incompatible elements Th and Cs, however, increase by less than a factor of 2 during this same interval. As stated earlier, there are no potential crystallizing phases in which Cr has a lower partition coefficient than Th or Cs, therefore these trace element variations could not have been produced via crystal fractionation alone.

Though the end-members are not related by a single LLD, it is still possible that the end-member compositions evolved from a common parental magma through fractional crystallization of distinct mineral assemblages owing to differences in pressure and associated volatile content. To quantitatively assess the possibility of a single parental magma composition, a least squares model has been constructed that incorporates our end-member whole rock compositions and amphibole analyses, the pyroxene and plagioclase analyses of Shcherbakov et

Table 1.2. Calculated mixing end-member and parental magma compositions

	EM-A	EM-B	EM-C	Parent
SiO_2	60.90	58.34	53.17	51.86
TiO_2	0.56	0.65	0.95	0.93
Al_2O_3	17.83	17.79	18.38	16.84
Fe_2O_3	6.35	7.27	9.29	10.27
MnO	0.13	0.13	0.14	
MgO	2.42	3.56	5.10	7.20
CaO	6.45	7.26	8.60	8.54
Na_2O	3.72	3.48	3.23	2.69
K_2O	1.32	1.20	0.88	0.76
P_2O_5	0.19	0.18	0.16	
Li	20.51	17.78	13.52	
Be	0.97	0.88	0.70	
Sc	11.42	17.71	30.50	36.80
V	103	153	272	
Cr	11.29	28.66	10.01	73.63
Ga	17.61	17.23	17.81	
Rb	24.95	22.72	16.39	14.84
Sr	354	340	313	268
Y	19.21	19.04	21.78	
Zr	110.4	105.8	88.9	72.09
Nb	2.27	2.01	1.66	
Cs	0.93	0.82	0.57	0.48
Ba	460	412	295	266
La	9.26	8.20	6.49	5.51
Ce	21.16	18.89	15.61	13.19
Pr	3.01	2.71	2.39	
Nd	13.17	12.13	11.35	9.62
Sm	3.10	2.97	3.05	2.66
Eu	1.05	1.00	1.05	0.95
Gd	3.21	3.13	3.50	
Tb	0.51	0.51	0.57	0.48
Dy	3.08	3.10	3.61	
Ho	0.64	0.65	0.75	
Er	1.87	1.87	2.16	
Yb	1.96	1.91	2.12	1.76
Lu	0.32	0.31	0.33	0.28
Hf	2.83	2.65	2.30	1.81
Ta	0.18	0.16	0.13	0.11
Th	1.29	1.13	0.78	0.68
U	0.88	0.77	0.53	

al. (2011), Fe-Ti-Oxide analyses (Jill Shipman, unpublished data), as well as partition coefficients for each of these phases (from multiple sources, see Supplementary Dataset A1.4). This model uses the equation for bulk fractional crystallization, operating under the assumption that the pure mixing end-members approximate the compositions of liquids fractionated from a single mafic parent. Though the material erupted at Bezymianny contains varying quantities of phenocrysts, the material is texturally and compositionally homogenous, with glass and mineral compositions that generally track the bulk rock compositions (Jill Shipman, personal communication). The model found a single parental composition that could be fractionated to produce each of the end-members to within 2.6% for major elements (4.5% for K_2O), with an average difference of 1.4%, and to within 8.1% for trace elements, with an average difference of 3.4%. This parental composition (Table 1.2) is fractionated 49% to obtain EM-A, 41% for EM-B and 17% for EM-C. The calculated parental magma is a high-Mg basalt, and is similar to some of the eruptive products of Kliuchevskoi volcano — Bezymianny's massive neighbor 10 km to the north. Fractionating assemblages used in the model are reported in Table 1.3, and detailed model results as well as a comparison to Klyuchevskoi can be found in Supplementary Dataset A1.4.

Table 1.3 Mineral assemblages and proportions used in fractionation model

	EM-A	**EM-B**	**EM-C**
	Total Fractionation		
	49%	41%	17%
	% Fractionating proportions		
Ol	20	18	0
Plag1	31	33	9
Plag2	6	0	0
Cpx	3	0	43
Opx	0	0	46
Hbl1	35	0	0
Hbl2	0	44	0
Mt	5	6	0
Il	0	0	1

EM-A and EM-B have similar fractionating assemblages, though EM-A was set to form via fractionation of a lower pressure (lower Al_2O_3) amphibole composition. This constraint was imposed because, as indicated above, the lower Al_2O_3 amphiboles are far more prevalent in samples from 1956, which are dominated by EM-A. The fractionating assemblages determined for EM-A and EM-B are roughly consistent with the experimental results of Grove et al. (2003) at the two P and T conditions calculated from amphibole thermobarometry.

EM-C is marked by the lack of amphibole in the crystallizing assemblage. The high percentage of pyroxenes, and lack of amphibole, in the assemblage for EM-C may be possible at pressures of greater than 1000 MPa, outside of the zone of amphibole stability. Though experimental verification under these crystallizing conditions has not been carried out for the exact compositions in question, experimental results for liquid compositions that are similar to the proposed Bezymianny parental composition support this fractionation model (Gust and Perfit, 1987; Liu et al., 2000). Additional support for crystallization of a pyroxene rich, amphibole free assemblage at high pressures is provided by the work of Shcherbakov and Plechov (2010), who examined crystallizing veins of volcanic glass exhumed in the extremely rare mantle xenoliths that were erupted at Bezymianny in 2007.

A zone of high pressure fractionation above the amphibole stability limit is also consistent with local seismic observations of a thickened crust (up to 42 km) in the region surrounding Bezymianny, likely due to extensive basaltic underplating (Churikova et al., 2001; Balesta, S. T., 1991). Alternatively, high pressure crystal fractionation could have been generated within the region of deep magma storage recently proposed by Koulakov et al. (2011) using seismic tomography.

A final test of both the mixing and fractionation models can be performed by considering the model results along with the liquid compositions calculated from amphiboles. If

the results of the fractionation model are valid, then it should be possible to reproduce the mixing end-members, which represent whole rock compositions, by taking phenocrysts that are similar to the fractionating assemblages and adding liquids to them. The liquid compositions calculated via the chemometric amphibole equations of RR12 then provide an opportunity to test both the mixing and fractionation models simultaneously.

As mentioned previously, the low pressure amphiboles, which were far more abundant in the earlier eruptions, are likely to be a component of EM-A, therefore these low-P amphiboles provide appropriate estimated liquid compositions for this end-member. EM-B is the only other mixing end-member that requires amphibole crystallization, suggesting that the high pressure amphiboles are a component of EM-B. The earliest sample with multiple high pressure amphiboles is sample B-65, a juvenile clast of a pyroclastic flow erupted in 1965. We use these amphiboles to estimate the high pressure liquid composition.

Using least squares optimization, we were able to find a range of possible combinations of mineral assemblages that are both consistent with the fractionation model and can be combined with the liquid compositions (calculated using RR12) to reproduce the whole rock compositions of EM-B and EM-A (major elements fit within 1%, TiO_2 and K_2O fit within 9%). The best fit solution can be found in Appendix A1.2. The data in this study thus are consistent with a model in which independent mixing end-members are produced from a common parental magma by crystal fractionation at different pressures. Though the mixing end-members may have a more complicated origin, the petrological data and analysis do not require it.

1.5.5 Physical model

A physical model of the Bezymianny magma system consistent with the above analysis must provide a mechanism for the storage and crystal fractionation of a single parental magma

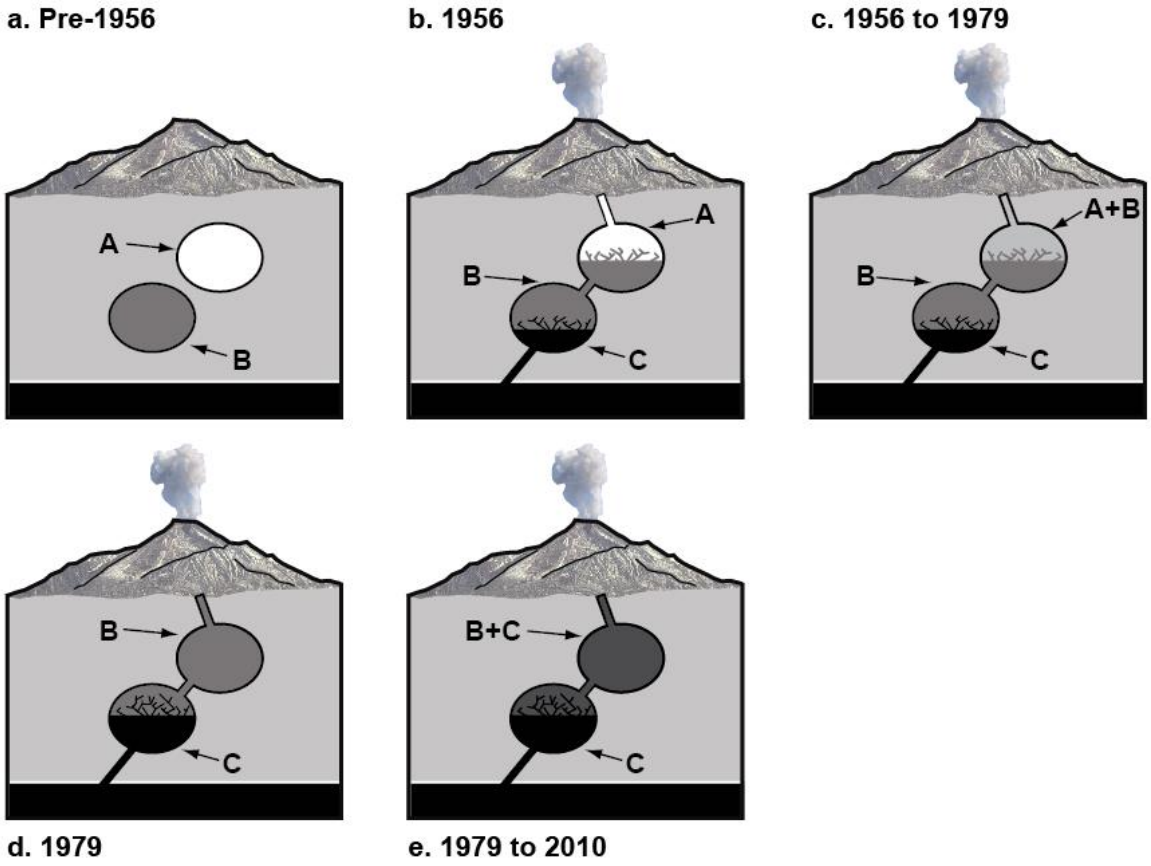

Figure 1.10: A cartoon model of physical processes capable of reproducing the model findings of this study. (a) Prior to 1956, the three mixing components of Bezymianny evolved in isolation, via crystal fractionation of a common source. (b) In 1956, influx of mafic magma into the lower chamber triggers an eruption. The 1956 eruption samples primarily the original composition of the upper magma chamber. (c) Between 1956 and 1979, the EM-A magma that originally dominated the upper chamber becomes increasingly diluted by EM-B magma, which originally filled the lower chamber. (d) By 1979, influence of EM-A magma has become very minor. Compositions of erupted magmas in the late 70s are primarily composed of EM-B. (e) Between 1979 and 2010, the erupted compositions become increasingly dominated by EM-C.

at three discrete pressures. Magmas stored at each of these pressures mix together in various proportions to form the erupted compositions of Bezymianny lavas. Following the end-member-mixing-analysis, the earliest episodes of the current eruptive cycle primarily tapped the lowest pressure reservoir (RES-1), which is at a pressure of 200 to 300 MPa, and which initially held magma similar in composition to EM-A. Between 1956 and 1977 the eruptive products became increasingly dominated by EM-B magma, which had been stored at a somewhat higher pressure

(500 to 750 MPa) in a second, deeper reservoir (RES-2). Starting in 1977 EM-C magma (the end-member produced by the lowest amount of fractionation at the highest pressure), began to mix into the erupted magmas. By 2010 EM-C accounted for ~56% of the total erupted composition. This constant influx of mafic magma is consistent with the results of Shcherbakov et al. (2011), who found evidence for frequent mafic recharge of the Bezymianny system between 2000-2007 on the basis of plagioclase zoning.

As shown in Figure 1.10, it is likely that RES-1 and RES-2 are connected in series. The trends towards increasingly mafic liquid compositions within each of these reservoirs, demonstrated using the chemometric amphibole equations of RR12 (Figure 1.7c), show that both RES-1 and RES-2 are both continuously replenished by mafic magma beginning soon after the onset of the eruptive cycle. The results of end-member mixing analysis show that the magma initially contained in RES-1 is injected with magma from RES-2, while RES-2 is apparently replenished by mafic magma (EM-C), from depth. Only RES-1 is directly connected to the vent, and so the erupted composition at the beginning of the current eruptive cycle is dominated by EM-A. Between 1956 and 1977 the EM-A magma in RES-1 erupted and was then gradually diluted by EM-B magma, drawn from RES-2. The EM-C laden magma was then drawn upward, toward RES-1, and erupted.

1.5.6 Comparison to Mount St. Helens and Soufrière Hills

Bezymianny volcano has been compared to Mount St. Helens (MSH) in terms of seismicity, eruptive dynamics, deposits, and petrology (Belousov et al., 2007; Thelen et al., 2010). However, the physical model of Bezymianny's plumbing system described above differs significantly from the detailed Pallister et al. (1992) and Pallister et al. (2008) models of MSH. During the 1980-1986 eruption of MSH, the erupted material was initially composed of 64-65%

SiO_2. As the eruption proceeded, wt% SiO_2 in the MSH lava decreased, reaching 61% by the middle of 1981. At this point, SiO_2 concentrations began to rise, and by 1986 had rebounded back to 64%. The magmas from the entire 1980-1986 episode were drawn from a depth of about 8.6 km. The 2004-2006 MSH eruptive products had a constant SiO_2 concentration of about 65%, and were drawn from a depth of about 5.2 km.

The magma system at MSH is modeled as a large, compositionally stratified reservoir; the compositional variations in this model are essentially a result of the reservoir being tapped at varying depths. Pallister et al. 1992 demonstrate that the shift towards more mafic magmas in 1981 can be produced as the fluid dynamic result of prior magma withdrawal. The deeper, less silicic magma is drawn into the conduit as the overlying dacitic magma is erupted. As the eruption slows down, the more buoyant dacitic magma once again dominates erupted compositions. The compositional variations in the 1980-1986 MSH lavas appear to be consistent with two-component mixing. The 2004-2006 eruption produced magmas with compositions that do not lie along the 1980-1986 trend, and are best accounted for as a separate batch of magma that pooled just beneath the roof of the reservoir (Pallister et al. 2008).

Soufrière Hills volcano (SHV), which is also similar to Bezymianny in terms of recent activity and eruptive dynamics (Belousov et al., 2007), may resemble it much more closely in terms of its underlying magma system than MSH. While the bimodal pressure distribution derived from the amphibole compositions of Bezymianny lavas is not seen at MSH, it has been observed within the amphiboles of SHV (Figure 1.11, adapted from Figure 1.6 of Ridolfi et al., 2010). At SHV, the existence of two discrete reservoirs within the crust has also been independently proposed on the basis of magma efflux and surface deformation, with crustal chambers at 6 km and 12 km below the surface (Elsworth et al. 2008). Though the crisp temporal trends in bulk erupted lava compositions at Bezymianny are not present at SHV, the

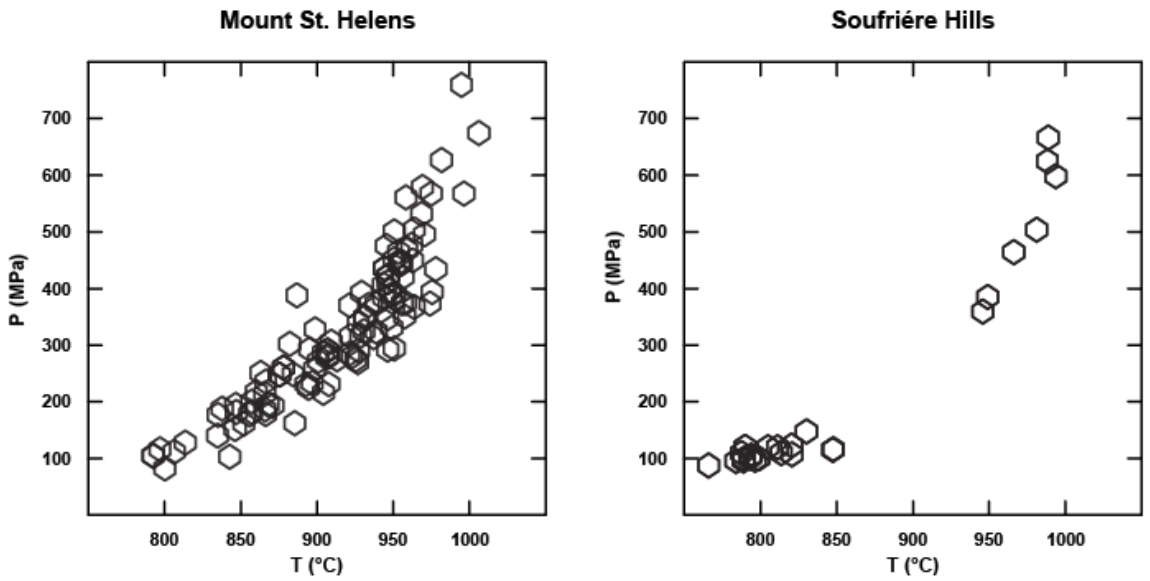

Figure 1.11: Pressure and temperature ranges in equilibrium with amphiboles from Mount St. Helens and Soufrière Hills. Figure adapted from Figure 6 of Ridolfi et al. (2010), using the thermobarometric equations from that study.

lavas at SHV are not well homogenized, and contain abundant mafic enclaves (Zellmer at al., 2003). Barclay et al. (2010) noted that the number of mafic enclaves at SHV has increased significantly between 1997 and 2007; thus, on a broader scale, the bulk erupted composition of SHV magmas is also becoming systematically more mafic with time. For these reasons, while the MSH system appears to be quite different from that of Bezymianny, SHV may be an excellent analog. Both the chemical trends examined in this study, as well as Shcherbakov et al. (2011)'s study of plagioclase phenocryst zoning, strongly suggest that the Bezymianny system is undergoing recharge by mafic magma from depth. This contrasts with MSH, where there is no chemical evidence requiring models to incorporate recent emplacement of mafic magma.

It is worth considering what factors may trigger episodes of mafic recharge, which are generally associated with large-amplitude eruptive cycles. The 1980 eruption at MSH was triggered by rapid unloading of pressure owing to a large earthquake-generated-landslide, rather than an influx of mafic magma from below (Pallister et al., 1992). Though the current activity at MSH does not appear to be actively driven by mafic recharge, there is evidence for

recharge at MSH during the earlier Kalama eruptive period, which started in 1480 and lasted about 300 years (Pallister et al., 1992). While it is certainly the case that the emplacement of mafic magma can initiate an eruptive cycle (e.g., Pinatubo, 1991, according to Pallister et al., 1996), it is also conceivable that an eruptive cycle triggered by a mechanism similar to the 1980 MSH eruption could itself lead to a new episode of mafic recharge. Such an eruptive episode, though not characterized by an initial influx of mafic magma, could result in significant unloading of the underlying system as the volcano erupts, which may in turn cause new magma to be drawn up from depth. The onset of the current eruptive cycle at Bezymianny is illustrated in Figure 1.10 as the result of mafic recharge, though Bezymianny's deep mafic component (EM-C) does not appear to have contributed significantly to bulk rock compositions until at least 22 years after the volcano reawakened (Figure 1.9c). From our data, it is not possible to determine whether the initial eruptions of the current eruptive cycle were driven by mafic recharge, or the mafic component began to infiltrate the lower chamber as a result of the initial eruptions. Collaborative work combining thorough seismic, geodetic, and chemical datasets for individual volcanoes through time may provide some resolution of such questions in the future.

1.6 Conclusions

This study provides constraints from bulk rock trace element and amphibole major element concentrations on the magma supply system of Bezymianny volcano. Our findings can be summarized as follows:

(1) The major and trace element variations of Bezymianny lavas require that magma mixing caused the eruptive products of Bezymianny to become increasingly mafic with time.

(2) Major element compositions of Bezymianny amphiboles have a bimodal distribution, which likely correspond to crystallization in two discrete reservoirs, with one between 200 and 300

MPa and another between 500 and 750 MPa. This suggests that the Bezymianny mixing components were initially stored in separate reservoirs, rather than a single compositionally zoned reservoir.

(3) Kinks in the arrays of several trace element plots, together with end-member mixing analysis, demonstrate that a total of three mixing components are both necessary and sufficient to account for the bulk compositions of all Bezymianny lavas, as well as the majority of enclaves.

(4) The compositions of the three mixing components, determined via end-member-mixing-analysis, can be produced from a common parental magma. If end-member magma compositions were produced from a common parental magma, it must be the case that each was produced via a unique fractionating mineral assemblage. These unique mineral assemblages are likely caused by different pressures of crystal fractionation.

(5) The constraints listed above can be combined to infer a physical model of the Bezymianny system from 1956 to 2010. Though Bezymianny is in many regards very similar to MSH, the physical model proposed in this work differs in several important ways from models of MSH, while models of SHV are much better analogs.

The model proposed can be tested by experimental studies under the appropriate conditions. Isotopic studies could be used to test whether the magmas of the current eruptive cycle were derived from a common parent, and U-series data could test or constrain the proposed timing.

1.7 **References**

Al'meev, R., Ariskin, A., Ozerov, A. and Kononkova, N., 2002. Problems of the stoichiometry and thermobarometry of magmatic amphiboles: an example of hornblende from the andesites of Bezymyannyi Volcano, Eastern Kamchatka. Geochemistry International, 40, 723-738.

Bacon, C.R. and Druitt, T.H., 1988. Compositional evolution of the zoned calcalkaline magma chamber of Mount Mazama, Crater Lake, Oregon. Contributions to Mineralogy and Petrology, 98, 224-256.

Balesta, S.T., 1991. Earth crust structure and magma chambers of the area of present Kamchatka volcanism. In: Fedotov, S. A. and Masurenkov, Y. P. (Eds.), Active volcanoes of Kamchatka, vol 1. Nauka, Moscow, pp. 166-197.

Barclay, J.,Herd, R. A., Edwards, B. R., Christopher, T., Kiddle, E. J., Plail, M., and Donovan, A., 2010, Caught in the act: Implications for the increasing abundance of mafic enclaves during the recent eruptive episodes of the Soufrière Hills Volcano, Montserrat, Geophysical Research Letters,37:L00E09.

Belousov, A., Voight, B. and Belousova, M., 2007. Directed blasts and blast-generated pyroclastic density currents: a comparison of the Bezymianny 1956, Mount St Helens 1980, and Soufrière Hills, Montserrat 1997 eruptions and deposits. Bulletin of Volcanology, 69(7), 701-740.

Bogoyavlenskaya, G.E., Braitseva, O.A., Melekestsev, I.V., Maximov, A.P., and Ivanov, B.V., 1991. Bezymianny volcano. In: Fedotov, S. A. and Masurenkov, Y. P. (Eds.), Active volcanoes of Kamchatka, vol 1. Nauka, Moscow, pp. 166-197.

Braitseva O.A., Melekestsev, I.V., Bogoyavlenskaya, G.E., and Maksimov, A.P., 1991. Bezymianny Volcano: Eruptive history and dynamics. Volcanology and Seismology, 12, 165-195 (in Russian).

Churikova, T., Dorendorf, F. and Worner, G., 2001. Sources and Fluids in the Mantle Wedge below Kamchatka, Evidence from Across-arc Geochemical Variation. Journal of Petrology, 42(8), 1567-1593.

Class, C.D., Miller, D.M., Goldstein, S.L., and Langmuir, C.H., 2000. Distinguishing melt and fluid subduction components in Umnak volcanics, Aleutian arc. Geochemistry, Geophysics, Geosystems, 1, Paper number 1999GC000010.

Couch, S., Sparks, R.S.J., Carroll, M.R., 2001. Mineral disequilibrium in lavas explained by convective self-mixing in open magma chambers. Nature, 411, 1037-1039.

Donovan, J.J., Kremser, D., and Fournelle, J.H., 2007. Probe for Windows User's Guide and Reference, Enterprise Edition, pp. 355.

Eichelberger, J.C., Izbekov, P.E. and Browne, B.L., 2006. Bulk chemical trends at arc volcanoes are not liquid lines of descent. Lithos, 87(1-2), 135-154.

Elsworth, D., Mattioli, G., Taron, J., Voight, B., Herd, R., 2008. Implications of magma transfer between multiple reservoirs on eruption cycling. Science, 322, 246-248.

Elliott, T., Plank, T., Zindler, A., White, W., and Bourdon, B., 1997. Element transport from slab to volcanic front at the Mariana arc. Journal of Geophysical Research, 102 (B7), 14991-15019.

Fedotov, S.A., Zharinov, N.F., and Gontovaya, L.I., The Magmatic System of the Klyuchevskaya Group of Volcanoes Inferred from Data on Its Eruptions, Earthquakes, Deformation, and Deep Structure, Journal of Volcanolgy and Seismology, 4, 3–32.

Girina, O.A., this issue. Chronology of Bezymianny Volcano activity, 1956-2010. Journal of Volcanology and Geothermal Research.

Grove, T.L., Elkins-Tanton, L.T., Parman, S.W., Chatterjee, N., Müntener, O. and Gaetani, G.a., 2003. Fractional crystallization and mantle-melting controls on calc-alkaline differentiation trends. Contributions to Mineralogy and Petrology, 145, 515-533.

Grove, T.L., Baker, M.B., Price, R.C., Parman, S.W., Elkins-Tanton, L.T., Chatterjee, N., Müntener, O., 2005. Magnesian andesite and dacite lavas from Mt. Shasta, northern California: products of fractional crystallization of H_2O-rich mantle melts. Contributions to Mineralogy and Petrology 148, 542–565.

Gust, D.A. and Perfit, M.R., 1987. Phase relations of a high-Mg basalt from the Aleutian Island Arc: Implications for primary island arc basalts and high-Al basalts. Contributions to Mineralogy and Petrology, 97, 7-18.

Hildreth, W., 1983. The compositionally zoned eruption of 1912 in the Valley of Ten Thousand Smokes, Katmai National Park, Alaska. Journal of Volcanology and Geothermal Research, 18, 1-56.

Hildreth, W. and Moorbath, S. 1988. Crustal contributions to arc magmatism in the Andes of Central Chile. Contributions to Mineralogy and Petrology, 98, 455-489.

Izbekov, P.E., Eichelberger, J.C., and Ivanov B.V., 2004. The 1996 eruption of Karymsky volcano, Kamchatka: Historical record of basaltic replenishment of an andesite reservoir. Journal of Petrology, 45, 2325–2345.

Kadik A.A., Maksimov, A.P., Ivanov, B.V., 1986. Physico-chemical Conditions for Crystallization of Andesites. Nauka, Moscow, pp. 158 (in Russian).

Kent A.J.R., Darr C., Koleszar A.M., Salisbury M.J., Cooper K.M., 2010. Preferential eruption of andesitic magmas through recharge filtering. Nature Geoscience 3 (9), 631–636.

Koulakov, I., Gordeev, E. I., Dobretsov, N. L., Vernikovsky, V. A., Senyukov, S., Jakovlev, A., 2011. Feeding volcanoes of the Kluchevskoy group from the results of local earthquake tomography. Geophysical Research Letters., 38, L09305.

Kent A.J.R., Darr C., Koleszar A.M., Salisbury M.J., Cooper K.M., 2010. Preferential eruption of andesitic magmas through recharge filtering. Nature Geoscience 3 (9), 631–636.

Liu T.C., Chen B.R., Chen, C.H., 2000. Melting experiment of a Wannienta basalt in the Kuanyinshan area, northern Taiwan, at pressures up to 2.0 GPa. Journal of Asian Earth Sciences 18, 519-531.

Malyshev, A. I., 2000. Life of the volcano. Ekaterinburg: Ural Branch of Russian Academy of Sciences (in Russian).

Melekestsev, I. V., Khrenov, A. P., and Kozhemyaka, N. N., 1991. The Tectonic Setting and a General Review of Volcanoes in the Northern Group and in the Sredinnyi Range. In: Fedotov, S. A. and Masurenkov, Y. P. (Eds.) Active Volcanoes of Kamchatka, vol. 1. Moscow: Nauka, pp. 74–81.

Miesch, A.T., 1980. Scaling variables and interpretation of eigenvalues in principal component analysis of geologic data. Journal of the International Association for Mathematical Geology, 12, 523-538.

Newman, S., Lowenstern, J.B., 2002. VolatileCalc: a silicate melt–H2O–CO2 solution model written in Visual Basic for excel. Computers and Geosciences, 28, 597-604.

Pallister, J.S., Hoblitt, R.P., Crandell, D.R., and Mullineaux, D.R., 1992, Mount St. Helens a decade after the 1980 eruptions; magmatic models, chemical cycles, and a revised hazards assessment: Bulletin of Volcanology, 54, 126–146.

Pallister, J.S., Hoblitt, R.P., Meeker, G.P., Knight, R.J., and Siems, D.F., 1996, Magma mixing at Mount Pinatubo; petrographic and chemical evidence from the 1991 deposits. In: Newhall, C.G., and Punongbayan, R. (Eds.) Fire and mud; eruptions and lahars of Mount Pinatubo, Philippines, Seattle: University of Washington Press, pp. 687–732.

Pallister, J.S., Thornber, C.R., Cashman, K.V., Clynne, M.A., Lowers, H.A., Mandeville, C.W., Brownfield, I.K., Meeker, G.P., 2008. Petrology of the 2004–2006 Mount St. Helens lava dome-implications for magmatic plumbing and eruption triggering. In: Sherrod, D.R., Scott, W.E., Stauffer, P.H. (Eds.), A Volcano Rekindled: The Renewed Eruption of Mount St. Helens, 2004–2006. U.S. Geolog. Surv. Prof. Pap., p. 1750.

Plank, T., Langmuir, C.H., 1988. An evaluation of the global variations in the major element chemistry of arc basalts. Earth and Planetary Science Letters, 90, 349-370.

Plechov, P.Y., Tsai, A.E., Shcherbakov, V.D. and Dirksen, O.V., 2008. Opacitization conditions of hornblende in Bezymyannyi volcano andesites (March 30, 1956 eruption). Petrology, 16, 19-35.

Ridolfi, F., Puerini, M., Renzulli, A., Menna, M., Toulkeridis, T., 2008. The magmatic feeding system of El Reventador volcano (Sub-Andean zone, Ecuador) constrained by texture, mineralogy and thermobarometry of the 2002 erupted products. Journal of Volcanology and Geothermal Research, 176, 94–106.

Ridolfi, F., Renzulli, A., Puerini, M., 2010. Stability and chemical equilibrium of amphibole in calc-alkaline magmas: an overview, new thermobarometric formulations and application to subduction-related volcanoes. Contributions to Mineralogy and Petrology, 160, 45-66.

Ridolfi, F. and Renzulli, A., 2012. Calcic amphiboles in calc-alkaline and alkaline magmas: thermobarometric and chemometric empirical equations valid up to 1,130°C and 2.2 GPa. Contributions to Mineralogy and Petrology, 163(5), 877-895.

Rock, N.M.S. and Leake, B.E., 1984. The International Mineralogical Association amphibole nomenclature scheme: computerization and its consequences. Mineralogical Magazine, 48, 211-227.

Scott, V.D., Love, G., and Reed, S.J.B., 1995. Quantitative Electron-Probe Analysis. Ellis Horwood Limited, Hemel Hempstead, Hertfordshire, England, pp. 311.

Shcherbakov, V.D., Plechov, P.Y., 2010. Petrology of mantle xenoliths in rocks of the Bezymyannyi Volcano (Kamchatka). Doklady Earth Sciences, 434, 1317-1320.

Shcherbakov, V.D., Plechov, P.Y., Izbekov, P.E. and Shipman, J.S., 2011. Plagioclase zoning as an indicator of magma processes at Bezymianny Volcano, Kamchatka. Contributions to Mineralogy and Petrology, 162, 83-99.

Sparks, R.S.J., Sigurdsson, H., and Wilson, L., 1977. Magma mixing: a mechanism for triggering acid explosive eruptions. Nature, 267, 315–318.

Streck, M. J., Dungan, M. A., Malavassi, E., Reagan, M. K. and Bussy, F., 2002. The role of basalt replenishment in the generation of basaltic andesites of the ongoing activity at Arenal volcano, Costa Rica: evidence from clinopyroxene and spinel. Bulletin of Volcanology, 64, 316–327.

Sun, Shen-su and McDonough, W.F., 1989. Chemical and Isotopic Systematics of oceanic basalts: implications for mantle composition and processes. Saunders, A.D. and Norry, M.J. (Eds.), Magmatism in the Ocean Basins, Spec. Publ. Vol. Geol. Soc. Lond., 42, pp. 313-345.

Thelen, W., West, M.E., Senyukov, S., 2010. Seismic characterization of the Fall 2007 eruptive sequence at Bezymianny Volcano, Russia. Journal of Volcanology and Geothermal Research, 194, 201–213.

Timerbaeva, K. M., 1967. The petrology of Kliuchevskoi group of volcanoes. Moscow: Nauka (in Russian).

Tindle, A. G. and Webb, P. C., 1994. Probe-AMPH: A spreadsheet program to classify microprobe-derived amphibole analyses. Computers and Geosciences, 20, 1201-1228.

Weltje, G.J., 1997. End-member modeling of compositional data: Numerical-statistical algorithms for solving the explicit mixing problem. Mathematical Geology, 29, 503-549.

Zellmer, G. F., Hawkesworth, C. J., Sparks, R. S. J., Thomas, L. E., Harford, C. L., Brewer, T. S. and Loughlin, S. C., 2003. Geochemical evolution of the Soufrière Hills Volcano, Montserrat, Lesser Antilles volcanic arc. Journal of Petrology 44, 1349–1374.

Chapter 2: The global chemical systematics of arc front stratovolcanoes: Evaluating the role of crustal processes

[Turner, S.J., Langmuir, C., 2015. The global chemical systematics of arc front stratovolcanoes: Evaluating the role of crustal processes. Earth and Planetary Science Letters, in press]

Abstract

Petrogenetic models for convergent margins should be consistent with the global systematics of convergent margin volcanic compositions. To explore these systematics as comprehensively as possible, we assembled a global database of geochemical analyses from arc front stratovolcano samples, using a newly developed tool for database assembly and screening from the on-line GEOROC database. For 227 volcanoes from 31 convergent margins, data are first averaged by volcano and then by arc to explore overall behavior. With the exception of three arcs influenced by mantle plumes and Peru/N. Chile, which is built on exceptionally thick crust, there are remarkably coherent systematics among major and trace elemental concentrations and ratios, as well as correlations between these chemical parameters and the thickness of the overlying arc crust. Consistent relationships exist using three different methods of data normalization, and persist across a wide range of Mg# [Mg#=Mg/(Mg+Fe)]. The correlations among major element concentrations confirm previous work, with $Na_{6.0}$ correlating negatively with $Ca_{6.0}$ and positively with crustal thickness. Additional strong correlations are observed between major element concentrations, trace element concentrations, and trace element ratios (e.g., La/Yb, Dy/Yb, Zr/Sm, Zr/Ti). Positive correlations include elements from "fluid mobile," "high field strength," and "large ion lithophile" element groups, which have concentrations that vary by a factor of five or more. Incompatible element enrichments also correlate well with crustal thickness, with the greatest enrichment found at arcs with the thickest crust. To evaluate the importance of intra-crustal processes in creating these systematics, the effects of low and high pressure crystal fractionation, deep crustal mixing of highly enriched melts, and a crustal buoyancy filter are evaluated. High pressure fractionation

produces intermediate magmas enriched in aluminum, but such magmas are rare. Furthermore, differences among magma compositions at various volcanic arcs persist from primitive to evolved compositions, so the global variations cannot be produced by crystal fractionation at any pressure. The linear relationships among elements would be consistent with mixing between primary and enriched magmas, and permit calculation of the theoretical enriched end members. The compositions of calculated mixing end-members, however, are not like those expected anywhere in the deep crust, or like any known rock composition. The large scale variations are therefore likely to be generated by processes in the subducting slab or mantle wedge, rather than the crust. These systematics of global arcs must be satisfied by any successful model of convergent margin processes.

2.1 Introduction

Constraining the diverse controls on the compositions of convergent margin magmas is central to our understanding of the plate tectonic geochemical cycle, which ultimately influences all crustal and mantle reservoirs. There is widespread agreement on a general framework: a flux from the down-going slab to the mantle wedge causes melting, and produces primary magmas. These magmas are modified during ascent and differentiation in the crust. The need for multiple components derived from subducted oceanic lithosphere and sediment is also abundantly clear (Morris et al., 1989; Miller et al., 1993; Elliott et al., 1997). Still uncertain, however, are the relative contributions from these sources and processes, and what aspects of arc volcanic compositions they produce. Some authors have argued for primary control of a crustal filter (e.g., Hildreth and Moorbath, 1988). Others have argued for a critical role for varied extents of melting of the mantle wedge (Plank and Langmuir, 1988), for reactive transport in the mantle wedge (Kelemen, 1995; Straub et al., 2008), and more recently for control by the thermal structure of the subducting slab (Ruscitto et al., 2012). Many of these proposals are based on

regional studies, data sets restricted to a few elemental compositions and ratios, or conceptual arguments.

Here we consider what new information and constraints a global data set can provide to clarify our understanding of convergent margin processes. All the proposed models predict certain relationships among the compositions of erupted magmas and the physical conditions of subduction. Crustal processes, for example, should be influenced by the thickness and composition of the crust on which the arc is constructed. Variations in mantle wedge melting should result from changes in the wedge thermal structure. Compositional control by the subducting slab should correspond with slab age, convergence rate, and depth to slab. Reactive transport should be influenced by the thickness and thermal structure of the mantle wedge.

To evaluate these relationships, a coherent global database is necessary. The first aim of this study is to provide a high quality dataset that is inclusive and global – incorporating major element, trace element, and Sr, Nd, Hf and Pb isotope compositions of arc stratovolcanoes along volcanic fronts worldwide. The second aim is to highlight variations among chemical parameters that must be accounted for by successful models of the subduction system and to explore which subduction parameters exert a controlling influence on the global chemical variations. Competing models can then be evaluated quantitatively to determine which best account for the observed systematics.

Past studies have carried out global analyses of arc volcanoes, but were more limited in the parameters considered. Early studies emphasized variations perpendicular to the volcanic front (Dickenson and Hatherton, 1967; Condie and Potts, 1969). Leeman (1983) found a global correlation between crustal thickness and some major element ratios as well as Sr isotopic compositions, interpreted as the result of enhanced interaction between melts and crust during transport. Plank and Langmuir (1988) demonstrated strong correlations for arc front lavas between major elements and

crustal thickness, and weaker correlations with other subduction parameters. These trends were found to be inconsistent with generation by intra-crustal processes, and attributed to variations in the extent of melting of their mantle source regions. Ruscitto et al. (2012) proposed that the H_2O/Ce ratio of primitive melt inclusions varied with proxies for the thermal state of the subducting slab.

This paper presents a more inclusive global data set to evaluate the importance of crustal processes on mafic and intermediate (> 4 wt. % MgO) magma compositions. We find, in accordance with previous work, compelling correlations between the thickness of overlying arc crust and the compositions of these magmas. Various models, such as Annen et al. (2006), have suggested that deep crustal processes may be ubiquitous in the evolution of arc magmas. It is a primary goal of this paper to investigate whether such processes are 1) supported by the global geochemical data and 2) may be responsible for the global geochemical trends. Chapter 3 extends this analysis to incorporate the full suite of subduction parameters in an effort to provide a comprehensive view of global arc volcanism and the outstanding questions that remain unresolved.

Arc magmas are generally more evolved than ocean ridge magmas due to fractionation processes in the crust. We seek to determine whether variations in crustal differentiation at convergent margins can produce signals that might be confused with those from primary magma compositions. We additionally provide evidence that stratocone magmas from global arcs do not generally differentiate at lower crustal levels.

2.2.1 The database

Stratovolcanoes are the primary magmatic flux at convergent margins and define the volcanic fronts of continental and island arcs. Here we study volcanic front magmas as designated largely by Syracuse and Abers (2006). While smaller eruptive centers, mostly monogenetic cones, are abundant in

continental arc settings, their eruptive volume is subsidiary to continental stratovolcanoes. For island arcs these small cones are either not present or are poorly sampled, and so samples from monogenetic cones are excluded from our database to avoid potential bias. Stratovolcanoes not on a volcanic front have also been excluded. Where dates were available, samples older than 200ka were excluded in order to mitigate the potential effects of temporal variation in chemistry.

The raw data used in this study were primarily extracted from the GEOROC geochemical database (http://georoc.mpch-mainz.gwdg.de/georoc/ accessed September 2013), with minor additions for some arc segments (Appendix A2.1). While GEOROC contains the most complete set of published analyses of arc lavas worldwide, additional processing was necessary to produce a suitably "clean" database. First, GEOROC suffers from occasional data entry errors and misattributed data. These outliers can have large effects on arc averages and apparent correlations among chemical parameters. Second, GEOROC contains no internal tools to filter out less accurate analytical methods. The GEOROC data compilation algorithm preferentially orders analytical methods for various elements, but when no high precision method is available, data gathered via any lower quality or unattributed methods are inserted automatically. These problems lead to outliers on plots of raw compiled GEOROC data, even among data matching published sources.

To produce a reliable data set, all outliers were cross-referenced against the original publications. In some instances, chemical analyses of a single volcanic center were available from multiple publications, making it possible to identify analytical errors for certain elements from a given source. Where identified, outlying data due to probable analytical errors were removed. Data reported with low precision by rounding were removed in instances where concentrations are low. Where raw data files were modified, original data entries have been deactivated but retained and tagged in the raw data files for reference. In addition, data were automatically removed if collected prior to 1975, listed as "Extensively Altered," or if XRF data report a loss on ignition greater than 2%.

After assembly of the clean data set, data compilation scripts were developed to filter the data. For the elements Sc, V, Cr, Mn, Co, Ni, Cu, Zn, Ga, Ge, Rb, Sr, Y, Zr, and Ba, data were included where the method was either isotope dilution mass spectrometry, ICP-MS, XRF, AES, or INAA, with preference given in that order. The remaining trace elements include data measured only by isotope dilution mass spectrometry, ICP-MS, INAA, or DCPAES, again, with preference given in that order. Sufficient data existed for the Colombia and Ecuador region only if ICPOES data were also included for all trace elements, and so lower precision data were allowed for this segment only.

2.2.2 Filtering the database

Most arc magmas have undergone cooling and crystal fractionation during transfer from the melt region to the surface, and many other magmas are the products of either magma mixing or excess crystal accumulation within the crust (e.g., Eichelberger et al., 2006). One goal of this study is to assess the chemical variability of arc magmas independently of these effects, requiring additional data filtration. To ensure the observations from filtering methods are robust, a variety of filtering methods were tested. These data filters aim to remove the obvious effects of magma differentiation. Once applied, the residual signal can be used to interpret the importance of other processes, crustal or otherwise.

The first aim was to determine isotope and incompatible element ratios for global arcs. This is possible with a larger data set because incompatible element and isotope ratios are little affected by early-stage fractionation. To estimate these ratios, samples from within a broad range of MgO contents, from 4 wt. % to 12 wt. %, was adopted. When magmas within this MgO range are produced by mixing between mafic and felsic end-members, however, incompatible element ratios can be affected. Evolved, felsic magmas are highly enriched in incompatible elements, and may have trace element ratios

modified by accessory phase crystallization or other late-stage processes. Mixing products of primitive and evolved magmas may then inherit trace element ratios that are not representative of the primitive composition. A screen to eliminate such magmas can make use of the fact that evolved magmas have typically undergone large extents of plagioclase fractionation, leaving them with large negative Eu anomalies (Weill and Drake, 1973). When intermediate magmas are formed by mixing, they will inherit this Eu anomaly from the evolved end-member. Therefore only samples with Eu anomalies in the range of 0.85 to 1.1 were included. The Eu anomaly was calculated as either Eu_N/Eu^* or Eu_N/Eu^{**}, with $Eu^* = (Sm_N+Gd_N)/2$ and $Eu^{**} = (2*Sm_N+Tb_N)/3$. The Eu** term was only used for samples lacking Gd data, and shows a near perfect correlation with Eu* among samples for which both values can be calculated.

Element abundances, unlike incompatible element ratios, are strongly affected by fractionation processes. To ensure a constant reference point for global arcs, normalization to a constant index of fractionation is required. There are diverse views on appropriate normalization criteria (e.g., Niu and O'Hara, 2008; Gale et al., 2014). To ensure that the results are not dependent on the method of normalization, three different normalization methods have been used. All of these methods lead to consistent results.

Method one normalizes erupted lavas to constant MgO (Klein and Langmuir, 1987; Plank and Langmuir, 1988). For consistency with Plank and Langmuir (1988), we normalize to 6 wt. % MgO, though we employ a different method. To avoid uncertainties in liquid lines of descent for arc magmas, we do not correct the data along constant slopes or by linear regression. Instead, 6-values are calculated by bracketing, where the 6-value for a given volcano is calculated as the average concentration of a given element using samples with 5.5<wt. % MgO<6.5. In this way there is no "correction" of the data and the reported values represent actual measured compositions.

Methods two and three normalize to two different ranges of Mg# (Mg#=100*(Mg+Fe)/Mg). Primary mantle melts fall within a narrow range of Mg#, so magmas with similar Mg# have usually crystallized to similar extents. Bracketing was also used to calculate Mg# normalized values. “Mg#>60” values use samples with Mg# greater than 60, while “Mg#55” values use samples with 50<Mg#<60. Mg#>60 values should be most similar to primary magma compositions, though far fewer samples fall within this high Mg# range, and no high Mg# samples at all are reported for certain arcs. It is thus useful to consider both the higher and lower brackets of Mg#.

To automate data filtration, MATLAB scripts were written to remove outliers, select reliable analytical methods, apply the various screens and calculations to the data, and average estimates of subduction parameters (Syracuse and Abers, 2006) and crustal thickness from 20 literature sources (Appendix A2.2). The scripts permit construction of clean and filtered GEOROC data from diverse environments, and are available, along with the raw data files as in Supplementary Dataset A2.1.

The filtered data were averaged first within volcanoes, and then within arc segments (largely as defined by Syracuse and Abers, 2006). For trace element ratios, at least two data points were required for the calculation of both the volcano and segment averages. For 6-values and Mg# normalized values, a single point was permitted to represent a volcano, and two volcano values were required for segment averages. There is slightly more scatter among plots using Mg#>60 values, which are based on fewer data, although relative variations in average arc magma concentrations are independent of the normalization scheme. In addition to the normalized segment averages, raw, un-normalized segment averages were also calculated. These values are referred to as “Raw” averages, and are calculated from all samples with >4 wt. % MgO, with no additional filters applied.

The volcano averages and arc segment averages are presented in Supplementary Dataset A2.2. The total number of samples present in the unfiltered database is 4,846. Of these, 48% have greater

than 4 wt. % MgO. Raw volcano averages were calculated for 211 volcanoes, and filtered averages were calculated for 190 volcanoes, to produce 31 segment averages. Of these, trace element ratios were calculated for 150 volcanoes, and 6-values were calculated for 101 volcanoes.

It is important to note various drawbacks of the database. First, for many volcanoes, few data pass the filters mentioned above. For example, only 27% of $Na_{6.0}$ values for individual volcanoes are based on more than five samples. Second, because the filters applied for incompatible element and isotope ratios differ from those applied for element abundances, the ratio and abundance data sets are not directly comparable. For example, 62% of volcano average Dy/Yb values include more than five samples, while only 12% of $Yb_{6.0}$ values include more than five samples. Third, arc averages for some elements are based on very different numbers of volcanoes. For Izu and South Central Chile, most trace element ratios include 9 or 10 volcano averages, while for other segments, some values are based on only two volcanoes. There is a clear need for more comprehensive high quality datasets on a global scale.

2.3 Results

The segment averages reveal global systematics of the data for internal chemical relationships and correlations with subduction parameters. In view of the drawbacks of the data set, we first explore the robustness of the global relationships.

2.3.1 Variability of unfiltered data, and validity of normalization methods

There are clearly significant variations within individual arcs that are important for understanding arc processes (e.g., Class et al., 2000; Elliott et al., 1997; Patino et al., 2000). Nonetheless,

there are distinct average variations among global arcs. This is evident in Figures. 1-4 from the excellent correlations observed, and from the fact that the average standard deviation within single arc segments is much lower than the total range of the data (Figure 2.1). This observation holds true for all normalization schemes, as well as the raw averages from all samples with greater than 4 wt. % MgO. A few arc segments show slightly more variance for certain elements, such as Sr in the Aegean and New Britain. In both of these cases, the large standard deviation is due to a single outlier. In other cases, such as the Dy/Yb values calculated from only samples with Mg#>60, larger standard deviations are sometimes present in segments with more limited data availability. Within arc variations are important. Nonetheless, global systematics emerge.

There are excellent correlations among the different normalization schemes, even though there is often little overlap among their base sample sets. For all elements with significant compositional variation among arcs, 6-values are highly correlated with Mg#55 values, Mg#>60 values, and even the raw averages (Figure 2.1). This demonstrates that normalization of the data is not controlling the observed relationships. Furthermore, because the normalized values should eliminate the effects of low pressure differentiation, correlations between normalized and raw values indicate that the observed variability must be produced by some other process. The data set includes half of all sampled arc front stratovolcano lavas erupted from nearly all of the world's volcanic arcs, and so this conclusion is robust.

2.3.2 Results: Data outliers

Four arc segments included in the global analysis appear as outliers on various plots. Of these four arc segments, three (S. Costa Rica, N. Tonga, Aeolian) have been linked by numerous studies to nearby hot spot tracks and/or seismically imaged deep mantle plumes (e.g., Gazel et al., 2011; Falloon et al, 2007; Montelli et al., 2006). All of these arcs have elevated incompatible element abundances when

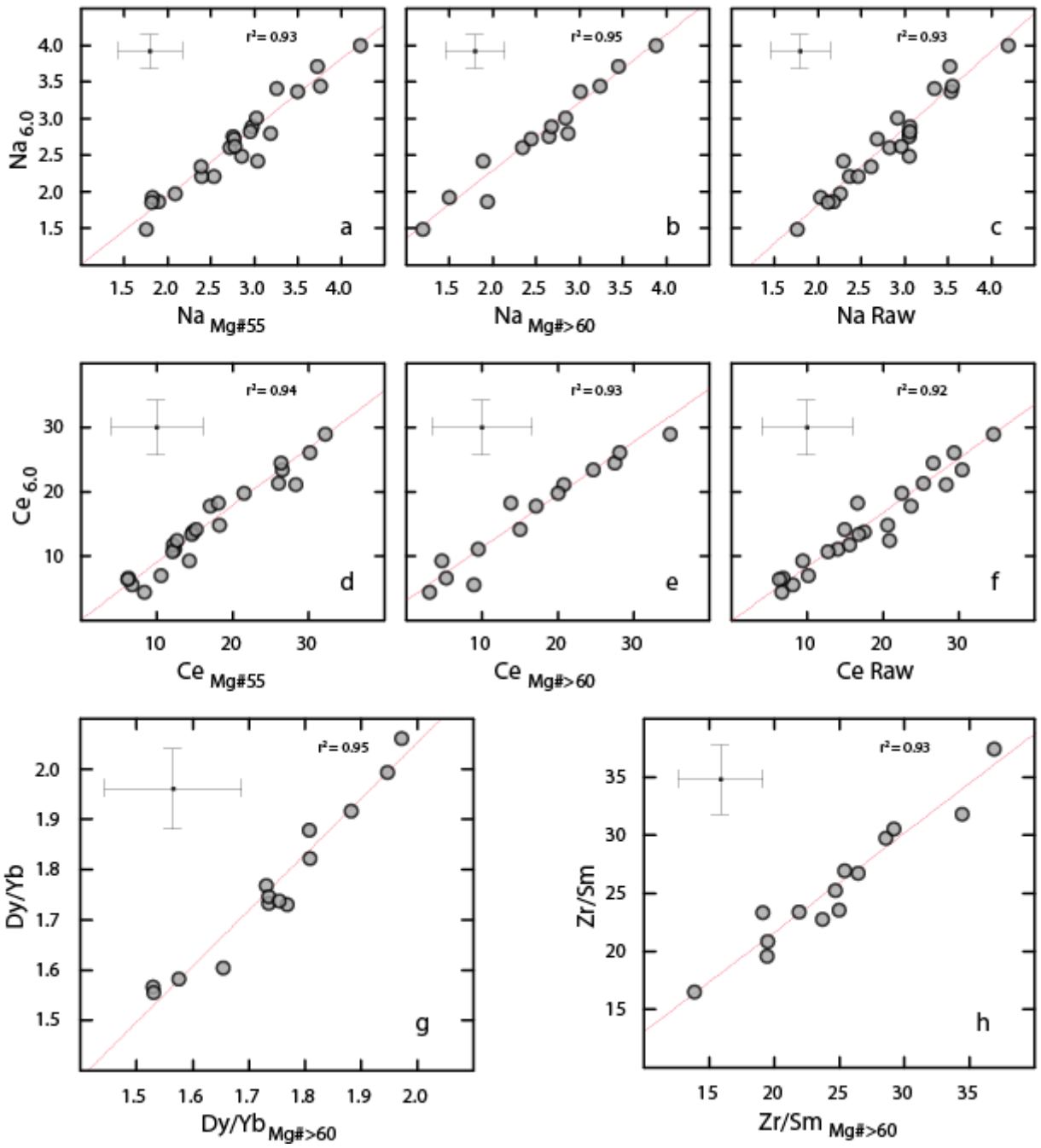

Figure 2.1: Direct comparison of data normalization and filtration methods used in this study. Each data point represents an arc segment average, based on volcano averages within the segment. For discussion of different normalization methods see main text. Red lines are best fit linear trendlines. The slope on plots of 6-values vs Mg#>60 values are generally around 0.9. Error bars show the average within-arc standard deviations. Arc averages are nearly identical for all normalization methods as well as for raw averages for all samples with >4 wt. % MgO. This observation holds true for all elements with significant variability among arcs.

compared to arcs apparently free of hot spot influences. Though of interest for understanding the details of interactions between hot spots and subduction zones, these hot spot influenced arcs are anomalous with regards to correlations between mafic arc chemistry and the physical subduction parameters, and are therefore excluded from figures and regressions.

In addition to the removal of arc segments associated with hot spots, the magma chemistry of the Peru/N. Chile segment is also anomalous, with isotopic ratios and certain incompatible elemental concentrations remarkably distant from all other averages. Insufficient data exist for this arc to calculate 6-values, and all other arcs have crustal thickness <47km, much less than the ~70 km thick crust underlying the central Andean arc. As similar isotopic anomalies are not found in any other arc segment, no other arc segment overrides crust approaching 70 km in thickness, and the Peru/N. Chile data are such outliers from a global perspective, we exclude Peru/N. Chile from further consideration here. In this arc, crustal processes may be overwhelmingly important.

2.3.3 Correlations among chemical parameters

Good correlations exist among many of the segment-averaged major element 6-values (Figure 2.2). As noted by Plank and Langmuir (1988), $Na_{6.0}$ correlates negatively with $Ca_{6.0}$ and $Fe_{6.0}$, and positively with $K_{6.0}$ and $Si_{6.0}$. There is relatively little variation in most $Al_{6.0}$ values, (17.5 - 18.5 $Al_{6.0}$.), though Tonga, Mexico, and Columbia/Ecuador all have somewhat lower $Al_{6.0}$ values of about 16.5 wt. %. There appears to be a weak correspondence between $Na_{6.0}$ and $Ti_{6.0}$, though low $Ti_{6.0}$ values for Mexico and Colombia/Ecuador lead to a lower r^2 between these elements. $Na_{6.0}$ also correlates well with $Mn_{6.0}$ and $P_{6.0}$ (r^2 values of 0.66 and 0.73). These systematic relationships are a primary characteristic of the global data set.

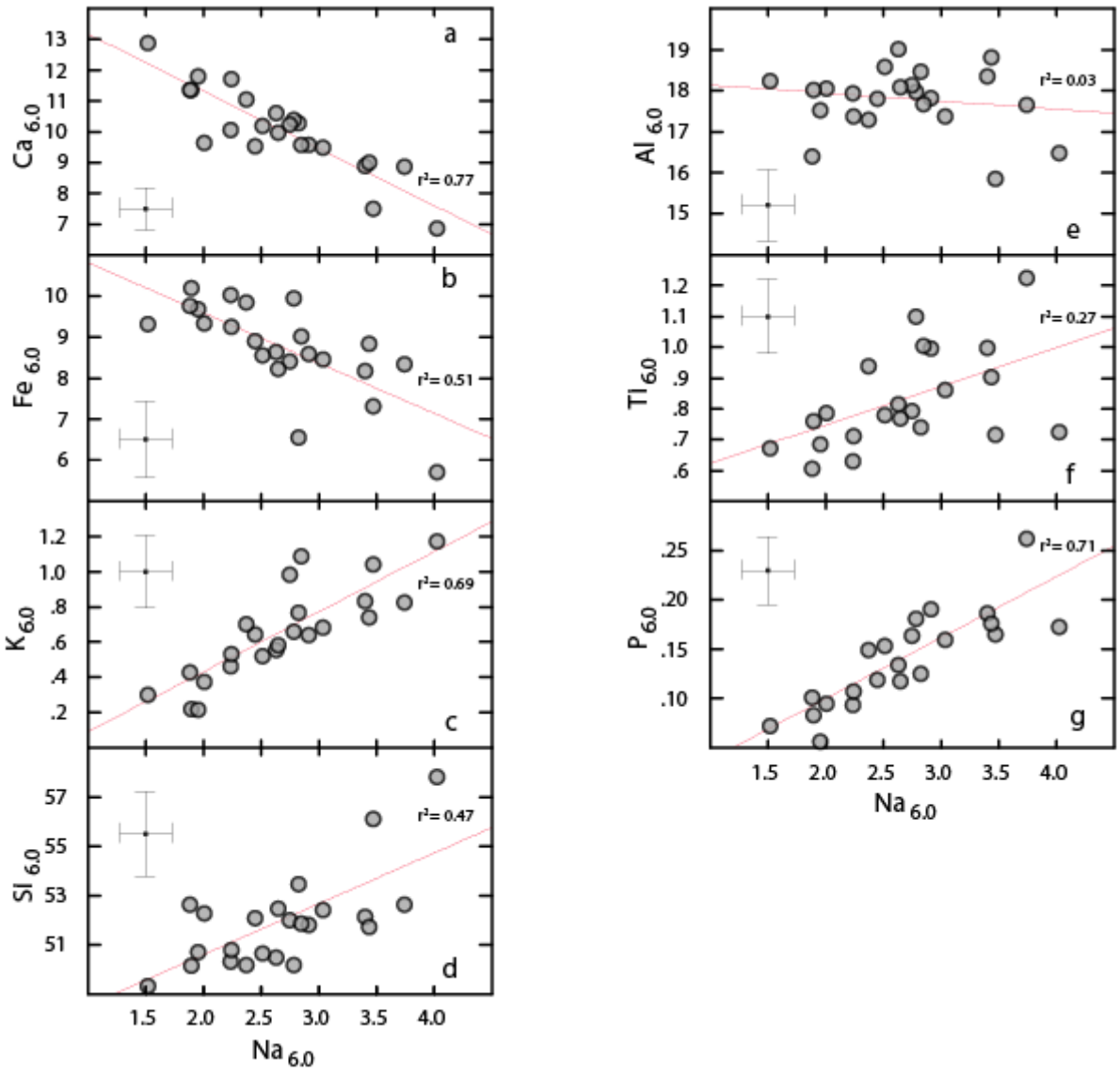

Figure 2.2: Major element 6-values for global arcs. $Na_{6.0}$ correlates negatively with $Fe_{6.0}$ and $Ca_{6.0}$, and positively with $K_{6.0}$ and $P_{6.0}$. Weaker positive correlations exists with $Si_{6.0}$ and $Ti_{6.0}$. The correlation between $Na_{6.0}$ and $Ti_{6.0}$ is weak as a result of outlying points (low $Ti_{6.0}$) for Mexico and Colombia/Ecuador. $Al_{6.0}$ shows little variation among arc segments. Error bars show average within arc standard deviation.

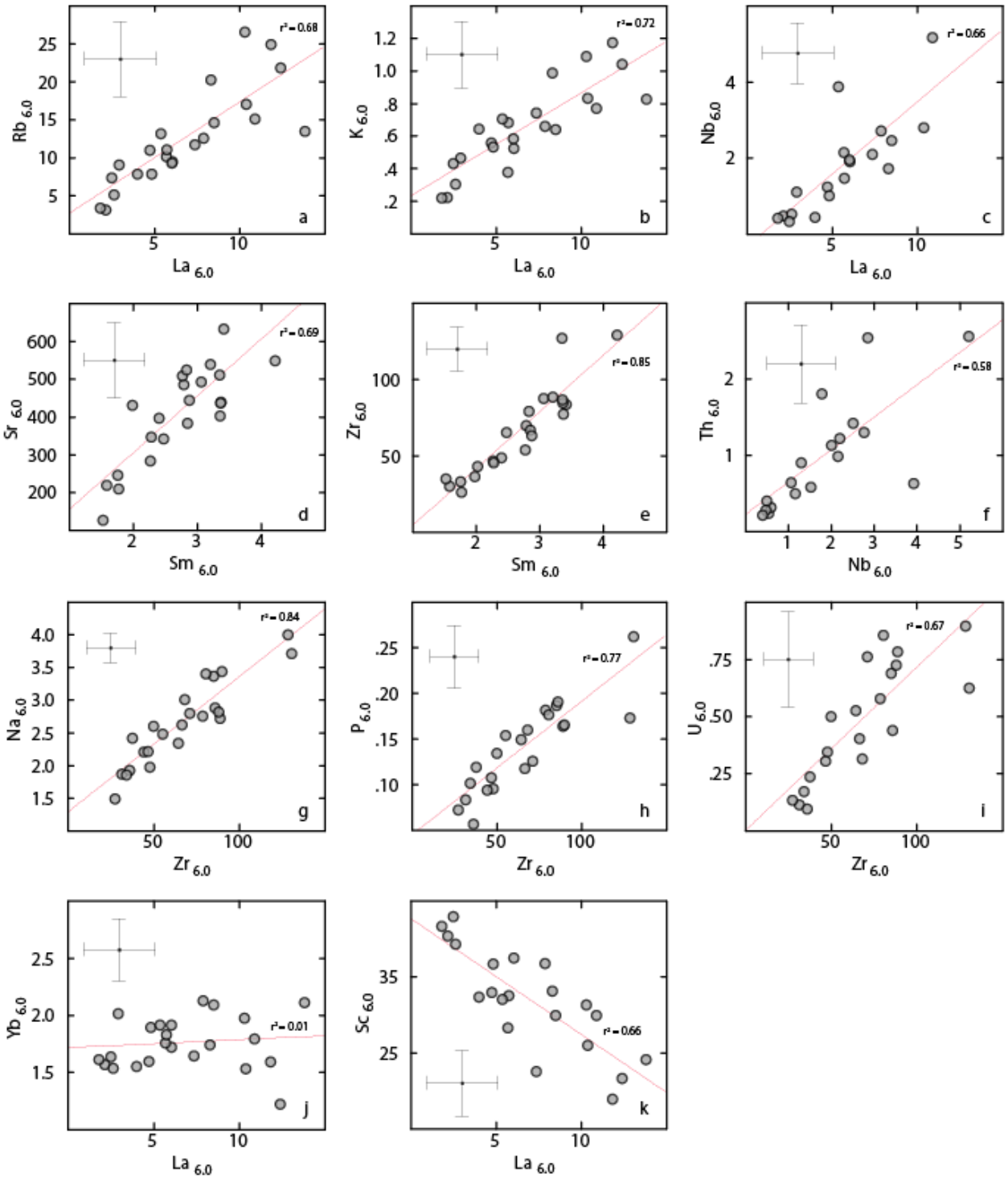

Figure 2.3: Correlations among trace elements. Most incompatible trace elements correlate positively across a factor of 5 variation (panels a-i). These correlations are not confined to specific groups of elements, such as HFSE, fluid mobile, or REE, but instead correlations occur across these groups. For example, $La_{6.0}$ correlates well with $Nb_{6.0}$ and $U_{6.0}$ correlates well with $Zr_{6.0}$. There is little variation among the HREE (panel j), while compatible elements ($Sc_{6.0}$, also $V_{6.0}$) show negative correlations (panel k). Error bars are average arc standard deviations

Strong correlations also exist among trace elements, with most incompatible trace elements correlating with one another across a factor of five or more variation in concentration (Figure 2.3a-i). The light rare earth elements (LREE), for example, correlate well with Rb, K, Sr, as well as Zr, Hf, and Nb (the Aegean and Nicaragua are often outliers for Nb). The high field strength element Zr correlates well with P, Na, Ca, and K, as well as Rb, Sr, LREE, Hf, Th and U. With the exception of Nicaragua, $Th_{6.0}$ correlates with $Nb_{6.0}$. Some elements with a strong and variable slab signature (e.g., Ba, Pb) correlate less well (not shown).

Rare earth element patterns vary from flat for segments with low concentrations of incompatible elements to highly LREE-enriched (Figure 2.4). There are strong correlations among the LREE, but no correlation between $La_{6.0}$ and the HREE. LREE 6-values vary by more than a factor of 4,

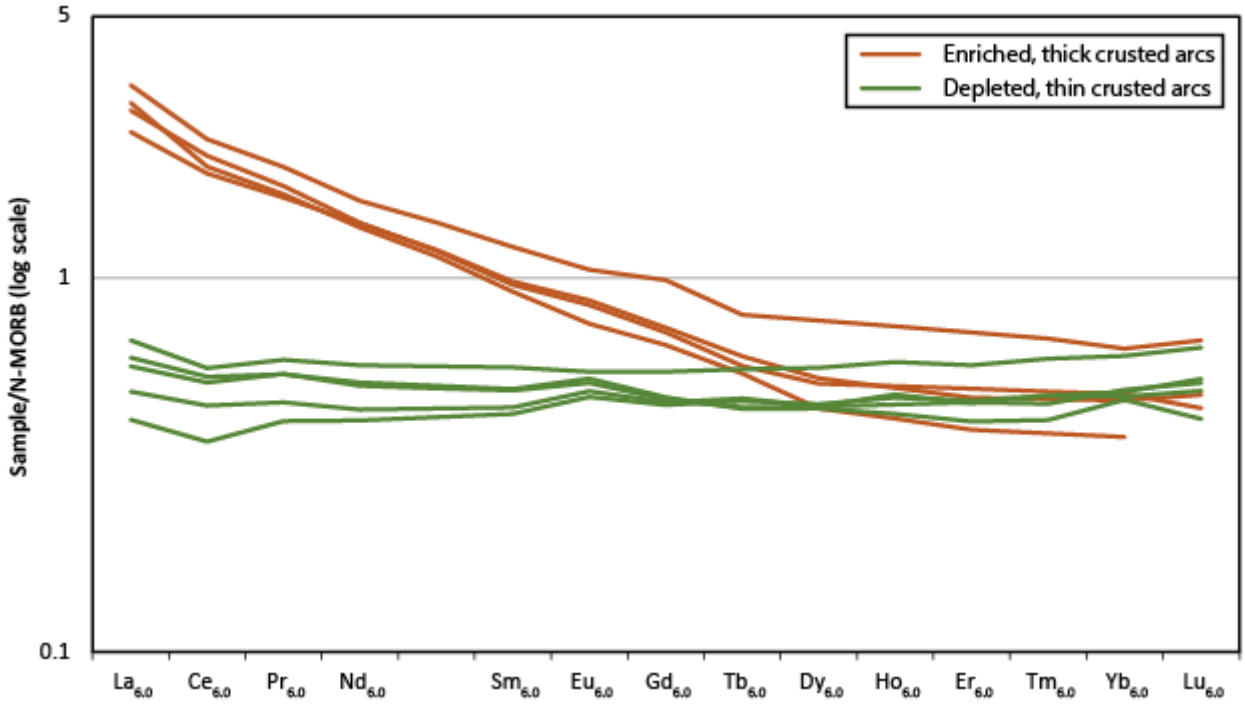

Figure 2.4: Rare earth element (REE) patterns of global arcs at 6% MgO, normalized to N-MORB from Gale et al. (2013), Orange lines show the 6-values from arcs with the thickest (>39 km) crust (highest to lowest $La_{6.0}$: Cascades, Colombia/Ecuador, Mexico, Central Chile). Green lines are arcs with the thinnest (<28km) crust (highest to lowest $La_{6.0}$: Kuriles, Kermadec, Tonga (S), Izu, South Sandwich). All of the arcs overlap in HREE contents, with HREE concentrations depleted relative to N-MORB. The thick-crust arcs show steep patterns of enrichment going from LREE to HREE, while the thin-crust arc patterns are flat across the entire range.

while $Yb_{6.0}$ varies by only a factor of 1.5, and average $Yb_{6.0}$ contents overlap globally (Figure 2.3j and Figure 2.4). The compatible trace elements Sc and V show negative correlations with the incompatible elements (Figure 2.3k).

Strong systematics also emerge from element ratios. The ratios are generally based on many more samples than the 6-values, because they include all samples between 4 and 12% MgO. Most pairs of incompatible elements are correlated along linear trends that nearly intersect the origin (Figure 2.3), and thus have limited variation in their ratio, typically around 50%. This is in stark contrast to the factor of five variation in incompatible element concentrations. Ratios of incompatible to moderately compatible elements can vary substantially (e.g La/Yb varies a factor of 5), and other ratios among moderately incompatible elements (e.g., Zr/Sm, Zr/Ti) can vary by a factor of two or more. These variations positively correlate with $Na_{6.0}$, and hence also with incompatible trace element abundances (Figure 2.5).

A major characteristic of the data is the co-variation of incompatible elements of all classes—"fluid-mobile", "high field strength elements", "melt-mobile", and the major elements Na, Ca, K and P. The striking correlations among major elements, trace elements, and trace element ratios, and the systematic changes with incompatibility -- independent of the element class -- are remarkable and robust characteristics of the global data set. These characteristics suggest a process that operates at convergent margins globally and produces variations of a factor of five or more in incompatible elements, as well as systematic changes in moderately compatible element ratios.

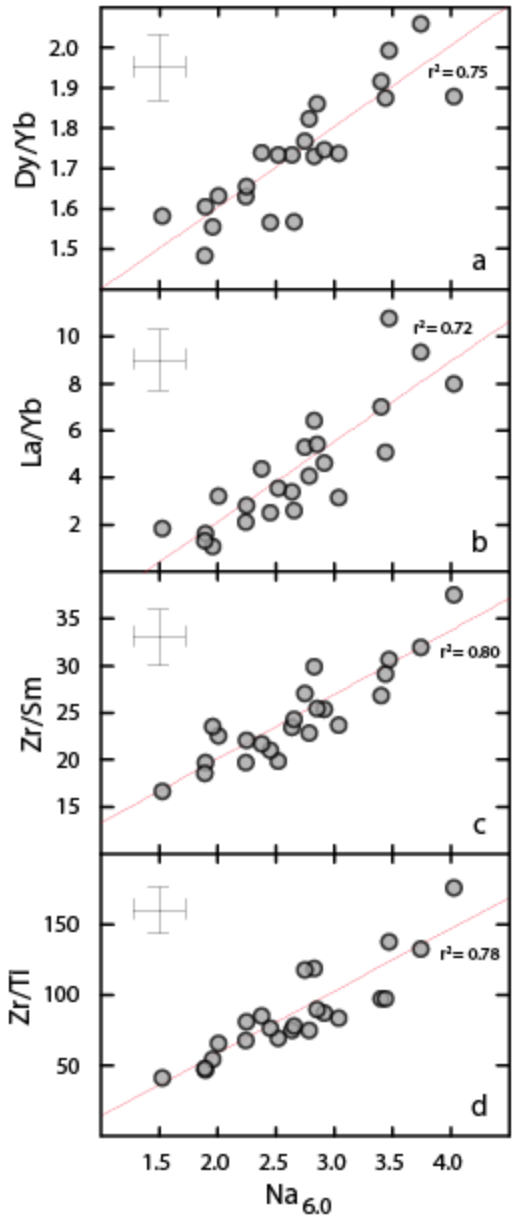

Figure 2.5: Examples of trace element ratios that correlate strongly with $Na_{6.0}$. The coherence of the major element and trace element data argues for a common petrogenetic process that controls both sets of elements. This contrasts with ocean ridge basalts, for example, where major elements and trace elements show independent variations (see Gale et al., 2014). The Dy/Yb ratio (panel a), is not strongly fractionated by phases present during early stage low pressure fractionation or typical upper mantle melting, and suggests the involvement of garnet in the petrogenesis of magmas from thick-crust arcs. Error bar shows average standard deviation for global arcs.

2.3.3 Correlations with crustal thickness

In addition to these relationships among the chemical parameters, there are correlations between these parameters and crustal thickness (CT). CT correlates strongly with the major elements $Na_{6.0}$, $Ca_{6.0}$, $K_{6.0}$, $Mn_{6.0}$ and $P_{6.0}$ (Figure 2.6). Most incompatible trace elements also correlate positively with CT. The positive correlations are particularly strong among the LREE, Sr, Zr, and Ba (Figure 2.7b-g),

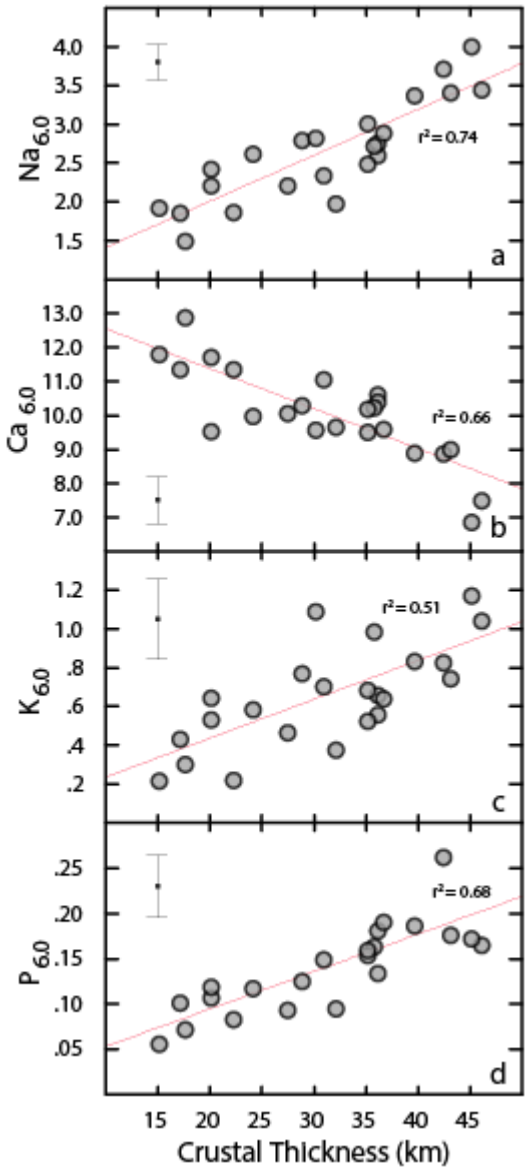

Figure 2.6: Major element correlations with crustal thickness. Correlations between crustal thickness and $Na_{6.0}$ $Ca_{6.0}$, and $K_{6.0}$ (panels a-c) confirm the results of Plank and Langmuir (1988). A strong correlation between crustal thickness and $P_{6.0}$ is also observed.

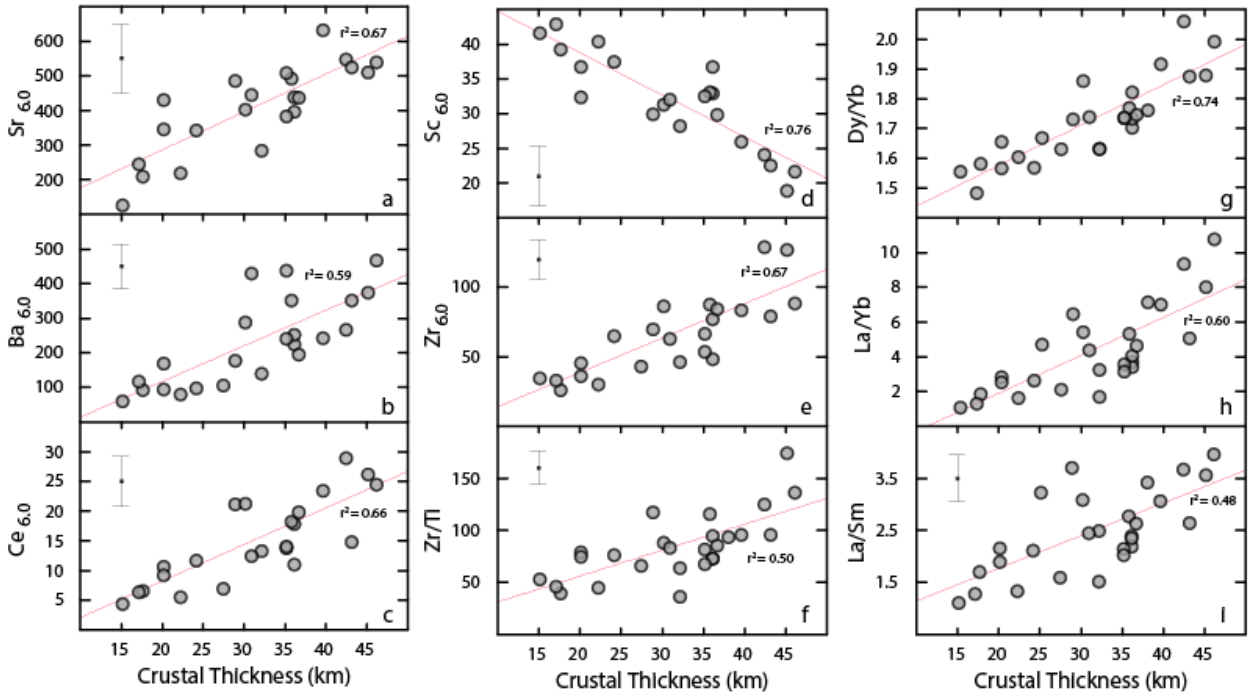

Figure 2.7: Examples of the pervasive strong correlations between the trace element 6-values, trace element ratios, and crustal thickness. The correlation is positive among incompatible elements (panels a, b, c, e) and negative for compatible elements (panel d). The increasing slope of REE with crustal thickness (see Figure 2.4) leads to correlations between crustal thickness and the ratio of nearly any two REE (panels g-i).

but are notably absent within the HREE (not shown, r^2 values < 0.1). For the most incompatible elements, the relative variation among arc segments is a factor of five, with the greatest enrichment at thick-crust arcs. In contrast, total relative variation is limited to within 50% for the HREE. The compatible trace elements V and Sc are anti-correlated with CT, with both of these elements decreasing by a factor of ~2 going from thin to thick crust (e.g., Figure 2.7d). These observations are independent of the normalization scheme employed.

The REE spider diagram in Figure 2.4, normalized to N-MORB, shows a steep slope going from LREE to HREE for thick-crust arcs (orange lines), with a comparatively flat slope for thin-crust arcs (green lines). This increase of REE slope with crustal thickness applies generally, and so the ratio of nearly any two average REE concentrations correlates strongly with CT (Figure 2.7g-i). Surprisingly, this correlation

is strongest for MREE/HREE ratios, such as Dy/Yb, which are not fractionated by typical enrichment processes attributed to other REE ratios.

2.4 Discussion

The coherent chemical systematics of global arc averages presented above are primary observations that need to be explained by viable models of arc petrogenesis. Such models should explain both the chemical correlations as well as their relationships with physical parameters. One class of models suggests that diversity in arc magmas is caused by primarily by processes that occur during magma transport within the crust, which would seem to be supported by the relationships with crustal thickness described above. An important role for crustal processes has long been argued on the basis of pervasive mixing textures in arc magmas (e.g., Eichelberger et al., 2006), correlations with crustal thickness in the Andes (e.g., the MASH model of Hildreth and Moorbath, 1988), and in some cases definitive chemical systematics (e.g., Reubi et al., 2011).

It is evident that low pressure processes cannot produce the large ranges in chemical compositions at constant Mg#, or constant wt. % MgO, that are apparent in the global data set. The observations are present in the raw data and across a very large range in fractionation. There is no evidence that low pressure processes are responsible. Therefore processes to be considered are high pressure fractionation and crustal melting/magma mixing. The possibility of removal of magmas by a crustal buoyancy filter is discussed in Appendix A2.3.

High pressure processing of convergent margin magmas has been supported recently by the influential model of Annen et al. (2006). They argue that intermediate and silicic magmas are generated in deep crustal “hot zones” where sills stall, crystallize at high pressure, and may assimilate lower crustal melts. This model has many similarities to the MASH model of Hildreth and Moorbath (1988), with the

important addition of quantitative modeling of the thermal budget of these deep hot zones. Annen et al. (2006) propose that "the chemical diversity in arc magmas is largely acquired in the lower crust." In the context of their paper, "chemical diversity" refers to the signal of magma evolution from basaltic parent magmas to silicic plutons and eruptives. However, deep crustal processes of fractionation and assimilation are also an inherent aspect of the Hildreth and Moorbath (1988) model, called upon to explain trace element and isotopic diversity among arc magmas. Therefore an important question is whether processes similar to those proposed by Annen et al. (2006) could lead to the striking relationships among the intermediate magmas shown here. If magma storage and modification within the deep crust is a common process, we might expect the extent and depth of this processing also to correspond to the thickness of the crust.

Of course there is an important distinction between a particular physical model and its chemical consequences. For example, deep crustal storage systems could play an important role in convergent margin volcanism, as suggested in Annen et al. (2006), without having a predominant role in producing the remarkable diversity among primitive and intermediate arc magmas. Therefore, the question to be addressed is not whether such hot zones may or may not exist as important crustal filters, but whether they impart the global relationships shown here. Since these relationships include correlations with crustal thickness, and crustal processing may also change with crustal thickness, crustal processing in deep crustal "hot zones" is an important hypothesis to be evaluated.

To state it simply, we seek to address two primary questions: "Are models of deep crustal generation for intermediate magmas supported by global magma chemistry?" and "Can crustal processing of any type produce the range of data apparent in global arcs from a less variable primary mantle melt?"

2.4.1 High-P Fractionation

Thicker overlying crust could lead to magma crystallization at higher pressures. Might a change in the pressure of fractionation lead to the correlations between chemical compositions of mafic and intermediate arc magmas and crustal thickness? Two lines of evidence that bear on this question are experimental data carried out on primitive arc melts at high pressures, and the detailed characteristics of the uncorrected global data.

Blatter et al. (2013) compile experimental evidence to show that at high pressures (>~0.4 GPa), primitive arc melts evolve towards peraluminous compositions prior to significant silica enrichment. High pressure fractionation results in clinopyroxene saturation closer to the liquidus, which limits Ca enrichment in the melt, and slows the rate of Si enrichment, Mg depletion, and Mg# reduction per unit fractionation. In addition, high pressure crystallization suppresses plagioclase crystallization, allowing enrichment of Al. The trend towards peraluminous compositions is conveniently represented by the aluminum saturation index (ASI= Al/(2Ca + Na + K), calculated on a cation basis). High pressure experiments produce steep increases in the ASI with initial silica enrichment. Figure 2.8 compares the experimental fractionation paths to all samples in our filtered database, grouped by crustal thickness. Most points for all crustal thicknesses fall between 0.1 and 0.4GPa, corresponding with upper to middle crust depths. Thick-crust arcs generally have a larger proportion of high SiO_2 samples, but these samples appear to reflect fractionation from 0.1 to 0.4GPa, which is the upper half of the crust. If the experimental data are correct, they do not appear to support a predominant role for deep crustal fractionation.

It is possible that some parental magmas may have ASI values lower than those used in the Blatter et al. study. If magmas from thick-crust arcs started with lower primary ASI values, might this affect our interpretation? The most primitive samples from arc segments built on thick crust (Central

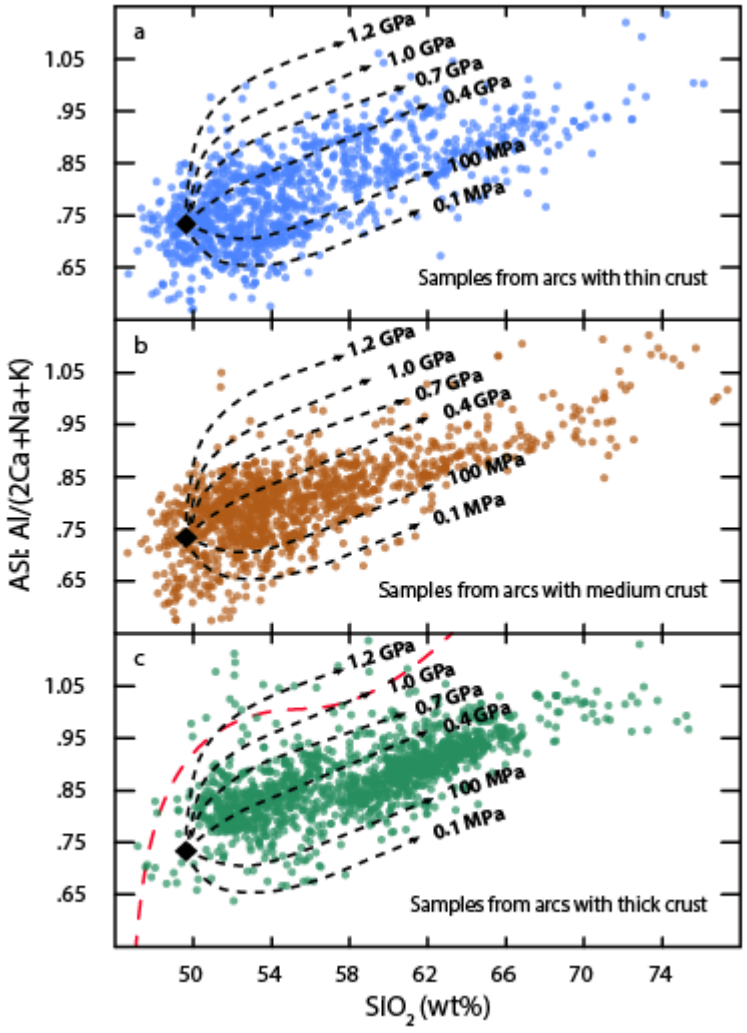

After Blatter et al. (2013) figure 7d

Figure 2.8: Liquid lines of descent (black dotted lines) from a typical primary melt composition (black diamonds) at variable pressures, from Blatter et al. (2013). The red line in panel a is a polynomial fit to the 0.7 GPa experiments of Nandedkar et al. (2014), which use a starting composition with lower ASI and SiO_2. At higher pressures of crystal fractionation, magmas reach high aluminum saturation index [ASI= molar Al/(2Ca +Na+K)] values prior to significant silica enrichment. As shown by the red line in panel c, this effect may be independent of starting ASI. Panel a shows samples taken from arcs with thin (<27 km) crust, panel b shows samples from arcs with medium (between 27 and 37 km) crust, and panel c shows only samples from arcs with thick (37 km to 47 km) crust. Although there are fewer samples on panel c at low levels of SiO_2, the samples on all three panels overlap. The majority of samples from all arc segments fall near the 0.4 GPa liquid line of descent, suggesting that even in arcs with very thick crust, high pressure crystal fractionation is atypical, and that most fractionation generally occurs at a depth between 3 and 12 km, that is, the middle and upper crust.

Chile, Colombia/Ecuador, Cascadia, and Mexico) almost exclusively have high ASI (>0.7). Furthermore, it is not clear that magmas with lower ASI starting points, even if they did exist at thick-crust arcs, would avoid reaching high ASI values prior to silica enrichment. This is demonstrated in the experimental work of Nandedkar et al. (2014), in which crystal fractionation is simulated using a basalt with a starting ASI of 0.6 at a pressure of 0.7 GPa. The LLD from this experiment is shown on panel c of Figure 2.8 (red dashed line), in which it is clear that a sharp increase in ASI occurs, reaching values near 1.0 at low (less than 52%) SiO_2. The LLD from this experiment is clearly unlike the actual data from thick-crust arcs.

Perhaps even more compelling evidence against any crystal fractionation process as the origin of the correlations found in the global dataset is that lava compositions from individual arcs remain distinct from low to high Mg#. Figure 2.9 shows Na_2O vs Mg# for 5 arcs which have a significant proportion of high Mg# samples (plots of Na_2O vs Mg# for additional arcs can be found in Appendix A2.4). Na_2O contents of samples from these arcs are distinct across the entire compositional range, from differentiated compositions with Mg#=50, to near primary melts with Mg#=70. Crystal fractionation at high pressures can potentially produce steeper slopes of Na_2O enrichment across this range of Mg#s. The data on Figure 2.9, however, appear to more closely match the shallow olivine-only fractionation trend (green line on Figure 2.9), than the average slope taken from the 1.2 GPa experiments of Müntener et al. (2001) (the red line on Figure 2.9) or the 0.7 GPa experiments of Nandedkar et al. (2014) (light blue dotted line of Figure 2.9). Rather than mimic the arc data, the high pressure fractionation trends cut across it.

The observation that crystal fractionation does not produce the chemical diversity of our dataset can be verified quickly by comparing 6-values with Mg#>60 values (Figure 2.1). The distinct ranges of Na contents within arc segments appear to be set at high Mg#. Figure 2.1 also demonstrates that this holds true not only for elemental concentrations, but also the ratios Dy/Yb and Zr/Sm. The average Dy/Yb and Zr/Sm ratios at high Mg#s are almost perfectly correlated with these same ratios

calculated from the entire dataset, indicating that the distinct ranges of these ratios within arc segments are also continuous to near primary Mg#s. For major elements, trace elements, and trace element ratios, the global relationships span the entire range of differentiation, which argues strongly that crystal fractionation from some common parent is not producing the relationships. If some other crustal process does generate the observed compositional variations, it must do so without significantly altering the Mg# of compositions in equilibrium with mantle olivine. It is thus unlikely that crystal fractionation at any pressure contributes substantially to the global chemical variability described here, which persists across large ranges of differentiation.

Again it is important to note that this does not argue for an absence of differentiation processes in the petrogenesis of these magmas, as such processes are evident in all arc volcanoes. Rather, the evidence suggests only that most of the chemical differences which occur across the range of primitive to moderately differentiated compositions are produced by a different mechanism.

2.4.2 Crustal melting/mixing of granitic melts

While crystal fractionation inevitably produces a decrease in Mg#, mixing of primitive melts with granitic melts or assimilation of solid material with a granitic composition can produce a large range in incompatible element abundances at high Mg#. This is because highly evolved magmas have low Mg and Fe contents, and so assimilating moderate amounts of a granitic melt will leave this ratio unperturbed. Granitic magmas can have extreme enrichments in incompatible elements, and mixing with them could lead to large variations in incompatibles with a minimal change in Mg#. Such a process is illustrated by the mixing curves in Figure 2.9. Mixing a depleted primary melt with an enriched granitic melt that contains 6 wt. % Na_2O could generate the entire global range of Na_2O while maintaining a high Mg#. If such mixing were to occur, subsequent low pressure fractionation may then be able to produce the near

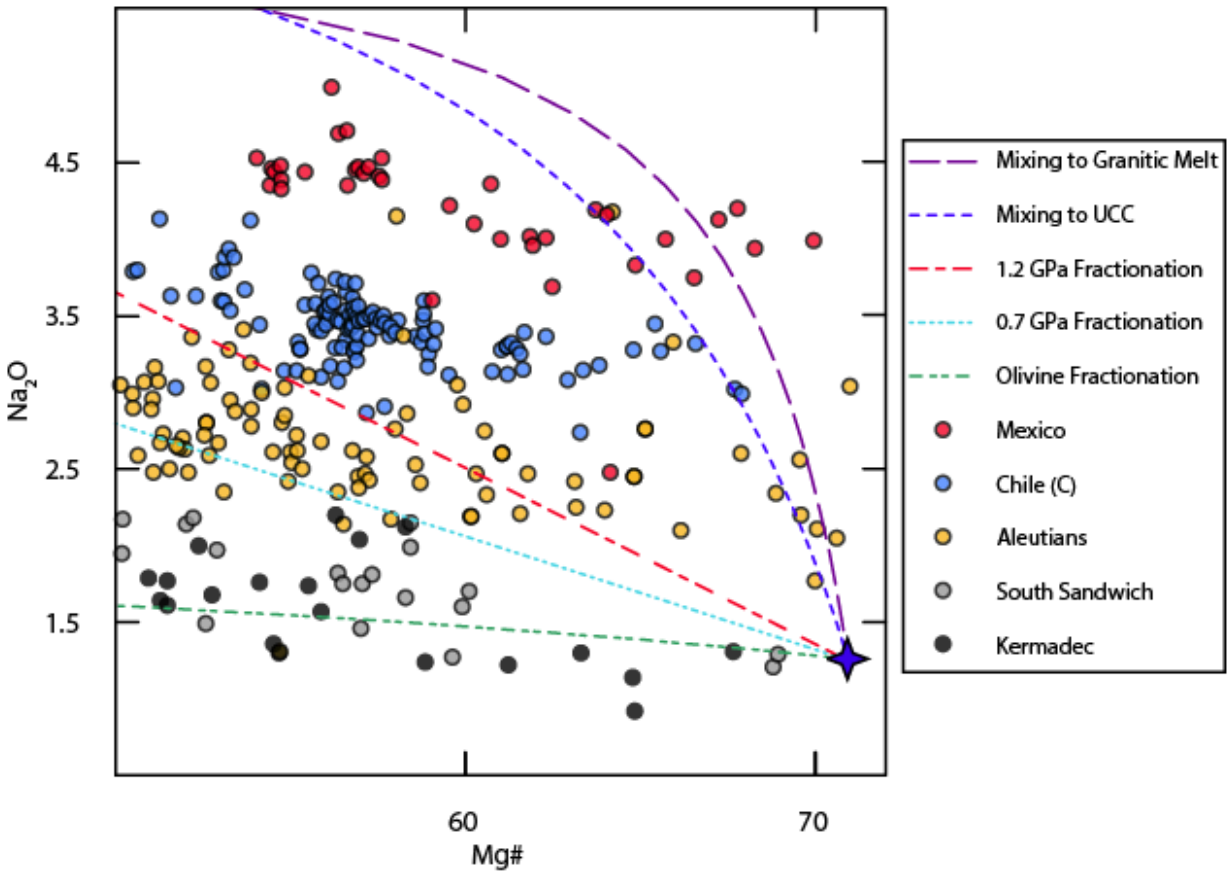

Figure 2.9: Plot of Na_2O content vs Mg# for all samples (with Mg#>50) from Mexico, Central Chile, the Aleutians, South Sandwich, and Kermadec. These arcs all have abundant high Mg# samples and represent the full range of crustal thicknesses. Each individual arc occupies a discrete range of Na_2O contents across a wide range of Mg#s, notably extending all the way to primary melt compositions at Mg#=70. This is also true for other arcs with high Mg# samples (see Appendix A2.4). The slopes of samples from each arc most closely resemble that of olivine fractionation (green dotted line), and are much shallower than either the 1.2 GPa fractionation line (red dashed line, slope adopted from Müntener et al., 2001) or the 0.7 GPa fractionation line (light blue dotted line, slope adopted from Nandedkar et al., 2014). Mixing between depleted primary melts (blue star) and granitic melts (purple dashed line) or upper continental crust (UCC, blue dashed line) can conceivably produce a wide range of Na_2O contents at high Mg#s, though the required compositions of these mixing end-members are unrealistic (see Figure 2.10 and discussion in text).

horizontal trends seen at each arc. Such a model is supported by the linear relationships among so many of the incompatible elements (Figures. 2.3 and 2.10), which are often diagnostic of mixing.

While granitic melts can be highly enriched in incompatible elements, they are not usually enriched in the entire suite of incompatible elements that show correlations among the arc data. They are usually saturated in zircon and apatite, which moderate their Zr and P contents (e.g., Lee et al.,

2014). If plagioclase is present during melting or crystallization, granitic liquids will also have low Sr. If K-feldspar is present, they will have low Ba (Ewart and Griffin, 1994). The global arc data have good correlations among Sm, P, Na, Zr and Sr (Figure 2.10), which require a contaminant formed in the absence of any of the phases that would fractionate these elements. It is unlikely that such conditions are common in the roots of volcanic arcs. Apatite saturation, for example, causes granites to have P_2O_5 concentrations that are typically below 0.15 wt. % (e.g., Bea et al., 1992), while our dataset shows that P_2O_5 contents for arc magmas with Mg#>60 extend to 0.28 wt. % (Figure 2.10b).

Because the relationships among many elements are linear, however, a mixing model is mathematically possible, given suitable end-members. To approximate the depleted, primary mantle melt end-member, olivine was added to the most primitive sample from Kermadec until its bulk composition was in equilibrium with Fo_{90} olivine. Two enriched end-members were tested, one with the Mg and Fe concentrations of the upper continental crust from Rudnick and Gao (2003), and one with the average Mg and Fe contents of experimental melts generated by Sisson et al. (2005). The experimental end-member has lower MgO contents (0.4 wt. % MgO) than the upper crust composition (2.48 wt. % MgO), as well as a lower Mg# (27 vs 47). If we require that any mixed magma must have an Mg# greater than 65, and MgO contents greater than 6 wt. %, then the maximum allowable proportion of either enriched end-member is ~50%. For a 50% mixture of these end-members to produce the highest observed Na Mg#>60 value, the enriched granitic end-member must have at least 6 wt. % Na_2O.

By assuming the maximum allowable contribution from the enriched granitic end-member, we can calculate the minimum incompatible element contents that it must contain by extrapolating linear regressions through element-element plots of the Mg#>60 values for global arc segments to 6 wt. % Na_2O. These end-members are plotted as the red stars on Figure 2.10. The mixing contaminant must have a minimum of 6 wt. % Na_2O, 0.43 wt. % P_2O_5, 1165 ppm Sr, and 235 ppm Zr. These values of Na, P, Sr, and Zr are very enriched. If the global range were to be produced by less than 50% contamination,

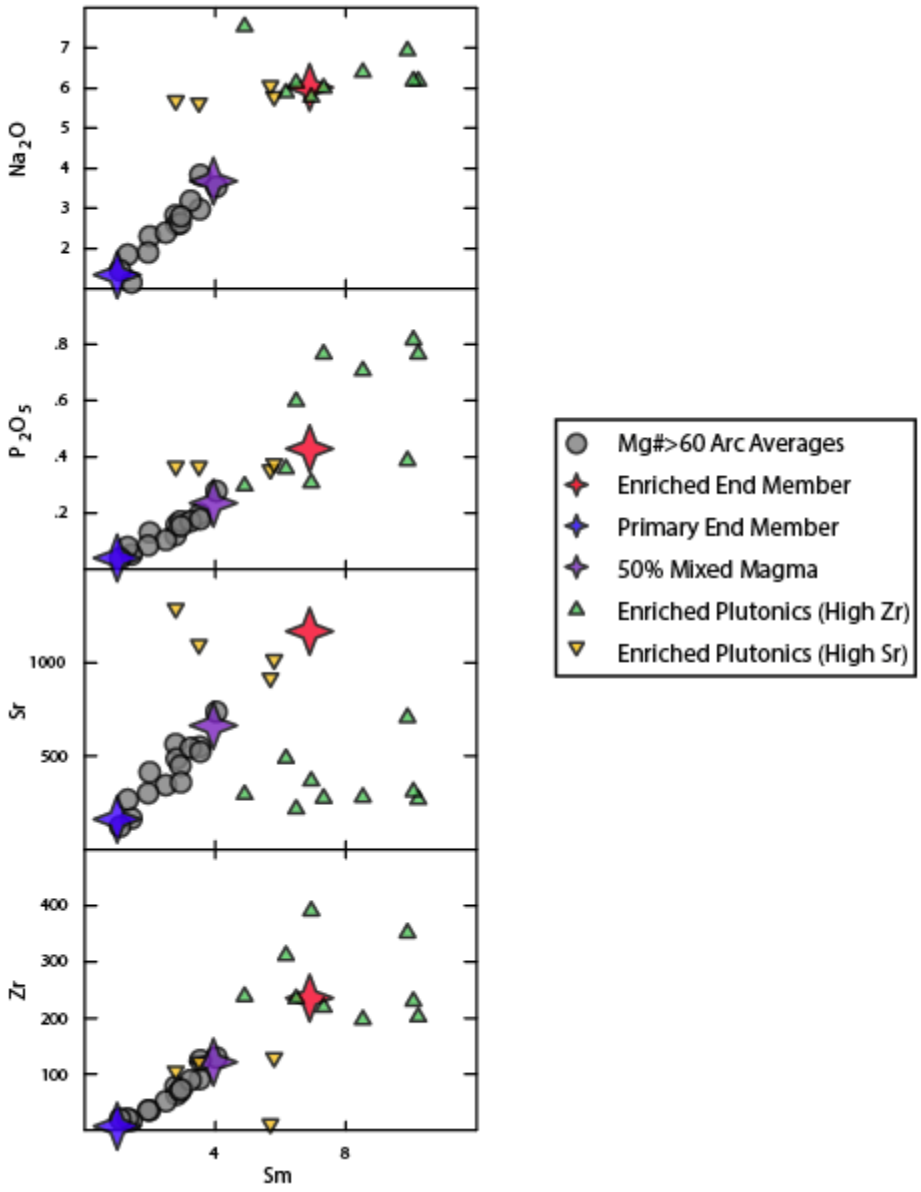

Figure 2.10: Test of a mixing model to explain the global arc correlations. Since the global arc data are linear on element-element plots, mixing is a mathematically viable model. Constraints on end-members can be visualized from diagrams of incompatible element arc averages (gray circles) using only samples with Mg#>60. The linear relationships can be modeled as simple two end-member mixing. Constraints from Mg and Fe concentrations (MgO must be finite in the granitic end-member, mixed magmas must contain >6 wt. % MgO, mixed magmas must have Mg#>65) provide a maximum mixing proportion of 50%. A 50% mix between a depleted primary melt (blue star) and an enriched granitic melt (red star) produces a mixed magma (purple star) with a composition similar to the most enriched arc averages. A search of GEOROC provides scarce granitic rocks (yellow and green triangles) with compositions similar to the projected mixing end-member on panels a and b. In panels c and d, however, it is clear that these granitic rocks do not approximate a suitable end-member for Zr and Sr. The compositions of mixing end-members and the mixed magma can be found in Appendix A2.5.

then even more extreme compositions for the granitic end-member would be required. The extent to which this mixing end-member is plausible can be explored through the GEOROC database.

The GEOROC database contains 2524 plutonic granites, diorites, and monzonites from continental settings that have been analyzed for Na, P, Sr, Zr, and Sm. Of these, only 34 have both greater than 5.5 wt. % Na_2O and 0.3 wt. % P_2O_5, constituting only 1.3% of the analyzed samples. These samples are plotted as triangles on Figure 2.10. While it appears that some of these samples are suitable end-members on the plots of Na_2O vs and P_2O_5 vs Sm, none of these samples are sufficiently enriched in both Zr and Sr, which appear to have an inverse relationship within this compositional space. As no single measured granite appears to have the required composition for the mixing end-member, it is unlikely a similar contaminant is pervasive at volcanic arcs worldwide. Furthermore, the physical model for this process is also unlikely. In the Annen et al. (2006) model, for example, mixing of granitic melts occurs progressively with crystal fractionation, which should lead to coupled changes in incompatibles and Mg#. To account for the characteristics of the data, however, the granitic mixing event would have to be a unique, large scale event that occurred prior to any differentiation. This analysis suggests granitic melt mixing is a highly implausible mechanism for generating the global diversity of arc magmas seen in our dataset.

2.5 Conclusions

This paper presents a newly compiled database of arc front volcanism that is more inclusive than previous efforts and global in scope. This dataset reveals salient systematics among major elements, trace elements, and trace element ratios, as well as correlations between these chemical parameters and the thickness of the overlying crust. Most incompatible elements are shown to correlate globally across variations in concentration spanning up to a factor of five or more. Moderately

incompatible trace element ratios, such as Zr/Sm and Dy/Yb, also correlate strongly with the enrichment of incompatible elements. These correlations are not restricted to traditional groupings of elements for arc magmas, such as LILE and HFSE, but instead persist across all groups with the notable exception of the HREE. The HREE do not vary with other incompatible elements, and instead show remarkably limited variance. Other compatible elements, such as Ca, Sc, and V, correlate negatively with incompatible elements.

Enrichment of incompatible elements is strongly correlated with the thickness of the overlying arc crust, implicating crustal processes as the origin of the global systematics. However, variable pressures of crystal fractionation cannot be responsible for the chemical variability of the global data. The data from thick-crust arcs do not follow fractionation paths consistent with high pressure crystal fractionation. Moreover, the individual arcs carry their characteristic chemical signatures across the entire range from primary to evolved magmas, inconsistent with a variable crystallization hypothesis at any pressure. A successful model can be constructed that calls upon mixing depleted primary melts with enriched evolved melts. Using a MgO-rich parent and a low MgO mixing end-member, it is possible to reproduce the range of magma compositions observed at high Mg#. This model is unlikely, however, because the required end-member composition is rare to absent within global chemical compositions. Furthermore, the distinct sequence of ubiquitous mixing of this phantom composition followed by distinct fractionation sequences beginning at high Mg# is physically untenable.

High pressure fractionation and crustal assimilation are the subjects of a large body of literature, and must be carefully considered in the interpretation of arc magma chemistry. Global chemical correlations between arc magma compositions and crustal thickness strongly implicate crustal processes, and so this paper focuses solely on them. We conclude, however, that crustal processes cannot produce the chemical systematics of the global dataset presented here. We find that the observed global systematics are instead most likely primary, representing diversity in the compositions

of melts extracted from the mantle. This primary magma diversity is likely produced either by variations in the melting regime in the mantle wedge, as proposed by Plank and Langmuir (1988), or by variation in the composition and magnitude of the slab contribution to the wedge. Quantitative assessment of these possibilities are discussed in depth in Chapter 3.

2.6 References

Annen, C., Blundy, J., Sparks, R., 2006. The genesis of intermediate and silicic magmas in deep crustal hot zones. Journal of Petrology 47, 505-539.

Bea, F., Fershtater, G., Corretgé, L., 1992. The geochemistry of phosphorus in granite rocks and the effect of aluminium. Lithos 29, 43-56.

Blatter, D.L., Sisson, T.W., Hankins, W.B., 2013. Crystallization of oxidized, moderately hydrous arc basalt at mid-to lower-crustal pressures: implications for andesite genesis. Contributions to Mineralogy and Petrology 166, 861-886.

Class, C., Miller, D.M., Goldstein, S.L., Langmuir, C.H., 2000. Distinguishing melt and fluid subduction components in Umnak Volcanics, Aleutian Arc. Geochemistry, Geophysics, Geosystems 1.

Condie, K.C., Potts, M.J., 1969. Calc-alkaline volcanism and the thickness of the early Precambrian crust in North America. Canadian Journal of Earth Sciences 6, 1179-1184.

Dickinson, W.R., Hatherton, T., 1967. Andesitic volcanism and seismicity around the Pacific. Science 157, 801-803.

Eichelberger, J.C., Izbekov, P.E., Browne, B.L., 2006. Bulk chemical trends at arc volcanoes are not liquid lines of descent. Lithos 87, 135-154.

Elliott, T., Plank, T., Zindler, A., White, W., Bourdon, B., 1997. Element transport from slab to volcanic front at the Mariana arc. Journal of Geophysical Research: Solid Earth (1978–2012) 102, 14991-15019.

Ewart, A., Griffin, W., 1994. Application of proton-microprobe data to trace-element partitioning in volcanic rocks. Chemical Geology 117, 251-284.

Falloon, T.J., Danyushevsky, L.V., Crawford, T.J., Maas, R., Woodhead, J.D., Eggins, S.M., Bloomer, S.H., Wright, D.J., Zlobin, S.K., Stacey, A.R., 2007. Multiple mantle plume components involved in the petrogenesis of subduction-related lavas from the northern termination of the Tonga Arc and northern Lau Basin: Evidence from the geochemistry of arc and backarc submarine volcanics. Geochemistry, Geophysics, Geosystems 8.

Gale, A., Dalton, C.A., Langmuir, C.H., Su, Y., Schilling, J.G., 2013. The mean composition of ocean ridge basalts. Geochemistry, Geophysics, Geosystems 14, 489-518.

Gale, A., Langmuir, C.H., Dalton, C.A., 2014. The global systematics of ocean ridge basalts and their origin. Journal of Petrology 55, 1051-1082.

Gazel, E., Hoernle, K., Carr, M.J., Herzberg, C., Saginor, I., den Bogaard, P.v., Hauff, F., Feigenson, M., Swisher III, C., 2011. Plume–subduction interaction in southern Central America: Mantle upwelling and slab melting. Lithos 121, 117-134.

Hildreth, W., Moorbath, S., 1988. Crustal contributions to arc magmatism in the Andes of central Chile. Contributions to Mineralogy and Petrology 98, 455-489.

Kelemen, P.B., 1995. Genesis of high Mg# andesites and the continental crust. Contributions to Mineralogy and Petrology 120, 1-19.

Klein, E.M., Langmuir, C.H., 1987. Global correlations of ocean ridge basalt chemistry with axial depth and crustal thickness. Journal of Geophysical Research: Solid Earth (1978–2012) 92, 8089-8115.

Lee, C.-T.A., Bachmann, O., 2014. How important is the role of crystal fractionation in making intermediate magmas? Insights from Zr and P systematics. Earth and Planetary Science Letters 393, 266-274.

Miller, D.M., Goldstein, S.L., Langmuir, C.H., 1994. Cerium/lead and lead isotope ratios in arc magmas and the enrichment of lead in the continents. Nature 368, 514-520.

Montelli, R., Nolet, G., Dahlen, F., Masters, G., 2006. A catalogue of deep mantle plumes: New results from finite-frequency tomography. Geochemistry, Geophysics, Geosystems 7.

Morris, J., Tera, F., 1989. 10Be and 9Be in mineral separates and whole rocks from volcanic arcs: Implications for sediment subduction. Geochimica et Cosmochimica Acta 53, 3197-3206.

Müntener, O., Kelemen, P.B., Grove, T.L., 2001. The role of H2O during crystallization of primitive arc magmas under uppermost mantle conditions and genesis of igneous pyroxenites: an experimental study. Contributions to Mineralogy and Petrology 141, 643-658.

Niu, Y., O'Hara, M.J., 2008. Global correlations of ocean ridge basalt chemistry with axial depth: a new perspective. Journal of Petrology 49, 633-664.

Patino, L.C., Carr, M.J., Feigenson, M.D., 2000. Local and regional variations in Central American arc lavas controlled by variations in subducted sediment input. Contributions to Mineralogy and Petrology 138, 265-283.

Plank, T., Langmuir, C.H., 1988. An evaluation of the global variations in the major element chemistry of arc basalts. Earth and Planetary Science Letters 90, 349-370.

Rudnick, R., Gao, S., 2003. Composition of the continental crust. Treatise on geochemistry 3, 1-64.

Ruscitto, D.M., Wallace, P.J., Cooper, L.B., Plank, T., 2012. Global variations in H2O/Ce: 2. Relationships to arc magma geochemistry and volatile fluxes. Geochemistry, Geophysics, Geosystems 13.

Sisson, T., Ratajeski, K., Hankins, W., Glazner, A., 2005. Voluminous granitic magmas from common basaltic sources. Contributions to Mineralogy and Petrology 148, 635-661.

Straub, S.M., LaGatta, A.B., Pozzo, M.D., Lillian, A., Langmuir, C.H., 2008. Evidence from high-Ni olivines for a hybridized peridotite/pyroxenite source for orogenic andesites from the central Mexican Volcanic Belt. Geochemistry, Geophysics, Geosystems 9.

Syracuse, E.M., Abers, G.A., 2006. Global compilation of variations in slab depth beneath arc volcanoes and implications. Geochemistry, Geophysics, Geosystems 7.

Weill, D.F., Drake, M.J., 1973. Europium anomaly in plagioclase feldspar: experimental results and semiquantitative model. Science 180, 1059-1060.

Chapter 3: What processes control the chemical compositions of arc front stratovolcanoes?

[Turner, S.J., Langmuir, C., 2015. What processes control the chemical compositions of arc front stratovolcanoes? Geochemistry, Geophysics, Geosystems, in press]

Abstract

Arc front stratovolcanoes have global chemical systematics that constrain processes at convergent margins. Positive correlations exist for arc averages among "fluid mobile," "high field strength," and "large ion lithophile" elements. $^{143}Nd/^{144}Nd$ and $^{87}Sr/^{86}Sr$ from rear-arc lavas lacking subduction signature align with the oceanic "mantle array," and correlate with arc front $^{143}Nd/^{144}Nd$. Most chemical parameters (but not isotopes) also correlate well with crustal thickness and slightly less well with the slab thermal parameter, but not with the depth of the slab or model slab surface temperatures. Successful models of arc volcanism should account for these global regularities.

Two distinct models can quantitatively account for the observations. In the first model, different extents of melting of the mantle wedge caused by variations in wedge thermal structure. In the second model, global compositional diversity is accounted for by varying contributions from the subducting slab owing to variations in the slab thermal structure. The wedge melting model has constant contributions from ocean crust, sediment and mantle wedge to lavas globally, while the slab model varies slab contributions with slab temperature. The wedge melting model fit improves by incorporating convergence rate and slab dip, which should affect the wedge thermal structure; the slab model is not supported by a similar analysis. The wedge model also more easily accommodates the isotope data. The two models predict different primary H_2O contents, with large variations in H_2O for the wedge model, and relatively constant H_2O for the slab model. An evaluation of the effects of varying

sediment compositions on arc lavas will benefit from considering the very different consequences of the two models.

3.1 Introduction

Subduction zone processes regulate fluxes among many of the earth's geochemical reservoirs. Subducted oceanic crust is recycled back into the mantle, where metamorphism of serpentinized peridotite, basaltic crust, and sediment causes addition of aqueous fluids, hydrous melts, or supercritical liquids to the mantle wedge (e.g., Morris et al., 1989; Miller et al., 1994; Elliott et al., 1997). Melting within the wedge results from depression of the solidus by this hydrous slab component, and possibly from decompression of peridotite (Grove et al., 2006; Cameron et al., 2003). Melts produced in the wedge may ascend rapidly to the surface and undergo closed system crystal fractionation, or could undergo a combination of fractionation and assimilation of crustal material (DePaolo, 1983). These complex processes produce a variety of arc magma compositions that are added to the continental crust, and transfer gases into the atmosphere. Since subduction zones influence the chemical characteristics of multiple earth reservoirs—mantle, continental crust, and atmosphere—a primary goal is to determine the relative importance of the various sources and processes in producing erupted magma variability, as well as the physical variables responsible for global variation in arc magma chemistry.

In order to further constrain the processes and fluxes operating in subduction zone settings, Chapter 2 provides a new, global database of major element, trace element, and Sr, Nd, Pb, and Hf isotopic compositions of arc front stratovolcanoes. That study confirms previously observed correlations among averaged major and trace element compositions of magmas erupted at volcanic fronts worldwide (Plank and Langmuir, 1988; Plank and Langmuir, 1993), as well as their correlation with crustal thickness, while adding new first order observations concerning the chemical systematics of arc front stratovolcanoes (Figure 3.1). These findings include global correlations among most incompatible element concentrations across large extents of enrichment, that in some cases span a factor of five. Global correlations among incompatible

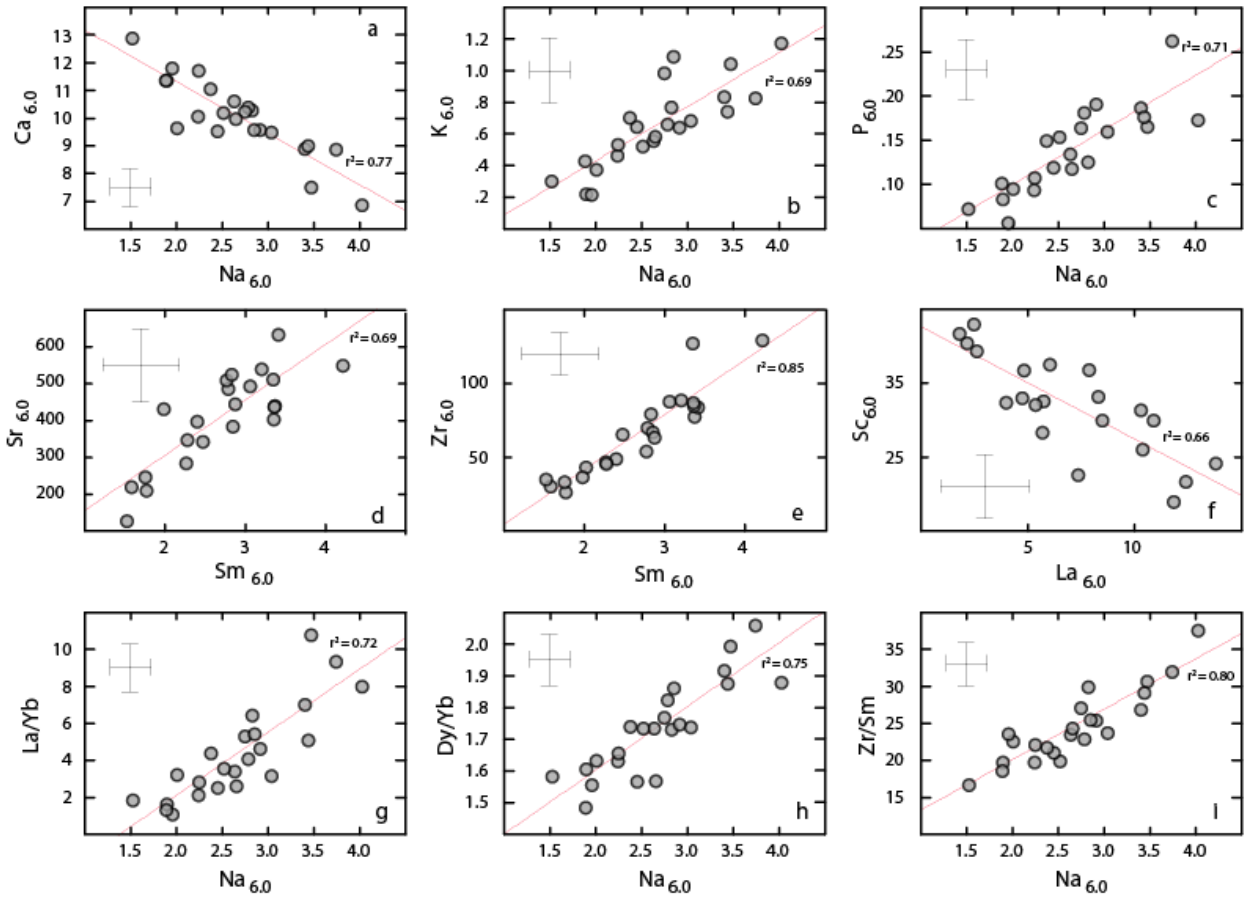

Figure 3.1: A subset of the correlations among major elements, trace elements, and trace element ratios presented in Chapter 2. "6-values" are calculated by averaging the compositions of samples that contain from 5.5 to 6.5 wt. % MgO first for individual volcanoes, and then for arc segments. Error bars represent the average standard deviation for volcano averages within arc segments. Positive correlations exist among nearly all incompatible elements, regardless of traditional element groupings (panels a-e). Negative correlations exist between incompatible and the moderately compatible elements Sc and V (panel f). Positive correlations exist between incompatible elements and La/Yb, Dy/Yb, and Zr/Sm. See Chapter 2 for a full discussion of the calculation and the first order assessment of global systematics.

elements are not limited within traditional groupings, and exist among elements from "large ion lithophile," "fluid mobile," and "high field strength" element groups. Most incompatible trace element ratios vary by less than 50%, in stark contrast to the element concentrations. While the overall variability of these ratios are limited, certain ratios, such as Zr/Sm and Dy/Yb also correlate strongly with these enrichments. The moderately compatible elements Ca, Sc, and V correlate negatively. Compositions of heavy rare earth elements (HREE) are not influenced by enrichment processes, and vary by only around

50%. These correlations are the global first order systematics of average arc volcano compositions worldwide. Any generally applicable model of arc volcanism must therefore account for these observations in a coherent, internally consistent framework.

Though these chemical parameters all correlate with the thickness of the overlying arc crust, the analysis of Chapter 2 concludes that the global correlations in average arc magma chemistry are most likely primary in nature, rather than the result of processes within the over-riding plate. This chapter builds upon this analysis by incorporating the full range of physical subduction parameters, isotopic compositions, and an additional global database of rear-arc volcanism, in order to assess the relative contributions of slab and mantle processes to the global chemical diversity of volcanic arcs.

3.2 Results

In addition to the global chemical systematics shown in Figure 3.1 and demonstrated in Chapter 2, this study incorporates Sr, Nd, Pb, and Hf isotopic data as well as additional samples from rear-arc settings. These additional data provide more comprehensive constraints on elemental fluxes through subduction zones worldwide. Note that in most figures, except where otherwise explicitly stated, a single average standard deviation is shown to represent the typical range of variation seen among volcano averages within a single arc. Of course, not all arcs have the exact same standard deviation, and moreover, the volcano averages themselves all encompass a range of values. The goal of this paper is to evaluate first order models that may account for differences and correlations among average arc values, and so we consider our figures to be the clearest method of data presentation. Details about specific data points and variance of data within arcs and volcanoes can be found in Chapter 2.

3.2.1 Rear-arc Database

Determining the composition of the wedge prior to enrichment by slab melts or fluids (the "ambient mantle wedge" composition) is a necessary first step towards constraining the flux of material from the slab to the mantle wedge. To explore variations in mantle wedge compositions, a database of back arc and rear-arc volcanics was compiled for arc segments with adequate data availability, and is available in Supplementary Dataset A3.1. We will refer to these samples collectively as "rear-arc." In continental rear-arc settings many element ratios and concentrations are affected by extremely low degrees of melting, and thus may not represent source compositions. The Nd and Sr isotopic compositions of rear-arc magmas, however, are less likely to be fractionated by melting processes, and likely to match source compositions. To minimize the effects of slab contributions on the selected rear-arc samples, compositions were screened based on the Th/Nb ratio. Both Th and Nb have bulk partition coefficients <<.01, so the Th/Nb ratio is little affected even by very low degrees of melting. The strong negative Nb anomalies and the notable enrichment of Th found in nearly all arc front samples indicate that the Th/Nb ratio is particularly sensitive to slab addition (Elliott et al., 1997). For our rear-arc database, only samples with Th/Nb<0.14 were included. Only 1% of all arc front samples for which both Th and Nb are measured have Th/Nb<0.14, while virtually all oceanic basalts have Th/Nb values below this threshold. This filtered dataset thus provides an estimate of the ambient mantle wedge isotopic compositions with minimal subduction influence for the 11 segments that are included, and is available in Supplementary Dataset A3.1.

Some of the rear-arc lavas have high Nb concentrations, but even high Nb lavas can be effectively screened for slab addition using the Th/Nb ratio. If a high Nb sample in the rear-arc were enriched due to slab input, rather than due to sampling of an enriched ambient mantle or low extents of melting, the sample would still be expected to have high Th/Nb. Samples from the volcanic front of Costa Rica, for example, have high Nb but also high Th/Nb.

There are legitimate questions about the comparability of rear-arc data from different regions. Some compositions come from back-arc basins, where there are large magmatic fluxes. In these cases, influx of mantle that is not beneath the current arc is possible. For the Central Aleutians, we use data from the Pribilof Islands to represent the unmodified ambient mantle. These islands are ~420 km from the arc front, much farther than rear-arc volcanics used in other arc segments, and could possibly be sampling a mantle domain that is distinct from the ambient sub-arc mantle. Despite these limitations, we find that all of the rear-arc samples have similar relationships to the samples from the arc front, and therefore provide a useful comparison to volcanic front compositions.

3.2.2 Isotope data

The database of Chapter 2 provided average arc segment values for $^{87}Sr/^{86}Sr$, $^{143}Nd/^{144}Nd$, $^{176}Hf/^{177}Hf$, $^{206}Pb/^{204}Pb$, $^{207}Pb/^{204}Pb$, and $^{208}Pb/^{204}Pb$, but limited discussion to major and trace element compositions. Average isotope ratios were calculated via the same method as trace element ratios – after removing samples with Eu anomalies, all samples with 4<wt. % MgO<12 were first averaged within volcanoes, and then within segments (see Chapter 2 for for details of data screening). Arcs that are influenced by nearby hot spots have an additional component that is not relevant to subduction parameters. Because our aim is to compare with subduction parameters, arcs with nearby hot spot tracks and/or seismically imaged deep mantle plumes are not included in the following discussion -- Southern Costa Rica, Northern Tonga, and the Aeolian (Gazel et al., 2011; Falloon et al, 2007; Montelli et al., 2006). Northern Chile/Peru is also excluded from this discussion, as magmas erupted in this region may be uniquely overprinted during transit through the 70 km thick continental crust of the Central Andes.

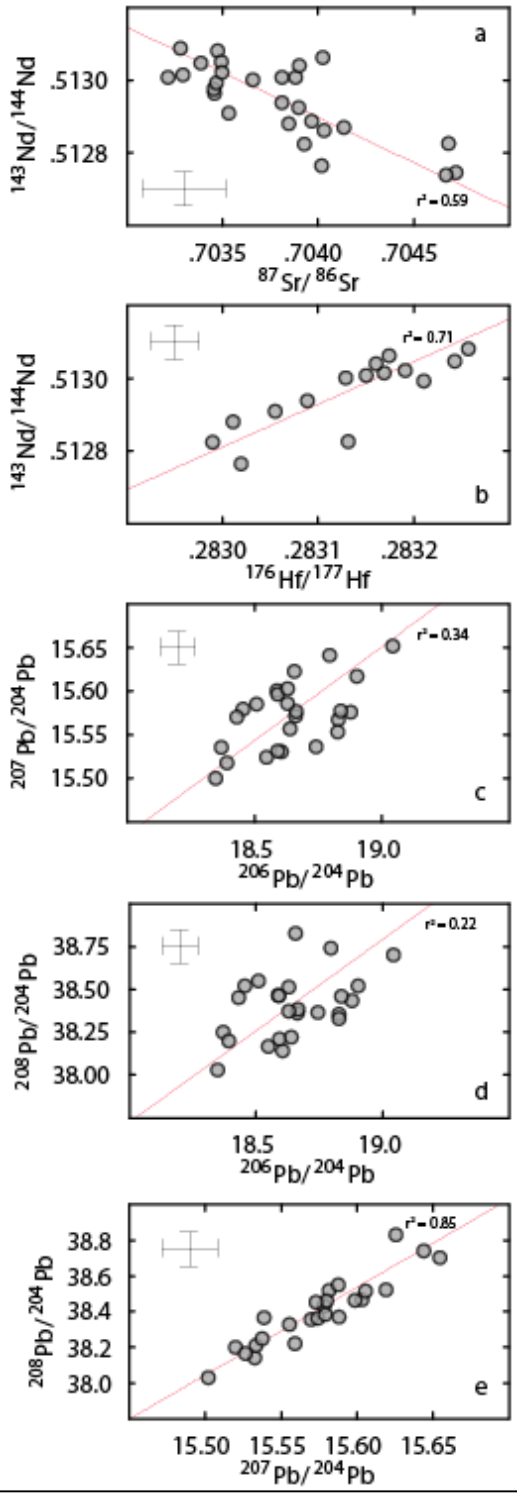

Figure 3.2: Relationships among average arc front Nd, Sr, Hf, and Pb isotopes. $^{143}Nd/^{144}Nd$ correlates negatively with $^{87}Sr/^{86}Sr$ and positively with $^{176}Hf/^{177}Hf$. $^{206}Pb/^{204}Pb$ has a weak positive correlation with $^{207}Pb/^{204}Pb$ and $^{208}Pb/^{204}Pb$, while $^{207}Pb/^{204}Pb$ and $^{208}Pb/^{207}Pb$ correlate strongly. These relationships between Pb isotopes likely reflect Pb isotope signatures dominated by the slab, as alteration of the slab on the seafloor will affect $^{206}Pb/^{204}Pb$ to a greater degree than $^{207}Pb/^{204}Pb$ or $^{208}Pb/^{207}Pb$. Errors bars reflect variation within volcanoes from a single arc as in Figure 3.1.

For global arcs, $^{143}Nd/^{144}Nd$ correlates well with $^{87}Sr/^{86}Sr$ (r^2=0.59, Figure 3.2a), strongly with $^{176}Hf/^{177}Hf$ (r^2=0.71, Figure 3.2b), and weakly with $^{208}Pb/^{204}Pb$ and $^{207}Pb/^{204}Pb$ (r^2=0.45, r^2=0.40). There is no correlation between $^{143}Nd/^{144}Nd$ and $^{206}Pb/^{204}Pb$. Among Pb isotopes, there is a weak correlation between $^{206}Pb/^{204}Pb$ and $^{207}Pb/^{204}Pb$ (r^2=0.34, Figure 3.2c) and a very weak correlation between $^{206}Pb/^{204}Pb$ and $^{208}Pb/^{204}Pb$ (r^2=0.22, Figure 3.2d). A notably strong linear correlation, with r^2=0.85, is present between $^{207}Pb/^{204}Pb$ and $^{208}Pb/^{204}Pb$ (Figure 3.2e). Because a large portion of the Pb contents of arc front magmas are slab derived (Kay, 1980), the weaker correlations with $^{206}Pb/^{204}Pb$ as compared to other Pb isotopes may be accounted for by the varying Pb isotope compositions of subducting sediments and alteration processes in the slab prior to subduction, as $^{206}Pb/^{204}Pb$ can be affected by U enrichment on relatively short timescales (e.g., Kelley et al., 2005).

High $^{143}Nd/^{144}Nd$ values tend to correspond to low $Nd_{6.0}$ values, though this relationship does not hold for Ryukyu, the Aegean, and Central Honshu, which have the lowest average $^{143}Nd/^{144}Nd$ but low to moderate Nd abundances (Figure 3.3a). $^{176}Hf/^{177}Hf$ values correlate more strongly with some 6-values, but this is most likely due to the lack of $^{176}Hf/^{177}Hf$ data for Ryukyu and Central Honshu, and so is not shown. A weak negative correlation is present between $^{143}Nd/^{144}Nd$ and the La/Sm ratio, while a positive, though possibly non-linear, relationship exists between $^{143}Nd/^{144}Nd$ and the Ba/Nb ratio (Figures 3.3b-c). $^{143}Nd/^{144}Nd$ also correlates well with Th/U (Figure 3.3d). As shown on Figures 3.3b-d, the arc average $^{143}Nd/^{144}Nd$ values range from estimates of the depleted MORB mantle (DMM, Workman and Hart, 2005), and the average $^{143}Nd/^{144}Nd$ of EM type Ocean Island Basalts (OIBs, calculated from the database of Stracke, 2012). The arc front averages with the highest $^{143}Nd/^{144}Nd$ have far higher Ba/Nb than oceanic basalts, similar to the Ba/Nb values found in ocean sediments (from Plank, 2013), while arcs with $^{143}Nd/^{144}Nd$ that is similar to EM-OIBs have lower Ba/Nb (EM-OIB trace

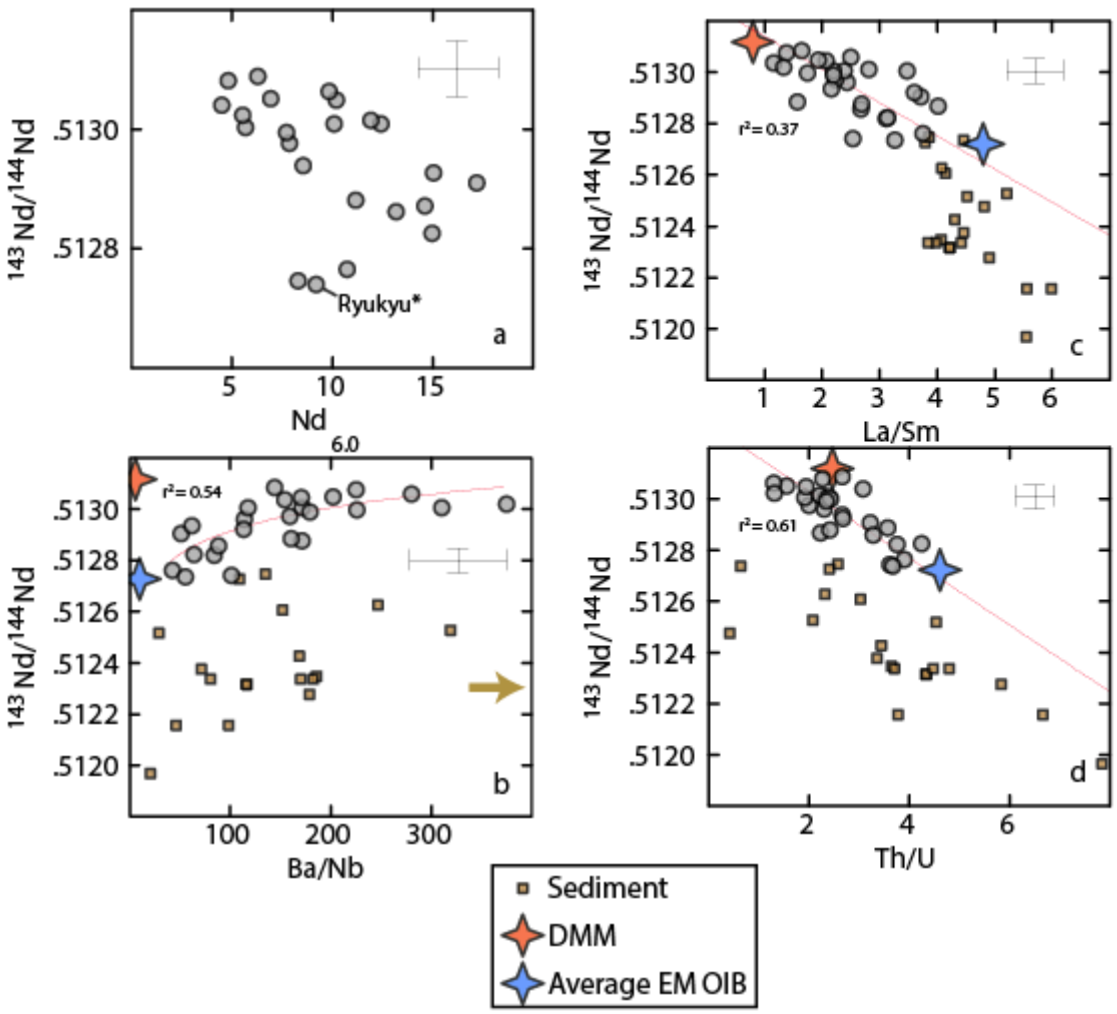

Figure 3.3: Panel a: Low $^{143}Nd/^{144}Nd$ values appear to generally correspond to high Nd concentrations, though this relationship does not hold for the three arcs with the lowest $^{143}Nd/^{144}Nd$ (Ryukyu, Central Honshu, and the Aegean). *Note: Due to insufficient 6-value calculation at Ryukyu, the Ryukyu Mg#55 value is plotted here instead. Chapter 2 demonstrated a 1:1 correlation between 6-Values and Mg#55 values, and so we consider this an accurate proxy of $Nd_{6.0}$. Panels b-d: $^{143}Nd/^{144}Nd$ correlates positively with Ba/Nb and negatively with La/Sm and Th/U. These are the only significant correlations found between trace element ratios and $^{143}Nd/^{144}Nd$. Yelloe arrow indicates two additional sediments plot off the scale of this figure.

element averages calculated from the database of Willbold and Stracke, 2006). The DMM and EM-OIBs bracket the arc data on Figures 3.3c-d, which has lower overall La/Sm and Th/U values than sediment.

No other strong correlations have been identified between isotope ratios and major element concentrations, trace element concentrations, or trace element ratios.

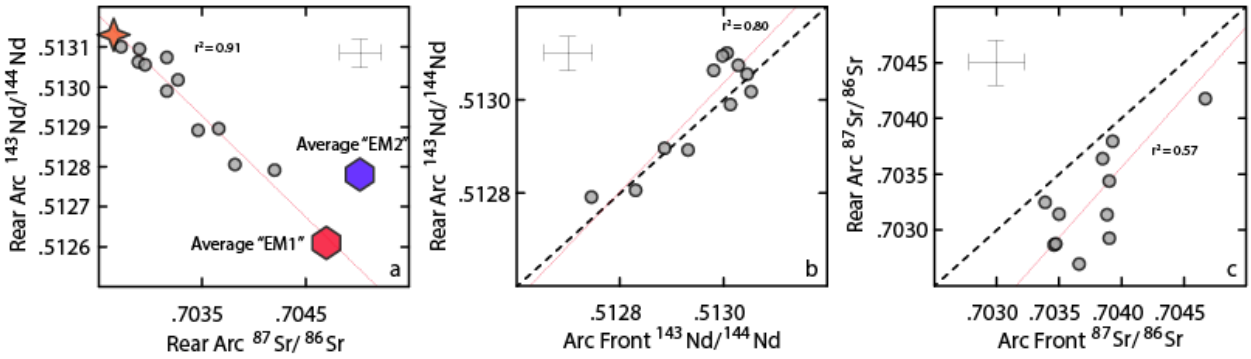

Figure 3.4: A subset of arc segments exhibit volcanic activity behind the arc front (both back-arc spreading centers and rear-arc volcanism) that is driven by extensional regional tectonics, which are referred to here as rear-arc volcanics. These rear-arc volcanics have been filtered to ensure their compositions have not been affected by subducting sediment (see text for details) in order to constrain the composition of the ambient mantle wedge. Among rear-arc volcanics, $^{143}Nd/^{144}Nd$ and $^{87}Sr/^{86}Sr$ correlate strongly (panel a), and overlap with the compositional field defined by MORB (based on global MOR segment averages from Gale et al., 2013). The rear-arc $^{143}Nd/^{144}Nd$ values also correlate well with the compositions of associated arc front volcanics (panel b). Any such relationship among $^{87}Sr/^{86}Sr$ values appears to depend on a single highly enriched segment (panel c).

The average $^{87}Sr/^{86}Sr$ and $^{143}Nd/^{144}Nd$ values from our rear-arc database can be compared to the isotopic composition of arc front lavas. As discussed in section 3.2.1, the rear-arc database has been filtered to retain only samples with Th/Nb ratios < 0.14, which should preclude the contribution of significant slab melt to their source region. Nd and Sr, like Th, are relatively immobile in low temperature aqueous fluids (Spandler et al., 2007), and thus are only transferred from the slab to the wedge in significant quantities by slab melts. We therefore consider rear-arc samples with low Th/Nb ratios to have Sr and Nd isotopic values that represent the ambient mantle wedge isotopic values. Among rear-arc averages, there is a near perfect linear correlation (r^2=0.91) between $^{87}Sr/^{86}Sr$ and $^{143}Nd/^{144}Nd$ (Figure 3.4a), and this correlation is consistent with enrichment trends found in oceanic basalts, providing further evidence that these data are free from any modification by the slab. In detail, the rear-arc basalts appear to be bracketed by DMM and the EM1 subset of EM-OIBs, as the EM2-OIB average has higher $^{143}Nd/^{144}Nd$ at a given $^{87}Sr/^{86}Sr$. Figure 3.4b shows that there is also a strong correlation (r^2=.80) between average rear-arc $^{143}Nd/^{144}Nd$ values (filtered for low Th/Nb) and average arc front $^{143}Nd/^{144}Nd$. For $^{143}Nd/^{144}Nd$, some of the more depleted (high $^{143}Nd/^{144}Nd$) values deviate slightly

from the 1:1 line (dotted black line). Where deviations from the 1:1 line occur, the higher $^{143}Nd/^{144}Nd$ is found in the rear-arc. The correlation between rear-arc and arc front values is significantly weaker for Sr isotopes, with any correlation existing primarily due to a single outlying point (Figure 3.4c). All arc front values of $^{87}Sr/^{86}Sr$ are higher than their rear-arc counterparts, and as with the Nd isotopes, rear-arcs with the most depleted (low $^{87}Sr/^{86}Sr$) values deviate farthest from the 1:1 line. There are no apparent correlations between arc front and rear-arc Pb isotope ratios (not shown).

3.2.3 Correlations with crustal thickness (CT), slab thermal parameter (Φ), depth to slab (H) and slab temperature

Chapter 2 demonstrated correlations among major and trace element compositions of arc magmas, as well as correlations among chemical parameters and crustal thickness (CT). Within the major elements, strong correlations exist between crustal thickness and $Na_{6.0}$, $Ca_{6.0}$, $K_{6.0}$, and $P_{6.0}$ (Figure 3.5, column 1). The correlations with bulk elemental concentrations are plotted here as 6-values, which are calculated using only samples with 5.5<wt.% MgO<6.5. Chapter 2 demonstrated, however, that these correlations are independent of the normalization scheme employed – bracketing by various Mg# criteria or using raw average values will produce nearly identical results to the data shown here, which are bracketed within a range of wt. % MgO.

To investigate additional processes that likely contribute to the chemical diversity of primary magmas, this analysis must be expanded to include additional subduction parameters. The thermal parameter, Φ, is a combination of multiple subduction parameters, calculated as the product of the slab age (A), convergence rate (V), and the sin of the slab dip angle (θ). It has been proposed as a proxy for the thermal state of the subducting slab (Kirby et al., 1991; England et al., 2004). In all figures here, Φ is calculated using the full spreading rate, which includes back arc spreading where present, following

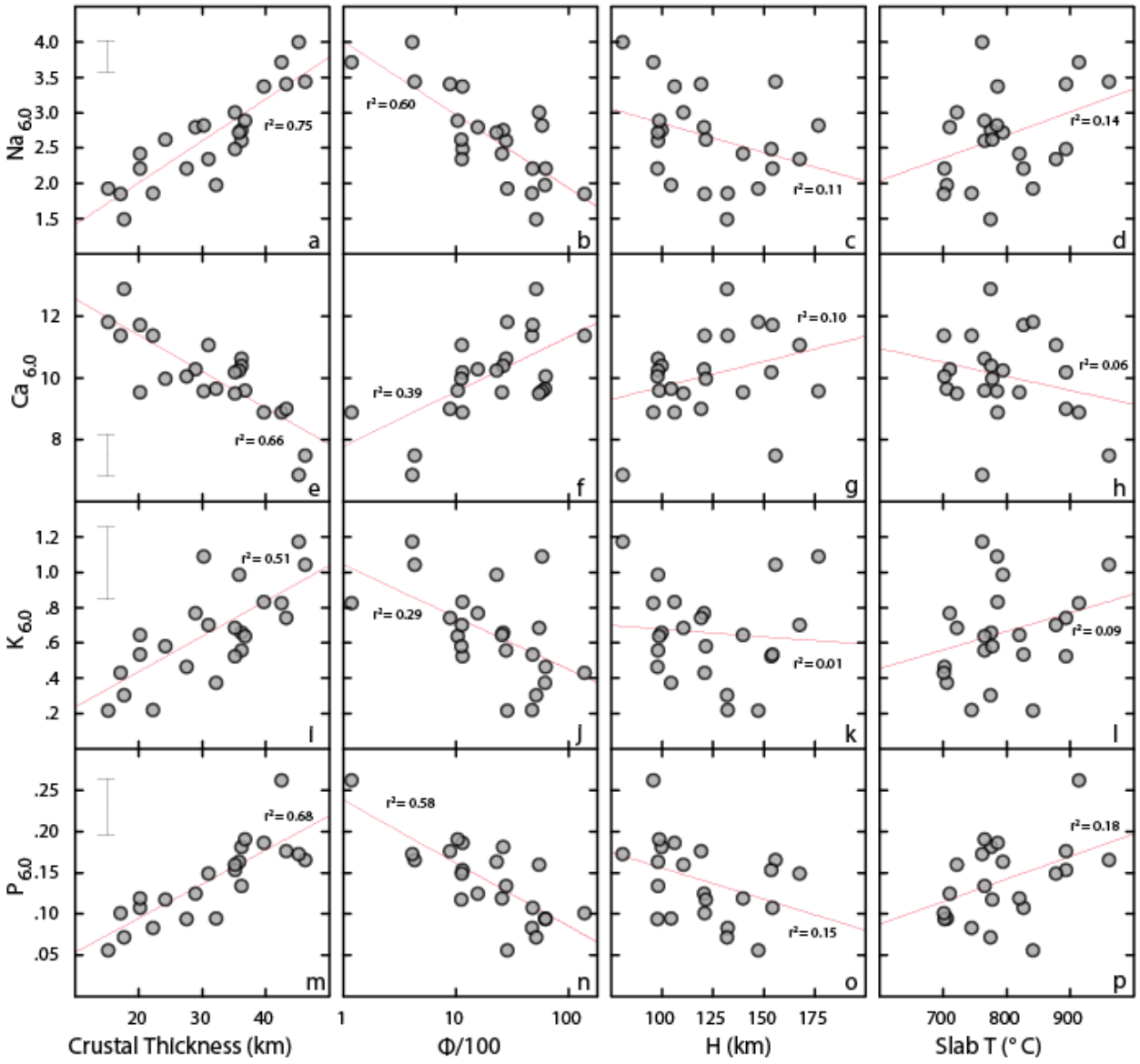

Figure 3.5: Relationships between major/minor element 6-values and subduction parameters. Column 1: As discussed in detail in Plank and Langmuir (1988) and Chapter 2, there are compelling relationships between Ca, Na, K, and P concentrations and the thickness of the overlying arc crust. Column 2: Correlations are also present between major/minor element concentrations and the thermal parameter (Φ), though these correlations are not as strong as the correlations with crustal thickness. Columns 3-4: No strong correlations exist between elemental concentrations and the depth to the subducting slab (H) or the slab surface temperatures of Syracuse et al. (2010). The slab surface temperatures above are from the D80 model of Syracuse et al. (2010), though the lack of correlation is independent of the specific model choice.

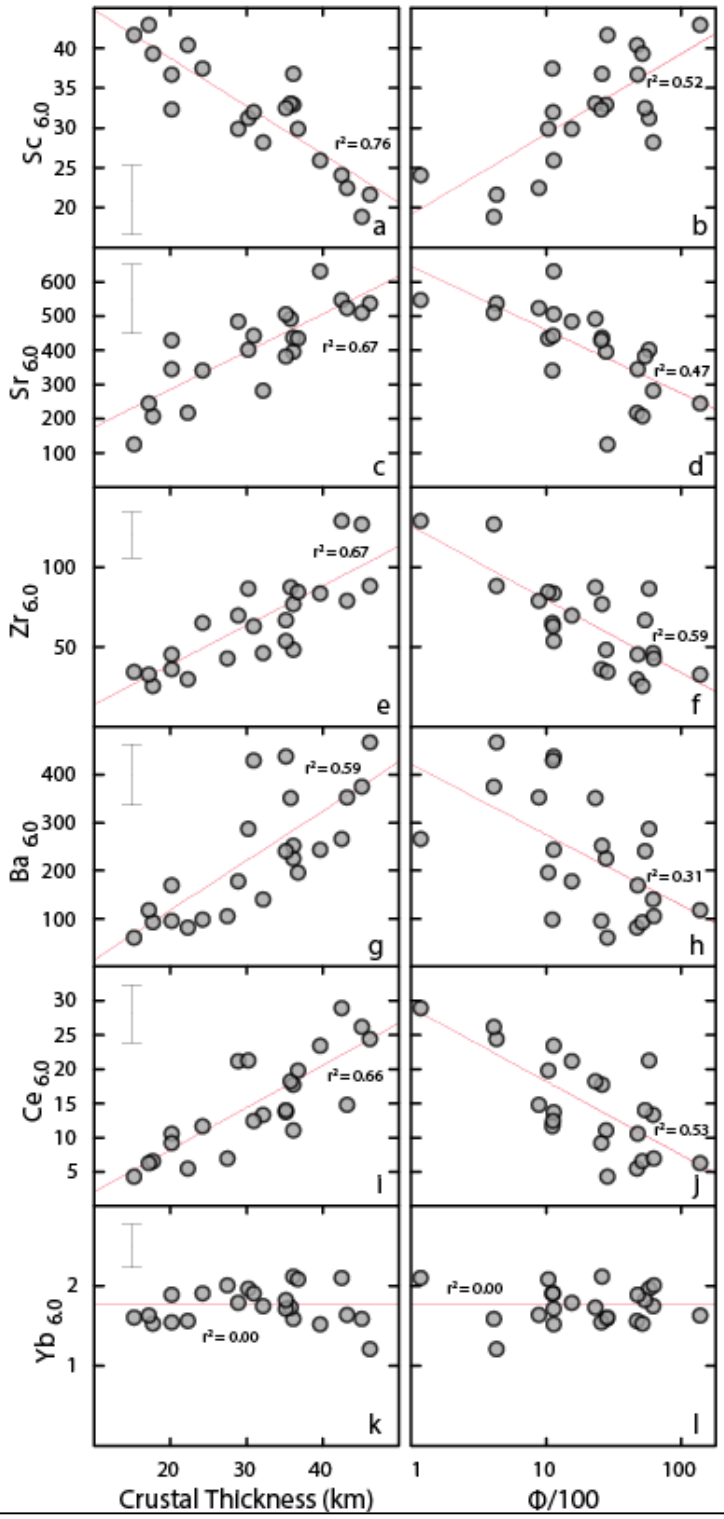

Figure 3.6: The compatible elements Sc (and V, not shown) correlate negatively with crustal thickness (panel a) and positively with the thermal parameter (Φ, panel b), while nearly all incompatible elements correlate positively with crustal thickness and negatively with Φ (panels c-j). Yb concentrations are relatively constant across all arc segments (panels k-l). As with major elements, correlations with crustal thickness are stronger than with Φ for all elements.

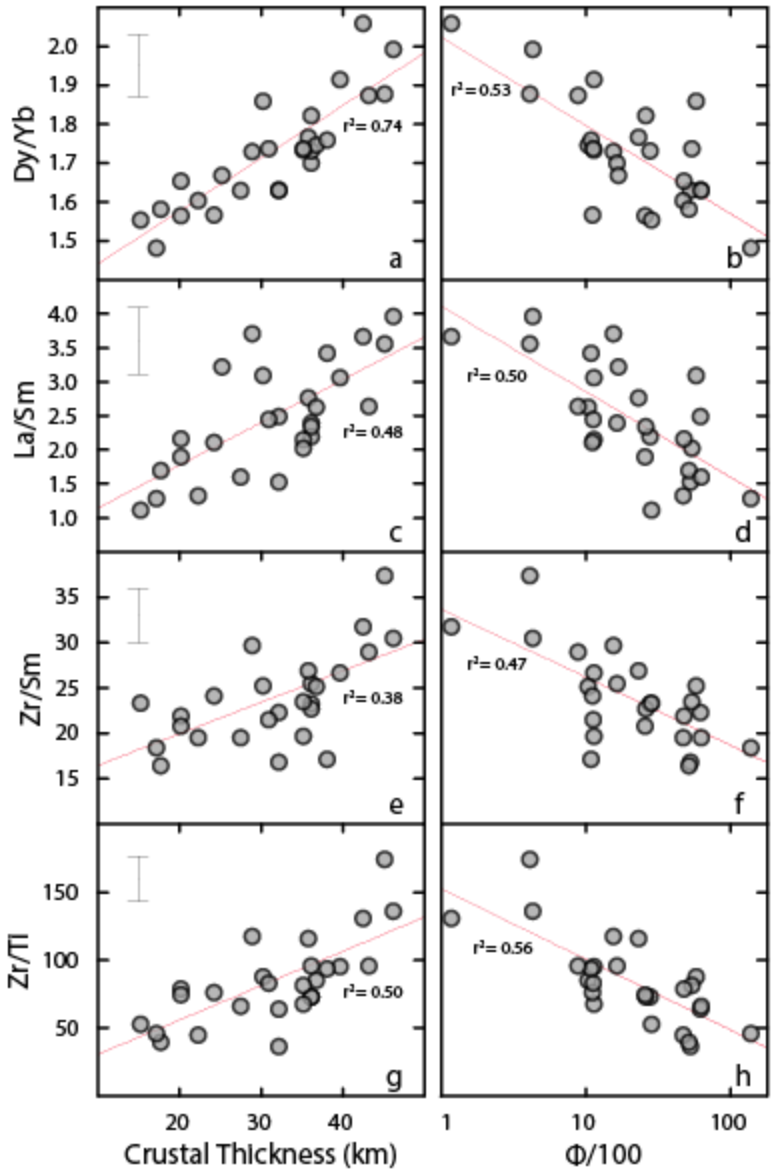

Figure 3.7: The trace element ratios Dy/Yb, La/Sm, Zr/Sm, and Zr/Ti all correlate positively with crustal thickness and negatively with the thermal parameter (Φ). Crustal thickness correlates much more strongly with Dy/Yb than Φ, but the remaining ratios have slightly stronger correlations with Φ than crustal thickness.

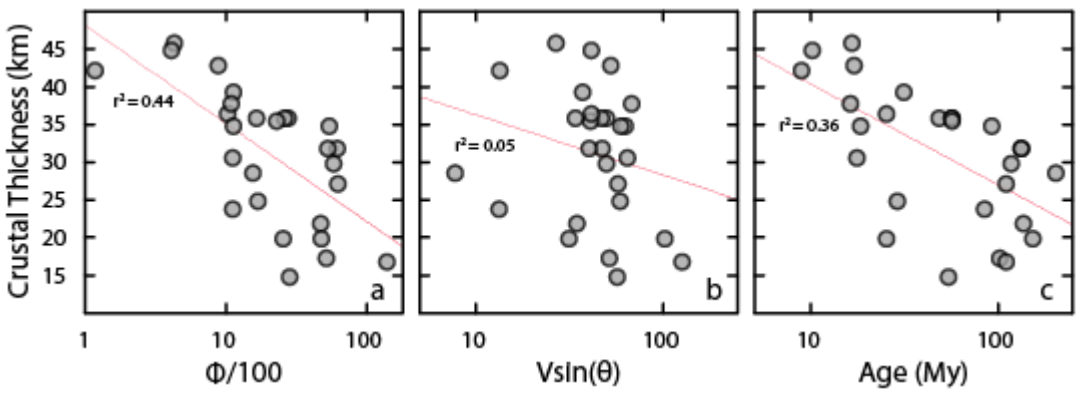

Figure 3.8: Among the arc segments included in this study, there is a significant negative correlation between crustal thickness and the thermal parameter (Φ, panel a). The correlation between crustal thickness and Φ does not extend to crustal thickness and the Vsin(θ) parameter, though a correlation is present between crustal thickness and the slab age (panels b-c).

Syracuse et al. (2010). If back arc spreading rates are not included, all correlations with Φ are weakened. Φ correlates significantly with the major elements listed above (Figure 3.5, column 2; note log scale) though correlations with Φ are somewhat weaker than correlations with CT. Within the arc segments included in this study, there is a weak correlation between crustal thickness and Φ (Figure 3.8a), so it is unsurprising that many of the chemical indices correlating with one of these parameters also correlate somewhat with the other. This correlation between crustal thickness and Φ appears to be mostly attributable to the slab age rather than Vsin(θ) (Figure 3.8b-c). The slab age term contributes a majority of the total variability to Φ, with slab age varying by a factor of 23, and Vsin(θ) varying by a factor of 16. There are no correlations between our major element dataset and the depth of the slab (H) beneath the arc front (Figure 3.5, column 3), in contrast to the findings of Dickenson and Hatherton (1967). This is likely due to our exclusion of samples erupted from fore arc or rear-arc vents within our segment averages. The sub-arc slab surface model temperatures reported by the D80 models of Syracuse et al. (2010) exhibit poor to absent correlations with major elements ($r^2 < 0.2$, Figure 3.5, column 4).

As with the major elements, most incompatible trace elements correlate positively with crustal thickness and negatively with Φ (Figure 3.6). The positive correlations are particularly strong among the LREE, Sr, Zr, and Ba, and are notably absent within the HREE. For most of these incompatible elements,

the relative variation among arc segments spans a factor of 3 or 4, with the greatest enrichment at thick-crust, low Φ arcs. In contrast, total relative variation is limited to 50% for the HREE. The compatible trace elements V and Sc are anti-correlated with crustal thickness, with both of these elements decreasing by a factor of ~2 going from thin to thick crust (Figure 3.6a). Finally, the trace element ratios described earlier also show coherent relationships with crustal thickness and Φ, with Dy/Yb, La/Sm, Zr/Sm, and Zr/Ti all increasing with crustal thickness and decreasing with Φ (Figure 3.7). As for the major elements, correlations between both normalized trace element concentrations and trace element ratios with H are crude, and the model slab surface temperatures of Syracuse et al. (2010) do not correlate well with chemical parameters (not shown). Isotopic ratios show no strong correlations with any subduction parameters (also not shown).

3.3 Discussion

The observations above show that variations in the mean compositions of global convergent margins correlate with crustal thickness and, slightly less well, with the slab thermal parameter. An important question is the causes of these correlations, and hence the origin of the global variations. This question can be considered in the context of two models, one based on wedge thermal structure, and the other based on slab thermal structure. The Wedge Thermal Structure (WTS) model attributes chemical diversity primarily to melting conditions in the mantle wedge caused by lithospheric thickness, and to a lesser extent the convergence rate and slab dip. Variation in the wedge thermal structure leads to large differences in the pressure and temperature conditions, and thus the extent of melting, beneath arcs. In this model, the flux from the slab is assumed to be constant globally except for those elements strongly controlled by sediment composition (e.g., Plank and Langmuir, 1993).

The Slab Thermal Structure (STS) model presumes that the thermal structure on the mantle wedge is relatively invariant, consistent with the possibility that the location of the arc front is

determined by certain wedge thermal conditions (e.g., Schmidt and Poli, 1998). Slabs have different temperatures beneath the arc due primarily to slab age, dip, and convergence rate, and these temperature variations lead to highly variable slab flux that changes the composition of the wedge prior to melting.

These models represent the classic geochemical problem of separating source variations from variations in extents of melting. Of course, source variations must exist beneath convergent margins, and the flux from the slab is not constant. This is required by the overwhelming evidence demonstrating the importance of sediment recycling, and variable sediment compositions, for convergent margin volcanics (e.g., Morris and Tera, 1989; Plank and Langmuir, 1998). These effects lead to variations in the ratios of highly incompatible elements with similar distribution coefficients (e.g., Ba/Th, Th/Nb, Ce/Pb) and produce the distinct chemical signature of subduction zone lavas. Such variations are not included in the following treatment, which emphasizes instead the factor of five variations that are observed in all classes of incompatible elements—both those that are slab-derived and those for which slab contributions are small (i.e. Nb, Zr) —as well as changes in moderately compatible elements (i.e Sc and V), and element ratios (e.g., Zr/Sm, HREE) that are less likely to be controlled by variations in the amounts and compositions of sediments.

After consideration of each of the end member models, the possibility of a hybrid model is considered, along with the implications for overall slab fluxes from slab to wedge. It is useful first, however, to consider the pure end member models: one with a constant slab flux and variable wedge thermal structure, and another with a variable slab flux and constant wedge thermal structure.

3.3.1 The Wedge Thermal Structure (WTS) model

Plank and Langmuir (1988) proposed that correlations among major element compositions of arc magmas could be produced by variations in the extent of melting of the mantle wedge (F). By assuming that H was constant, as was generally accepted at that time, they inferred that the distance between the slab and the base of the crust, or the "length of the melting column," was the critical parameter in determining F. This inference, however, is not consistent with more recent data, because the value of H may vary by at least as much as crustal thickness, and correlations with crustal thickness do not extend to correlations that include H (Figure 3.5, column 3).

The suggestion that varying F accounts for a large portion of the chemical variability of arc magmas, however, is still a viable hypothesis. The physical mechanism controlling the extent of melting, however, must differ from the model proposed by Plank and Langmuir (1988). An alternative mechanism is the F is controlled by the wedge thermal structure, which is influenced by the thickness of the overlying lithosphere. Lithospheric thickness likely correlates with the thickness of the overlying arc crust, because thicker crust pushes cold isotherms deeper. Lithospheric thickness may be an important control on the extent of melting of the mantle wedge, because sub-arc lithospheric thickness could influence both the temperature and pressure of melt generation. Thicker lithosphere is likely to displace melting to higher pressures and lower temperatures (see cartoon in Figure 3.9). A convenient measure of this effect on mantle melting is the parameter $T\text{-}T_s$, where T_s is the anhydrous solidus temperature at a given pressure (e.g., Langmuir et al., 2006). $T\text{-}T_s$ is a measure of the energy available for melting, so higher values lead to greater extents of melting (at a given H_2O concentration). Increasing pressure increases T_s, and so melting at higher pressures decreases $T\text{-}T_s$ and hence decreases the extent of melting. For a given H, increasing lithospheric thickness may also displace the hottest wedge isotherms away from the trench, thus reducing the maximum temperature of the mantle beneath the arc front, which further reduces $T\text{-}T_s$ (Karlstrom et al., 2014). By the same logic, varying H alone may not

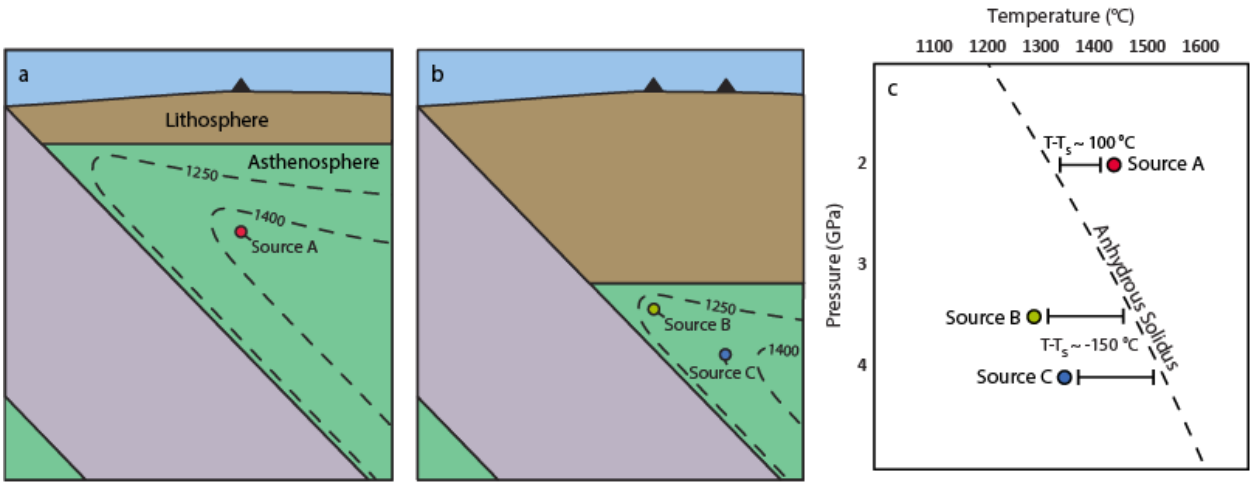

Figure 3.9: A cartoon illustrating the potential relationship between lithospheric thickness and the extent of melting, as proposed for the WTS model. As lithospheric thickness increases, hotter isotherms are displaced away from the trench, and the depth of mantle melting (and thus pressure) increases. Mantle source A, at a thin-crust arc, therefore lies at a higher temperature and lower pressure than mantle source B, at a thick-crust arc. Both temperature and pressure control the extent of melting, which is a function of the difference between the temperature of the mantle and the dry mantle solidus (T-T_s). T-T_s is about 250 °C higher for source A than source B. Variation in H can be accomplished either by shifting the arc front away from the trench (compare source b to source c) or by changing the slab angle. Either of these may increase the source temperature, but will also increase the source pressure. As a result, there is no net change in T-T_s, and thus changing H alone may not affect the extent of melting.

significantly affect T- T_s, because an independent increase in H is likely to increase P and T simultaneously (Figure 3.9b-c).

The potential viability of this model (the WTS model) depends upon its ability to satisfy the new results presented here, such as the enrichment of a host of incompatible trace elements, the co-variation of this enrichment pattern with certain trace element ratios (Dy/Yb, La/Sm, Zr/Sm, Zr/Ti), and the concurrent depletion of Sc and V. A particularly important new observation in this regard is the correlation between crustal thickness and Dy/Yb, as fractionation among the HREE does not occur during melting in the spinel peridotite stability field. This relationship requires that there be a significant signal from residual garnet transferred either from the deep mantle wedge or the slab.

The success of this model is demonstrated in Figure 3.10. The global geochemical trends can be reproduced by assuming simple linear relationships between crustal thickness and the pressure and temperature of mantle melting. In order to reproduce the smooth correlation between crustal thickness and Dy/Yb, melting must occur within the garnet stability field, at pressures greater than 2 GPa. We thus proscribe a pressure range from 2 to 3.5 GPa and a temperature of range of 1450 to 1300 °C that corresponds to crustal thickness range between 15 and 50 km. This pressure and temperature range is within P and T conditions of melting predicted dynamic models of Wilson et al. (2014).

The models shown in the Figure 3.10-3.13 have a constant mantle H_2O content of 0.6 wt. %, and equilibrate near the hot nose of the mantle wedge, at a single P and T. Of course, in reality, the relationship between crustal thickness and the P and T conditions of melting is likely not linear, H_2O contents are likely not constant, and melting probably occurs over a range of P and T. The goal of this model is not to emulate the full range of mantle processes that ultimately affect the compositions of primary magmas, but rather to determine if a simple first order model can reproduce the coherent first order variability among global arcs. We should also note that the linear parameterization of P and T with CT results in melting regions that are close to or within the slab at a few arcs that have very thick crust and very shallow slab depths (such as Mexico). In reality, the very short melting columns in such arcs probably result in particularly low sub-arc mantle temperatures, so the low extents of melting we predict in these settings are expected (see Karlstrom et al., 2014, for a physics based description of this process). The resulting extents of melting were calculated using the equations of Katz et al. (2003), taking into account an enthalpy of fusion of 180 cal/g. The resulting range in the extent of melting is from F~.05 to F~0.20. The parameterization of subsolidus mantle modes, melting reaction coefficients, and element partition coefficients are available in the Supplementary Dataset A3.2.

The model outputs shown as green diamonds on Figure 3.10 are generated from a mantle composition (taken from Workman and Hart, 2005) that has been modified by a 7% addition of an

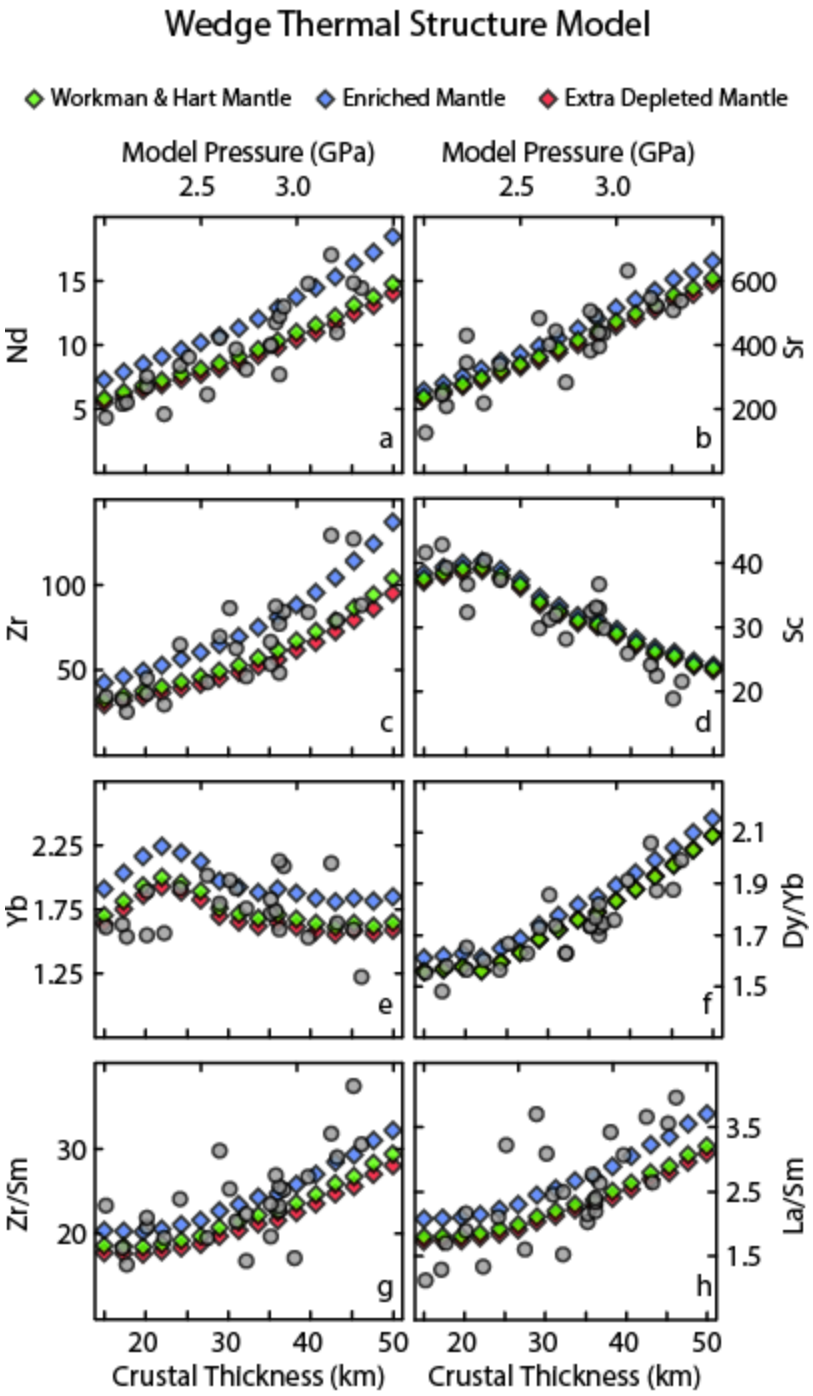

Figure 3.10: A comparison of the WTS model with average arc data, adjusted for the likely effects of fractional crystallization. Green diamonds represent values calculated using the mantle composition of Workman and Hart (2005) as a starting composition. Blue diamonds use the Workman and Hart mantle with the addition of 2% E-MORB from Gale et al. (2013), and red diamonds use the Workman and Hart mantle after extraction of 0.5% melt. The WTS model is successful at reproducing the trends in trace element compositions and ratios. For model details see text and Appendix A3.1.

N-MORB (Gale et al., 2013) melt, and 1% addition of sediment melt. Consideration of heterogeneity in the background composition of the mantle wedge is discussed below. The sediment composition used in the model is the mean of sediment compositions from each of the segments in our dataset, which for Central American segments are the hemipelagic sediment composition from Patino et al. (2000) and for all other segments are the estimated subducting sediments from Plank et al. (2013). The hemipelagic sediment from Central America was used for relevant segments because including the underlying carbonate section results in Sr enrichments much greater than are observed, and because a sediment flux dominated by hemipelagic sediment for most Central American volcanic centers is indicated by the mixing lines in Patino et al. (2000). Sediment and AOC melt compositions were calculated for a slab melt at 875 °C, using the methods described below in section 3.3.2. Once again, in reality, a constant slab composition and proportion are of course not added at every arc. They are used in this model to determine if variations in mantle melting alone may account for the first order global geochemical trends. If this model does in fact represent the basic process responsible for these trends, then the variables held constant in this simple model may be responsible the scatter on Figures 3.1-8.

A comparison of model outputs (green diamonds) and actual arc averages (gray circles) is shown in Figure 3.10. The enrichments of incompatible elements produced by changing modal mineralogy and extents of mantle melting as pressure increases and temperatures decrease closely reproduce the concurrent incompatible element enrichment (Figure 3.10a-c) and Sc depletion (Figure 3.10d) observed in the global dataset. The trends for Zr/Sm and Dy/Yb are also well reproduced (Figure 3.10f-g). These modeling results demonstrate the plausibility of variations in the extent of melting of a mantle wedge of constant composition as a primary driver of global correlations between magma chemistry and crustal thickness, and thus provide a quantitatively viable model for variations in the global chemical compositions of convergent margin chemical compositions.

Variations in major element concentrations are also important, though not explicitly modeled here. The most obvious major element trends are with Na, Ca, and K, which are well known to vary with extent of melting (Jaques and Green, 1980; Plank and Langmuir, 1988). Thick-crust arcs are also associated with high $Si_{6.0}$ and low $Fe_{6.0}$, and these relationships are likely to be somewhat more complicated (Plank and Langmuir, 1988; Chapter 2). It is difficult to assess these variations partly due to the lack of experimental data that are high P, hydrous, and at low extents of melting. Though the experiments of Baker et al. (1995), demonstrate that low $Fe_{6.0}$ high $Si_{6.0}$ liquids (much like those frequently found at thick-crust arcs) can be produced by low F melting, these experiments were anhydrous and at pressures of only 1 GPa. Balta et al. (2011) conducted hydrous, high P (3 GPa) experiments, and demonstrated that adding water can produce slightly elevated SiO_2 concentrations, though these experiments do not attempt to evaluate the added effect of very low extents of melting. Lee et al. (2009) compile experimental data to produce a thermobarometer for peridotite melts based on the activity of silica, and suggest that many Cascades lavas appear to have equilibrated at temperatures close to the Moho. Equilibration with the mantle just below the Moho is not necessarily inconsistent with the WTS model, as a garnet influence on trace elements could be inherited from melting at depth, followed by major element re-equilibration at shallower levels.

3.3.1.1 How important is heterogeneity of the ambient mantle wedge?

Some ratios, such as La/Sm (Figure 3.10h), vary to a greater extent than would be predicted by the melting model alone. The La/Sm ratio is particularly sensitive to the composition and quantity of sediment that is transferred to the mantle wedge in a given arc, and so additional scatter in this ratio is unsurprising. Variability in the background enrichment of the ambient mantle wedge (the wedge prior to slab addition) can also affect the La/Sm ratio. Many arcs with low La/Sm compositions are associated

with back-arc basins, while particularly elevated La/Sm compositions, suggestive of an enriched ambient mantle wedge, appear to be present at several mature arcs with thick crust. There is also evidence of enrichment of the mantle wedge in some locations based on rear-arc $^{143}Nd/^{144}Nd$ and $^{87}Sr/^{86}Sr$ systematics (Figure 3.4a), which indicates that mantle wedge enrichment may follow similar trends to the enrichment seen in EM1 type OIBs. That background mantle wedge compositions play a potentially important role in determining arc front magma compositions is additionally supported by the strong correlation between rear-arc Nd isotope concentrations and those seen in the arc front (Figure 3.4b). The proposal that enriched ambient mantle wedge compositions are associated with mature arcs, and can have large effects on magma compositions (see also Chin et al., 2014) therefore merits further consideration.

While variability in ambient mantle wedge enrichment can significantly affect certain trace element ratios and concentrations, heterogeneity of the ambient mantle wedge is unable to account for most of the chemical variability of the global dataset. The red and blue diamonds on Figure 3.10 demonstrate the effect of starting with an extra depleted or extra enriched mantle composition. Extra depleted mantle is calculated by removing 0.5% melt from the mantle composition of Workman and Hart (2005). Enriched mantle is calculated by adding 2% E-MORB (Gale et al., 2013) to the ambient mantle, based on the assumption that enrichment of the ambient mantle wedge follows the same trends observed in MORB, to first order. It is apparent on Figure 3.10 that varying the enrichment of the ambient mantle is able to accommodate some of the scatter on plots of compositional parameters vs crustal thickness, but that this effect is in most cases quite small compared to the variations produced by varying F.

In these model calculations, Nb is treated as completely immobile from the slab to the mantle wedge, and so the maximum allowable level of ambient mantle enrichment is constrained by the final Nb concentrations in the melt. As shown on Figure 3.11a, it is possible to account for the entire range of

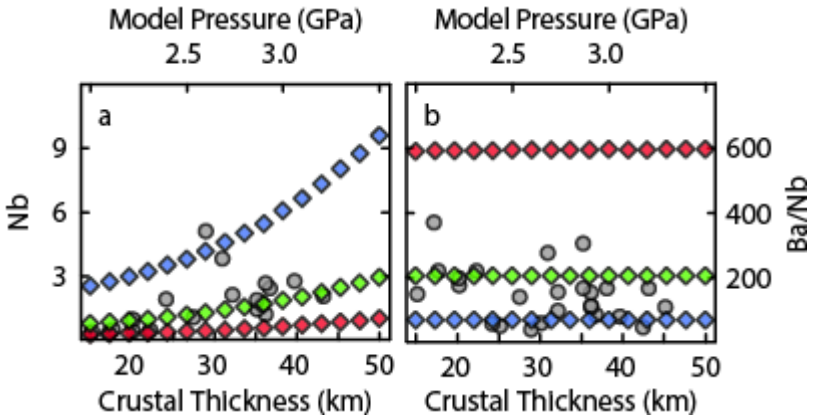

Figure 3.11: Results of the WTS model for Nb concentrations (a) and the Ba/Nb ratio (b) as compared to actual arc data adjusted for the likely effects of fractional crystallization. Symbols as on Figure 3.10. Though $Nb_{6.0}$ values are not available for a number of segments, this plot can be used to demonstrate the maximum allowable levels of source enrichment. In the WTS model, a maximum of 2% source enrichment can take place before exceeding observed Nb concentrations. Note the extreme sensitivity of the Ba/Nb ratio to source depletion.

arc Nb compositions given this assumption. Particularly notable is the extreme sensitivity of Nb concentrations to background mantle enrichment and depletion processes at low extents of melting (produced at arcs with thick crust using the WTS model). Nb concentrations in arc magmas are particularly sensitive to wedge heterogeneity, and as a result, Nb is a particularly poor indicator of F, unless the ambient mantle composition is somehow independently constrained. This result will apply to any element that is not efficiently transferred from the slab to mantle wedge, but is highly incompatible during mantle wedge melting. Also of note is the observation that the entire range in Ba/Nb, a ratio typically considered indicative of variable slab contributions, can be accounted for by variations in ambient mantle enrichment alone (Figure 3.11b). This occurs because enriched arcs, with high background concentrations of Nb, are less prone to variation in elemental ratios normalized to Nb. High Ba/Nb values in arc lavas must be produced by sediment addition to the wedge. It has also been shown that Ba fluxes into the mantle wedge are themselves highly variable, and correspond to Ba contents erupted at volcanic arcs (Plank and Langmuir, 1993). Background wedge composition for certain elements, however, may also contribute to large variability to certain trace element ratios, and may be important for the correlation between $^{143}Nd/^{144}Nd$ and Ba/Nb shown on Figure 3.3b.

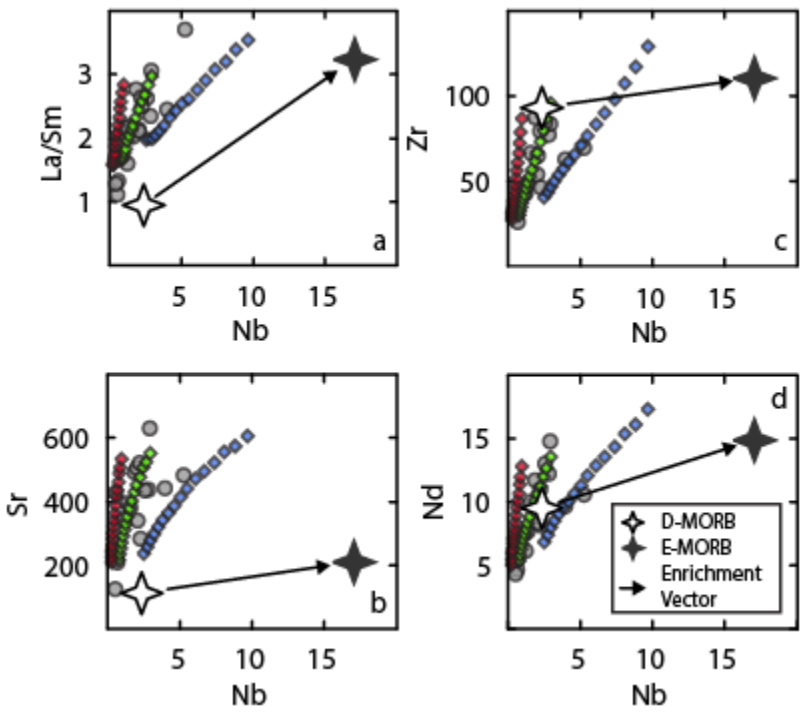

Figure 3.12: A comparison of the WTS model with average arc data, adjusted for the likely effects of fractional crystallization. Nb is more sensitive to mantle enrichment processes than many other trace elements. The blue diamonds display model results using a starting mantle composition of Workman and Hart (2005) DMM composition plus 2% E-MORB taken from Gale et al. (2013). Enriched mantle melts intersect the highest arc Nb concentrations, and additional mantle enrichment would generate compositions more enriched in Nb than are observed. It is also apparent from these plots that trends produced by typical mantle enrichment and depletion processes (black vectors connecting the D-MORB and E-MORB values from Gale et al., 2013) are orthogonal to the observed data, while trends generated by variable extents of mantle melting are more or less parallel to the observed data.

Within the context of the WTS model, mantle enrichment by 2% addition of low F melts is an upper limit. At this maximum level of enrichment, most bulk elemental compositions are barely altered, but Nb concentrations vary significantly. Figure 3.12 demonstrates both the effect of changing F and the effect of source enrichment and depletion of the ambient mantle for La/Sm, Sr, Zr, and Nd compositions as compared to Nb. As on Figures 3.10 and 3.11, the red, green, and blue diamonds show the range of melt compositions that will be produced by varying the extent of melting of a given starting mantle composition. The blue diamonds, which use the Workman and Hart mantle plus 2% E-MORB, intersect those arcs with the highest average Nb. Additional source enrichment would produce curves plotting well to the right of the observed values (gray circles).

The plots also illustrate that while wedge mantle heterogeneity is significant, it is not sufficient to explain the overall global trends. Wedge mantle heterogeneity does not reproduce the slope of trends seen for La/Sm vs Nb, and produces negligible variability in Sr, Zr, and Nd abundances as compared to the range observed for global arcs. It is also clear from Figure 3.12 that the range of average arc front compositions aligns well with the curves expected from varying the extent of mantle melting, but is essentially orthogonal to the compositional vectors associated with enrichment and depletion processes in oceanic basalts.

The importance of wedge heterogeneity varies for different element abundances, ratios and isotope ratios. Since $^{143}Nd/^{144}Nd$ shows strong dependence on wedge composition (see Figure 3.4b), correlations with Nd isotopes can potentially be used to test the importance of the wedge heterogeneity signal. The weak correlation between $^{143}Nd/^{144}Nd$ and La/Sm is evidence for a weak, but detectable effect of mantle heterogeneity on La/Sm. The somewhat stronger correlation between $^{143}Nd/^{144}Nd$ and Th/U may indicate a more prominent role for mantle heterogeneity in altering this ratio.

These various considerations show the importance of mantle wedge heterogeneity to the global variability. For some elements (e.g., Nb) it is very important. For Nd isotopes it may be determinative. For some trace element ratios (La/Sm and Th/U) it appears to contribute importantly. The overall global systematics, however are not accounted for by heterogeneity (Figure 3.12). Therefore modest heterogeneity in the ambient mantle wedge is a necessary component of a successful WTS model.

3.3.1.2 Further tests of the Wedge Thermal Structure (WTS) Model

A further test of the WTS model is to determine whether the fit of chemical parameters to the overlying crustal thickness is improved by including other subduction parameters relevant to the thermal conditions of the wedge. In addition to the effect of crustal thickness on $T\text{-}T_s$, convergence rate

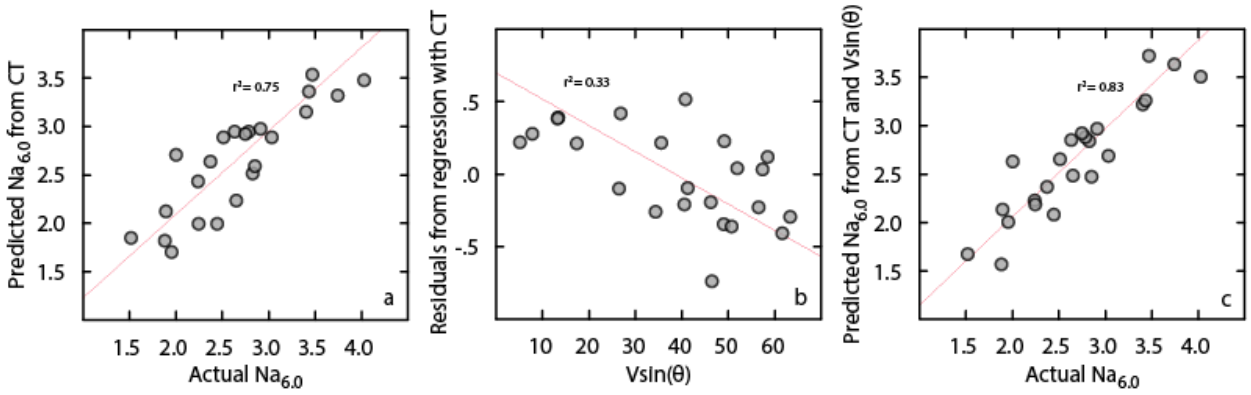

Figure 3.13: A regression of crustal thickness against $Na_{6.0}$ provides prediction of actual $Na_{6.0}$ values with r^2=0.75. The parameter Vsin(θ) should also affect the mantle wedge thermal structure, hence if wedge thermal structure were the the significant variable, one would predict that residuals from crustal thickness vs $Na_{6.0}$ would correlate Vsin(θ). Panel b shows that this is indeed the case. A multiple linear regression of both CT and Vsin(θ) improves predictions of $Na_{6.0}$ (panel c).

and slab dip also influence the wedge thermal structure. Faster plate convergence increases the flux of hot mantle into the wedge corner, raising the wedge temperature beneath the arc. Increasing slab dip increases the separation between the thermal boundary layers of the subducting plate and overlying lithosphere, also influencing wedge temperature. Thermal models (e.g., England and Katz, 2010) show that Vsin(θ) should scale with wedge temperature. Increased Vsin(θ) should lead to larger T-T_s and greater extents of melting and thus correlate with the chemical parameters..

To test this possibility, Figure 3.13b plots Vsin(θ) vs the residuals of a linear regression between $Na_{6.0}$ and crustal thickness (see Figure 3.13a). The plate velocities used in Figure 3.13 have back-arc spreading rates removed, following the logic of England et al., (2004), who suggest that any additional heat advection produced by the increased spreading rates that result from back-arc spreading is likely to be directed towards the spreading center itself rather than the wedge corner. An increase in Vsin(θ) should increase values of T-T_s and thus lower $Na_{6.0}$. This will lead to a negative residual for $Na_{6.0}$ vs crustal thickness, and hence a negative correlation between Vsin(θ) and the residuals, as is observed. We can qualitatively evaluate the significance of including Vsin(θ) by observing points from this multiple regression with residuals>0.1. For points corresponding to Vsin(θ)<40, 88% have positive residuals, while

for points corresponding to Vsin(θ)>40, 82% have negative residuals. Including both Vsin(θ) and crustal thickness in a multiple regression significantly improves predictions of chemical parameters, with r^2=0.83 for $Na_{6.0}$ (Figure 3.13c) and p-values for each independent variable well under 0.01. While the function relating CT, Vsin(θ), and $Na_{6.0}$ is unlikely to be linear in reality, the multiple regression approach still provides a useful first order assessment of the relationship between these variables. The fact that inclusion of Vsin(θ) with lithospheric thickness improves the fit of the data to a wedge melting model lends confidence to the wedge melting hypothesis.

The parameter Vsin(θ) also affects the slab thermal structure, so variations in slab thermal structure might also contribute to the improved results of the multiple regression. In addition to convergence velocity and dip, however, the slab age also plays an additional important role in determining the slab thermal structure. If the slab thermal structure is the critical variable, then incorporating the full slab thermal parameter should produce better predictions of chemical parameters than Vsin(θ) alone. This is not the case. The fit is slightly degraded (r^2 of 0.81 vs 0.83) if slab age is included. More importantly, the slab thermal parameter should in theory provide a better analog for the slab thermal state if convergence rates including back arc spreading are used (Jarrard, 1986). In this case, predictions of $Na_{6.0}$ are not improved at all compared to the regression using CT alone. This analysis suggests that wedge rather than slab thermal structure is the important parameter.

3.3.2 Evaluation of the Slab Thermal Structure (STS) model

Slab temperatures must vary among arcs. The importance of the slab thermal parameter, for example, is clearly indicated by its relationship with the maximum depths of earthquakes among subduction zones (Jarrard, 1986). As shown above, the thermal parameter (Φ) also correlates with several major element concentrations, trace element concentrations, and trace element ratios, though

correlations with Φ are typically weaker than those with crustal thickness. These correlations lend credence to the hypothesis that erupted magma compositions are controlled by the thermal state of the subducting slab (e.g., Plank et al., 2009; Cooper et al., 2012).

These factors motivate a second end member model, the Slab Thermal Structure model, in which the slab flux to a mantle wedge is variable, while the mantle thermal structure is constant. The essence of the STS model is that increasing slab temperature leads to higher concentrations of elements in the slab melt, and higher mass flux of slab material into the mantle wedge. Like the WTS model, the STS model has many complexities that are difficult to take into account. Large thermal gradients occur in the slab at any depth, and both dehydration and melting are progressive open system processes. Slabs have variable compositions and form at different spreading rates with different sediment compositions (Plank and Langmuir, 1998). There is evidence for multiple slab components in many arcs (e.g., Miller et al. 1994; Elliott et al., 1997). The variable slab output interacts with and flows through the mantle wedge along pathways that are poorly constrained (e.g., Wilson et al., 2014). And so on.

Despite these complexities, a first order evaluation is possible. The model takes a constant wedge thermal structure and adds slab components, varying slab melt compositions and total slab flux as a function of slab temperature, from 800°C to 1000°C. Model details and the MATLAB scripts used to generate all model results are available in Appendix A3.1 and Supplementary Dataset A3.3. The model has the following conditions:

- A constant wedge thermal structure is used, with melts forming at 1.8 GPa and 1350 °C. These values were selected because they provide a successful model.
- The ambient wedge composition is constant, with the composition of DMM from Workman and Hart (2005).

- H_2O contents in the mantle, and thus the extent of mantle melting, vary based on the amount of slab addition and the H_2O contents of slab melts. The H_2O content of slab melts varies as a function of slab temperature.
- Elements likely to be dominated by fluid flux (such as Cs and Pb) are not considered.
- The slab component varies in composition only as a function of slab temperature. In general, the compositions of slab melts are constrained by experimental results of Hermann and Rubatto (2009) and Kessel et al. (2005).
- The total mass flux of slab melts increases with increasing slab temperature.

Figure 3.14 demonstrates that a successful STS model can be produced such that average arc data fall between a cold slab with small amounts of slab addition, and a hot slab with high amounts of slab addition. The Figure 3.14 also demonstrates that a wide variety of models are possible, as long as there are large variations in slab temperature. The selection of parameters is sufficiently unconstrained that these results do not provide a real test of this model. Instead, they demonstrate that such models cannot be ruled out. It is useful, however, to consider the common features of all successful STS model implementations, and what these imply for convergent margin processes.

One common feature of successful STS models is that the extent of melting of the mantle wedge remains roughly constant, from F=0.15 to F=0.20. This result is necessary in order to simultaneously produce the variations in element ratios and abundances. In order to produce the low end of global Dy/Yb, garnet cannot be present in the mantle wedge. Within the framework of the STS model, there is no mechanism available to systematically regulate the garnet contents of the residual mantle wedge, and so all melting occurs outside of the garnet stability field. Possible alternatives to this scenario are discussed in a later section. The AOC melting experiments of Kessel et al. (2005) and the sediment melting experiments of Hermann and Rubatto (2009) indicate that the bulk D for Dy between a hydrous

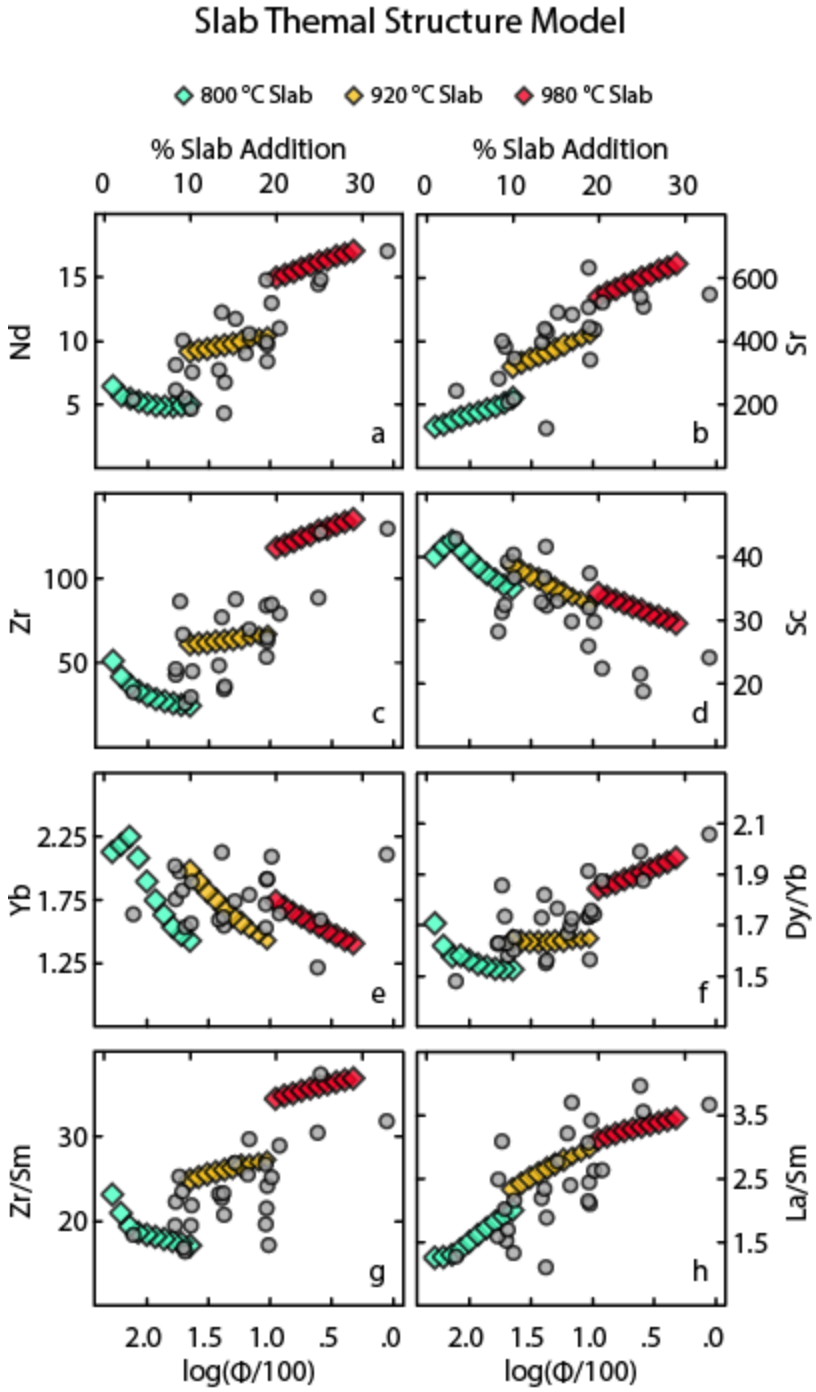

Figure 3.14: A comparison of the STS model with average arc data. Green, yellow, and red diamonds indicate model results using slab temperatures of 800, 920, and 980 °C, respectively. The STS model invokes both increasing slab contributions and increasing slab temperatures which correspond to a decreasing slab thermal parameter. In this parameterization, up to 30% slab addition from a 980 °C slab is required for the most enriched arc segments. The STS model is able to reproduce the average arc data fairly well, though there is great flexibility in the parameters chosen for this model.

melt and a subducting slab is at least 5, while the bulk D for Yb is >15-20. As a consequence, although the Dy/Yb ratios of slab melts are high, the HREE concentrations in slab melts are very low. Because slab melts have very low Yb, slab melt addition does not significantly affect mantle Yb concentration. In the absence of residual garnet, Yb is an incompatible element during mantle melting, so Yb concentrations in mantle melts vary as a function of F. As was shown in Figure 3.6m-n, Yb concentrations of averaged arc lavas are relatively constant. As a consequence, to reproduce the global Yb concentrations in the STS model, F can vary by no more than a factor of 1.3, and the variation is not systematic among arcs.

High extents of melting are also necessary from consideration of the Dy/Yb ratio. If variations in the Dy/Yb ratios between arc segments are generated by variable slab flux rather than by variable conditions within the mantle wedge, then the Dy/Yb ratio of the source must change as a consequence of slab addition. Because of the low HREE concentrations in the slab component, a very large slab flux is required to reach the upper range of Dy/Yb found globally. For arcs with high Dy/Yb such as the Cascades, Mexico, and Colombia/Ecuador, ~25% slab material must be added to the mantle source. Such a high slab flux then leads to sources with very high concentrations of many elements (including Dy), requiring high extents of melting to match arc values.

The requirement for high F at all arcs appears to be a robust requirement of STS models. The STS model produces this result because at cooler slab temperatures the slab mass flux is low, and the slab melt has high water content, while for hot slabs there is a larger mass flux with lower water content. Water contents in the wedge thus fall in a narrow range, and arc magmas all have roughly the same amount of water in their primary magmas. This model is therefore able to reproduce the results from melt inclusions where many arc volcanoes appear to have similar primary water contents (Plank et al., 2013). These are major contrasts with successful WTS models, where extents of melting vary from ~5% to ~20% and water contents would vary inversely with the extent of melting.

3.3.2.1 Further tests of Slab Thermal Structure model

The STS model adequately reproduces the global trends in arc magmas, but in its current form it does not adequately reproduce the observed range in Sc. In the WTS model, low Sc contents for thick-crust arcs result from garnet in the mantle wedge residue. In the STS model, the maximum variation in Sc is 30%, equal to the amount of dilution produced by adding 30% of a slab melt that is virtually Sc free. A potential solution to this problem would require large volumes of slab melt react significantly with the mantle wedge, producing elevated modal pyroxene and a high bulk D for Sc. A similar mechanism has been proposed by Straub et al. (2013) to account for both high whole rock SiO_2 contents and high olivine Ni contents in the Mexican arc, though that study found that the Dy/Yb ratio was unaffected by slab additions.

Another test of the feasibility of the slab temperature model comes from the observations of substantial variation in H beneath arcs. Slabs at greater depth are hotter, so one might expect a relationship between H and magma chemistry. This is not observed (Figure 3.5, column 3). One can better quantify this test by using slab surface temperature, which takes into account all the subduction parameters. No correlations are found between arc chemical compositions and the calculated slab surface temperatures (Figure 3.5, column 4) of Syracuse et al. (2010). The apparent contradiction of this result with the results from H_2O/Ce ratios (Cooper et al., 2012) are discussed further below.

The lack of correlations between predicted sub-arc slab surface temperatures and magma chemistry is perhaps less surprising than it may seem at first glance. Though slab surface temperatures must increase with depth, the value of $T-T_s$ on the slab surface may peak well before reaching the arc front. A simple parameterization of the slab solidus (taken from Cooper et al., 2012) compared to the slab surface profiles (Syracuse et al., 2010) of arcs with large values of H (Figure 3.15) illustrates this fact.

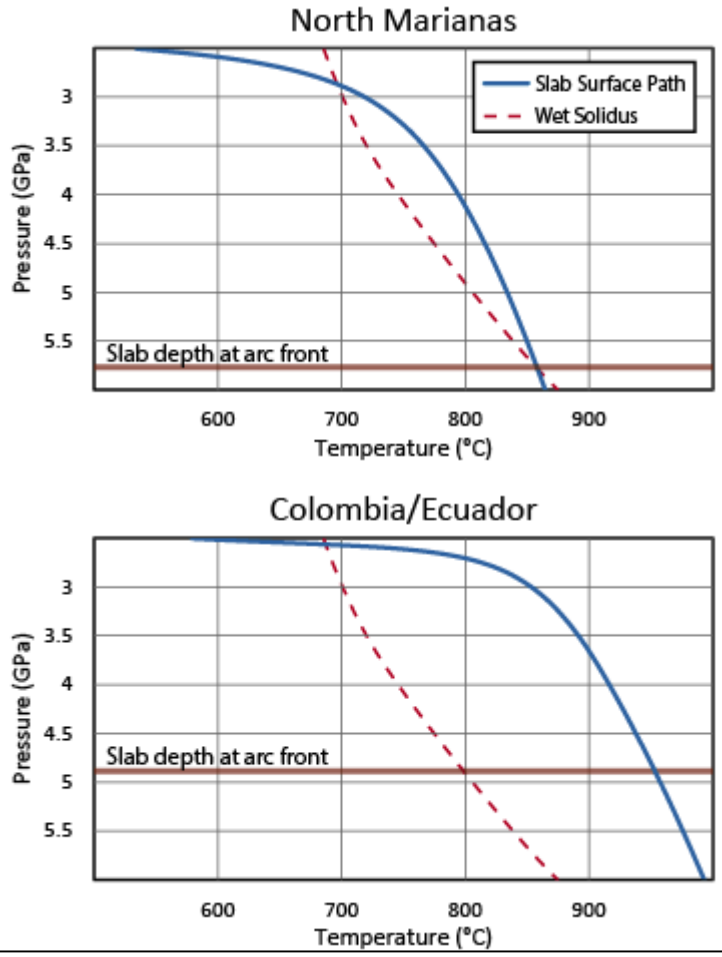

Figure 3.15: A comparison of the D80 slab surface temperature paths for the North Marianas and Colombia/Ecuador from Syracuse et al. (2010) to the wet slab solidus plotted in Cooper et al. (2012). Note that the maximum value of $T\text{-}T_s$ is reached at much shallower depths than are present below the arc front. If the maximum extent of slab melting is reached well before the arc front, this may account for the lack of relationship between the sub-arc slab surface temperatures of Syracuse et al. (2013) and chemical parameters. It would also imply that depth to slab may not be relevant to arc chemical systematics.

In the examples on Figure 3.15, the maximum extent of melting of slab materials of both Colombia/ Ecuador and the Northern Marianas may be reached well before the arc front. If true, then the temperature of the slab directly beneath the arc front may not be a relevant parameter at these arcs. The high extents of slab melting would occur at maximum $T\text{-}T_s$ within the slab rather than directly beneath the volcanic front. Further support for the possibility that temperatures directly beneath the arc are not the relevant parameter comes from the results of Wilson et al. (2014), who use dynamic

models to show that fluids released from the slab at P and T conditions well past the arc front may flow upslope on the slab back into the nose of the mantle wedge.

Despite these caveats**,** slab temperature may be an important factor in controlling arc chemical compositions. The experimental data and physical processes are sufficiently unconstrained that definitive tests other than plausibility are not yet possible. The fact remains, however, that the wedge thermal structure model not only accounts well for the data to first order, but also improves when additional subduction parameters are considered. The slab temperature models do not yet have this supporting evidence.

3.4 Additional constraints from isotopes, rear-arc lavas, and sediments

Eleven of the arc segments included in the dataset have additional constraints from both rear-arc volcanics and subducting sediment compositions. For these arcs, more rigorous testing of the models is possible, as well as determination of the proportions of Sr and Nd erupted at arcs that originate from sediment, AOC, or the ambient mantle.

Experimental work suggests Nd does not partition strongly into sediment melts (e.g., Hermann and Rubatto, 2009; Skora and Blundy, 2010), in contrast to elements that are highly mobile or highly abundant in sediments (e.g., Pb, Ba, Th). Nonetheless, observations such as the correlations between Th/Nd and $^{143}Nd/^{144}Nd$ in the Marianas (Eliott et al., 1997), or the global relationship between $Nd_{6.0}$ and $^{143}Nd/^{144}Nd$ for most arc segments (Figure 3.3a) support an important role for sedimentary Nd in arc volcanics. If true, the co-variation of $^{143}Nd/^{144}Nd$ and $^{87}Sr/^{86}Sr$ may also derive from sediments. An alternative possibility, however, is that Nd and Sr isotope variations reflect a strong imprint from the ambient mantle wedge. This possibility is supported by the correlation of $^{143}Nd/^{144}Nd$ between arc front and rear-arc magmas screened for minimal subduction signature (Figure 3.4b). In this case, a significant

proportion of Nd in erupted arc magma could be sourced from the ambient mantle wedge, and the correlation between $^{143}Nd/^{144}Nd$ and $^{87}Sr/^{86}Sr$ in arc front lavas may originate from the excellent correlation between these isotope systems in the rear-arc (Figure 3.4a). To assess these possibilities rigorously requires determination of the element and isotope budgets. These budgets then also have significance for the STS and WTS models. The aim is to determine for each of the WTS and STS models what additional constraints are required to satisfy the isotope data.

For each of the 11 arcs considered, forward modeling was undertaken using as an ambient mantle composition the Sr and Nd isotope ratios based on the Th/Nb filtered rear-arc samples. Most sediment compositions were taken from the compilation of Plank et al. (2013), though Guatemala and El Salvador were assigned the hemipelagic sediment compositions of Patino et al. (2000). AOC was assigned $^{87}Sr/^{86}Sr$ and $^{143}Nd/^{144}Nd$ values of .7035 and .5131 for all arcs, consistent with average Pacific MORB values for Nd and altered MORB values for Sr (Staudigel et al., 1995). For both models, the mantle trace element composition was set to the DMM of Workman and Hart (2005) for all runs, as an appropriate model relating ambient mantle isotopic variability to trace element compositional variability is still in development. Other model details are identical to those described in sections 3.3.1, 3.3.2, and in Appendix A3.1.

The WTS and STS end member models are based on separate sets of assumptions concerning the origin of global composition diversity among arcs, and make different predictions about the origin of the isotopic variation. In the WTS model, the global compositional diversity is produced as a function of the wedge thermal structure, while the proportions of slab components are relatively constant. Therefore for this model, slab component proportions were restricted to the narrow windows of 5 to 8% and 0 to 4%, slab temperature restricted to 825 to 875 °C, and each arc segment assigned a pressure and temperature of melting based on its crustal thickness. These constraints assure the isotope mass

balance is consistent with the WTS model. In this case, much of the isotope variation in $^{143}Nd/^{144}Nd$ must be inherited from the mantle wedge.

In the STS model, global compositional diversity is produced as a function of the slab thermal structure resulting from increasing slab surface temperatures and slab contributions to the mantle wedge, while the mantle thermal structure is held constant. Because any free H_2O present during slab melting will be incorporated into the melt, the total flux of H_2O to the mantle wedge is not a function of slab surface temperature. Higher extents of slab melting will dilute the H_2O content of slab melts relative to other elements, but the total mass of H_2O in the slab melt will be constant. Other mechanisms that may be able to relate slab thermal structure and H_2O flux to the mantle wedge are discussed in section 3.6. To ensure the isotope mass balance was consistent with the STS model, the extent of mantle wedge melting was fixed between 0.17 and 0.19 at a pressure of 1.8 GPa, while slab T and the proportions of AOC and sediment melt were allowed to vary from 750 to 950 °C, 0 to 40%, and 0 to 4%. For the STS model, much of the variation in isotopes must come from changes in the slab component.

To account for crystal fractionation, model results were compared to average 6-values reduced by a factor of 0.9, (the typical factor evident from plots of incompatible element 6-values vs Mg#>60 values from Chapter 2). Any combination of parameters that produced results within 15% of average Nd, Sr, 20% of Dy, and Yb bulk compositions, within 0.1 of average Dy/Yb values, within .00015 of average $^{143}Nd/^{144}Nd$ values and within .00025 of average $^{87}Sr/^{86}Sr$ values was considered successful. This range of acceptable isotope variation had to be made quite large, as closer matches for Central Chile and Guatemala could not be found in the STS implementation, as discussed below.

For the WTS model, successful solutions were found for each of the arcs considered. Because the proportions of added components were kept within a narrow range, the solutions have proportions

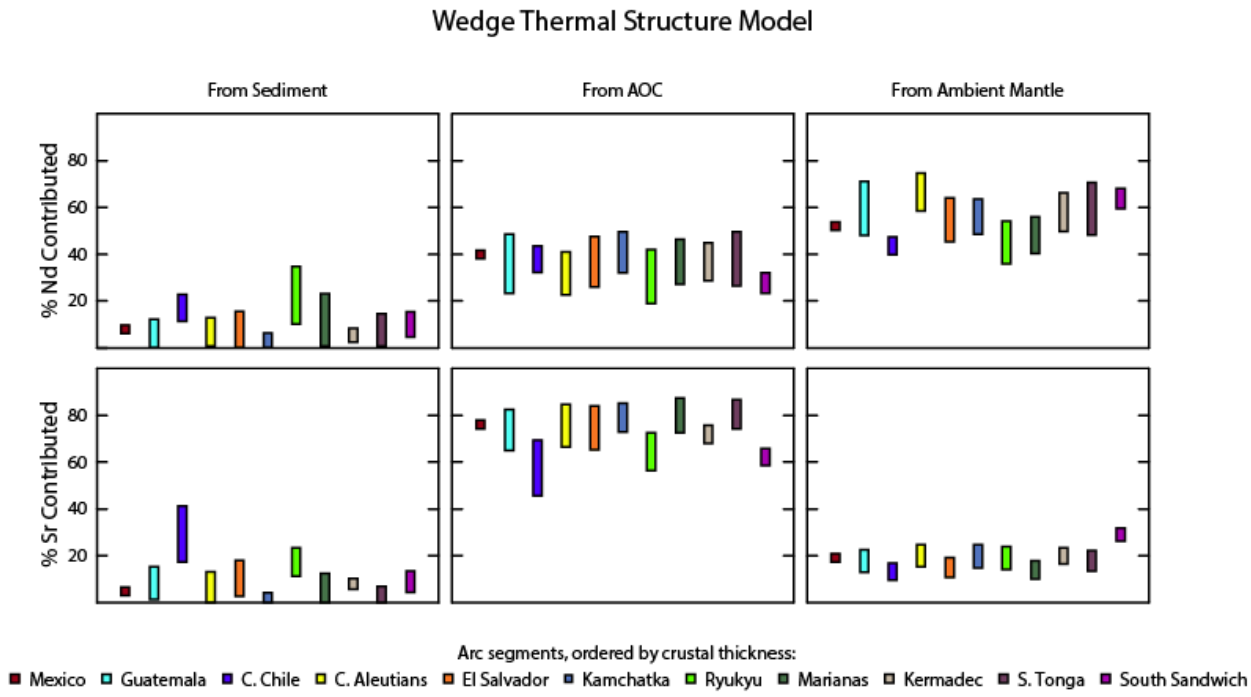

Figure 3.16: Presentation of the relative contributions of sediment, AOC, and the ambient mantle to the Nd and Sr contents of arc magmas from the WTS model using constraints from sediment and back arc compositions. In the WTS model, the contributions from each source are relatively constant among arc segments. Nd is sourced about 10%, 40%, and 50% respectively from the sediment, AOC, and ambient mantle, while Sr is sourced primarily from the AOC.

of Nd and Sr from the various source components that are relatively constant across all arcs, as expected (Figure 3.16). The majority of solutions result in 45 to 65% of Nd contributed from the ambient mantle, 30 to 40% from AOC, and 0 to 20% from sediment. For Sr, 10 to 20% is contributed from the ambient mantle, 60 to 80% of Sr from AOC, and 0 to 15% from the sediment. The Central Chile segment extends to higher sediment contributions and lower AOC contributions for Sr. One possible explanation for this discrepancy is that average Pacific MORB may not accurately represent the isotopic composition of AOC subducting in the Chilean Trench, as Sturm et al. (1999) have reported anomalously enriched ridge segments offshore of this volcanic margin. Incorporating more enriched AOC for Chile would produce results more similar to those observed at other arcs. In addition, the DMM composition used as the ambient mantle trace element composition for all arcs may not be appropriate for Chile, which has one of the most enriched rear-arc isotopic compositions.

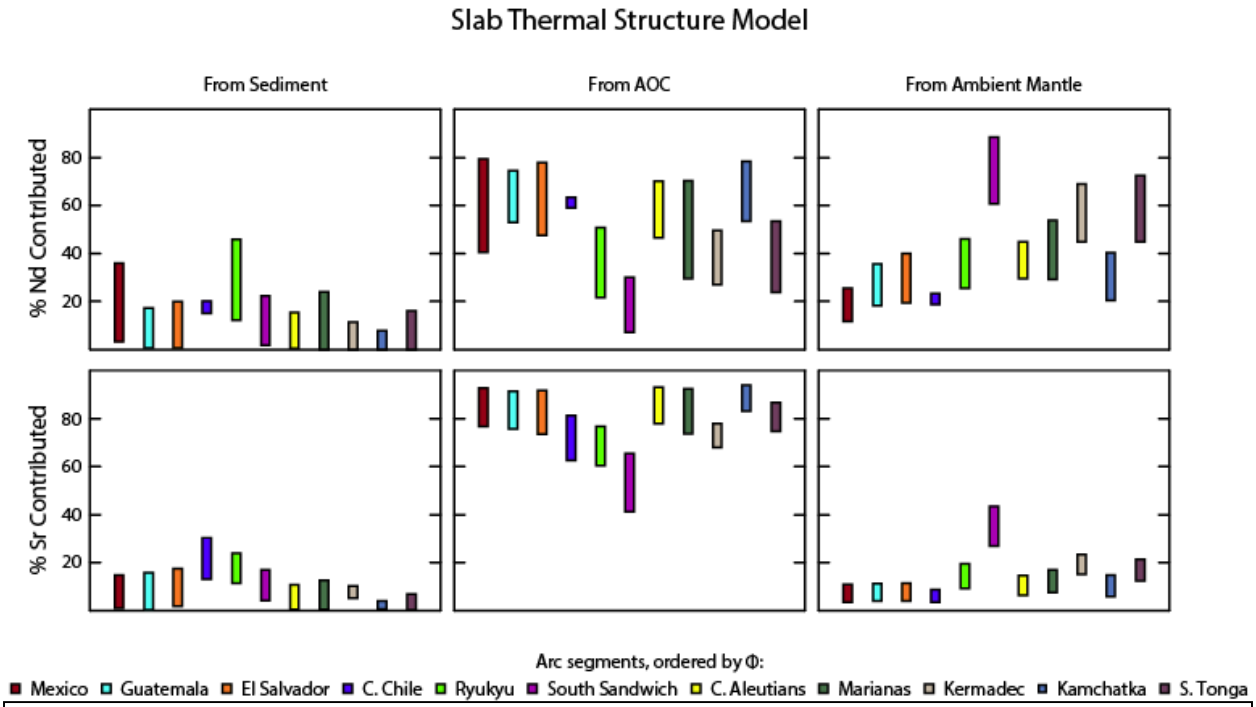

Figure 3.17: Demonstration of the relative contributions of sediment, AOC, and the ambient mantle to the Nd and Sr contents of arc magmas from the STS model using constraints from sediment and back arc compositions. In this model, the mantle contributions to Nd must vary systematically with the thermal parameter, with contributions as low as 20% at arcs with very low values of Φ. These very low mantle contributions to arc Nd contrast with what might be expected based on the strong correlation between arc front and back arc Nd isotope concentrations shown in Figure 3.4b. As in the WTS model, Sr contents are primarily delivered from the AOC.

The STS model also produces successful solutions for most arcs, with worse results for Central Chile and Guatemala. In contrast to the WTS model, however, the proportions of sediment, AOC, and ambient mantle contributions must vary considerably from one arc to another. Proportions of the slab components must increase as the average bulk Nd and Sr contents of the arcs increase, seen most readily in the increase in ambient mantle contribution with thermal parameter (Figure 3.17c). For successful solutions, the amount of Nd from the ambient mantle ranges from 15% for hot slabs and arcs with high Nd concentrations, to 80% for cold slabs at depleted arcs. The amount of Sr from the ambient mantle ranges from 5% to 30%. Hotter slabs cause the subduction component to increasingly dominate element budgets.

While both models can satisfy the isotope data within the rather loose limits listed above, the conclusions about the sources of elements and the goodness of fit are very different in the two models. For the WTS model, successful runs are found at each arc that have $^{143}Nd/^{144}Nd$ within 2σ of the arc average. For the STS model, this is not true for Guatemala or Central Chile where the closest matches for $^{143}Nd/^{144}Nd$ isotopes were higher than those found in the arc. A second caveat for the STS model is lack of a smooth change in proportions with thermal parameter apparent in Figure 3.17. As described in section 3.2.3, and shown in Figure 3.8a, crustal thickness and Φ correlate fairly well for the full dataset. Within the subset of arc segments used in this additional analysis the correlation between Φ and crustal thickness is also present, though it is notable that South Sandwich has low crustal thickness for its Φ value, and Kamchatka has high crustal thickness for its Φ value. South Sandwich and Kamchatka have the largest (and opposite) offsets in Figure 3.17c.

Finally, as a general comment, if the filtered rear-arc data are representative of the ambient mantle wedge compositions, the strong correlation between arc front and rear-arc Nd isotopes is more plausibly produced by the WTS model. Most successful runs of the WTS model allow for more than 50% of arc Nd to be contributed from the ambient wedge mantle, providing an explanation for why the arc front magmas resemble the ambient mantle wedge isotopic values. In the STS model, the fraction of arc Nd derived from the ambient mantle reaches very low proportions, and most of the Nd contributed to mantle melts for enriched arcs comes from either subducting sediment or AOC. In this scenario, a fortuitous balancing act between the enriched sediment and depleted AOC must take place in order to produce a metasomatized mantle that is compositionally similar (for $^{143}Nd/^{144}Nd$ values) to the original ambient mantle.

The proposal that $^{143}Nd/^{144}Nd$ values in arc front magmas reflect the composition of the ambient mantle source also provides simple explanations for the correlation between $^{143}Nd/^{144}Nd$ and Ba/Nb shown in Figure 3.3, and the anti-correlation between Ba/Nb and La/Sm apparent in the same figure. A

depleted wedge will have high $^{143}Nd/^{144}Nd$ and low Ba and Nb contents, so is easily dominated by the slab component. Ba/Nb is little affected by melting, so depleted wedges have the high Ba/Nb characteristic of the slab component. Depleted wedges also have low La/Sm, but these elements are less influenced by the slab. Variable wedge compositions and constant slab addition therefore account for the anti-correlation between Ba/Nb and La/Sm by a straightforward process.

3.6 Early dehydration models, and the potential for hybrid models

The models described above present plausible mechanisms that can account for the global correlations identified in our dataset, but they are not unique solutions, nor are they an exhaustive list of possibilities. The WTS model, for example, provides a mechanism capable of modulating the extent of melting in the mantle wedge. It is also possible to influence the extent of mantle melting by varying mantle water contents, rather than varying the pressure and temperature of the melting regime.

It may be possible to decouple the slab to mantle H_2O flux from the slab to mantle flux of other elements by delivering a significant portion of H_2O via a low T aqueous fluid, which is solute poor. As long as the pressure of melting remains within the garnet stability field, regulating the extent of mantle melting exclusively via water contents should lead to results very similar to the WTS model. Several factors could lead to variations in the rate of H_2O delivery to the mantle wedge, including variable initial H_2O contents in the slab, variable extents of slab dehydration prior to reaching depths relevant to the arc front, and variable extents of slab dehydration beneath the arc front itself.

A test of this model is to compare predicted water fluxes for different arcs with the chemical data. Fortunately, Van Keken et al. (2011) have provided models of variable slab dehydration that can be used to carry out such tests. As shown in Figure 3.18, there appears to be no relationship between the predicted H_2O flux from van Keken et al. (2011), and the chemical parameters in this study. This

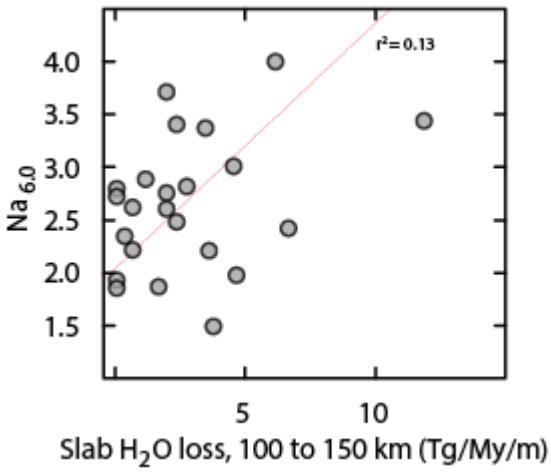

Figure 3.18: Variable extents of melting might be caused by variations in the water flux from the subducting slab. In this case, a correlation between the water flux and $Na_{6.0}$ would be expected. However, no relationship between the modeled slab H_2O losses from van Keken et al. (2011) and the chemical parameters is present, and so these results do not appear to support a model in which variable extents of mantle melting are produced by variable slab dehydration.

result is unsurprising, as the van Keken et al. study indicates that only Cascadia, British Colombia, and Mexico should lose significant H_2O prior to their prescribed depth of slab-mantle coupling, while the majority of other arcs undergo most dehydration immediately following this depth. This abrupt step-wise change in behavior contrasts with the relatively smooth systematics associated with increasing thermal parameter and the progressive changes observed in global arcs. Though variable slab dehydration and H_2O flux from the slab to the mantle wedge provide a potential mechanism to regulate the extent of mantle wedge melting, current modeling appears to be inconsistent with the hypothesis that such a process serves as a critical regulator of the global arc chemical systematics.

The results of Wilson et al. (2014) provide a possible explanation for why the particular depths of slab dehydration may not determine sub-arc mantle H_2O contents. Their models show that fluid released over a large range of slab depths may be transported towards the arc front. The majority of subducted water is transported within the ocean crust and serpentinized mantle (van Keken et al., 2010), so this downgoing flux may be fairly similar among arcs. Current estimates of the amount of H_2O subducted in these reservoirs are far higher than the upper limits on the amount of H_2O transported

into the deep mantle past the arc (Parai and Mukhopadhyay, 2012), and so much of the subducted water may be lost from the slab at fairly shallow depths. One possible scenario, then, is that large, semi-constant quantities of subducted water are released from the slab over a large range of depths, but eventually transported to the sub-arc mantle. If true, this scenario could lead to fairly constant water contents in the sub-arc mantle despite highly variable wedge thermal conditions.

A hybrid model between the WTS model and the STS model may also be possible, though such a model would require a serendipitous combination of co-varying factors in order to produce the strong linear correlations between subduction parameters and magma chemistry. It is possible, for example, that the Dy/Yb and Sc signals are the result of variations in modal garnet associated with crustal thickness, while other aspects of magma chemistry are a function of both F and slab flux. As we know, Φ and crustal thickness are themselves correlated within our dataset. If this correlation is merely a coincidence, both subduction parameters may be able to linearly reinforce many of the same trends in magma chemistry. Adopting a modeling approach which allows all of these free variables to change simultaneously is of course possible, though we will not attempt it here, as we do not believe this exercise would enhance our understanding of magma generation in subduction zones. Further, the pronounced and relatively simple systematics of the global arc system lead us to prefer a dominant status for one of the two models above.

3.7 Implications for primary H_2O and slab surface thermometers

The models described in this paper each make unique predictions about the mechanisms that regulate the concentration of H_2O in primary arc magmas. The WTS model produces enrichment of incompatible elements via changes in the extent of mantle melting, which are driven by variable P and T conditions in the mantle wedge. This model predicts primary magma H_2O contents that closely co-vary

with other incompatible element concentrations. In other words, in the WTS model H_2O behaves just like other incompatible elements, with melt concentrations that are set by the thermal structure of the mantle wedge. The WTS model is able to reproduce trace element variability using a constant 0.6% H_2O in the mantle source, and thus predicts primary H_2O concentrations that vary from ~3% at thin-crust arcs to ~12% at thick-crust arcs. It is also possible to obtain similar results with slightly higher or lower primary water contents by slightly shifting the P and T range of melting, but the factor of ~4 variation in H_2O contents is still a consistent model prediction.

The STS model, on the other hand, requires a relatively constant F in order to reproduce the relatively constant Yb concentrations. In order to maintain a relatively constant F, the STS model maintains similar P and T conditions beneath all arcs as well as similar H_2O contents in the mantle wedge. To produce relatively constant H_2O contents in the wedge, an increasing slab flux is coupled with decreasing H_2O contents in the slab component. This outcome is plausible, as both higher slab flux and lower H_2O concentrations in slab melts may result from increasing slab T (Hermann and Rubatto, 2009). The STS model, therefore, predicts relatively constant H_2O concentrations in primary melts while concentrations of other slab-mobile elements increase from arcs with a cold slab, to arcs with a hot slab.

A slab dehydration model, unlike the WTS model or STS model, invokes significant variability in the total flux of H_2O to the mantle wedge. According to this model, a hot slab will lose a larger portion of its H_2O prior to reaching depths relevant to arc front volcanism, and thus the mantle wedge above a cold slab may be wetter than a mantle wedge above a hot slab. As discussed in the previous section, such a dehydration model can only be consistent with the bulk elemental systematics we observe (i.e., greater incompatible enrichment at hot arcs with low Φ) if the cold arc H_2O flux is transferred as a dilute aqueous fluid. This larger H_2O flux would produce a greater extent of melting and thus a depleted incompatible element signature at cold, high Φ arcs. Because arcs with a high F are then associated with a high H_2O flux, the primary H_2O contents of magmas generated by this model are relatively constant.

The slab dehydration model is thus similar to the proposal of Plank et al. (2013): the extent of mantle melting increases roughly proportionally to the increase in source H_2O, resulting in fairly constant primary H_2O concentrations. Plank et al. (2013) propose such a model due to the finding that the average maximum H_2O contents in melt inclusions are similar among all studied arcs.

If primary H_2O contents of arc magmas are in fact fairly constant (relative to other elements with similar bulk D values), the WTS model can be ruled out entirely. As noted by Plank at al. (2013), however, the relatively invariant H_2O contents of arc lava melt inclusions could be due instead to re-equilibration of melt inclusions with a surrounding H_2O saturated magma over a relatively narrow range of crustal depths. This possibility is additionally supported by laboratory dehydration experiments on melt inclusions (Gaetani et al., 2012). In this scenario, magmas from thin-crust arcs will have primary water contents of around 3-4 wt. %. These magmas stall in magma chambers at shallow depths of ~6 km, not far from H_2O saturation, and thus melt inclusions formed in thin-crust arcs may reflect their primary H_2O concentrations. At arcs with ~50 km crust, on the other hand, the WTS model predicts primary H_2O contents of around 12%. These magmas most likely stall and differentiate at depths similar to those from thin-crust arcs (Blatter et al., 2013; Chapter 2), and so are highly oversaturated in H_2O and must de-gas extensively, eventually reaching H_2O concentrations similar to primary magmas from thin-crust arcs. Melt inclusions formed in the plumbing systems of thick-crust arcs will thus re-equilibrate with the de-gassed magma, which contain 3-4 wt. % H_2O, and thus will not reflect primary H_2O concentrations. If the melt inclusion H_2O contents are a result of H_2O re-equilibration following melt inclusion formation, then they will not be directly related to primary magma H_2O compositions, and thus do not provide direct constraints on global petrogenetic models.

Cooper et al. (2012) suggest that slab surface temperatures predicted by the H_2O/Ce contents of melt inclusions correlate well with the model slab surface temperatures of Syracuse et al. (2010). If the H_2O/Ce values of these melt inclusions do represent primary magmas, this result appears to provide

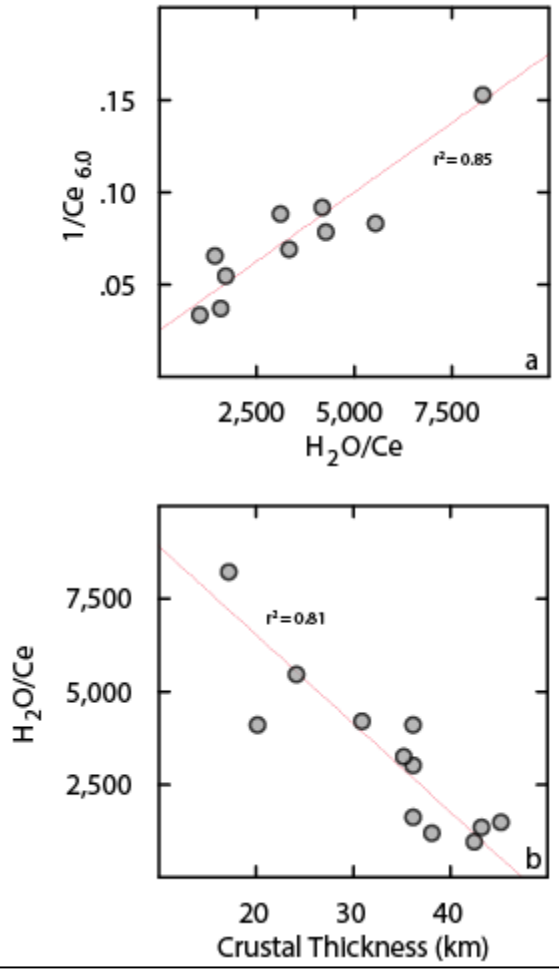

Figure 3.19: Panel a: The inverse of $Ce_{6.0}$ concentrations correlate with the H_2O/Ce melt inclusion values from Cooper et al. (2012), showing that H_2O/Ce depends primarily on variations in Ce contents. This suggests that variations in Ce are the controlling parameter, and that the melt inclusion and $Ce_{6.0}$ values as presented here are in close agreement. Panel b: While H_2O/Ce ratios of primitive magmas may be generated by the slab, this parameter also correlates well with crustal thickness. The WTS model, however, would not predict this relationship, because both H_2O and Ce should vary with extent of melting of the mantle wedge. For the WTS model to be correct, the constant H_2O contents of melt inclusions must reflect a relatively constant pressure of melt inclusion re-equilibration, rather than constant primary water contents.

evidence supporting the STS model or perhaps a dehydration model, and conflicts with the expected results of the WTS model. In contrast, our dataset shows no strong correlations between magma chemistry and the slab surface temperatures of Syracuse et al. (2010). This discrepancy does not appear to be due to the quality of the datasets used in either study. As shown in Figure 3.19a, the H_2O/Ce melt inclusion data closely correspond to our average $Ce_{6.0}$ data. Because there is little variation in average melt inclusion H_2O contents of global arcs (Plank et al., 2013), it is evident that the large variations in the

melt inclusion H_2O/Ce values are primarily driven by variations in Ce. Thus, the strong correlations between $Ce_{6.0}$ values and H_2O/Ce in melt inclusions support the proposition that both datasets accurately represent variation of Ce contents in primary arc magmas.

Melt inclusion H_2O/Ce ratios not only correlate well with our $Ce_{6.0}$ values, they also independently correlate with crustal thickness, as shown in Figure 3.19b. If most arc front magmas do in fact undergo crystallization across a narrow range of pressures, and melt inclusions are in fact prone to re-equilibrating with surrounding H_2O saturated magmas at these pressures, then the variable Ce contents of melt inclusions can thus be considered evidence in support of, rather than in conflict with, the WTS model.

Plank et al. (2013) prefer a model in which melt inclusion H_2O contents reflect primary magma H_2O contents, in part because of correlations between H_2O/Ce and Nb/Ce in the Aleutians. Nb/Ce contents of primitive melt inclusions almost certainly represent Nb/Ce in primary magmas, and so this argument is compelling. This line of reasoning is not at odds with the WTS model, however, which only requires that melt inclusion H_2O is re-equilibrated with de-gassed magma chambers at thick-crust, continental arcs. Future experimental work on melt inclusions as well as measurements of multiple chemical indices on melt inclusions from additional subduction settings will likely provide further insight on the relative roles of these subduction parameters in regulating H_2O and other volatile fluxes through subduction zones.

3.8 Conclusions

A newly compiled global data set can be used to evaluate relations between subduction parameters and global arc geochemistry. There are remarkably clean relationships among chemical parameters across the entire range of element behavior, and between chemical parameters and the

crustal thickness of the overlying arc. Somewhat weaker but still impressive correlations exist between the chemical parameters and the slab thermal parameter, which should reflect variations in slab temperature at constant depth. There is also remarkable coherence between Sr and Nd isotopic compositions of volcanic front magmas and the compositions of rear-arc magmas that have the least subduction influence. Any successful model of arc volcanism and processes must account for the global systematics presented here.

We have presented two quantitative end member models that both produce the global arc variability. The Wedge Thermal Structure model calls on a constant slab flux to a mantle wedge that varies in composition and thermal structure. This model is remarkably successful at producing the global observations. It is further supported by the fact that results are improved by including additional parameters that control the wedge thermal structure. This model provides a simple explanation why Sr, Nb, Zr, K, P and La all correlate well in global arcs—their relative abundances are controlled largely by extent of melting. Flux from the slab is similar across global arcs.

The Slab Thermal Structure model instead invokes a relatively constant extent of melting of the wedge, with a source that varies in composition as a function of slab additions. Flux from the slab varies substantially from one arc to another. While successful implementations of this model can be constructed, this chemical model is poorly constrained by experimental data and thermal models. In order to successfully reproduce depletions of Sc and V, this model requires that significant melt rock reaction takes place in the mantle wedge. A drawback of the model is that results are not improved by incorporating additional subduction parameters that ought to be relevant.

Variations in wedge thermal structure, and hence $T\text{-}T_s$, at convergent margins are inevitable. Given this fact, a model in which chemical systematics of volcanic arcs are primarily regulated by changing extents of melting is intuitively appealing. Simple thermal models and co-variations among

elements and subduction parameters are also quantitatively consistent with the variations in extents of melting required to produce the observations. As such, models that include an important role for variations in extent of melting associated largely with lithospheric thickness and convergence rate are strongly supported. An alternative mechanism to produce variable extents of melting would be a globally varying water flux. Quantitative estimates of variations in water flux, however, do not correlate with the extents of melting inferred from arc geochemistry.

It is also true that variations in slab temperature are inevitable, and are quantitatively supported by the maximum depths of earthquakes at subduction zones. It is not necessarily the case, however, that the total chemical flux from the slab will be strongly dependent on slab temperature. Slabs clearly release chemical components to the mantle wedge to be incorporated in arc magmas, but the particular depth at which this happens may be of secondary importance. Slab melting, for example, may initiate well before the volcanic arc front. The top of the slab may also develop into a diapric mélange and ascend into the core of the mantle wedge, rather than remain stratified and at the base of the wedge (e.g., Marschall and Schumacher, 2012). In these cases, flux from the slab to the wedge may be relatively constant across a wide range of thermal parameters. Even in these scenarios, however, the effects of slab temperature may be apparent for the hottest slabs, where slab melting may occur at shallow depths, or where dehydration and chemical transport of particularly mobile elements occur at shallower depths than the convecting mantle wedge.

Two critical parameters that would distinguish between these models are the volumes of magma produced at arcs with a variety of crustal thickness and Φ values, and firm constraints on the primary water contents of arc magmas from a variety of subduction settings. The WTS model predicts a factor of four variation in water contents, and higher magmatic output at crusts built on thin crust, provided variations in mantle composition are accounted for. The STS model predicts constant water contents and magma volumes. If the WTS model is correct, primary water contents would vary

significantly. In this case, the observation that the average arc melt inclusions globally have similar H_2O contents must be accounted for by the tendency for melt inclusions to re-equilibrate with surrounding magmas (Gaetani et al., 2012) within a limited range of depths.

It is important to note finally that the work presented here is not inconsistent with observations of the importance of variations in sediment composition for certain elements in global arcs as demonstrated by Plank and Langmur (1993). As shown by that study, the sediment signal emerges only after the effects of varying extents of melting are taken into account, consistent with the WTS model. For the STS model, an evaluation of variations in sediment would need to first take into account the different proportions of subduction components added to the wedge, owing to slab temperature.

3.9 References

Baker, M., Hirschmann, M., Ghiorso, M., Stolper, E., 1995. Compositions of near-solidus peridotite melts from experiments and thermodynamic calculations. Nature 375, 308-311.

Cameron, B., Walker, J., Carr, M., Patino, L., Matıas, O., Feigenson, M., 2003. Flux versus decompression melting at stratovolcanoes in southeastern Guatemala. Journal of Volcanology and Geothermal Research 119, 21-50.

Chin, E.J., Lee, C.-T.A., Barnes, J.D., 2014. Thickening, refertilization, and the deep lithosphere filter in continental arcs: Constraints from major and trace elements and oxygen isotopes. Earth and Planetary Science Letters 397, 184-200.

Cooper, L.B., Ruscitto, D.M., Plank, T., Wallace, P.J., Syracuse, E.M., Manning, C.E., 2012. Global variations in H2O/Ce: 1. Slab surface temperatures beneath volcanic arcs. Geochemistry, Geophysics, Geosystems 13.

DePaolo, D.J., 1981. Trace element and isotopic effects of combined wallrock assimilation and fractional crystallization. Earth and planetary science letters 53, 189-202.

Dickinson, W.R., Hatherton, T., 1967. Andesitic volcanism and seismicity around the Pacific. Science 157, 801-803.

Elliott, T., Plank, T., Zindler, A., White, W., Bourdon, B., 1997. Element transport from slab to volcanic front at the Mariana arc. Journal of Geophysical Research: Solid Earth (1978–2012) 102, 14991-15019.

England, P., Engdahl, R., Thatcher, W., 2004. Systematic variation in the depths of slabs beneath arc volcanoes. Geophysical Journal International 156, 377-408.

England, P.C., Katz, R.F., 2010. Melting above the anhydrous solidus controls the location of volcanic arcs. Nature 467, 700-703.

Gaetani, G.A., O'Leary, J.A., Shimizu, N., Bucholz, C.E., Newville, M., 2012. Rapid reequilibration of H2O and oxygen fugacity in olivine-hosted melt inclusions. Geology 40, 915-918.

Gale, A., Dalton, C.A., Langmuir, C.H., Su, Y., Schilling, J.G., 2013. The mean composition of ocean ridge basalts. Geochemistry, Geophysics, Geosystems 14, 489-518.

Gazel, E., Hoernle, K., Carr, M.J., Herzberg, C., Saginor, I., Van den Bogaard, P., Hauff, F., Feigenson, M., Swisher, C., 2011. Plume–subduction interaction in southern Central America: Mantle upwelling and slab melting. Lithos 121, 117-134.

Grove, T.L., Chatterjee, N., Parman, S.W., Médard, E., 2006. The influence of H2O on mantle wedge melting. Earth and Planetary Science Letters 249, 74-89.

Hermann, J., Rubatto, D., 2009. Accessory phase control on the trace element signature of sediment melts in subduction zones. Chemical Geology 265, 512-526.

Jaques, A., Green, D., 1980. Anhydrous melting of peridotite at 0–15 kb pressure and the genesis of tholeiitic basalts. Contributions to Mineralogy and Petrology 73, 287-310.

Jarrard, R.D., 1986. Relations among subduction parameters. Reviews of Geophysics 24, 217-284.

Karlstrom, L., Lee, C.T., Manga, M., 2014. The role of magmatically driven lithospheric thickening on arc front migration. Geochemistry, Geophysics, Geosystems.

Katz, R.F., Spiegelman, M., Langmuir, C.H., 2003. A new parameterization of hydrous mantle melting. Geochemistry, Geophysics, Geosystems 4.

Kay, R.W., 1980. Volcanic arc magmas: implications of a melting-mixing model for element recycling in the crust-upper mantle system. The Journal of Geology, 497-522.

Kelley, K.A., Plank, T., Farr, L., Ludden, J., Staudigel, H., 2005. Subduction cycling of U, Th, and Pb. Earth and Planetary Science Letters 234, 369-383.

Kessel, R., Schmidt, M.W., Ulmer, P., Pettke, T., 2005. Trace element signature of subduction-zone fluids, melts and supercritical liquids at 120–180 km depth. Nature 437, 724-727.

Kirby, S.H., DuRHAM, W.B., Stern, L.A., 1991. Mantle phase changes and deep-earthquake faulting in subducting lithosphere. Science 252, 216-225.

Langmuir, C., Bézos, A., Escrig, S., Parman, S., 2006. Chemical systematics and hydrous melting of the mantle in back-arc basins. Back-Arc Spreading Systems: Geological, Biological, Chemical, and Physical Interactions, 87-146.

Lee, C.-T.A., Luffi, P., Plank, T., Dalton, H., Leeman, W.P., 2009. Constraints on the depths and temperatures of basaltic magma generation on Earth and other terrestrial planets using new thermobarometers for mafic magmas. Earth and Planetary Science Letters 279, 20-33.

Miller, D.M., Goldstein, S.L., Langmuir, C.H., 1994. Cerium/lead and lead isotope ratios in arc magmas and the enrichment of lead in the continents. Nature 368, 514-520.

Morris, J., Tera, F., 1989. 10Be and 9Be in mineral separates and whole rocks from volcanic arcs: Implications for sediment subduction. Geochimica et Cosmochimica Acta 53, 3197-3206.

Patino, L.C., Carr, M.J., Feigenson, M.D., 2000. Local and regional variations in Central American arc lavas controlled by variations in subducted sediment input. Contributions to Mineralogy and Petrology 138, 265-283.

Plank, T., 2013. The chemical composition of subducting sediments. The Crust, Treatise on Geochemistry 4.

Plank, T., Cooper, L.B., Manning, C.E., 2009. Emerging geothermometers for estimating slab surface temperatures. Nature Geoscience 2, 611-615.

Plank, T., Kelley, K.A., Zimmer, M.M., Hauri, E.H., Wallace, P.J., 2013. Why do mafic arc magmas contain~ 4wt% water on average? Earth and Planetary Science Letters 364, 168-179.

Plank, T., Langmuir, C.H., 1988. An evaluation of the global variations in the major element chemistry of arc basalts. Earth and Planetary Science Letters 90, 349-370.

Plank, T., Langmuir, C.H., 1993. Tracing trace elements from sediment input to volcanic output at subduction zones. Nature 362, 739-743.

Plank, T., Langmuir, C.H., 1998. The chemical composition of subducting sediment and its consequences for the crust and mantle. Chemical geology 145, 325-394.

Schmidt, M.W., Poli, S., 1998. Experimentally based water budgets for dehydrating slabs and consequences for arc magma generation. Earth and Planetary Science Letters 163, 361-379.

Skora, S., Blundy, J., 2010. High-pressure hydrous phase relations of radiolarian clay and implications for the involvement of subducted sediment in arc magmatism. Journal of Petrology 51, 2211-2243.

Spandler, C., Mavrogenes, J., Hermann, J., 2007. Experimental constraints on element mobility from subducted sediments using high-P synthetic fluid/melt inclusions. Chemical Geology 239, 228-249.

Staudigel, H., Davies, G., Hart, S.R., Marchant, K., Smith, B.M., 1995. Large scale isotopic Sr, Nd and O isotopic anatomy of altered oceanic crust: DSDP/ODP sites417/418. Earth and Planetary Science Letters 130, 169-185.

Straub, S.M., Zellmer, G.F., Gómez-Tuena, A., Espinasa-Pereña, R., Martin-del Pozzo, A.L., Stuart, F.M., Langmuir, C.H., 2013. A genetic link between silicic slab components and calc-alkaline arc volcanism in central Mexico. Geological Society, London, Special Publications 385, SP385. 314.

Sturm, M.E., Klein, E.M., Graham, D.W., Karsten, J., 1999. Age constraints on crustal recycling to the mantle beneath the southern Chile Ridge: He-Pb-Sr-Nd isotope systematics. Journal of Geophysical Research: Solid Earth (1978–2012) 104, 5097-5114.

Syracuse, E.M., van Keken, P.E., Abers, G.A., 2010. The global range of subduction zone thermal models. Physics of the Earth and Planetary Interiors 183, 73-90.

van Keken, P.E., Hacker, B.R., Syracuse, E.M., Abers, G.A., 2011. Subduction factory: 4. Depth-dependent flux of H2O from subducting slabs worldwide. Journal of Geophysical Research: Solid Earth (1978–2012) 116.

Wilson, C.R., Spiegelman, M., van Keken, P.E., Hacker, B.R., 2014. Fluid flow in subduction zones: The role of solid rheology and compaction pressure. Earth and Planetary Science Letters 401, 261-274.

Workman, R.K., Hart, S.R., 2005. Major and trace element composition of the depleted MORB mantle (DMM). Earth and Planetary Science Letters 231, 53-72.

Chapter 4: Global and regional implications of the chemical systematics along Chile's Southern Volcanic Zone

Abstract

The Chilean Southern Volcanic Zone (SVZ) provides an excellent natural laboratory in which to gain understanding of the mechanisms that generate chemical diversity among arc volcanics on a global scale. This is due to the relative ease of working in the region, because the volcanoes of the SVZ erupt such a remarkable range of compositions, and because multiple physical subduction parameters (slab dip, slab depth, crustal thickness) vary significantly along strike of the arc. This study incorporates a large dataset of both new analyses and literature data, first filtering the sample set for the effects of crustal processing via the Eu anomaly, Rb excesses, and Mg contents. The remaining sample set displays coherent systematics among major elements, trace elements, and isotope ratios. These systematics mimic those seen among the global arc dataset of Chapter 2, with correlations among major and trace elements that overlap the global range, varying across the upper half of global arc averages in Na and other incompatible element contents. We confirm the systematic along strike variations within the SVZ, which include south to north enrichment of incompatible elements and REE ratios, but north to south depletion of Sc and Ca. Nd and Sr isotopes, as well as the trace element ratios Zr/Nb and Th/U follow a different along strike pattern, with an inflection at the middle latitudes of the study area.

The possibility of generating the along strike variability within the filtered dataset by increasing levels of baseline crustal contamination is ruled out on the basis of the nearly identical chemical systematics with the SVZ and global dataset, as the necessarily pervasive common contaminant has an extremely unlikely composition, as shown by Chapter 2. Trace element ratios sensitive to variable slab contributions do not vary along strike, indicating that a similar contribution from the slab to the wedge

is present at all latitudes. Furthermore, the possibility of generating along strike compositional trends is inconsistent with thermal models of subducting slabs within this study region. Enrichments of trace elements in the northern portion of the arc are consistent with a model of lower extents of melting in the northern latitudes, which is the result of thicker lithosphere and decreased slab dip, similar to the Wedge Thermal Structure model of Chapter 3. The systematics of Sr, Nd, and Hf isotopes among rear arc samples are consistent with a heterogeneous mantle, produced by mixing end members similar to the Ambient Atlantic Mantle and the EM1-type Gough Island OIB suite. On the basis of relative variations of Nd isotopes and the Th/Nb ratio, the rear arc Nd isotope variation cannot be produced by slab input, and must the result of mantle heterogeneity. The rear arc variation of Nd isotope follows the same systematic variation along strike as the arc front samples, indicating an important role for mantle heterogeneity in both domains, which likely drives variation of Zr/Nb and Th/U, as well. Quantitative modeling demonstrates the feasibility of applying the Wantle Thermal Structure model, along with a model of mantle heterogeneity based on the Gough Island Basalts, to generate these along strike trends. Because the compositional systematics of the SVZ are a microcosm of the global chemical systematics, these results also bear on the likely mechanisms for generating compositional diversity among arc segments worldwide.

4.1 Introduction

The Chilean Southern Volcanic Zone (SVZ) spans approximately 1500 km, comprising dozens of active volcanic centers from 33° S to 46° S. The volcanic front from Maipo Volcano (34° S) to Osorno Volcano (42° S), and the corresponding rear arc volcanism in Argentina, are particularly well suited for comprehensive regional studies of continental volcanic arcs, given that the majority of the volcanic centers are accessible, well exposed, and erupt relatively mafic (>5 wt. % MgO) material. As a result, several large regional sample sets from the SVZ have been compiled and analyzed, confirming coherent regional trends in magma chemistry both along and across the arc front. Some ambiguity remains, however, in the interpretation of these regional variations in magma chemistry. This is partially due to the fact that multiple physical subduction parameters, which are associated both with the subducting slab (slab age, dip angle, and depth beneath the arc front) and the overriding plate (crustal thickness) are variable along the arc front (Figure 4.1).

Many of the subduction parameters along the SVZ vary across much of the range observed globally, and so the outstanding questions about the relationships between physical subduction parameters and arc magma compositions within the SVZ are much like outstanding question that remain for the global dataset (Plank and Langmuir, 1988; Chapter 2 and Chapter 3). Specifically, Chapter 2 found that global arc average compositions correlate with both crustal thickness and the slab "thermal parameter," and because of this, the global compositional variability can be accounted for by two very different physical models. In one model, the magma variability results primarily from variation in the thermal structure of the mantle wedge, which is regulated by lithospheric thickness. In the other model, magma variability results primarily from variation the thermal structure of the subducting slab, which is regulated by the slab age, dip angle, and convergence rate. Both slab parameters and crustal thickness vary also within the SVZ, and so the SVZ serves as a natural laboratory in which to investigate the relationships between physical and chemical

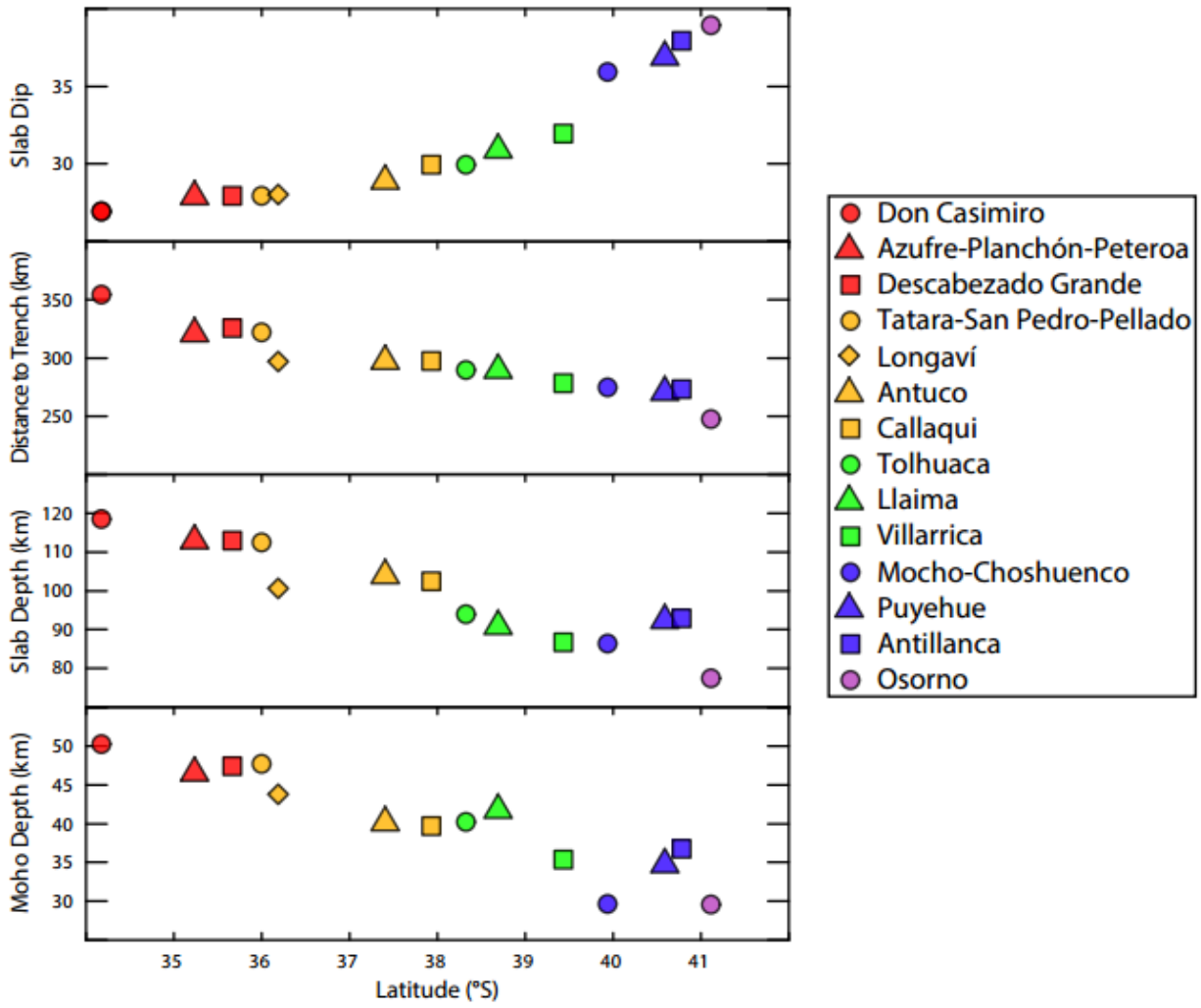

Figure 4.1: Variation of subduction parameters long the SVZ: From north to south within the SVZ, the slab dip angle increases, while the distance from the trench to the volcanic front, the depth of the slab beneath the arc front, and the depth of the Moho all decrease.

observations about volcanic arcs. A detailed comparison of the systematic chemical variability within the global arc dataset to the variability found within the SVZ yields a confirming analysis of these global relationships. On this basis we rule out certain models and, further, elucidate additional details of the mechanisms that drive the chemical variability of arc volcanoes.

4.2 Prior work on regional chemical variation in the SVZ

Lopez-Escobar et al. (1977) conducted the first regional study of the SVZ, identifying differences in magma chemistry between northern and southern volcanoes. They proposed that the enrichment of light rare earth elements (LREE) relative to heavy rare earth elements (HREE) in the northern most volcanic centers (33° S to 34° S) were consistent with 3% partial melting of a garnet bearing peridotite source. Further to the south (37° S to 41° S), they found that lava compositions were more consistent with 10 to 15% partial melting of a garnet free peridotite. They associated this variation in chemistry with the variation in the dip angle of the subducting slab, which at the time was thought to vary from 10° to 25° across their region of study.

Hildreth and Moorbath (1988) bolstered this regional dataset with additional samples and data, including the first regional picture of $^{87}Sr/^{86}Sr$ and $^{143}Nd/^{144}Nd$ isotopic variation along the arc. They confirmed the northern enrichment of incompatible element abundances and LREE/HREE ratios and additionally showed a northern increase in $^{87}Sr/^{86}Sr$ and decrease in $^{143}Nd/^{144}Nd$. They showed that the LREE/HREE ratios and isotopic compositions increase not only from the south to the north, but also within individual volcanic suites. They further identified large variations of Rb and Ba concentrations relative to other highly incompatible elements both within and among volcanoes. Hildreth and Moorbath proposed that the trends of incompatible element fractionation within volcanic suites were indicative of assimilation of crustal material during magma differentiation, as they cannot be accounted for by any closed system process. Because the baseline values for many of these within suite trends are higher in the north, where the overriding continental crust is thickest, they proposed that the correlation of magma chemistry with latitude is the result of extensive processing of northern magmas in zones of mixing, assimilation, storage, and homogenization within the lower crust (MASH). In this scenario, the primary magma composition is relatively constant along the arc front, while the extent of baseline crustal assimilation increases to up to tens of percent.

Subsequent studies of individual volcanic centers in the northern part of the SVZ (e.g., Tormey et al., 1991; Dungan et al., 2001) conflict with the MASH hypothesis, however. These studies acknowledged a role for lower crustal assimilation, but noted that the observation of compositional diversity among basaltic lavas within individual volcanic centers is inconsistent with the existence of a zone of homogenization. Tormey et al. (1991) characterized the composition of the lower crustal contaminant for the Azufre-Planchon-Peteroa (APP) complex (~35° S) and demonstrated that such a contaminant cannot relate the composition of the most primitive magmas at this location to those magmas found farther to the south. They additionally highlighted that regional correlations of Na and Ca concentrations with crustal thickness correspond to the global array of Plank and Langmuir (1988), which Plank and Langmuir suggested was a result of variations in the extent of melting of primary magmas, rather than intra-crustal processing. They suggested, finally, that variability of certain trace element ratios may indicate that contributions from the slab to the mantle wedge are not constant, and may influence the extent of mantle melting as well as the composition of the sub arc mantle wedge.

Jacques et al. (2013, 2014) have recently presented a new regional dataset for the SVZ, along with fresh perspectives on the processes responsible for regional chemical variations. Jacques et al. additionally provide an analogous sample set from the rear arc region in Argentina, which they used to constrain the relative contributions from the slab and mantle to the erupted magmas. Their sample set includes mostly basalts and basaltic andesites, in order to mitigate the effects of crustal processing. They found that arc front $^{87}Sr/^{86}Sr$, $^{143}Nd/^{144}Nd$, and $^{176}Hf/^{177}Hf$ compositions largely occupy the same range as compositions in the rear arc. They further demonstrated that the rear arc and arc front compositional variability of $^{87}Sr/^{86}Sr$, $^{143}Nd/^{144}Nd$, and $^{176}Hf/^{177}Hf$ is partially due to heterogeneity in the mantle wedge, which they suggest may reflect contributions from the subcontinental lithosphere. Lastly, they found that certain trace element ratios such as Ba/Nb, U/Th, and Pb/Ce, indicate a larger flux of slab fluid to southern mantle source. Following this logic, they model the along strike variations in trace element

abundances and ratios by varying the extent of mantle melting from ~1% to ~6%, which is primarily the result of variable contributions of H_2O from the slab. They note that in their model, the slab contribution required to match trace element compositions differs from that required to match isotopic compositions by up to a factor of 3.

Each of these regional studies has provided valuable insight into the systematics of the SVZ, but do not provide a generalizable physical framework for their chemical interpretations. Our goal in this study is to provide a holistic model of the along strike chemical variability of the SVZ that is motivated by the physical subduction setting, and that is consistent both for the arc itself and with variations that are observed globally (Chapters 2 and 3).

4.3 Methods

This paper provides extensive new data for a set of samples from SVZ stratovolcanoes. In addition to newly collected samples, a number of sample previous collected by Rosemary Hickey-Vargas and colleagues have been re-analyzed. This study also draws from a large literature database of arc front and rear arc lavas from the SVZ, as well as the global arc database of Chapter 2. This comprehensive approach results in a substantial sample set for each volcano, enabling individual interpretation of crustal processes affecting the volcanic centers, and assessment of the range of processes which have likely affected their compositions during their ascent through the continental crust.

For new analyses, whole rock powders were crushed to a grain size of ~1 mm and then powdered using either an agate mill of a shatterbox with an alumina ceramic crucible until a flour-like texture was produced. Major elements were measured by X-ray fluorescence (XRF) at the University of Lausanne following Pfeifer et al. (1991). For both new samples, as well as samples provided by Rosemay Hickey-Vargas, trace elements were analyzed at Harvard University by solution nebulized inductively

coupled plasma mass spectrometry. Detailed analytical methods and uncertainties of ICP-MS measurements can be found in Chapter 1. Sr, Nd, and Pb isotopic analyses were done at Woods Hole Oceanographic Institution following chemical separations at Harvard University, using the methods described in Gale et al. (2013). All new major element, trace element, and Sr, Nd, and Pb data can be found in Supplementary Dataset A4.1.

4.4 Filtering the data

The goal of this paper is to assess the mechanisms that generate primary magma diversity, and so the dataset must be filtered to minimize the effects of chemical modification during magma ascent through the crust. Previous studies have demonstrated that the magma diversity within individual volcanic centers of the SVZ is largely produced by the combined effects of crystal fractionation, magma mixing, excess crystal accumulation, and crustal assimilation (e.g., Tagiri et al., 1993; Tormey et al., 1995; Reubi et al., 2011; Dungan et al., 2001; Jicha et al., 2007; etc). Within the dataset presented in this study, there is also abundant evidence for crustal overprinting of magma compositions. Three separate chemical indices have thus been applied in order to identify samples that are most likely to represent primary magmas.

Most crustal processes will decrease the Mg content of a magma, and there is evidence that this crustal overprinting is most significant among lavas that have lower Mg abundances. This can be observed on plots of MgO content vs other elemental abundances, on which the range found among most elemental abundances typically increases with decreasing wt. % MgO, creating a characteristic "wedge shaped" array (see Appendix A4.1 for figures). For most volcanoes, this wedge shape comes to a point at >5 wt. % MgO, which indicates that lavas with >5 wt.% MgO are less affected by crustal overprinting. Therefore, only samples with 5 wt. %>MgO contents are included.

In the SVZ, some magmas with >5 wt. % MgO are produced by mixing between higher MgO magmas and evolved, low MgO magmas (e.g., Gerlach et al., 1988). Evolved magmas are typically highly enriched in incompatible elements due to magma differentiation, and so mixed magmas do not represent primitive compositions. We make use of the fact that evolved magmas have typically undergone extensive plagioclase fractionation, which imparts them with large negative Eu anomalies (Weill and Drake, 1973). When mixed magmas are generated, they will therefore inherit a negative Eu anomaly. In other cases, arc magma can accumulate excess plagioclase that has crystallized from previous magma batches. This plagioclase will dilute the magma's incompatible element abundances, and leave it with positive Eu anomalies (as shown by Tagiri et al., 1993, for Osorno volcano). Because both of these processes have been identified within the SVZ, we apply a strict filter, only including samples with Eu anomalies between 0.9 and 1.

Magma modification by crustal assimilation has been identified along the entire SVZ (Reubi et al., 2011; Dungan et al., 2001; Jicha et al., 2007). As shown by Dungan et al. (2001) and Jicha et al. (2007), crustal assimilation typically results in preferential enrichment of certain elements -- most notably Rb -- that are particularly abundant in crustal lithologies. We thus examined each volcano for open system behavior of Rb relative to either K or Y, in order to filter out samples with excessive Rb enrichments. Because the ratio of Rb to K and Y can also vary among primary magmas, this filtration can only be applied relative to other samples from the same volcano. The details of data filtration for Rb excess and other indices, as well as the specific data filters applied at each location, are available in Appendix A4.1.

Magmas that have not been affected by these open system processes evolve via crystal fractionation. Early stage crystal fractionation does not produce fractionation among incompatible elements, but does lead to variable elemental abundances. Therefore, this study will only consider variability of elemental abundances among magmas that have within 5.5<wt.% MgO<6.5, which

corresponds to a narrow range of extents of crystal fractionation. This study will also make use of volcano "6-values," following the methodology of Chapter 3, which are calculated as the average concentration of a given element for all samples within 5.5<wt.% MgO<6.5 at each volcano. The filtered dataset used in this study is provided in Supplementary Dataset A4.2.

4.5.1 Results: Variations among 6-values, trace element ratios, and crustal thickness

Once the data have been filtered to minimize the imprint of compositional variability arising from crustal assimilation, magma mixing, fractional crystallization, and excess crystal accumulation, relationships among whole rock compositions can be used to constrain earlier stages of petrogenesis. As seen in Figure 4.2, correlations exist among $Na_{6.0}$ and $Ca_{6.0}$, $K_{6.0}$, $P_{6.0}$, and $Mn_{6.0}$, producing trends that mimic those from the equivalent range of concentrations seen in the global arc averages from Chapter 2. Within the SVZ, $Na_{6.0}$ values occupy the upper half of global arc average $Na_{6.0}$, varying from 2.7 to 3.6 within the SVZ, while the global arc averages vary from 1.5 to 4. $Si_{6.0}$, $Fe_{6.0}$, and $Al_{6.0}$ also vary within the range of compositions seen in the global data, though correlations are less clear (not shown). There is limited variability among $Si_{6.0}$, $Fe_{6.0}$, and $Al_{6.0}$ within the SVZ: $Si_{6.0}$ varies from 51 to 53.5, $Fe_{6.0}$ from 7.5 to 8.9, and $Al_{6.0}$ from 17.5 to 18.6. There is also lower overall variability among these elements globally. $Ti_{6.0}$ is slightly higher among those SVZ volcanoes with the highest $Na_{6.0}$, though $Ti_{6.0}$ is also constricted to a limited range from 0.86 to 1.01 (Figure 4.1).

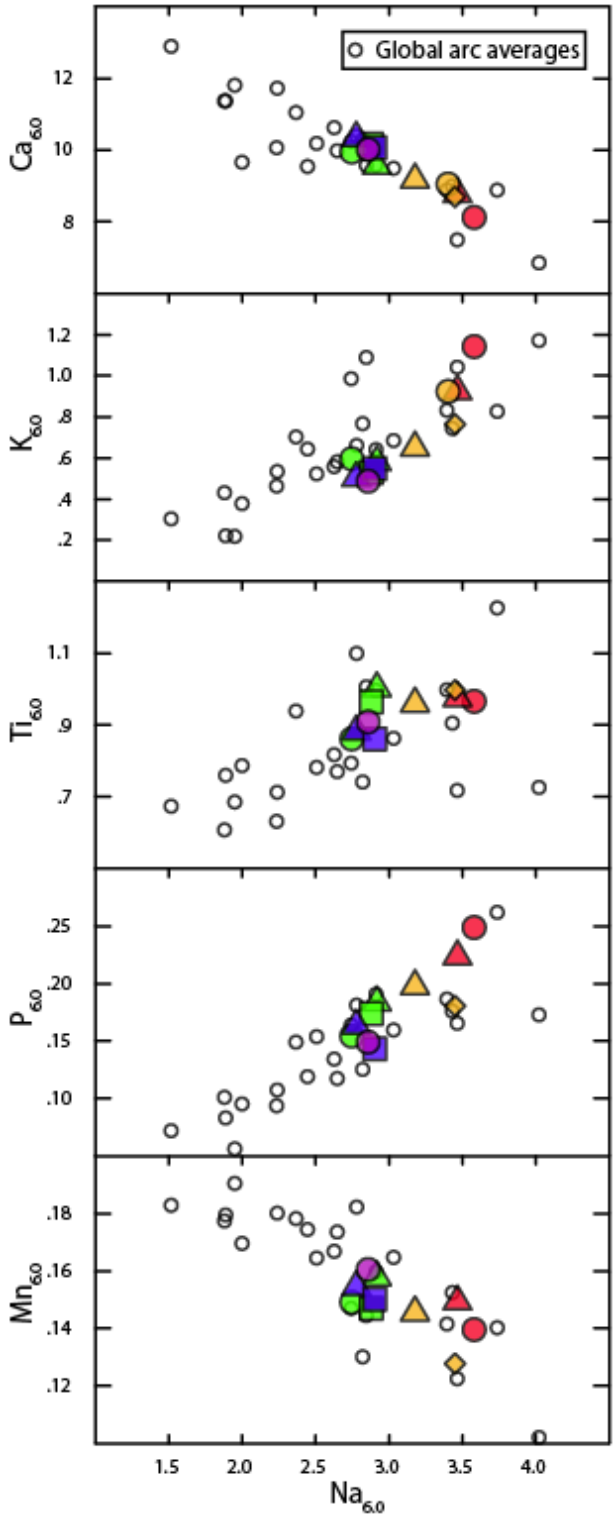

Figure 4.2: Within the SVZ, correlations are present among the 6-values of major elements, including between $Na_{6.0}$ and $Ca_{6.0}$, $K_{6.0}$, $P_{6.0}$ and $Mn_{6.0}$. $Ti_{6.0}$ in the SVZ is confined to a narrow range of values. The relationships between major element 6-values in the SVZ follow the same patterns as the global arc averages from Chapter 2, covering the upper half of the global range.

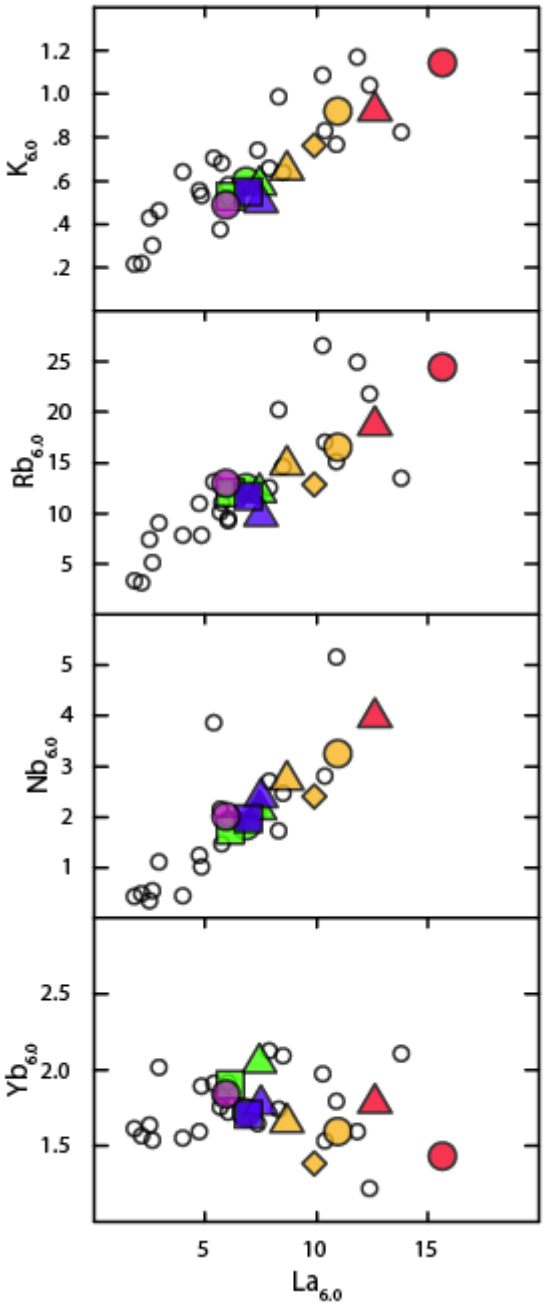

Figure 4.3: Within the SVZ, correlations are present among the 6-values of most incompatible trace elements, and there are also correlations between the trace elements and major elements, such as $La_{6.0}$ and $K_{6.0}$. Correlations among trace elements are not confined to traditional groupings of elements from arc settings, such as "high field strength" and "large ion lithophile," as shown here by the correlations between $La_{6.0}$ and both $Nb_{6.0}$ and $Rb_{6.0}$. $Yb_{6.0}$, in contrast, varies within a narrow range. As with the major elements in Figure 4.1, trace elements within the SVZ follow the same patterns as the global arc averages, covering the upper half of the global range.

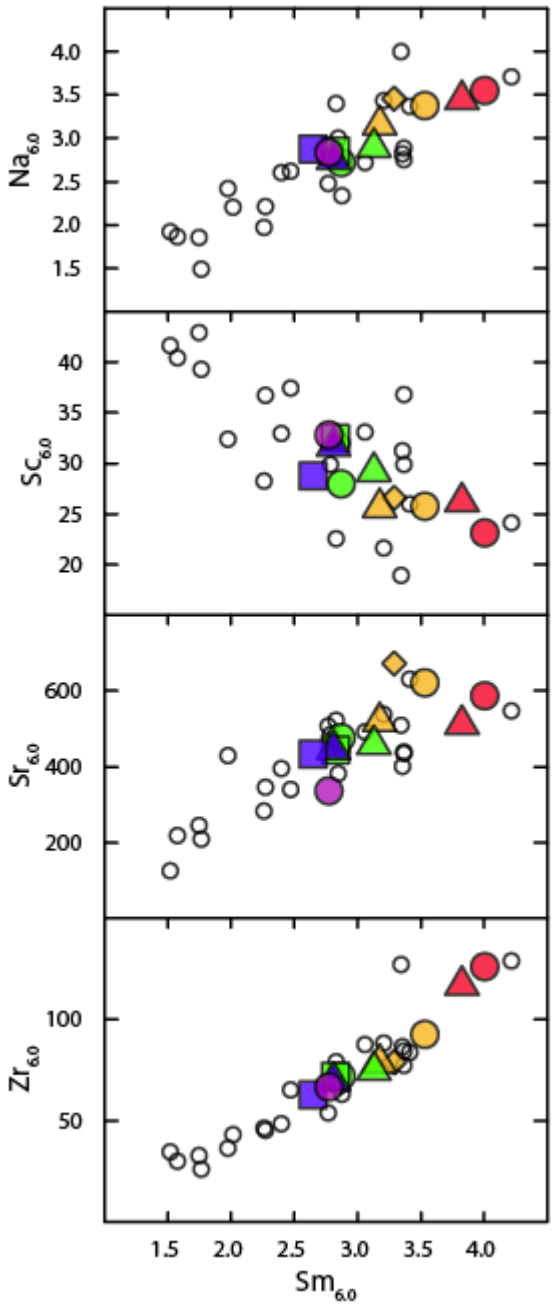

Figure 4.4: Within the SVZ, positive correlations are present among the 6-values of most incompatible trace elements, and there are also correlations between the trace elements and major elements, such as $Sm_{6.0}$ and $Na_{6.0}$. Correlations among trace elements are not confined to traditional groupings of elements from arc settings, such as "high field strength" and "large ion lithophile," as shown here by the correlations between $Sm_{6.0}$ and both $Sr_{6.0}$ and $Zr_{6.0}$. $Sc_{6.0}$, which is moderately compatible, correlates negatively. As with the major elements in Figure 4.1, trace elements within the SVZ follow the same patterns as the global arc averages, covering the upper half of the global range.

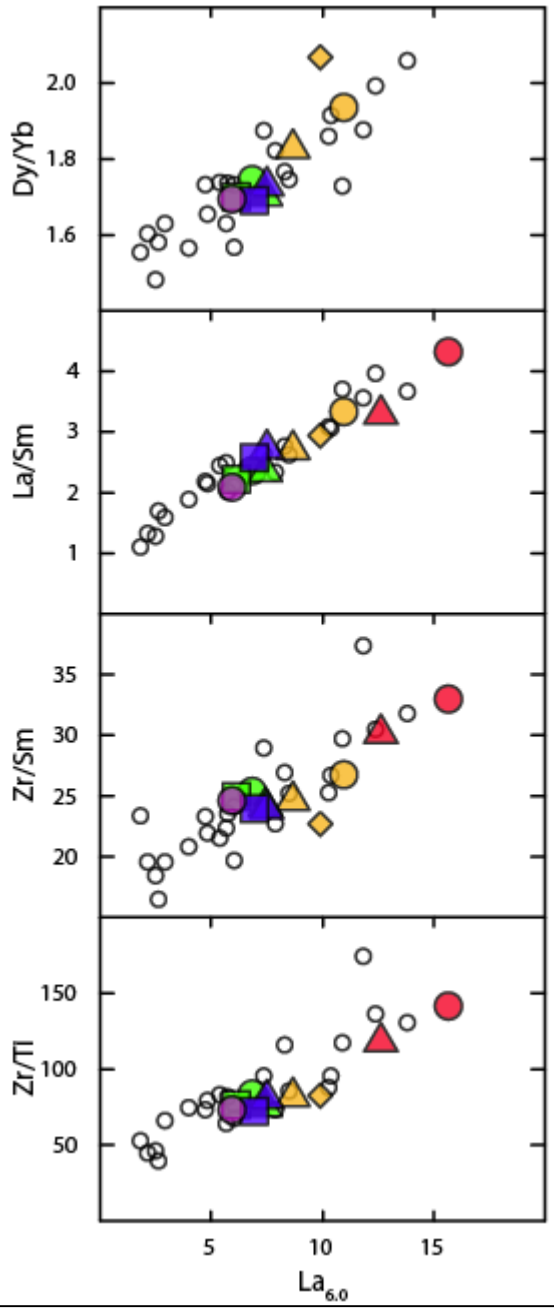

Figure 4.5: Within the SVZ, incompatible element 6-values also correlate with several trace element ratios, such Dy/Yb, La/Sm, Zr/Sm, and Zr/Ti. As with Figures 4.2 to 4.4, the relationships between these chemical indices within the SVZ are the same as those found globally, indicating a similar mechanism for their origin.

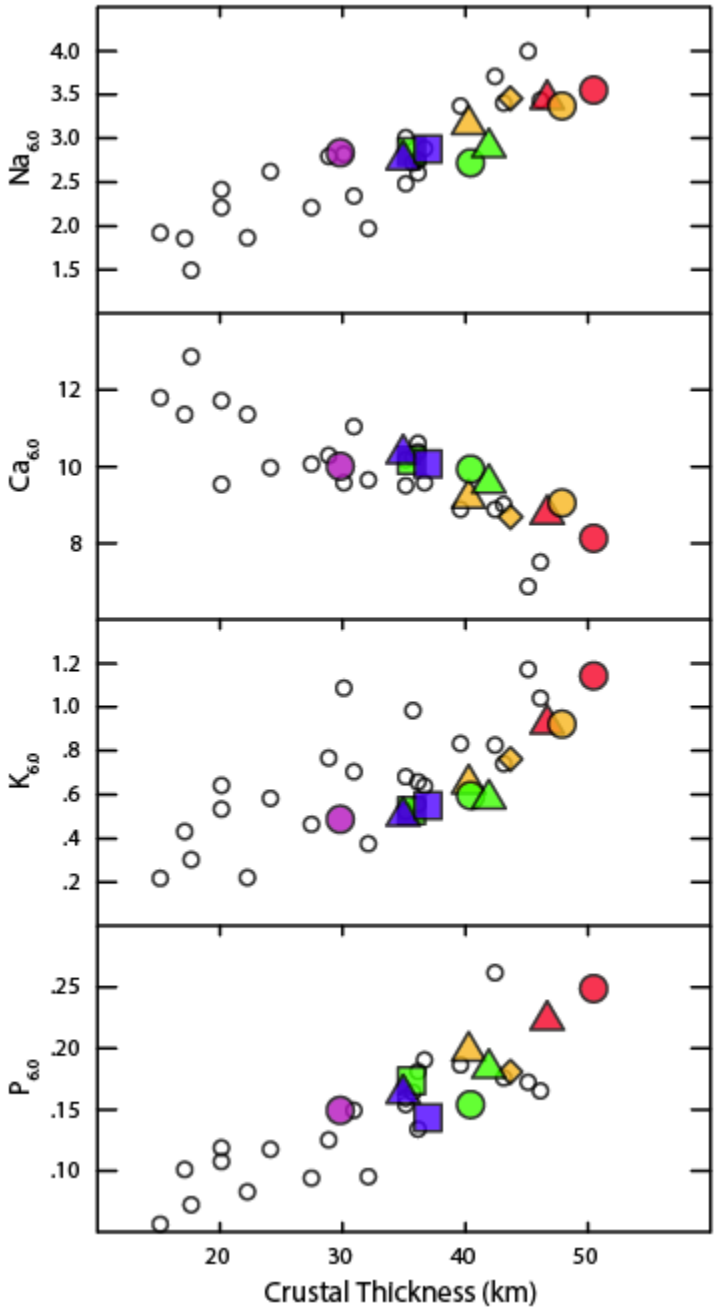

Figure 4.6: Within the SVZ, 6-values for several major elements correlate with crustal thickness. The relationship between crustal thickness and lava composition within the SVZ is suggestive of a physical process related to crustal thickness that produces compositional variability of magmas both within the SVZ, and the same is true globally.

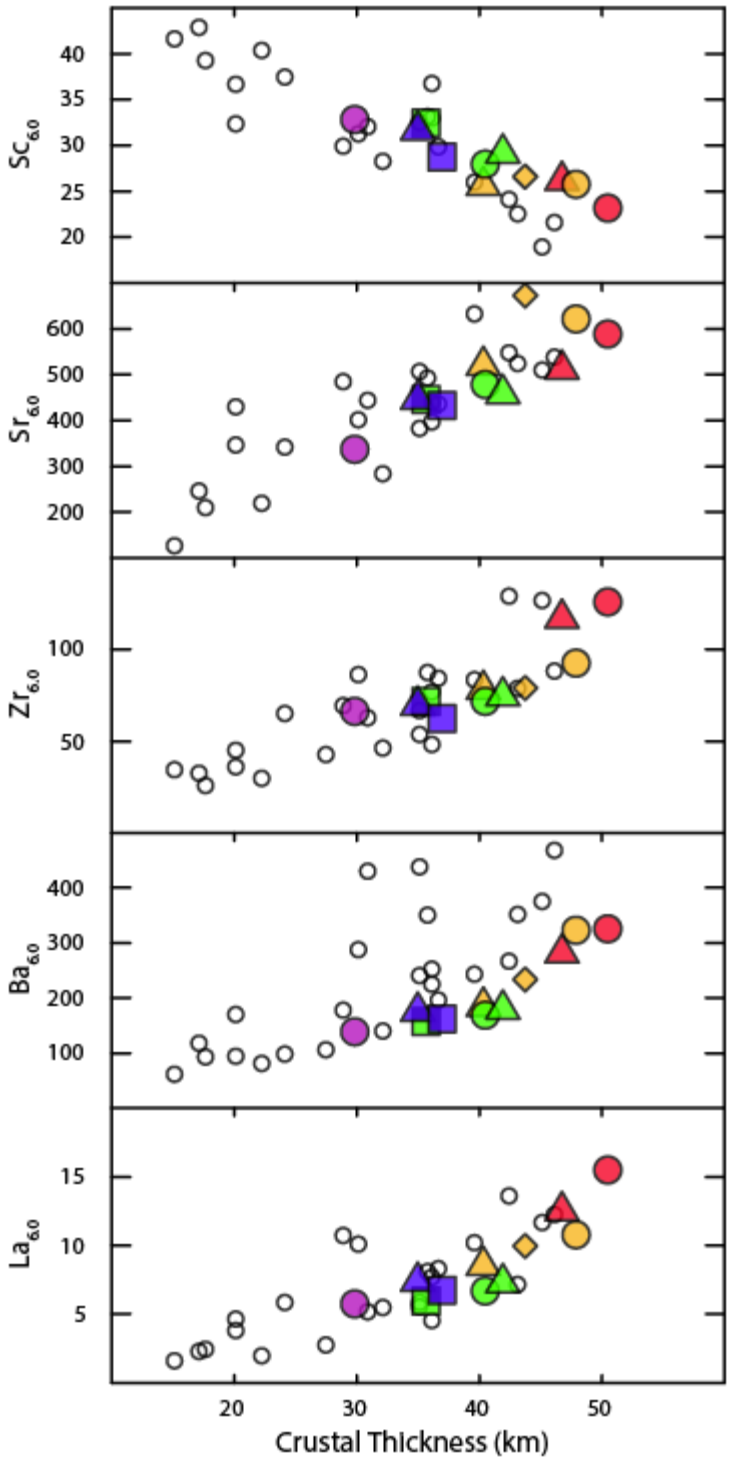

Figure 4.7: Within the SVZ, 6-values for most incompatible elements correlate positively with crustal thickness, while $Sc_{6.0}$ correlates negatively. The relationship between crustal thickness and lava composition within the SVZ is the same as that for global arc segments, suggestive of a single physical process related to crustal thickness that produces compositional variability of magmas on both scales.

Most incompatible trace element 6-values correlate both with major elements and with each other, overlapping entirely with the global trends (Figures 4.3 and 4.4). As with the global averages, these correlations appear to transcend customary groupings of elements in volcanic arc samples, such as "large ion lithophile" and "high field strength" elements. $La_{6.0}$ correlates strongly with $K_{6.0}$, $Rb_{6.0}$, and $Nb_{6.0}$, with values varying by a factor of ~3, and corresponding to the upper half of the global range. The northernmost samples from Don Casimiro extend slightly beyond the global range. In contrast, HREE compositions fall within a more limited range and do not correlate. $Sm_{6.0}$ correlates positively with $Na_{6.0}$ and $Zr_{6.0}$, but negatively with $Sc_{6.0}$. Many of the incompatible trace elements do not co-vary along a 1:1 slope, and so their ratios correlate with elemental abundances (Figure 4.5). $La_{6.0}$, for example, correlates with Dy/Yb, La/Sm, Zr/Sm, and Zr/Ti.

Globally, there are correlations not only among the average elemental abundances and trace element ratios of volcanic arcs, but also between arc chemistry and the thickness of overlying crust (Plank and Langmuir, 1988; Chapter 2. This relationship also holds true for the average volcano compositions within the SVZ, as shown on Figures 4.6 and 4.7. In both the SVZ and globally, higher crustal thickness correlates positively with $Na_{6.0,}$ $K_{6.0}$, $P_{6.0}$, and incompatible element 6-values, and negatively with $Ca_{6.0}$ and $Sc_{6.0}$. The relationship between crustal thickness and magma chemistry within the SVZ is almost exactly the same as that observed globally, with SVZ volcano compositions overlapping the compositions of arc segments with between 30 and 50 km thick crust.

These observations demonstrate that the SVZ is a remarkable microcosm of the global systematics of arc volcanism. The co-variations among elements mimic the variations observed globally, covering half of the global range. These variations also correlate with crustal thickness, just as observed with the global arc averages. Understanding the mechanisms behind these variations in the SVZ thus serves not only to illuminate the inner workings of a single arc, but also is a means to investigate the causes of global variability. The well constrained regional setting links the local variations in magma

chemistry to the local physical conditions of the subduction zone, providing perspectives on the global variations and the hypotheses to account for them (Chapter 3).

4.5.2 Results: Variations among isotope ratios

Several studies have discussed variations among SVZ rear arc and arc front isotopic ratios, which are generally agreed to indicate a heterogeneous mantle source containing a depleted component with characteristics of South Atlantic Mid-Ocean Ridge Basalts (MORB) and an enriched component with characteristics of EM1 type Ocean Island Basalts (OIB) (e.g., Dyhr et al., 2013; Kay et al., 2007; Kay et al., 2013; Jacques et al., 2013; Jacques et al., 2014; Varekamp et al., 2010). A summary of these relationships will thus be presented in the context of the Ambient Upper Mantle (AUM) composition derived by Douglass et al. (1999) and Andres et al. (2002) for the South Atlantic and the Gough Island Basalts (GIB), which are EM1 type OIBs.

As shown on Figure 4.8, the rear arc basalts form a tight linear array between AUM and GIB on a plot of $^{143}Nd/^{144}Nd$ vs $^{87}Sr/^{86}Sr$. As shown by Chapter 3 and in Figure 4.8, global rear arc samples -- filtered to minimize the effects of slab input -- also have strongly correlated $^{143}Nd/^{144}Nd$ vs $^{87}Sr/^{86}Sr$. The relationship within the SVZ is consistent with the global systematics, as both rear arc arrays stretch between depleted MORB and EM1-OIBs. The rear arc array from the SVZ aligns with the global array, but also extends it to lower $^{143}Nd/^{144}Nd$ overall, and the two arrays taken together span the entire range of compositions from AUM to GIB.

The arc front data from volcanoes between Don Casimiro and Antuco overlap the rear arc array almost entirely on Figure 4.8, while samples from Callaqui to Osorno fall to slightly higher $^{87}Sr/^{86}Sr$ at a given $^{143}Nd/^{144}Nd$, and many of these volcanoes have higher $^{143}Nd/^{144}Nd$ overall. For the global data, the arc front lavas are also offset to higher $^{87}Sr/^{86}Sr$ at a given $^{143}Nd/^{144}Nd$, though for clarity global arc front

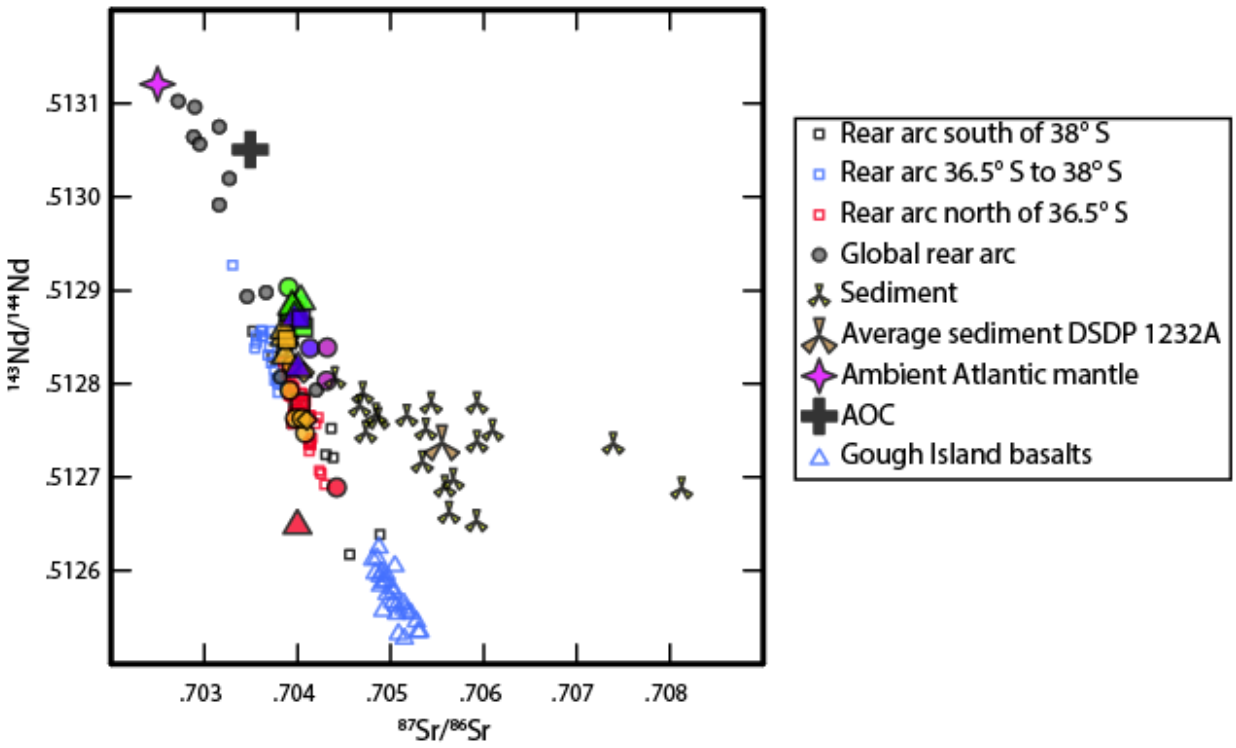

Figure 4.8: A plot of $^{143}Nd/^{144}Nd$ vs $^{87}Sr/^{86}Sr$ for SVZ from the rear arc and arc front, as well as samples of sediment taken offshore near the Chilean trench. The rear arc samples align well with the Ambient Upper Mantle composition for the Atlantic determined by Douglass et al. (1999) and the Gough Island basalts, which are EM1-type OIBs found in the South Atlantic. The arc front samples are offset from the rear arc samples towards the sediment and AOC compositions. Global rear arc averages from Chapter 3 are also on the figure, and also align well with the Ambient Atlantic Mantle and the Gough Island basalts, suggestive of a similar enrichment process for both the SVZ, and worldwide.

averages are not plotted on Figure 4.8. The solitary arc front sample on the lower $^{87}Sr/^{86}Sr$ side of the array is an older measurement of the APP volcanic center from Tormey et al. (1995), and actually overlaps with the array within its reported analytical error. Sediments and Altered Ocean Crust (AOC) from the downgoing plate also lie to higher $^{87}Sr/^{86}Sr$ at a given $^{143}Nd/^{144}Nd$. Figure 4.9 demonstrates the same relationship on a plot of $^{143}Nd/^{144}Nd$ vs $^{176}Hf/^{177}Hf$, both within the SVZ, and globally. Note that all of the SVZ data used on Figure 4.9 are from Jacques et al., (2013) or Jacques et al. (2014). Very few of the samples from the Jacques et al. studies pass the filtering steps used here, though crustal processes are far less likely to affect the Nd and Hf isotopes systems, and so for this figure no data filters were

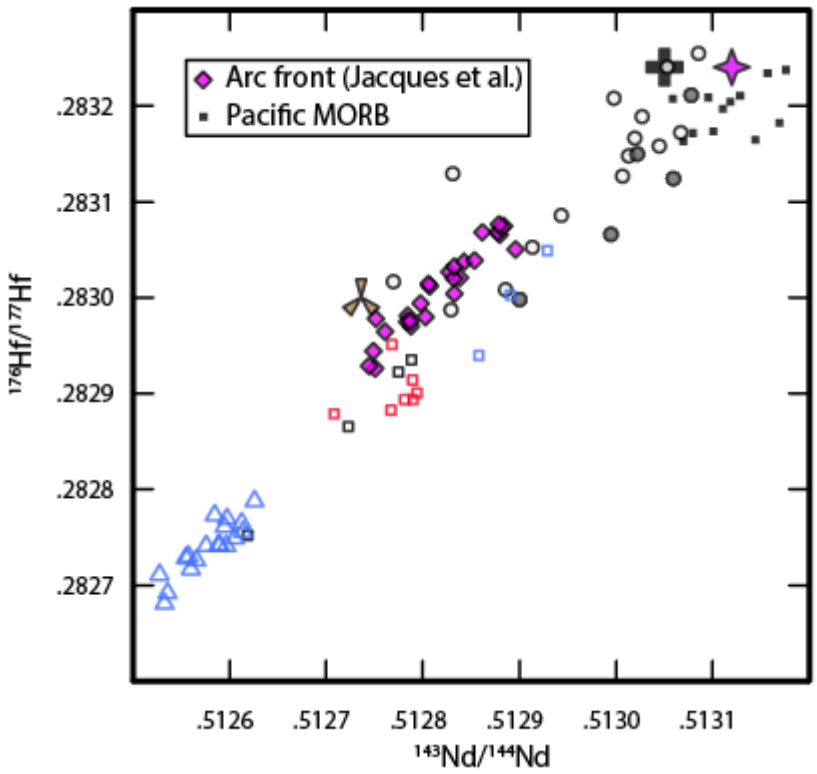

Figure 4.9: A plot of $^{143}Nd/^{144}Nd$ vs $^{176}Hf/^{177}Hf$. All SVZ data are taken from Jacques et al (2013) or Jacques et al. (2014). Most of the arc front data do not pass the filters described in the text, but the coherent systematics on this plot indicate that these isotopic systems have not been greatly affected by crustal processes. As on Figure 4.8, the rear arc samples stretch between the Gough Island basalts and the Ambient Atlantic Mantle. Also as on Figure 4.8, the arc front samples are offset towards the sediment and AOC compositions, and the global rear arc compositions align with the samples from the SVZ rear arc. Finally, the global arc front averages are offset from the rear arc compositions just as in the SVZ.

applied. As shown in Figure 4.8, the arc front samples are offset from the rear arc towards the sediment composition, and so it is inferred that the AOC composition is also likely offset (within the field of Pacific MORB) towards slightly lower $^{143}Nd/^{144}Nd$ at a given $^{176}Hf/^{177}Hf$ (discussed below).

$^{143}Nd/^{144}Nd$ and some trace element ratios also correlate among arc front lavas. As seen on Figure 4.10, $^{143}Nd/^{144}Nd$ correlates fairly well with Zr/Nb (r^2=.61, or .69 without the questionable $^{143}Nd/^{144}Nd$ analysis from the APP volcanic center), and Th/U (r^2=0.56). Only INAA trace element data are available for the samples from the northernmost volcanoes within our filtered dataset, so the Th/U values of these samples, which have some of the lowest measured $^{143}Nd/^{144}Nd$, are not available.

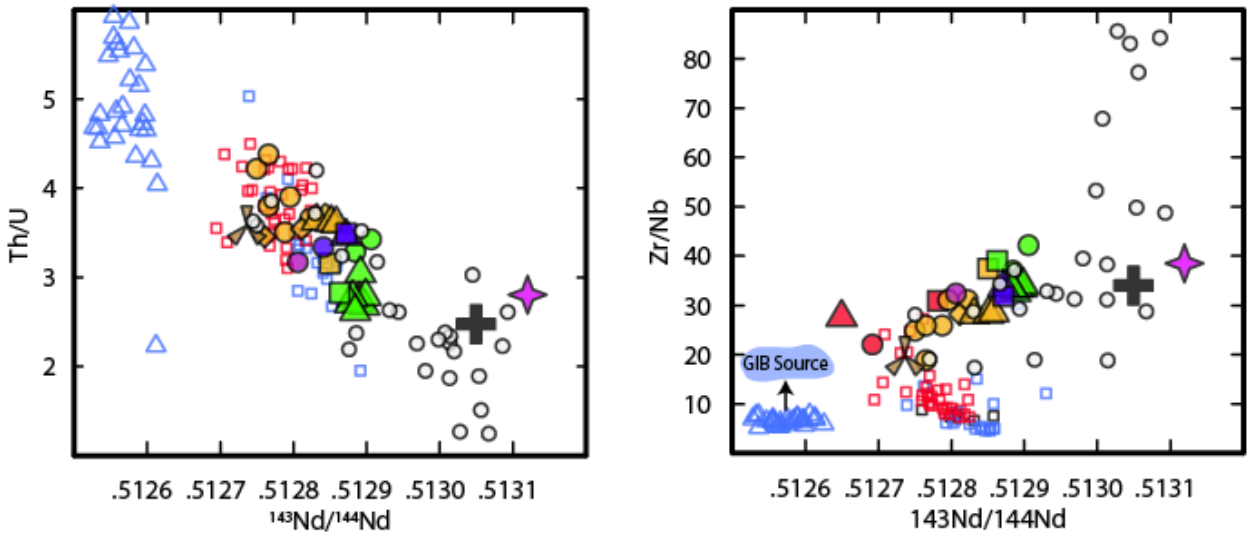

Figure 4.10: $^{143}Nd/^{144}Nd$ of arc front samples correlates with Th/U and Zr/Nb. As on Figures 4.8 and 4.9, the arc front samples are bracketed by the Gough Island basalts and a depleted mantle composition, suggestive of a common process which regulates these chemical indices. For Th/U, the rear arc samples overlap the samples from the arc front, while for Zr/Nb the rear arc samples are lower, likely as a result of very low extents of melting (see text for details). An inversion of the mantle source composition of the Gough Island basalts (see Appendix A4.2), indicates that their mantle source has Zr/Nb that is approximately three times that of the basalts. The global arc averages also correlate on both panels, and stretch from the SVZ arc front compositions, to far more depleted compositions.

Similarly to Figures 4.8 and 4.9, the arc front arrays on Figure 4.10 lie between AUM and GIB. On Figure 4.10a, the rear arc basalts lie to much lower Zr/Nb than the arc front array, while on Figure 4.10b, the rear arc and arc front samples overlap. Global correlations also exist among arc front $^{143}Nd/^{144}Nd$, Th/U, and Zr/Nb, and the relationship between the global arc front averages on Figure 4.10 is similar to the relationship shown among global and SVZ volcanics on Figures 4.8 and 4.9, with the SVZ occupying the lowest $^{143}Nd/^{144}Nd$ portion of the global array, and extending beyond the global array towards the GIB.

As shown by Jacques et al. (2013 and 2014) and reproduced in Figure 4.11, Pb isotope ratios in samples from the arc front overlap almost entirely with those measured in the sediment, though might be slightly offset towards the AOC (plotted on Figure 4.11 as the average of Pacific MORB segments from Gale et al. (2013)). Rear arc Pb values extend from the sediment towards either AUM, GIB, or AOC. It should be noted that the GIB data on Figure 4.11 are limited, consisting of old analyses from either

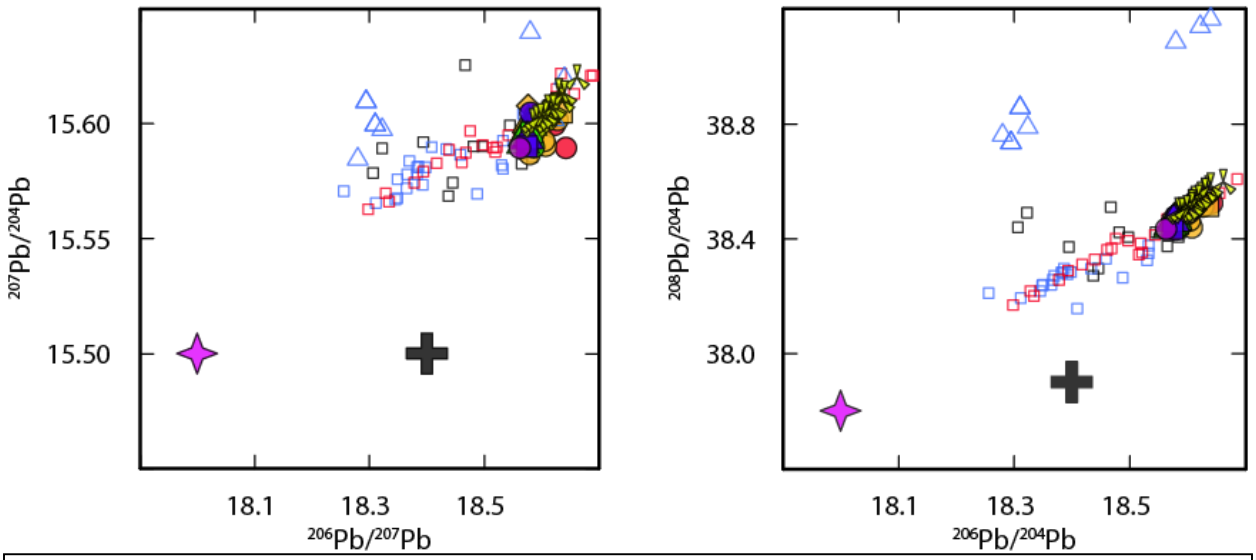

Figure 4.11: Pb isotope ratios of SVZ arc front samples overlap almost entirely with the sediment composition, indicating that the Pb of the arc front lavas is almost entirely derived from the slab sediment. Rear arc samples extend towards either the AOC (which is plotted here as the average of Pacific MORB values from Gale et al. (2013), the Ambient Atlantic Mantle, or toward the Gough Island Basalts. Note that the Gough Island basalt Pb isotope data is taken from older sources, and most likely does not represent the range of compositions from the Gough Islands seen on other figures.

Gast et al. (1964) or Le Roex et al. (1985), and so likely are of much lower precision and may not represent the full range observed on other figures. All other GIB data used in this study are from either Willbold and Stracke (2006, 2010), or Salters et al. (2011).

As with major and trace elements, the SVZ isotopic systematics serve as a microcosm of the global systematics. Globally, $^{143}Nd/^{144}Nd$, $^{87}Sr/^{86}Sr$, and $^{176}Hf/^{177}Hf$ of rear arc volcanics extend from a depleted MORB composition to a composition similar to EM1-OIBs. The rear arc lavas from the SVZ overlap this trend, extending it towards even more enriched compositions. The same is true for the arc front lavas on both scales, though at a given $^{143}Nd/^{144}Nd$, the $^{87}Sr/^{86}Sr$ and $^{176}Hf/^{177}Hf$ are offset towards the sediment composition. Both globally, and within the SVZ, the Zr/Nb and Th/U ratios correlate with $^{143}Nd/^{144}Nd$, and also fall between depleted and EM1 like compositions.

4.5.3 Results: Along arc variation of magma chemistry from 34° to 42° S in the SVZ

Major element and trace element 6-value samples (samples that pass the filters described above, and also have 5.5<wt. % MgO<6.5) vary regularly along strike between 34° S and 42° S in the SVZ (Figures 4.12 and 4.13). $Ca_{6.0}$ increases monotonically from south to north, while $K_{6.0}$, $Na_{6.0}$, and $P_{6.0}$ decrease monotonically. As previously discussed, $Ti_{6.0}$ occupies a limited range of compositions, though the southern volcanoes extend to lower values (not shown). $Sc_{6.0}$ behaves similarly to $Ca_{6.0}$ (Figure 4.13), increasing monotonically to the south. $Rb_{6.0}$, $Nb_{6.0}$, $Ba_{6.0}$, and $La_{6.0}$ decrease rapidly from 34° S to 38° S, and are more or less constant between 38° S and 42° S. $Yb_{6.0}$ has a limited range of compositions, though extends to slightly lower values in the north than in the south.

Ratios of REEs also vary regularly with latitude (Figure 4.14), following patterns similar to incompatible trace elements, though some of the southernmost volcanoes appear to be slightly offset. It is important to note that the samples with particularly high La/Yb and La/Sm values from TTSP (plotted as open symbols on Figures 4.10-4.14) are also significantly enriched in incompatible trace element abundances. Jweda (2013) has shown that within TTSP, enriched samples such as these likely represent variation among primary magmas which arise due to heterogeneity of the TTSP source region. Because these samples likely indicate primary source variability, for completeness they are plotted as 6-value samples on Figures 4.12 and 4.13, despite not falling within the required range of MgO (both samples have >6 wt. % MgO).

The ratios of Th/U, Zr/Nb, $^{143}Nd/^{144}Nd$ and $^{87}Sr/^{86}Sr$ follow slightly more complex along strike variations than are observed for elemental abundances and REE ratios (Figure 4.15). As noted by previous studies (e.g., Tormey et al., 1991), $^{143}Nd/^{144}Nd$ values increase from 34° S to 39° S, and then decrease slightly between 39° S and 42° S. $^{87}Sr/^{86}Sr$ values display inverse behavior to $^{143}Nd/^{144}Nd$. Zr/Nb and Th/U behave similarly to the $^{143}Nd/^{144}Nd$ and $^{87}Sr/^{86}Sr$ isotopes, as would be expected from their

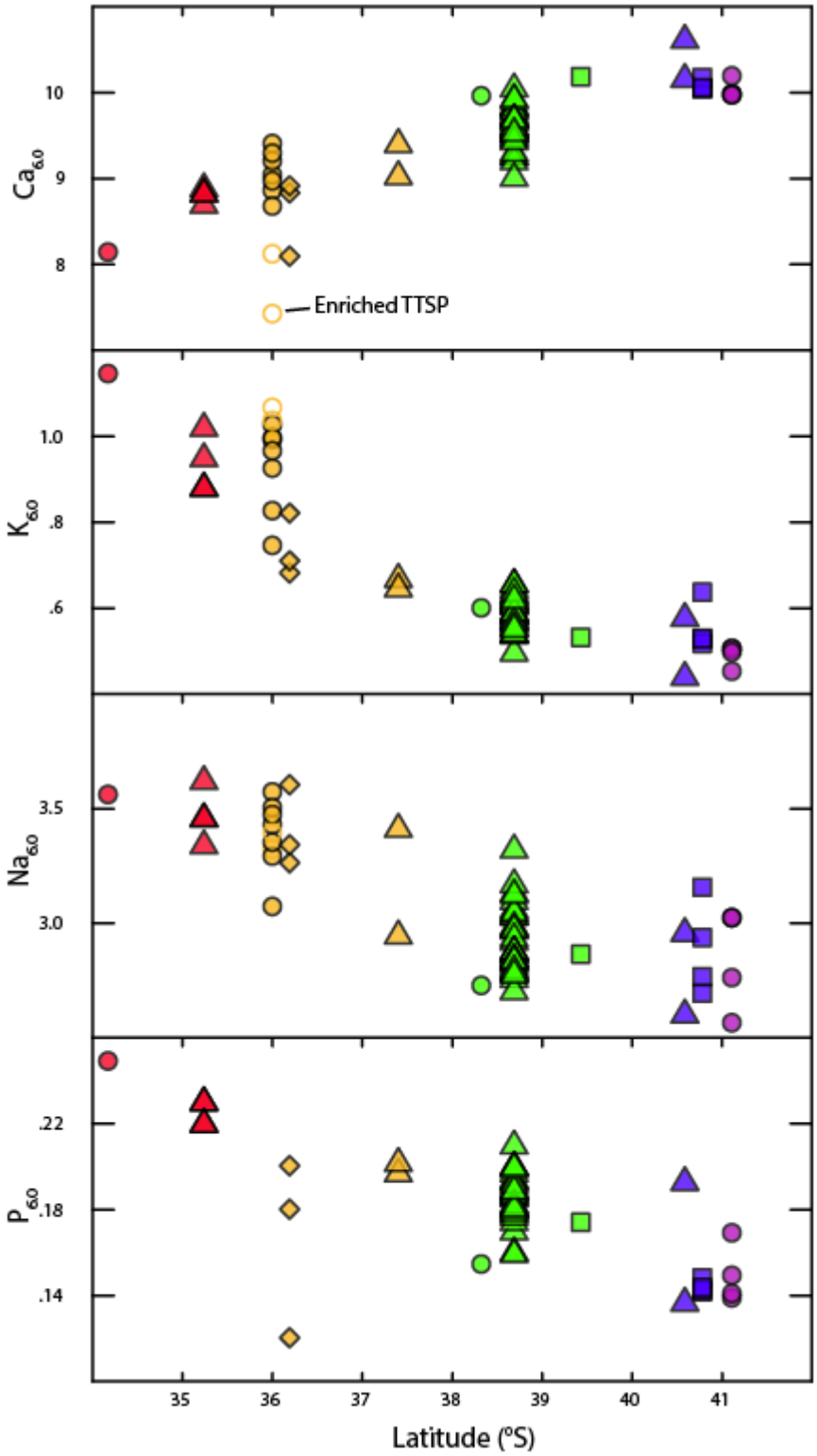

Figure 4.12: Variations of major elements in the SVZ with latitude. The samples plotted in this figure are "6-value samples," which means simply that they all have 5.5<wt. % MgO<6.5. From north to south, Ca increases while K, Na, and P all decrease.

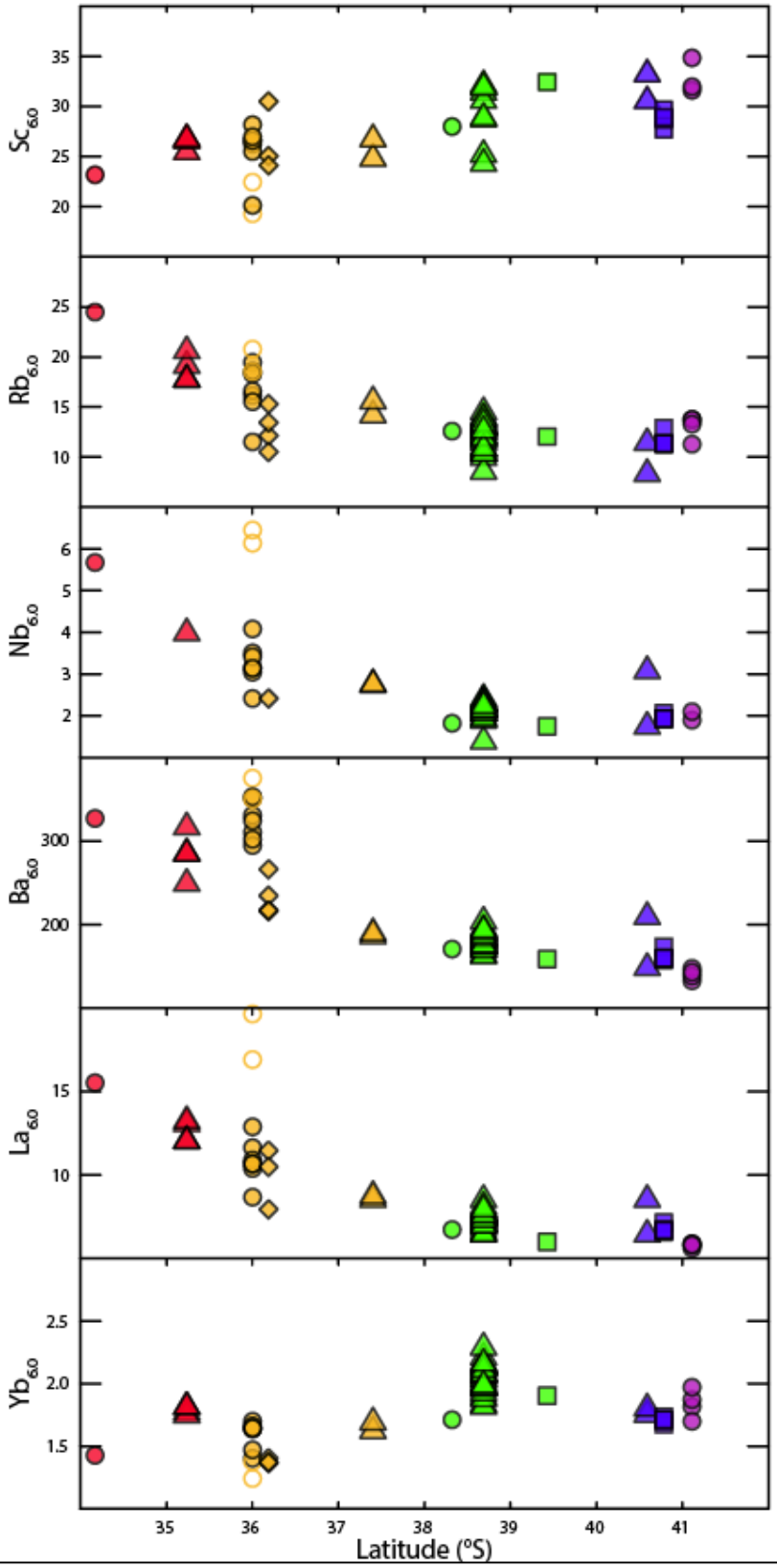

Figure 4.13: Trace elements vs latitude. The samples plotted are "6-value samples," as on Figure 4.12. Sc increases to the south while incompatible elements decrease. Yb has a limited range.

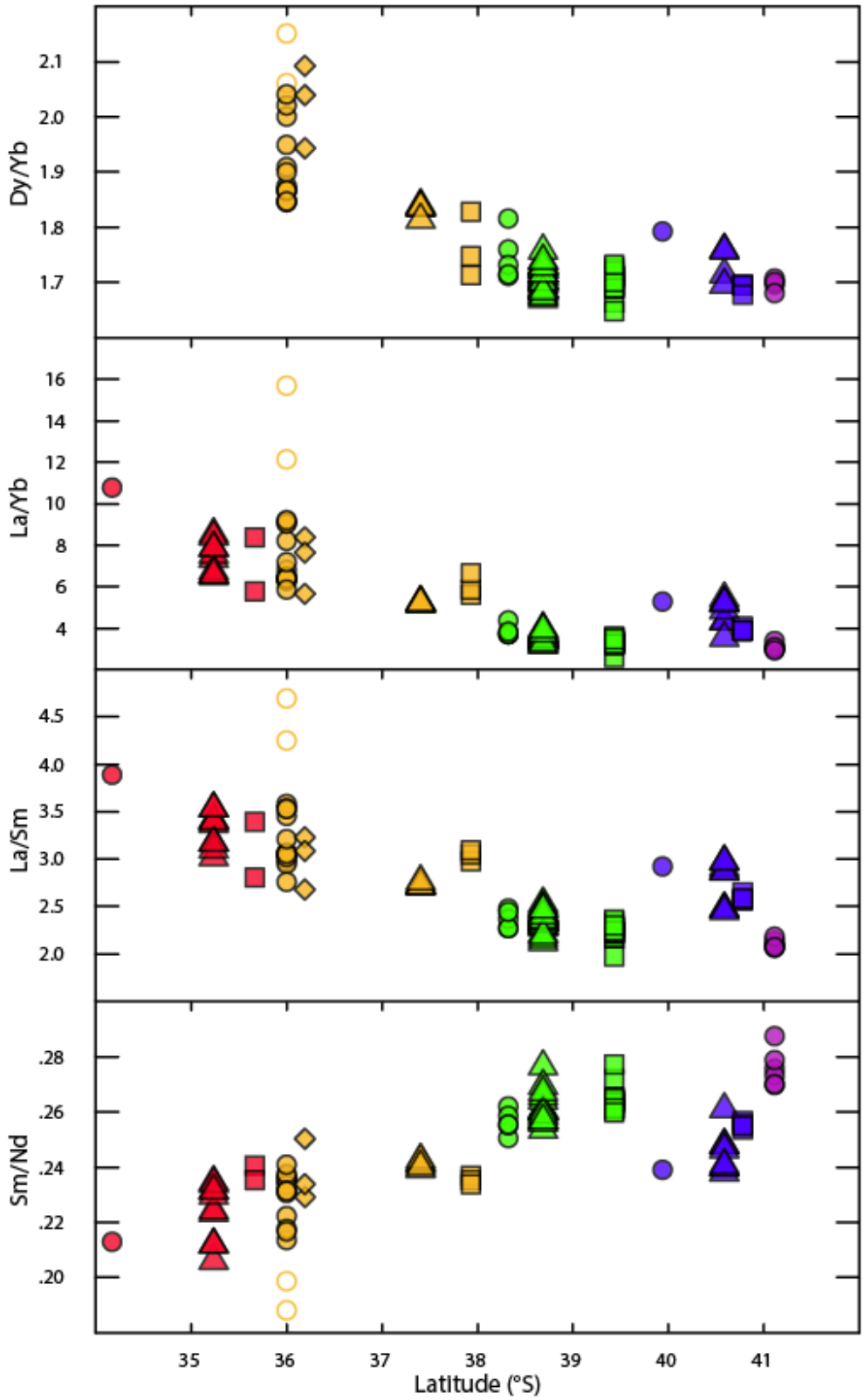

Figure 4.14: REE ratios vs latitude. The REE vary systematically with latitude, though the southernmost volcanoes appear to be offset as compared to the general along strike trends.

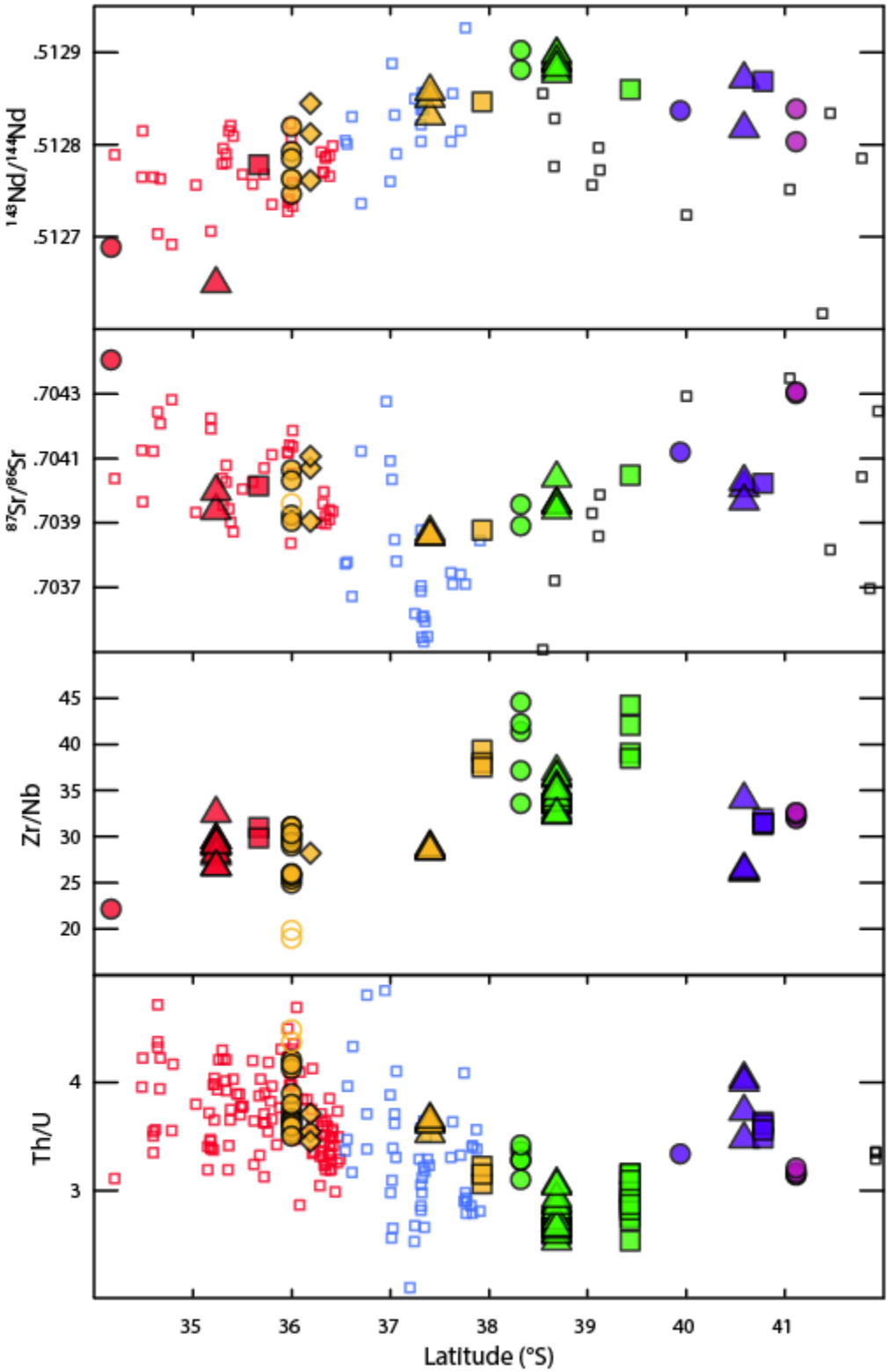

Figure 4.15: $^{143}Nd/^{144}Nd$, $^{87}Sr/^{86}Sr$, Zr/Nb, and Th/U follow similar systematic patterns with latitude, with an inflection near the center of our study region. $^{143}Nd/^{144}Nd$, $^{87}Sr/^{86}Sr$, and Th/U for rear arc samples appear to follow the same patterns as in the arc front.

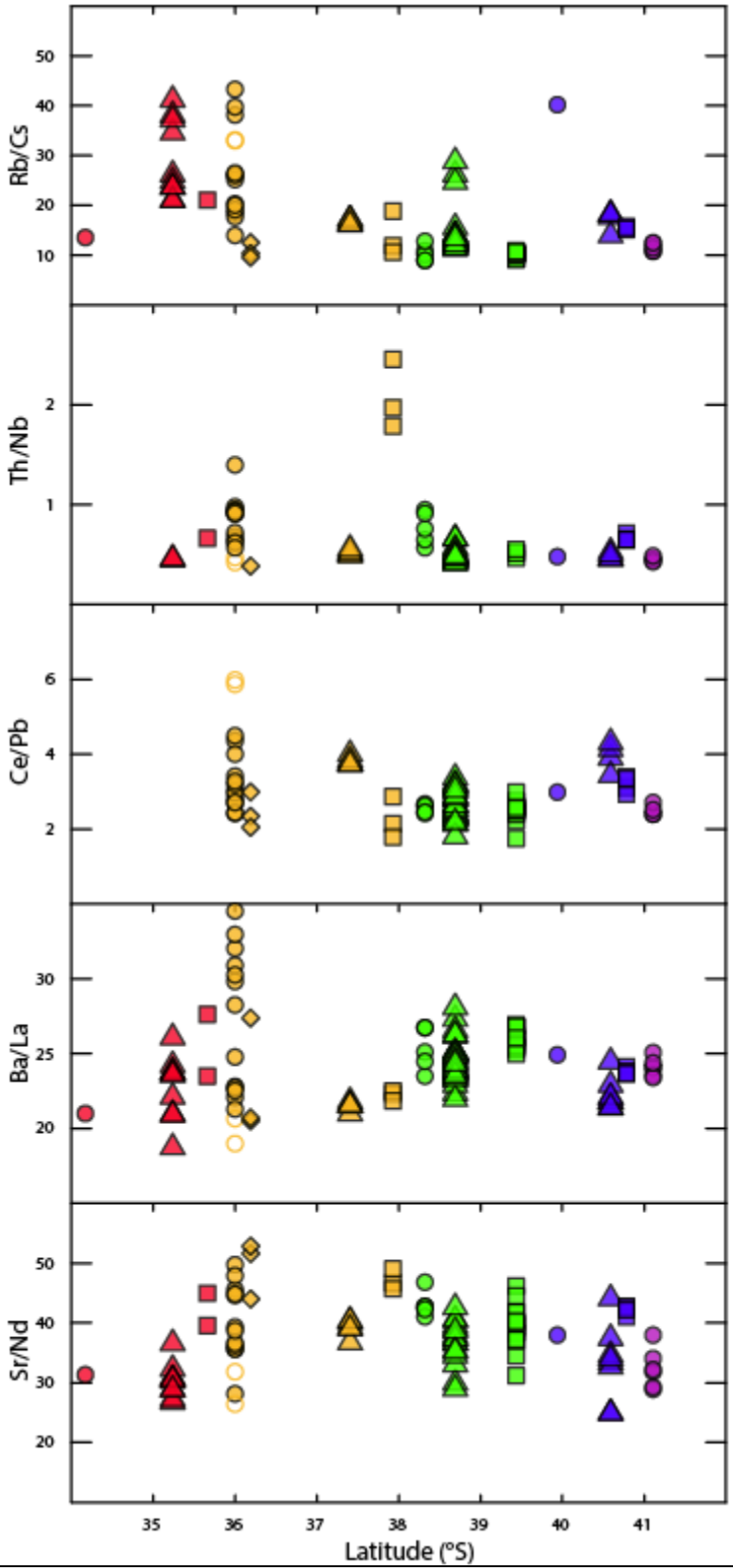

Figure 4.16: These trace element ratios can be used as indices of slab contributions to the sub-arc mantle, and do not vary systematically with latitude, overlapping within most of the volcanoes. Within individual volcanoes, however, many of these ratios have large variations.

correlations with $^{143}Nd/^{144}Nd$. Jacques et al. (2014) suggested that the rear arc samples in their study largely overlap in $^{143}Nd/^{144}Nd$, with the exception of several particularly low $^{143}Nd/^{144}Nd$ samples located far to the south. However, when the data from our rear arc literature compilation are plotted against latitude, it is apparent that the rear arc and arc front samples follow similar along strike trends in $^{143}Nd/^{144}Nd$, $^{87}Sr/^{86}Sr$, and Th/U, suggestive of a process which regulates these values across both domains. Chapter 3 showed that for the global arc dataset, the average $^{143}Nd/^{144}Nd$ compositions of arc front stratovolcanoes correlate strongly with the average $^{143}Nd/^{144}Nd$ of their corresponding rear arc volcanics, and so the correspondence between arc front and rear arc $^{143}Nd/^{144}Nd$ compositions within the SVZ yet again mimic global systematics in this way.

Other trace element ratios which often vary among arc lavas have no systematic variation with latitude in the SVZ (Figure 4.16). It is notable, however, that many of these ratios exhibit significant variability within individual volcanic centers. The TTSP and APP volcanic complexes, for example, have Rb/Cs values which vary by more than a factor of 2. In detail, the Rb contents of these volcanoes are fairly stable and vary along with other incompatible elements along strike (Figure 4.13), and so the variation is apparently driven primarily by Cs depletion. Th/Nb overlaps for nearly all volcanoes, with a notable exception at Callaqui, which has anomalously high Th/Nb. Ce/Pb does not vary along strike, though the two samples from TTSP that have high La/Yb also have higher Ce/Pb. Ba/La and Sr/Nd also overlap in all volcanoes with the exception of TTSP, which extends to higher Ba/La.

4.6 Discussion

The chemical systematics of the major and trace element compositions of SVZ volcanoes, as well as their relationship to crustal thickness, are remarkably similar to the global systematics of volcanic arcs found by Plank and Langmuir (1988) and Chapter 2. This similarity may indicate that a similar set of

processes generate variable magma compositions on both global and regional scales. Global interpretations of volcanic arc chemistry benefit from the assessment of the broadest possible range of chemical and physical parameters, but interpretations that make use of averages taken across broad regions suffer from a lack of precision, as such studies cannot easily incorporate small-scale variations within these regions. The compositions of lavas erupted from SVZ volcanoes correspond to approximately half of the range of compositions seen globally. Thus, the SVZ provides a valuable natural laboratory in which to consider the interpretations that have been made on the global scale. At the same time, the global modeling framework developed in Chapter 3 can be applied at the regional scale to assess certain hypotheses within the SVZ.

4.6.1 Crustal contamination in the SVZ

The chemical variability within individual volcanic centers of the SVZ is rarely consistent with closed system crystal fractionation. As described above, and in agreement with previous studies, there is evidence for magma mixing and excess crystal accumulation, as well as crustal assimilation. The extensive work of previous authors has provided a good understanding of the effects of crustal contamination in this region, which is typically (but not always) minor among basaltic magmas. These studies have verified that Rb excess relative to other incompatible elements is diagnostic of crustal assimilation in the SVZ, and this observation is thus used here to filter out samples which have been contaminated by crustal material. The chemical variability within this filtered dataset is thus unlikely to reflect crustal contamination, though correlations among volcano compositions and crustal thickness intuitively support a model in which magmas that erupt through thicker crust also assimilate more crust. Additional difficulties arise in the northernmost sections of the SVZ, because truly primitive magmas

have not been found, and so within a regional framework it is difficult to conclusively determine to what extent the samples from the northernmost volcanoes have been affected by intra-crustal processes.

Despite the intuitive appeal of a model invoking crustal contamination, the striking similarities among the chemical systematics of the global and SVZ datasets provides evidence that the SVZ systematics are not produced in the crust. Tormey et al. (1991) demonstrated that a crustal contaminant capable of relating the primitive magmas at APP, which is closer to the north, and Puyehue, which is in the southern section of our study area, is unlikely to exist. Chapter 2 took a similar approach in their interpretation of the global systematics, demonstrating that a mixing end member composition which can relate the primitive magma compositions from arcs with thin and thick overlying crust has not only never been observed, but also may be impossible to produce. The global systematics among arc volcanoes are thus highly unlikely to have been generated by variable levels of baseline contamination, as proposed for the SVZ by Hildreth and Moorbath (1988). The same systematics are present within the SVZ as are found globally, so the same logical framework can be applied within this region. The coherent systematics among the filtered, primitive SVZ lavas indicate that if varying degrees of baseline contamination are responsible, then this contaminant must have a similar major and trace element composition along the entire arc. The similarity of the chemical systematics within the SVZ and worldwide indicates that this hypothetical contaminant must have a similar major and trace element composition across the entire globe. As shown by Chapter 2, a rock with this composition has not been recorded anywhere to our knowledge. The SVZ magma variability presented here is thus likely to represent variation among primary magmas, and so processes which may generate variability among primary SVZ magmas will be considered in the following discussion.

4.6.2 Approach: Applying global interpretations within the SVZ

Chapter 3 demonstrated that the average compositions of volcanic arcs correlate globally with both crustal thickness and the "thermal parameter," or Φ, which is a proxy for the thermal state of the subducting slab [Φ=convergence rate*slab age*sin(slab dip)]. That study showed that the global relationship between magma chemistry and crustal thickness can be modeled as the result of variations in the extent of mantle melting produced by changing pressures and temperatures of the mantle wedge. Lower extents of mantle melting produce mantle melts with increasing abundances of incompatible elements, and fractionates elements that have different bulk partition coefficients. Lower extents of melting and higher pressures of melting also lead to increasing proportions of garnet and clinopyroxene in the residual mantle source, which enhances fractionation of certain elements. These effects may arise as a result of variations in the thickness of the overlying crust, because increasing crustal thickness likely increases the pressure of melting as well decreases the temperature of the mantle beneath the arc front, as discussed below. Crustal thickness along the SVZ varies across the upper range of global arc crustal thickness (excluding the Central Andes), and so the global model of crustal thickness may be applicable within the SVZ as well.

The global correlations between magma chemistry and Φ supports a different model of global magma variability. This relationship can be modeled as the result of variations in the composition and volume of slab melts delivered to the mantle wedge that may be produced by changing slab temperature. In the SVZ, the magnitude of Φ is essentially constant when compared to the global range (in the SVZ: 9.1 to 11.5; global arcs: 1.15 to 62.26). This is in contrast to the large relative range of SVZ crustal thickness, and so the slab model for the SVZ is less intuitively appealing. However, the slab depth beneath the arc varies by ~40 km along our study region, and so the slab temperature beneath the arc front should increase from the south to the north. Since more slab melts are consistent with the increasing enrichments northwards, the slab model must be considered as well. Chapter 3 showed that

it is difficult to conclusively assess whether global chemical variability of volcanic arcs is largely driven by variable slab contributions to the mantle wedge, or variable extents of melting of the mantle wedge. This difficulty arises because global chemical variations correlate with both crustal thickness and Φ, as well as a lack of detailed constraints on the functions that relate these observable physical parameters to their chemical outcomes. The SVZ provides an additional series of constraints that hold the possibility of resolving these ambiguity in this region, with possible applications to the global regularities.

4.6.3 Does slab temperature regulate along strike chemistry in the SVZ?

The likelihood of slab temperature variations producing the SVZ along strike chemical variability can be assessed from physical models, and chemical observations. The feasibility of slab-driven along strike variability in the SVZ will first be considered in the context of thermal models. Syracuse and Abers (2010) provided models of global arc segments relating slab depth to slab surface temperature, including models representing multiple cross sections of the Chilean subduction zone. The two cross sections relevant to our study area are nearly identical (owing to similarity in Φ values) and so the along strike variability will be considered here entirely in the context of their slab models designated as "Central Chile," which correspond specifically to 35.24° S. Syracuse and Abers (2010) produced four different families of models based on different assumptions about the conditions under which the subducting slab couples with the asthenospheric mantle wedge. This depth of slab-mantle coupling is a critical parameter in such thermal models. In all cases, the slab surface remains at temperatures well below the hydrous solidus expected for slab materials (~700 °C; Hermann and Rubatto, 2009) prior to reaching the coupling depth. Until the depth of coupling is reached, the slab surface is in contact with the isolated "cold nose" of the mantle wedge, and so material from the slab cannot be transported to

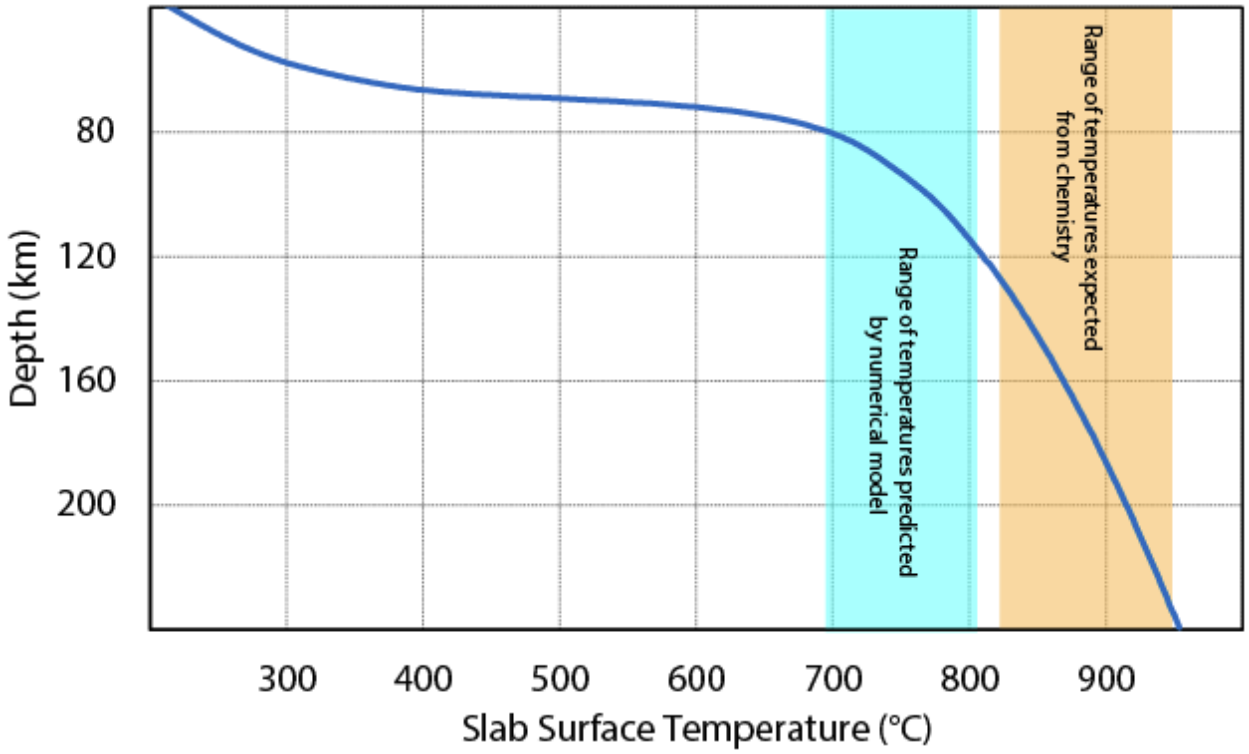

Figure 4.17: This figure demonstrates how slab surface temperature varies with slab depth, according to the T550 model for Central Chile from Syracuse and Abers (2010). As in all slab thermal models, the slab surface heats slowly until the depth of slab mantle coupling (at 67 km, in this model). Within the ~40 km following the depth of coupling, the slab surface heats rapidly. At depths beginning approximately 40 km beyond the depth of coupling, and the rate of slab becomes more gradual. Because the slab depths below volcanoes within the SVZ correspond to the lower half of the global range in slab depths, the slab surface temperatures beneath the SVZ likely corresponds to the lower half of global slab temperatures. In an alternate scenario, the depth of coupling could be set at an even shallower depth, and the maximum slab surface temperature beneath the SVZ might approach the higher end of slab surface temperatures expected globally. At slab depths that are much greater than the coupling depth, however, the rate of heating is lower, and to the total range of slab temperatures corresponding to the ~40 km variation of slab depth beneath the SVZ would be narrow. These scenarios are in contrast with either the maximum temperature, or range of temperatures, that are required by a model that accounts for SVZ compositional variability as a function of slab temperatures, because the SVZ volcanoes occupy the upper half of the global range of incompatible element abundances.

the region of melting below the arc prior to reaching this depth. For Central Chile, three of these four models have depths of coupling at 80 km or deeper. This assumption cannot be true for the SVZ, however, as estimates of slab depth beneath the SVZ reach <80 km at Osorno volcano, and mantle melting cannot occur in the cold wedge nose. Only one of the slab models, the T550 model, provides a

depth of coupling that is lower than 80 km (at 67 km) for Central Chile, so slab temperature variation will be explored in the context of this modeling result, which is shown in Figure 4.17.

The possibility of slab control on chemical variability in the SVZ is not consistent with qualitative observations that apply generally to current thermal models of subducting slabs. As in all of the slab thermal models, the slab depicted in Figure 4.17 remains cold until the depth of coupling is reached, heats rapidly over the ~40 km below the depth of coupling, and thereafter continues to heat at a slower rate. Figures 4.2-4.5 clearly show that incompatible trace element abundances of SVZ volcanoes range from around the mid-point of the global chemical array up to the most enriched end (and sometimes beyond). If the correlations among volcano/arc chemical indices are the product of variations in slab temperature, then the slab temperatures beneath the SVZ should approximately correspond to the upper range of slab temperatures expected globally, or from ~825 to ~950 °C, indicated by the khaki bar on Figure 4.17. This is in stark contrast to the range of temperatures predicted by the thermal model, which is indicated by the cyan bar. If the model's depth of coupling was set even lower, then the predicted range of temperatures beneath the SVZ might fall within the range expected from chemistry after all. However, at slab depths greater than 40 km beneath the coupling depth, the rate of temperature increase is much lower. In order to occupy the full upper range of global slab temperatures, the slab depth must vary by 80 km, while in the SVZ the slab depth varies by only 40 km. It thus appears unlikely that either the large range of compositions observed in the SVZ, or that the particularly enriched incompatible abundances found within the SVZ, are consistent with the slab model, when considered within a global context.

In addition to inconsistencies between thermal models of subduction zones and observed chemical variation within the SVZ, a model in which slab parameters primarily control magma chemistry is at odds with observations of trace element ratios that are most sensitive to slab contributions to the

wedge (Figure 4.16). These ratios do not vary systematically along the arc, though as noted previously, some of these ratios vary significantly within individual volcanoes.

The variations within individual volcanoes seem to relate to particularities of those edifices and their position above the slab. Tormey et al. (1991) suggested that high Rb/Cs ratios in the northern portion of our study area may indicate a lower fluid flux to the northern section of the arc. Rb abundances are also particularly sensitive to crustal assimilation, however (Dungan et al., 2001). Our sample set was filtered for crustal contamination based on the K/Rb ratio, and within this filtered dataset, high Rb/Cs samples remain only at AAP, TTSP, and Mocho-Choshuenco. If the Rb/Cs samples approaching MORB-like (>60 Rb/Cs, Gale et al., 2013) values at these volcanoes were indicative of low slab flux, the high Rb/Cs samples within these volcanoes should also have lower, more MORB-like, Rb and Cs abundances. However, as shown on Figure 4.13, Rb abundances of samples from northern volcanoes are higher than those volcanoes to the south. The Rb/Cs ratio appears to be driven upward as a result of low Cs concentrations alone. Magma compositions of the northern volcanoes have many similarities to the GIB, and Cs abundances in GIB also vary wildly across a relatively narrow range of Rb abundances (Rb/Cs values of GIB range from 13 to 500), and so it may be the case that fractionation of these elements may be driven by a similar mechanism in both sample suites, and is unrelated to local subduction processing. Alternatively, Cs, which has abundances in SVZ volcanoes <1 ppm, might be fractionated by volatilization during high temperature de-gassing (Hinkley et al., 1994), potentially indicating higher primary H_2O contents of magmas from these volcanic complexes.

TTSP is also unique in having a very large range of Ba/La values. Within the TTSP samples, Ba/La correlates positively with other indicators of slab contributions (Pb/Ce, Th/Nb) indicating that the slab flux to this volcano is sometimes larger than the regional baseline flux. This could potentially be related to the Mocho Fracture Zone, which projects towards Longavi and probably TTSP volcanoes (Selles et al., 2004). Jacques et al. (2014), Dzierma et al. (2012), and Wehrmann et al. (2014), have all suggested that

the Th/U ratio and Ba/Nb ratio indicate variable fluid flux along the SVZ. These ratios, however, do not have the same along strike variations as elemental abundances (Figure 4.12, 4.13, and 4.15). As will be discussed in section 4.6.5, these ratios are also sensitive to heterogeneity of the mantle wedge prior to slab modification, and are likely to indicate variable enrichment of the ambient mantle, rather than variable fluid contributions to the wedge. If trace element abundances and REE ratios were controlled by the slab in the SVZ, then one should expect these sensitive slab indicators to co-vary with them. Therefore, the temperature of the slab, or variable slab flux in general, is not likely to produce the regular along strike trends on the basis of both chemical and physical considerations.

4.6.4 Crustal thickness, lithospheric thickness, and the extent of melting along the SVZ

Global variations in average arc chemistry are consistent with a model in which increasing crustal thickness leads to higher pressures and lower temperatures beneath the arc front Chapter 3. As shown on Figures 4.6 and 4.7, elemental abundances from the SVZ exhibit nearly identical correlations with crustal thickness as the global arc averages, and so a similar model should be applicable within the SVZ. In detail, however, the along strike variations of subduction parameters in the SVZ are unique, and not entirely similar to the co-variation of subduction parameters observed globally. Consideration must be given to whether the physical basis for the global model is also applicable here.

Tassara and Echaurren (2012) provide a model of lithospheric thickness for South America which indicates a nearly constant depth of the Lithosphere Asthenosphere Boundary (LAB) directly below the SVZ arc front, while the model of Chapter 3 is most consistent with LAB depths that generally correlate with Moho depths beneath arc fronts. The LAB depth model of Tassara and Echaurren (2012), however, is based largely on seismic data, and operates under the assumption that “subcrustal seismic velocity

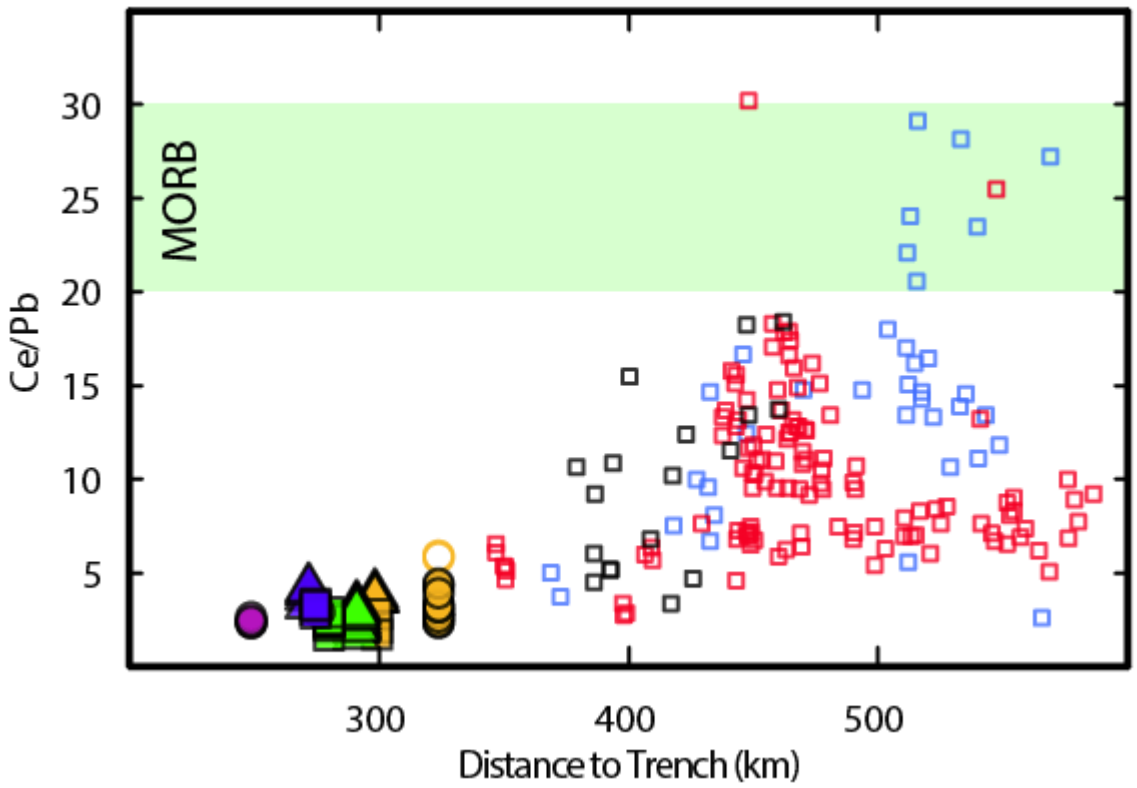

Figure 4.18: Variation of the Ce/Pb ratio of arc front and rear arc samples with their distance from the trench. The maximum observed Ce/Pb of rear arc samples from 34° S to 36.5° S (red squares) first increase, then decrease with distance from the trench. The maximum Ce/Pb of rear arc samples from 36.5° S to 38° S (blue squares) increases continuously with distance from the trench. Rear arc samples from south of 38° S are from a comparatively narrow range of distances from the trench. Rear arc samples are found up to 600 km from the trench with Ce/Pb ratios much lower than MORB, indicating that slab material reaches the mantle across this entire rear arc region.

structure is primarily sensitive to mantle temperature." As discussed by Dzierma et al. (2012), the addition of fluids into the mantle may also have a significant effect on the seismic velocity structure. This competition between varying fluid content and varying mantle temperature may lead to difficulties in attempting to constrain either of these parameters independently using seismic data within a subduction setting.

To try to separate the role of water, trace element ratios that should be sensitive to fluid input from the slab can be applied. In Figure 4.18 the Ce/Pb ratio for arc front and back arc samples is plotted vs the distance from the trench to the sample location. Normal MORB and EM1 OIBs both have Ce/Pb

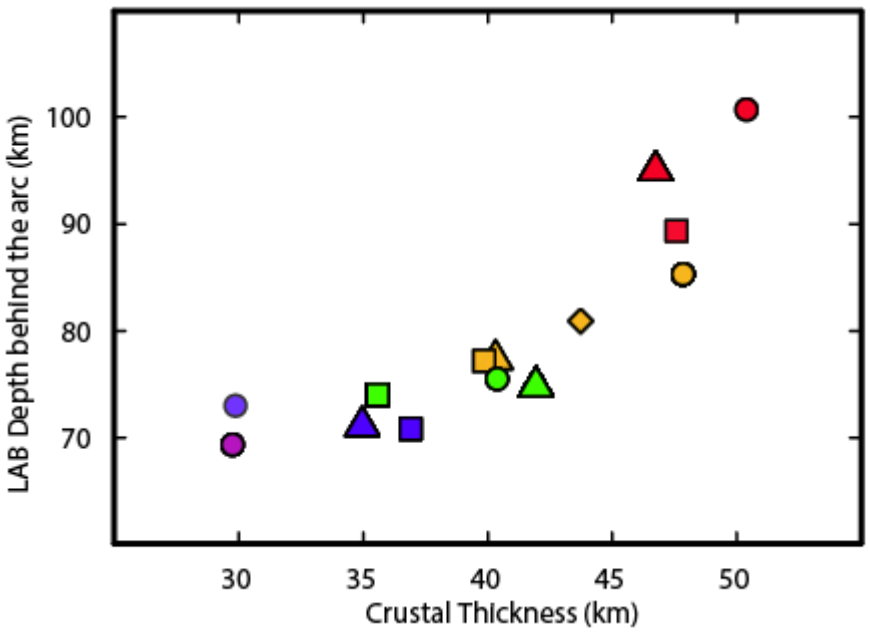

Figure 4.19: A comparison of the crustal thickness at the arc front and the depth of the Lithosphere Asthenosphere Boundary (LAB) at 2.5° behind the arc front, according to the model of Tassara et al. (2012). Where the crust is thickest, the lithosphere behind the arc is thickest. While the model of Tassara et al. does not indicate LAB depth variation behind the arc front itself, this may arise partially due to complications arising from mantle hydration (see text for details).

ratios almost exclusively >20 (Willbold and Stracke, 2006). The lower Ce/Pb of the back arc samples suggests that a hydrous slab component has pervasively infiltrated the mantle up to at least 200 km behind the arc front, 500 km from the trench. Back arc samples with Ce/Pb ratios approaching those seen in the arc front are erupted along the entire interval from the arc front up to 600 km behind the arc. If LAB estimates behind this boundary are compared to the crustal thickness determined beneath the corresponding arc front, a clear relationship between the two emerges (Figure 4.19). A thicker lithosphere behind the arc front itself may have a significant effect of the thermal structure at the arc front as well. Quantitative models that incorporate a variable LAB with distance from the arc front would be useful in this regard.

A second consideration is that the proposed relationship between crustal thickness and sub arc mantle temperature from Chapter 3 is based on the observation that with other parameters held

constant, a thicker lithosphere will effectively squeeze wedge isotherms farther from the trench, resulting in colder temperatures in the wedge beneath the arc front. This can be thought of quantitatively as a change in the radial distance from the wedge corner to the hot core of the wedge, in the equations of England and Katz (2010). The relationship between crustal thickness and mantle melting has also been demonstrated numerically by Karlstrom et al. (2014) in the context of arc front migration. Along strike in the SVZ, however, the crustal thickness and slab depth increase simultaneously, and so the radial distance may not have the same relationship with crustal thickness as elsewhere. On the other hand, the dip of the slab beneath the arc front also exerts a primary control on sub arc mantle wedge temperature (also shown quantitatively by England and Katz, 2010), and the decreasing slab dip angle from south to north should lead to decreasing mantle temperatures in the mantle wedge in the northern part of the SVZ. Physical observations and thermal models of subduction zones are therefore consistent with a model in which the depth of mantle melting, as well as the temperature of the sub arc mantle wedge, vary systematically along the arc. As a result, crustal thickness and extent of melting would co-vary along the SVZ, and globally. Within this framework, the extent of melting of the SVZ mantle source should decrease from south to north, with the pressure of melting tracking lithospheric thickness, and the sub-arc mantle temperature tracking the slab dip angle.

Observations of regionally variable Ce/Pb among rear arc samples provide additional support for a model of increasing lithospheric thickness and decreasing mantle temperature from south to north along the SVZ. From 38° S to 34° S, the maximum Ce/Pb found in rear arc samples decreases from MORB-like values to arc front-like values, despite the fact that rear arc samples from this entire region erupt at a similar range of distances from the trench (Figure 4.20). An increase in the hydrous flux from the slab to the mantle will lower the mantle Ce/Pb ratio, as well as decrease the mantle solidus temperature. Therefore, it is evident that at 38° S, where some back arc samples have high Ce/Pb, some portions of the rear arc mantle have melted despite a very low hydrous flux. Near 34° S, all rear arc

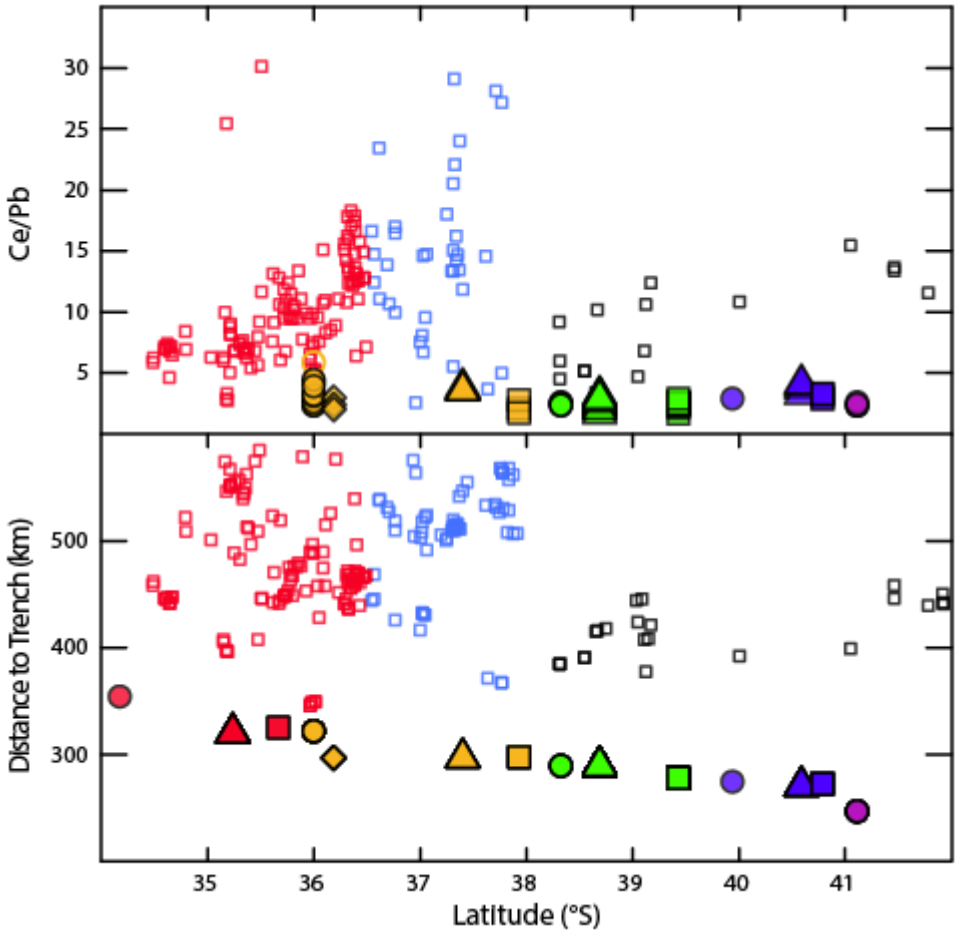

Figure 4.20: Variations in Ce/Pb, and the distance from sample locations to the trench with latitude. North of 38° S, back arc samples are from a similar range of distances to the trench. Despite this, the maximum Ce/Pb of back arc samples decreases from 38° S to 34° S. This is likely because the temperature of the mantle near 34° S lies farther from the anhydrous solidus, and so the rear arc mantle is only able to melt where the slab flux is highest (see text for details).

samples have low Ce/Pb, and so rear arc mantle melting only occurs in the presence of a large hydrous flux. This observation is consistent with the hypothesis that the mantle pressure and temperature conditions near 38° S are much closer to the anhydrous solidus than they are farther to the north.

The variation of Ce/Pb among both arc front and rear arc lavas are also consistent with the numerical models of Wilson et al. (2014), in which the majority of slab material is transported updip the slab towards the arc front, with intermittent additions of slab material behind the arc. Rear arc samples with low Ce/Pb are erupted along the entire arc, indicating occasional hydrous flux behind the arc occurs

at all latitudes. The constant, low Ce/Pb along the arc front indicates the large hydrous flux to the arc front is continuous. The range of Ce/Pb among back arc samples may be determined primarily by whether the mantle is able to melt without a significant addition of H_2O, as regulated by thermal structure of the mantle. The mantle's thermal structure is also likely to control the extent of melting along the arc front, and can account for much of the along strike chemical variability in the SVZ, as well as global chemical variability among volcanic arcs.

4.6.5 Evidence for a heterogeneous mantle source along the SVZ arc front

Chapter 3 found that certain aspects of global chemical variability among arc magmas are best accounted for by variations in the composition of the mantle wedge prior to slab addition (the ambient mantle wedge), and the same may be true for the SVZ. A simple model of regularly varying extents of melting and increasing melting pressures along the SVZ may account for much of the variation observed in major elements, trace elements, and REE ratios (Figures 4.12-4.14), but cannot account for the along strike patterns observed for $^{143}Nd/^{144}Nd$, $^{87}Sr/^{86}Sr$, Zr/Nb and Th/U (Figure 4.15). The along strike enrichment observed for highly incompatible elements and REE ratios are also not entirely accounted for by variable extents of melting, as these chemical parameters are nearly constant from 38° S to 42° S, while slab dip and Moho depth are not.

Jacques et al. (2013) found that isotopic enrichment of the northern portion of our study region is best accounted for by heterogeneity of the ambient mantle wedge, but suggested the effect of mantle heterogeneity on trace element concentrations was minimal. Jacques et al. (2014) found that ambient mantle enrichment was more prevalent in the rear arc and northern arc front regions, possibly because the enriched portions of mantle were extracted preferentially by melting in the back arc, and diluted by higher degrees of melting south of 38° S. According to Jacques et al., the lower extents of melting in the

northern part of the arc are a result of lower flux of slab fluid to the mantle wedge, as indicated by higher Th/U and Ce/Pb. Within our filtered dataset, however, most indices of slab contributions to the mantle wedge, including Ce/Pb, overlap within all of the SVZ volcanoes (Figure 4.16). Th/U and Zr/Nb, on the other hand, co-vary along the arc with $^{143}Nd/^{144}Nd$ and $^{87}Sr/^{86}Sr$. If mantle heterogeneity influences isotopic variability of SVZ arc front magmas, the co-variations of $^{143}Nd/^{144}Nd$ and $^{87}Sr/^{86}Sr$ with Th/U and Zr/Nb may also be caused by mantle heterogeneity, rather than a variable slab flux, and this possibility merits further consideration.

Some compositional characteristics of rear arc samples may be representative of the ambient mantle wedge, because rear arc volcanics lie farther from the trench, and at a greater distance above the slab. Jacques et al. (2014) found that the rear arc samples within their dataset largely overlapped in isotopic compositions (with the exception of three unusually enriched samples). Within the broader literature database, however, it is apparent that the rear arc $^{143}Nd/^{144}Nd$, $^{87}Sr/^{86}Sr$, and Th/U compositions follow along strike patterns that are similar to those observed in the arc front (Figure 4.15), indicating a similar origin for this pattern in both domains. If the rear arc samples do indeed represent the ambient mantle wedge compositions, then mantle heterogeneity most likely controls $^{143}Nd/^{144}Nd$, $^{87}Sr/^{86}Sr$, and Th/U not only in the rear arc, but also the arc front. Alternatively, the co-variation of rear arc and arc front magmas on Figure 4.15 may indicate that contributions from the subducting slab are controlling these ratios in both domains. As discussed in the previous section, it is possible that mantle melting in the northern rear arc may require a larger flux of slab material than in the south, and so it is possible that the isotopic compositions and other trace element ratios of the northern rear arc sample are disproportionally affected by slab contributions.

Diagrams of $^{143}Nd/^{144}Nd$ vs trace element ratios that are sensitive to slab additions, such as Th/Nb, provide evidence that the Nd isotope system is not significantly affected by slab contributions in the SVZ, and that the regional variations of $^{143}Nd/^{144}Nd$ in back arc lavas are the result of mantle

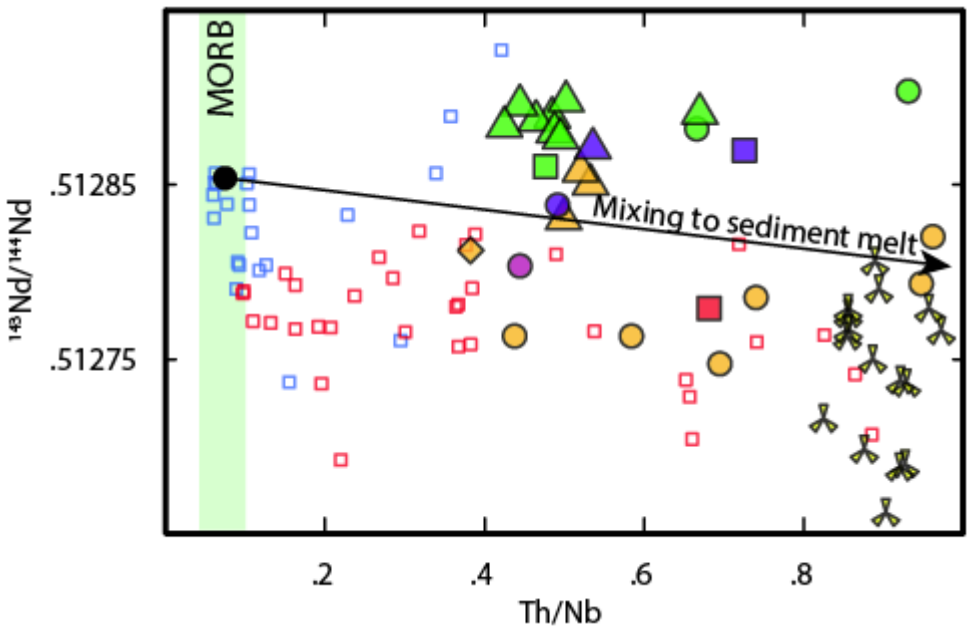

Figure 4.21: This plot of $^{143}Nd/^{144}Nd$ vs Th/Nb can be used to rule out the possibility that $^{143}Nd/^{144}Nd$ is primarily controlled by sediment addition to the mantle source. Sediment melts have lower $^{143}Nd/^{144}Nd$, but very high Th/Nb, and so any addition of sediments will drive the mantle composition almost straight to the right on this diagram, as shown by the black arrow. The regional variation in $^{143}Nd/^{144}Nd$ is present even at very low Th/Nb, and thus is likely the result of regional heterogeneity of the ambient mantle, rather than modification by the slab.

heterogeneity instead. As shown on Figure 4.21, only a small fraction of rear arc lavas have Th/Nb that overlap MORB, and so most rear arc lavas have compositions modified by the slab. The addition of sediments to the rear arc mantle source cannot account for variability of $^{143}Nd/^{144}Nd$, however, because the sediment sampled offshore of the Chilean trench has Th/Nd and Th/Nb ratios that are each about an order of magnitude higher than MORB, and so sediment mixing will lead to a large increase in Th/Nb across a narrow range of $^{143}Nd/^{144}Nd$ as shown by the mixing line on Figure 4.21. A large range of $^{143}Nd/^{144}Nd$ exists among rear arc values even at Th/Nb<0.2, and must be produced by a different mechanism. Furthermore, even at low Th/Nb, the rear arc samples from 36.5° S to 38° S have higher $^{143}Nd/^{144}Nd$ than rear arc samples from 34° S to 36.5° S, which is consistent with regional mantle heterogeneity. This same heterogeneity is preserved in the arc front, where it can be observed that the samples with green symbols have higher $^{143}Nd/^{144}Nd$ than the samples with yellow symbols from farther

north, even among the narrow range of 0.4<Th/Nb<0.5. Therefore, several observation from Figure 4.21 are consistent with regional heterogeneity of the ambient mantle wedge, but not with $^{143}Nd/^{144}Nd$ variations produced by sediment addition.

The $^{143}Nd/^{144}Nd$, $^{87}Sr/^{86}Sr$, and $^{176}Hf/^{177}Hf$ isotope diagrams provide additional evidence that these isotope systems have not been significantly affected by slab contributions in the rear arc. Rear arc lavas form tight linear arrays between AUM and GIB on the plots of $^{143}Nd/^{144}Nd$ vs $^{87}Sr/^{86}Sr$ and $^{176}Hf/^{177}Hf$ (Figures 4.8 and 4.9) and do not deviate significantly towards the sediment or AOC composition. The ratios Sr/Nd and Hf/Nd are similar in both enriched and depleted oceanic mantle sources, and so linear mixing between AUM and the GIB source compositions can account well for the back arc, precluding contributions from the slab. In contrast, most of the arc front lavas are offset at a fairly constant distance from the rear arc array towards the slab components, further suggesting that the arc front source receives a fairly constant addition of slab material.

The arc front variability in $^{143}Nd/^{144}Nd$ is most consistent with control by variable enrichment of the ambient mantle wedge, and therefore correlations among $^{143}Nd/^{144}Nd$, Th/U, and Zr/Nb (Figure 4.10) indicate that Th/U and Zr/Nb are also controlled by mantle heterogeneity. The conclusion that Th/U and Zr/Nb vary as a function of mantle enrichment is additionally supported by the fact that the AUM and GIB compositions, which serve as excellent mixing end members on the $^{143}Nd/^{144}Nd$, $^{87}Sr/^{86}Sr$, and $^{176}Hf/^{177}Hf$ diagrams, also serve as mixing end members on Figure 4.10. While back arc and arc front lavas overlap in $^{143}Nd/^{144}Nd$, $^{87}Sr/^{86}Sr$, and Th/U, the same is not true, however, for Zr/Nb. Mantle melts have Zr/Nb reflecting the composition of their source region unless the extent of melting (F) is less than ~0.04. At F<0.04, peridotite melts are typically silica undersaturated (e.g., Laporte et al., 2014). Arc front magmas are not silica undersaturated, and thus are generated by melting with F>4%, and so their Zr/Nb should be representative of their source composition. The rear arc and Gough lavas, however, have major element compositions characteristic of very low degree melting (alkali basalts), and so their Zr/Nb

ratios most likely do not represent their source compositions. An inversion of the GIB suite for its source composition (details in Appendix A4.2) indicates that Zr/Nb in the Gough source, for example, is approximately three times that of the Gough Basalts, as shown on Figure 4.8a. The good correlation between Zr/Nb and $^{143}Nd/^{144}Nd$ among arc front lavas indicates that mantle heterogeneity is likely influencing Zr/Nb within the arc front suite. This signal is not observed in the rear arc magmas, due to Zr/Nb fractionation during low F melting. The variations of Zr/Nb and Th/U, like $^{143}Nd/^{144}Nd$, $^{87}Sr/^{86}Sr$ and $^{176}Hf/^{177}Hf$, are thus all consistent with generation by the same mantle enrichment trends. Th/U of arc front lavas therefore most likely do not reflect variable fluid flux from the slab to the mantle in the SVZ, in contrast to the findings of Jacques et al. (2014).

Variability of $^{143}Nd/^{144}Nd$ vs $^{87}Sr/^{86}Sr$ and $^{176}Hf/^{177}Hf$ in both the rear arc and arc front of the SVZ appears to be primarily controlled by heterogeneity of the mantle source prior to the addition of slab components. As shown on Figures 4.8-4.9, the relationships observed within these isotope systems in the SVZ are the same as those observed globally, indicating that the mechanism which generates heterogeneity within the SVZ may also apply to volcanic arcs generally. This mantle heterogeneity appears to be consistent with mixing between a component similar to the Ambient Upper Mantle of the South Atlantic, and an enriched source that is similar to the source of basalts erupted at the Gough Islands. It also appears likely that this mantle source is not only isotopically heterogeneous, but also heterogeneous in trace element abundances and ratios, and may produce variations in Zr/Nb and Th/U along the arc front. A successful model of along strike variability in the SVZ should account for these observations.

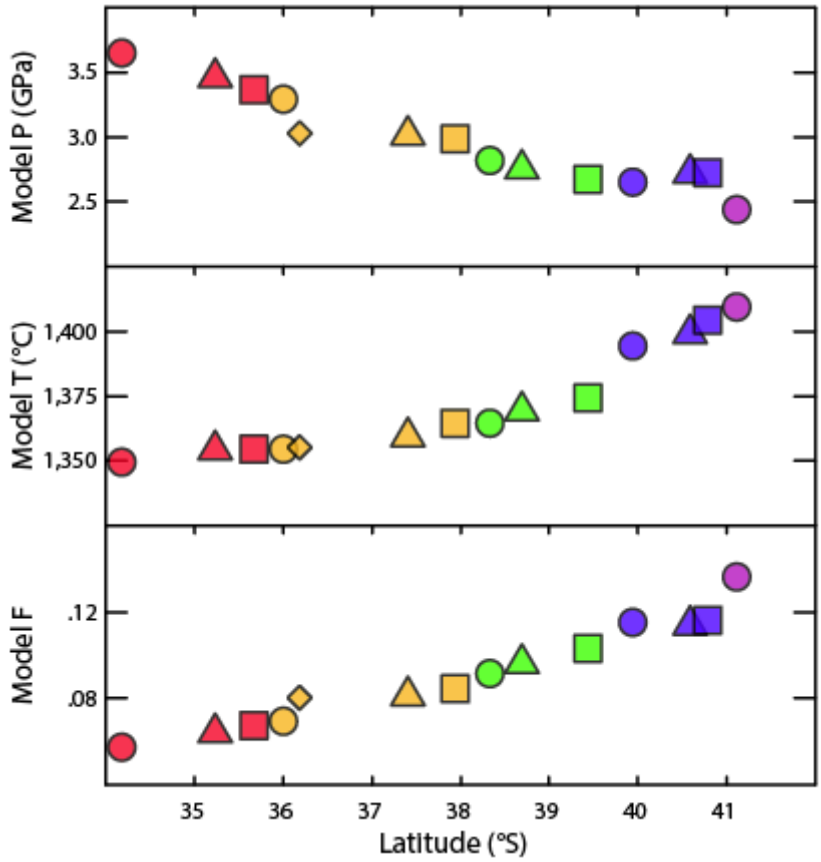

Figure 4.22: Input parameters used for modeling. The model P at each volcano is set halfway between the depth to slab beneath the arc front and the LAB behind the arc front, while the model T varies linearly with the slab dip angle. The resulting extents of melting are calculated using the parameterization of Katz et al. (2003) with a constant 0.6 % H_2O.

4.7 A general model for the SVZ

As was found in the preceding discussion, the chemistry of lavas erupted along the arc front of the SVZ appears to vary as a function of both mixing between depleted and EM1 like mantle sources, and the extent and pressure of melting as regulated by the lithospheric thickness and dip of the subducting slab. To test this hypothesis requires a quantitative model of SVZ chemical variation capable of taking both mantle heterogeneity and subduction parameters as inputs. To estimate the composition of the enriched mantle source, Gough Island basalts appear to provide a successful mixing end member

on the figures presented thus far. Another advantage of using the GIB is that they appear to have been generated by a range of extents of melting, which can be used to provide a well constrained estimate of the source composition. The details of the GIB source inversion can be found in Appendix A4.2.

Other model inputs include the temperature and pressure of the mantle wedge (Figure 4.22). For this input, it is assumed that all melting occurs half way between the pressure at the LAB estimated behind the arc front (Figure 4.19) and the top of the slab beneath the arc front (Figure 4.1). Another simplifying assumption is made for estimates of the mantle temperature, which in this model correspond linearly to the dip of the slab beneath the arc front (Figure 4.1) at a temperature interval of 1360 to 1410 °C. The extent of mantle melting was calculated using the parameterization of Katz et al. (2003) with a constant mantle H_2O content of 0.6%, following Chapter 3. The compositions of sediment and AOC melts were determined using the methods described by Chapter 3 for a slab at 875 °C, using the NMORB composition from Gale et al. (2013) for AOC and the average composition of sediments from ODP Hole 1232A. The required portion of sediment melt and AOC are fairly well constrained within this modeling framework, as both isotopic compositions and trace element abundances are sensitive to the proportions and total volume of slab contributions to the mantle wedge. The isotopic compositions of model components can be found in Appendix A4.3. A successful modeling result is obtained with the addition of 1.5% sediment melt and 7% AOC melt. This is a much higher volume of slab melt than found in the studies of Jacques et al., but is consistent with the range of slab additions required globally, as determined by Chapter 3. The lower contribution of slab melt to the mantle wedge found by the studies of Jacques et al. probably reflect their choice of an extremely low degree of melting (~1%) for the northern volcanoes, which in turn may have been required as a result of assuming a depleted MORB mantle source trace element composition along the entire arc (varied between E-DMM and D-DMM). The difference in the present modeling results from those of Jacques et al., in general likely reflect the

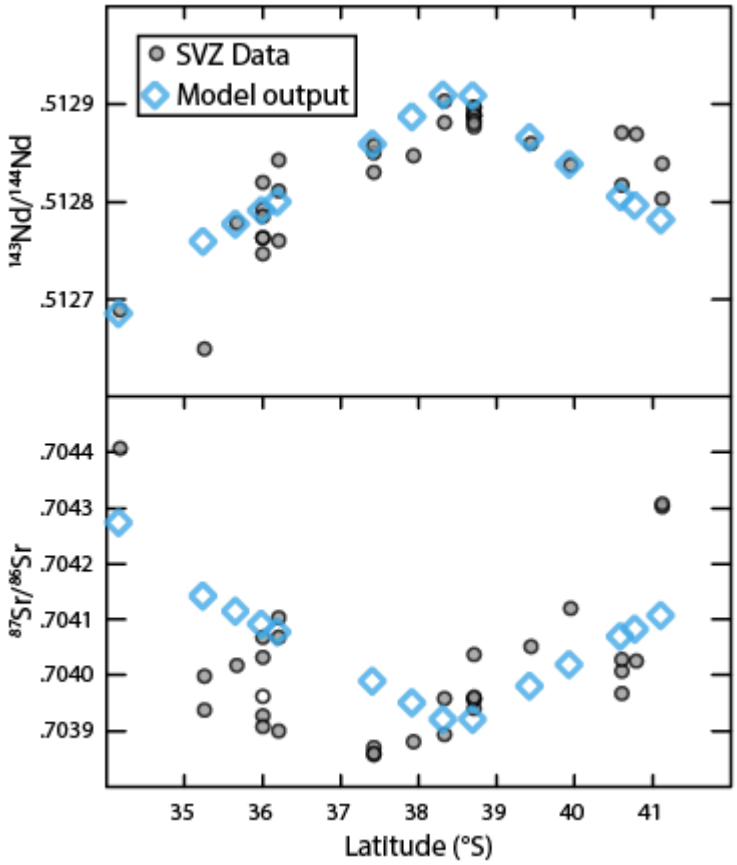

Figure 4.23: Comparison of model outputs and data for $^{143}Nd/^{144}Nd$ and $^{87}Sr/^{86}Sr$. The regional variation of $^{143}Nd/^{144}Nd$ is well reproduced, though $^{87}Sr/^{86}Sr$ is somewhat high between 35 °S and 36 °S, and fairly low at 41 °S. Open circle is enriched TTSP.

limitations of using a catch-all modeling framework such as the "Arc Basalt Simulator" of Kimura et al. (2009) in application to a complicated natural system.

The proportions of depleted and GIB mantle source used for the mantle composition were set based on $^{143}Nd/^{144}Nd$ variability of the back arc lavas with latitude, varying linearly from 56% GIB source at 35° S to 6% GIB Source at 38° S, and then back up to 48% by 41° S. There are no back arc samples that fall directly behind the arc from Don Casimiro to the north, and so for this volcano a 90% GIB source was used, which produced the best fit to the $^{143}Nd/^{144}Nd$ value at that volcano. The along strike variations of $^{143}Nd/^{144}Nd$ and $^{87}Sr/^{86}Sr$ that are produced by this model (after adding the slab components to the mixed mantle) are shown in comparison to the data on Figure 4.23. As can be seen on Figure 4.24, the

model reproduces the correlations between $^{143}Nd/^{144}Nd$ and both Th/U and Zr/Nb, in support of the hypothesis that these ratios may reflect variable mantle heterogeneity with a constant slab addition. Figure 4.25 shows that the model also accounts for the along strike variation of REE ratios and trace element abundances. The successful models show that along strike compositional variability within the SVZ is consistent with constant slab addition to the mantle wedge along strike, mantle heterogeneity that varies as a result of mixing between depleted and EM1 like mantle source, and extents of melting

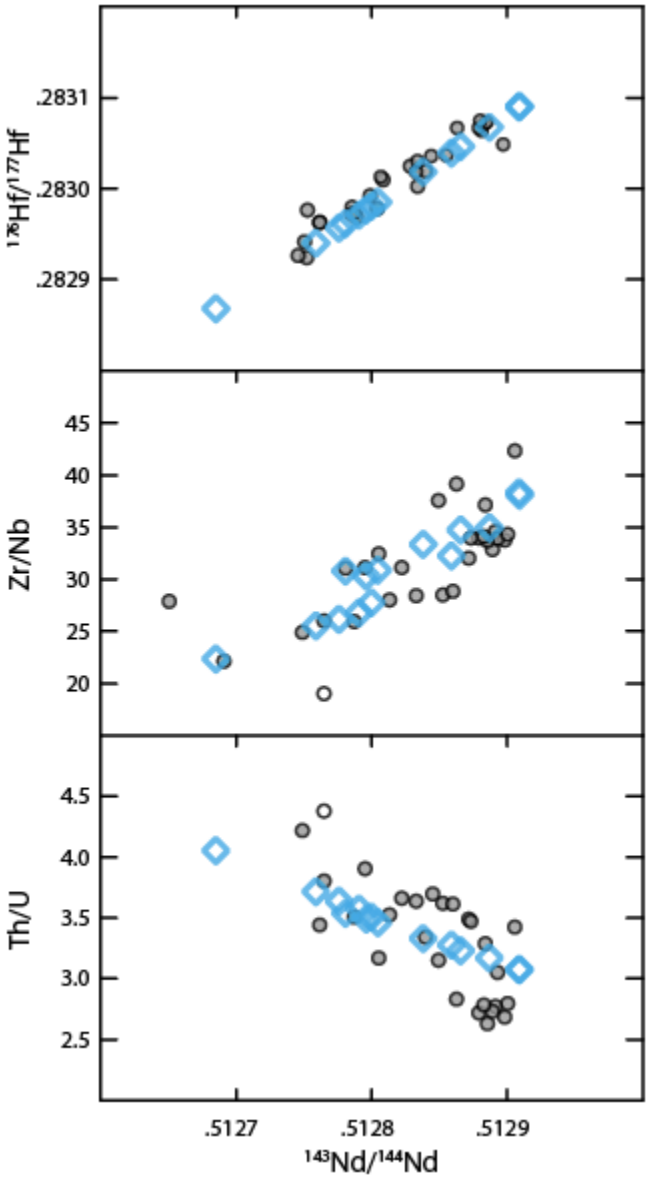

Figure 4.24: Comparison of model output to data on plots of $^{143}Nd/^{144}Nd$ vs $^{176}Hf/^{177}Hf$, Zr/Nb, and Th/U. Variations in mantle heterogeneity are able to reproduce these trends well.

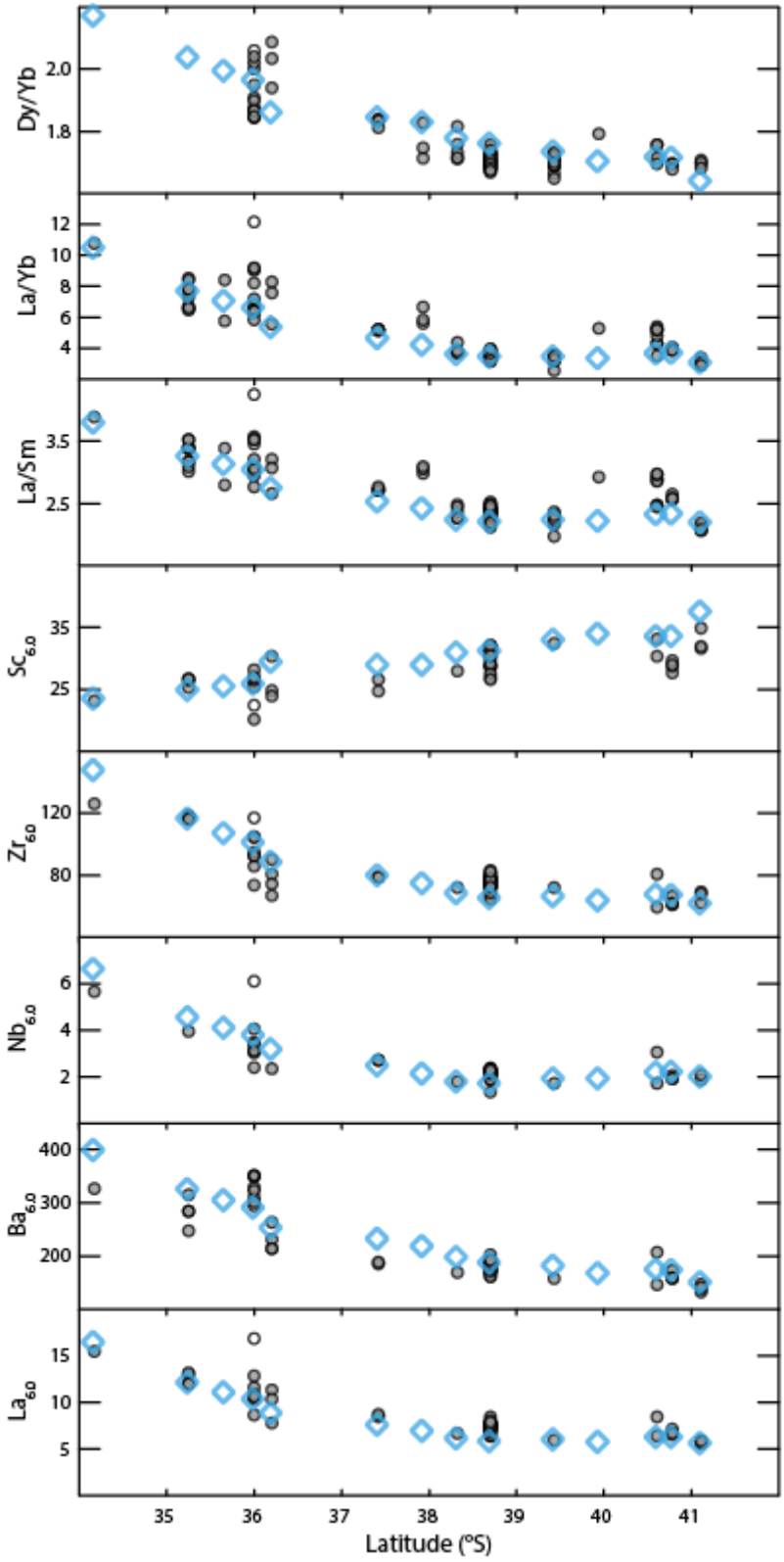

Figure 4.25: Model outputs and data on plots of trace element ratios and abundances vs latitude. The model of variable mantle heterogeneity and melting extents reproduces regional trends.

that are controlled by lithospheric thickness and the slab dip angle. Because correlations among crustal thickness and elemental abundances, as well as $^{143}Nd/^{144}Nd$, Zr/Nb, and Th/U in the SVZ follow the same trends as are observed globally, this model is also able to account for chemical variation among arc segments on a global scale.

Though the variations among the average volcano compositions are accounted for by the model, the variations within single volcanic centers are not reproduced. Variability among basaltic lavas found at individual volcanic centers suggests that the model parameters are not actually constant at a given latitude. In particular, many of the indices reflecting contributions from the slab vary within the volcanoes by a factor of 2 or more. TTSP, in particular, has erupted a range of magma compositions that indicate its mantle source is probably heterogeneous at a small scale. Figure 4.25 also shows that the range of Ba concentrations at TTSP extend above the range of compositions predicted by our model. On Figure 4.22, it is also apparent that the range of $^{87}Sr/^{86}Sr$ concentrations at TTSP is lower than model predictions at this latitude, despite matching well for $^{143}Nd/^{144}Nd$. This discrepancy may reflect additional fluid sourced from the serpentinized portion of the subducting slab, possibly arising from the Mocho Fracture Zone, as proposed by Sellés et al. (2004). On Figure 4.23, it is apparent that Osorno, the volcano on the southernmost end of the arc, has an elevated $^{87}Sr/^{86}Sr$ concentration that is not reproduced by the model, also despite closely for $^{143}Nd/^{144}Nd$. The most likely explanation for this is a slightly higher proportion of sediment contribution to the slab component added to the Osorno mantle source, possibly related to the extremely shallow depth of the slab and the relatively short distance between the trench and this volcano. This observation is also consistent with the offset between Osorno and the other volcanoes towards the sediment composition on Figure 4.6.

These details of variation applicable to individual volcanic centers demonstrate the complexity of continental arc magma petrogenesis and the diverse sources and processes that contribute to individual volcanoes. Within individual volcanoes therefore, source and process variations occur that are

unrelated to the regional variations across the SVZ based on volcano average compositions. The fairly simple model presented here accounts well for the regional variations, but should not be applied on an individual volcano scale where there are not the large scale variations in subduction parameters.

4.8 Conclusions

An extensive database of lava compositions from the Southern Volcanic Zone of Chile and the corresponding back arc in Argentina has been assembled from literature sources, re-analyses of existing samples, and analyses of numerous additional samples collected from stratovolcanoes along the arc front. The database has been used, following findings of various studies, to select samples which are the least likely to have been affected by crustal contamination, magma mixing, excess crystal accumulation, and crystal fractionation. Within this filtered dataset, there are coherent systematics among the compositions of SVZ volcanoes, and these systematics mimic those within the global arc database of Chapter 2. In both the global and SVZ arc front datasets, the following observations, hold:

(1) Nearly linear correlations exist among most major, minor, and trace elements. Na correlates positively with K, P, and incompatible trace elements from all element groups, such as “high field strength elements,” and “large ion lithophile elements,” but negatively with the moderately compatible elements Mn, Ca, and Sc.

(2) Ratios of lighter to heavier rare earth elements correlate with incompatible abundances. This includes Dy/Yb, indicating a role for garnet.

(3) The incompatible elements correlate positively with crustal thickness, and the moderately compatible elements correlate negatively.

(4) $^{143}Nd/^{144}Nd$ correlates negatively with $^{87}Sr/^{86}Sr$, and Th/U, and positively with $^{176}Hf/^{177}Hf$ and Zr/Nb. On all of these plots, the data span compositions from depleted mantle to EM1-OIBs.

Along strike of the SVZ from south to north, crustal thickness and slab depth increase, while the dip of the slab beneath the arc decreases. In agreement with previous studies, incompatible element abundances increase from south to north along strike of the arc. $^{143}Nd/^{144}Nd$, and the chemical parameters listed in (4), do not increase regularly from south to north, but do vary systematically along the arc, with an inflection near 38° S. Additionally, within the SVZ, the results of this study indicate that trace element ratios typically indicative of contributions from the subducting slab to the arc front mantle source do not vary systematically along strike, and these ratios overlap for most volcanoes, in contrast to the findings of Jacques et al. (2014).

Chapter 2 found that on a global scale, these systematics are inconsistent with varying contamination from continental crust, due to the improbable composition of the required contaminant. The similarity of global systematics and those within the SVZ lead to the same conclusion, in contradiction to the MASH model of Hildreth and Moorbath (1988). The hypothesis that along strike systematics are produced by varying slab temperature is also inconsistent with thermal models of the SVZ, as well as the lack of variability of elemental ratios that should be affected by variable slab contributions.

The systematic along strike variability of the chemical parameters described in (1) to (3) are consistent with a physical model of decreasing extents of melting from south to north as a result of increasing sub-arc pressures, and decreasing sub-arc temperatures that are expected from variations in crustal thickness and slab dip. The chemical parameters described in (4) are most consistent with a heterogeneous mantle source along strike of the arc. This model of mantle heterogeneity is supported by linear correlations of back arc lavas on plots of $^{143}Nd/^{144}Nd$ vs $^{87}Sr/^{86}Sr$ and $^{143}Nd/^{144}Nd$ vs $^{176}Hf/^{177}Hf$ that extend between AUM compositions and EM1 type OIBs from the Gough Islands. These variations cannot be produced by slab addition, based on lack of variations of $^{143}Nd/^{144}Nd$ with Th/Nb. The offset of arc front and rear arc lavas on these plots are consistent with a fairly constant slab addition to the

mantle wedge, both globally and within the SVZ. The global modeling of framework of Chapter 3 is able to quantitatively account for the regional variations of the SVZ by assuming a constant slab addition coupled with varying extents/pressure of melting and varying mantle heterogeneity. Mantle heterogeneity is reproduced by mixing between depleted mantle and a mantle source inverted from the Gough Island basalt suite of Willbold and Stracke (2006). This model is successfully generates the systematic along strike variations in the SVZ.

Because variability within the SVZ is remarkably similar to the global chemical variability, the SVZ serves as a microcosm of global arcs. Chapter 3 found that global chemical variability corresponds to both the thickness of the overlying arc crust, as well as the slab thermal parameter, and that the variability might be produced by either changing slab flux to the mantle wedge, or changing extents of melting. In the SVZ, the slab thermal structure model is inconsistent with physical observations, while the wedge thermal structure model remains successful. Based on the similarity of the two systems, the SVZ provides evidence conflicting with the slab model not just within the SVZ, but also on a global scale. Finally, because the effects of mantle heterogeneity are well constrained within the SVZ, and once again similar to those found globally, a model of varying mantle enrichment due to mantle mixing between a depleted and an EM1-like mantle source may successfully account for the effects of mantle heterogeneity in global arcs, contributing to global variations in $^{143}Nd/^{144}Nd$, $^{87}Sr/^{86}Sr$, Th/U, and Zr/Nb among arc magmas.

4.9 References

Andres, M., Blichert-Toft, J., Schilling, J.G., 2002. Hafnium isotopes in basalts from the southern Mid-Atlantic Ridge from 40 S to 55 S: Discovery and Shona plume–ridge interactions and the role of recycled sediments. Geochemistry, Geophysics, Geosystems 3, 1-25.

Douglass, J., Schilling, J.G., Fontignie, D., 1999. Plume-ridge interactions of the Discovery and Shona mantle plumes with the southern Mid-Atlantic Ridge (40°-55° S). Journal of Geophysical Research: Solid Earth (1978–2012) 104, 2941-2962.

Dungan, M.A., Wulff, A., Thompson, R., 2001. Eruptive stratigraphy of the Tatara–San Pedro complex, 36 S, Southern Volcanic Zone, Chilean Andes: reconstruction method and implications for magma evolution at long-lived arc volcanic centers. Journal of Petrology 42, 555-626.

Dyhr, C.T., Holm, P.M., Llambias, E.J., Scherstén, A., 2013. Subduction controls on Miocene back-arc lavas from Sierra de Huantraico and La Matancilla and new 40 Ar/39 Ar dating from the Mendoza Region, Argentina. Lithos 179, 67-83.

Dzierma, Y., Rabbel, W., Thorwart, M., Koulakov, I., Wehrmann, H., Hoernle, K., Comte, D., 2012. Seismic velocity structure of the slab and continental plate in the region of the 1960 Valdivia (Chile) slip maximum—insights into fluid release and plate coupling. Earth and Planetary Science Letters 331, 164-176.

England, P.C., Katz, R.F., 2010. Melting above the anhydrous solidus controls the location of volcanic arcs. Nature 467, 700-703.

Gale, A., Dalton, C.A., Langmuir, C.H., Su, Y., Schilling, J.G., 2013a. The mean composition of ocean ridge basalts. Geochemistry, Geophysics, Geosystems 14, 489-518.

Gale, A., Laubier, M., Escrig, S., Langmuir, C.H., 2013b. Constraints on melting processes and plume-ridge interaction from comprehensive study of the FAMOUS and North Famous segments, Mid-Atlantic Ridge. Earth and Planetary Science Letters 365, 209-220.

Gast, P.W., Tilton, G., Hedge, C., 1964. Isotopic composition of lead and strontium from Ascension and Gough Islands. Science 145, 1181-1185.

Gerlach, D.C., Frey, F.A., Moreno-Roa, H., Lopez-Escobar, L., 1988. Recent Volcanism in the Puyehue—Cordon Caulle Region, Southern Andes, Chile (40• 5° S): Petrogenesis of Evolved Lavas. Journal of Petrology 29, 333-382.

Hermann, J., Rubatto, D., 2009. Accessory phase control on the trace element signature of sediment melts in subduction zones. Chemical Geology 265, 512-526.

Hildreth, W., Moorbath, S., 1988. Crustal contributions to arc magmatism in the Andes of central Chile. Contributions to Mineralogy and Petrology 98, 455-489.

Hinkley, T.K., Le Cloarec, M.-F., Lambert, G., 1994. Fractionation of families of major, minor, and trace metals across the melt-vapor interface in volcanic exhalations. Geochimica et cosmochimica acta 58, 3255-3263.

J, J., 2013. Geochemistry of the Tatara-San Pedro continental arc volcanic complex and implications for magmatism in the Chilean Southern Volcanic Zone. PhD Thesis, Columbia University.

Jacques, G., Hoernle, K., Gill, J., Hauff, F., Wehrmann, H., Garbe-Schönberg, D., van den Bogaard, P., Bindeman, I., Lara, L., 2013. Across-arc geochemical variations in the Southern Volcanic Zone, Chile (34.5–38.0 S): constraints on mantle wedge and slab input compositions. Geochimica et Cosmochimica Acta 123, 218-243.

Jacques, G., Hoernle, K., Gill, J., Wehrmann, H., Bindeman, I., Lara, L.E., 2014. Geochemical variations in the Central Southern Volcanic Zone, Chile (38–43 S): The role of fluids in generating arc magmas. Chemical Geology 371, 27-45.

Jicha, B.R., Singer, B.S., Beard, B.L., Johnson, C.M., Moreno-Roa, H., Naranjo, J.A., 2007. Rapid magma ascent and generation of 230 Th excesses in the lower crust at Puyehue–Cordón Caulle, Southern Volcanic Zone, Chile. Earth and Planetary Science Letters 255, 229-242.

Karlstrom, L., Lee, C.T., Manga, M., 2014. The role of magmatically driven lithospheric thickening on arc front migration. Geochemistry, Geophysics, Geosystems.

Katz, R.F., Spiegelman, M., Langmuir, C.H., 2003. A new parameterization of hydrous mantle melting. Geochemistry, Geophysics, Geosystems 4.

Kay, S.M., Ardolino, A., Gorring, M., Ramos, V., 2007. The Somuncura Large Igneous Province in Patagonia: interaction of a transient mantle thermal anomaly with a subducting slab. Journal of Petrology 48, 43-77.

Kay, S.M., Jones, H.A., Kay, R.W., 2013. Origin of Tertiary to Recent EM-and subduction-like chemical and isotopic signatures in Auca Mahuida region (37–38 S) and other Patagonian plateau lavas. Contributions to Mineralogy and Petrology 166, 165-192.

Kimura, J.I., Hacker, B.R., van Keken, P.E., Kawabata, H., Yoshida, T., Stern, R.J., 2009. Arc Basalt Simulator version 2, a simulation for slab dehydration and fluid-fluxed mantle melting for arc basalts: Modeling scheme and application. Geochemistry, Geophysics, Geosystems 10.

Laporte, D., Lambart, S., Schiano, P., Ottolini, L., 2014. Experimental derivation of nepheline syenite and phonolite liquids by partial melting of upper mantle peridotites. Earth and Planetary Science Letters 404, 319-331.

Le Roex, A.P., 1985. Geochemistry, mineralogy and magmatic evolution of the basaltic and trachytic lavas from Gough Island, South Atlantic. Journal of Petrology 26, 149-186.

Lopez-Escobar, L., Frey, F., Vergara, M., 1977. Andesites and high-alumina basalts from the central-south Chile High Andes: geochemical evidence bearing on their petrogenesis. Contributions to Mineralogy and Petrology 63, 199-228.

Plank, T., Langmuir, C.H., 1988. An evaluation of the global variations in the major element chemistry of arc basalts. Earth and Planetary Science Letters 90, 349-370.

Reubi, O., Bourdon, B., Dungan, M., Koornneef, J., Selles, D., Langmuir, C., Aciego, S., 2011. Assimilation of the plutonic roots of the Andean arc controls variations in U-series disequilibria at Volcan Llaima, Chile. Earth and Planetary Science Letters 303, 37-47.

Salters, V.J., Mallick, S., Hart, S.R., Langmuir, C.E., Stracke, A., 2011. Domains of depleted mantle: New evidence from hafnium and neodymium isotopes. Geochemistry, Geophysics, Geosystems 12.

Selles, D., Rodriguez, AC, Dungan, MA, Naranjo, JA, Gardeweg, M, 2004. Geochemistry of Nevado de Longavi Volcano (36.2 degrees S): a compositionally atypical arc volcano in the Southern Volcanic Zone of the Andes. REVISTA GEOLOGICA DE CHILE 31, 293-315.

Syracuse, E.M., van Keken, P.E., Abers, G.A., 2010. The global range of subduction zone thermal models. Physics of the Earth and Planetary Interiors 183, 73-90.

Tagiri, M., Moreno, H., López-Escobar, L., Notsu, K., 1993. Two magma types of the high-alumina basalt series of Osorno Volcano, Southern Andes (41° 06'S)-Plagioclase dilution effect. Ganko 88, 359-371.

Tassara, A., Echaurren, A., 2012. Anatomy of the Andean subduction zone: three-dimensional density model upgraded and compared against global-scale models. Geophysical Journal International 189, 161-168.

Tormey, D.R., Frey, F.A., Lopez-Escobar, L., 1995. Geochemistry of the Active Azufre—Planchon—Peteroa Volcanic Complex, Chile (35° 15′ S): Evidence for Multiple Sources and Processes in a Cordilleran Arc Magmatic System. Journal of Petrology 36, 265-298.

Tormey, D.R., Hickey-Vargas, R., Frey, F.A., López-Escobar, L., 1991. Recent lavas from the Andean volcanic front (33 to 42 S); interpretations of along-arc compositional variations. Geological Society of America Special Papers 265, 57-78.

Turner, S.J., Izbekov, P., Langmuir, C., 2013. The magma plumbing system of Bezymianny Volcano: Insights from a 54year time series of trace element whole-rock geochemistry and amphibole compositions. Journal of Volcanology and Geothermal Research 263, 108-121.

Varekamp, J., Hesse, A., Mandeville, C., 2010. Back-arc basalts from the Loncopue graben (Province of Neuquen, Argentina). Journal of Volcanology and Geothermal Research 197, 313-328.

Wehrmann, H., Hoernle, K., Garbe-Schönberg, D., Jacques, G., Mahlke, J., Schumann, K., 2014. Insights from trace element geochemistry as to the roles of subduction zone geometry and subduction input on the chemistry of arc magmas. International Journal of Earth Sciences 103, 1929-1944.

Weill, D.F., Drake, M.J., 1973. Europium anomaly in plagioclase feldspar: experimental results and semiquantitative model. Science 180, 1059-1060.

Willbold, M., Stracke, A., 2006. Trace element composition of mantle end-members: Implications for recycling of oceanic and upper and lower continental crust. Geochemistry, Geophysics, Geosystems 7.

Willbold, M., Stracke, A., 2010. Formation of enriched mantle components by recycling of upper and lower continental crust. Chemical Geology 276, 188-197.

Wilson, C.R., Spiegelman, M., van Keken, P.E., Hacker, B.R., 2014. Fluid flow in subduction zones: The role of solid rheology and compaction pressure. Earth and Planetary Science Letters 401, 261-274.

Appendices

Appendix A1.1: Analytical conditions

Sample Preparation

Rock samples were crushed to 5-10-mm size chips with a geological hammer. After visual inspection, chips with no signs of contamination were handpicked for further particle size reduction. Small samples were crushed manually in an agate mortar under alcohol. Samples exceeding 25 cm^3 in volume were crushed for 10 minutes using a SPEX 8500 shatter box with an alumina ceramic grinding container. Sample powders were dried for 24-48 hours in oven at 65-70 C.

Whole Rock XRF Analysis

For XRF analysis, the samples were prepared as 40-mm-diameter fused disks using automated Claisse M4 fluxer. First, 1.5 g of sample powder was mixed with 1.0 g of LiNO3 (oxidizer) and 1.5 g of 50/50 ultra-pure flux (50% lithium tetraborate and 50% lithium metaborate), after which the sample was loaded at the bottom of a Pt crucible. Following this, 7.0 g of the same ultra-pure flux was loaded on top of the mixture. The duration of fusing was 20 minutes. Sample, mold, and crucible were weighed together before and after fusing to account for any weight loss or gain. Blanks with pure flux were run between samples to clean the crucible and mold. The manufactured glass disks were visually inspected for homogeneity.

X-ray fluorescence analysis was performed using PanAlytical Axios four kilowatt wavelength dispersive spectrometer at the Advanced Instrumentation Laboratory at UAF. The instrument was calibrated at the beginning of the analytical session using AGV-1 BHVO-1, BIR-1, JB-2, JGb-1, JP-1, and JR-1 standard reference materials prepared as glass disks following the same technique as described. Based on duplicate analyses of working standards, the typical analytical uncertainty in rel. % was better than 0.1 for SiO_2, CaO, TiO_2, and Fe_2O_3; better than 0.2 for Al_2O_3, K_2O, and MgO; better than 0.5 for MnO and Na_2O; and better than 0.6 for P_2O_5. The analytical uncertainty for minor and trace elements in rel. % was better than 1.5 for Sr and Zr, better than 3 for Cr, Zn, and Cu; better than 4 for Y and Ni; better than 5 for V; better than 8 for Rb, and better than 16 for Ba.

Whole Rock ICP-MS Analysis

The powders prepared at the University of Alaska Fairbanks were analyzed for trace elements by solution nebulized-inductively coupled-mass spectrometry (SN-ICP-MS) at Harvard University. 100 mg of powder was first digested in an HF:HNO_3 mixture. The solution was then evaporated to dryness and dissolved in 8N HNO_3 two separate times. Samples were diluted (1:5K) using a matrix solution of 0.2N HNO_3, with Ge (10 ppb), In (3 ppb), Tm (3 ppb), Rh (3ppb), and Bi (3 ppb) as internal standards. Measurements were obtained on a Thermo X series quadrupole mass spectrometer. Standard powders BHVO-2, DNC-1, JB-2, W-2, and BCR-2 were used to generate calibration curves. Based on repeat analysis, the precision for trace elements measured is under 3% RSD (2σ) for all elements, with the exception of Nb, Ta, Cr, Rb, and Ga which are within 4% RSD (2σ), Be, which is within 6% RSD (2σ), and Ni and Cu, which are within 5% RSD (2σ), but degrade as concentrations approach detection limits at about 5 ppm.

Electron Probe Microanalysis of Amphiboles

For electron probe microanalysis (EPMA), all samples were prepared as standard petrographic thin sections, polished, and carbon-coated to a thickness of ca. 250 Å. Amphiboles were analyzed for major elements at the University of Alaska Fairbanks using a Cameca SX-50 electron microprobe, which is equipped with four wavelength-dispersive and one energy-dispersive spectrometers. The electron probe is fully automated with Probe for Windows software (Donovan et al., 2007). The 15 keV, 10 nA, 1-3- µm-diameter focused electron beam was used for all analyses. Major oxides are reported in wt.% with Fe_2O_3 calculated using Probe Amph v.3 (Tindle and Webb, 1994) following stechiometric considerations of Rock and Leake (1984). Details about counting times, standards, and typical analytical errors calculated after Scott et al. (1995) are summarized below.

Table A1.1 Analytical conditions for EPMA analyses of amphiboles

Element /Line	Crystal	Counting time, seconds		Standard	Analytical Error (rel%)
		On peak	Off peak		
Si ka	TAP	25	20	Tiburon albite	0.4
Al ka	TAP	25	20	Orthoclase (CM Taylor)	0.7
Ca ka	PET	10	10	Fluorite (CM Taylor)	1.4
Mg ka	TAP	10	10	Spinel (CM Taylor)	1.4
Fe ka	LIF	15	15	Hornblende (HB1), USNM 111356	2.4
K ka	PET	15	14	Orthoclase (CM Taylor)	2.6
Na ka	TAP	10	10	Tiburone albite	4.0
Ti ka	LIF	10	10	Sphene (CM Taylor)	6.8
Mn ka	LIF	10	10	Willimite (CM Taylor)	>25
Cl ka	PET	15	10	Scapolite, USNM R6600-1	>25
F ka	TAP	10	10	Fluorite (CM Taylor)	>25

References

Donovan, J.J., Kremser, D., and Fournelle, J.H. (2007) Probe for Windows User's Guide and Reference, Enterprise Edition. Probe Software, Inc, Eugene, OR, p 355.

Rock, N.M.S. and Leake, B.E. (1984) The International Mineralogical Association amphibole nomenclature scheme: computerization and its consequences. Mineralogical Magazine 48 (347), 211–227.

Scott, V.D., Love, G., and Reed, S.J.B. (1995) Quantitative Electron-Probe Analysis. Ellis Horwood Limited, Hemel Hempstead, Hertfordshire, England, 311 pp.

Tindle, A. G. and Webb, P. C. (1994). Probe-AMPH: A spreadsheet program to classify microprobe-derived amphibole analyses. Computers and Geosciences 20, 1201-1228.

Appendix A1.2: Model details

Table A1.2: Mineral compositions consistent with fractionation model and liquid compositions

Liquid compositions based on amphiboles from sample B-65

	SiO_2	TiO_2	Al_2O_3	FeOT	MgO	CaO	K_2O
low-p	70.85954	0.356258	15.74094	2.506853	0.695344	2.928836	2.458184
high-p(1)	62.51206	0.517741	18.28671	5.359587	1.504054	5.022167	1.408216
high-p(2)	61.24082	0.58493	18.5439	5.707873	1.822966	5.241821	1.297872

Phenocryst and liquid proportions combined to produce end members

	%liq	%p1	%p2	%amph	%cpx	%opx	%mt	%il
low-p	54.2	0.0	29.3	7.1	5.0	1.6	2.8	0.0
high-p(1)	76.4	6.0	0.0	12.5	5.2	0.0	0.2	0.0
high-p(2)	80.8	4.7	0.0	7.4	7.0	0.3	0.3	0.0

Error (%RSD) between mixing end members members and sum of phenocrysts+liquids

%RSD	SiO_2	TiO_2	Al_2O_3	FeOT	MgO	CaO	K_2O
EM-A	0.0	9.3	0.3	0.0	0.8	0.4	5.0
EM-B	0.0	6.1	0.0	0.0	0.1	0.0	4.5
EM-B	0.0	6.2	0.0	0.0	0.1	0.1	7.5

Appendix A2.1: Non GEOROC data sources

Three data sources were added to this dataset that were not included in GEOROC at the time data was compiled:

Central and South Central Chile:

-Jacques G, Hoernle K, Gill J, Hauff F, Wehrmann H, GarbeSchonberg D, van den Bogaard P, Bindeman I, Lara LE (2013). Across-arc geochemical variations in the Southern Volcanic Zone, Chile (34.5–38.0 S): constraints on mantle wedge and input compositions. Geochim Cosmochim Acta.

Alaska:

-Steiner, A. K., Browne, B. L. & Nye, C. J. (2012). Quenched mafic inclusions in <2200 years B.P. deposits at Augustine Volcano, Alaska. International Geology Review 54(11) 1241-1270.

Appendix A2.2: Data sources for estimates of crustal thickness

Aegean

Mitropolous, P., Tarney, J., Saunders, A. D., & Marsh, N. G. (1987). Petrogenesis of Cenezoic volcanic rocks from the Aegean island arc. *Journal of volcanology and geothermal research*, *32*(1), 177-193.

Alaska/Aleutians

Van Avendonk, H. J., Shillington, D. J., Holbrook, W. S., & Hornbach, M. J. (2004). Inferring crustal structure in the Aleutian island arc from a sparse wide-angle seismic data set. *Geochemistry, Geophysics, Geosystems*, *5*(8).

Cascades

Eagar, K. C., Fouch, M. J., James, D. E., & Carlson, R. W. (2011). Crustal structure beneath the High Lava Plains of eastern Oregon and surrounding regions from receiver function analysis. *Journal of Geophysical Research: Solid Earth (1978–2012)*, *116*(B2).

Chile

Tassara, A., Götze, H. J., Schmidt, S., & Hackney, R. (2006). Three-dimensional density model of the Nazca plate and the Andean continental margin. *Journal of Geophysical Research: Solid Earth (1978–2012)*, *111*(B9).

Colombia/Ecuador

E. Poveda, G. Monsalve, C. A. Vargas-Jimenez, Receiver function study of the crustal structure beneath the Northern Andes (Colombia). Presented at 2012 Fall Meeting, AGU, San Francisco, Calif.

Costa Rica/Nicaragua

MacKenzie, L., Abers, G. A., Fischer, K. M., Syracuse, E. M., Protti, J. M., Gonzalez, V., & Strauch, W. (2008). Crustal structure along the southern Central American volcanic front. *Geochemistry, Geophysics, Geosystems*, *9*(8).

El Salvador

Carr, M. J., Feigenson, M. D., & Bennett, E. A. (1990). Incompatible element and isotopic evidence for tectonic control of source mixing and melt extraction along the Central American arc. *Contributions to Mineralogy and Petrology*,*105*(4), 369-380.

Guatemala

Ligorría, J. P., & Molina, E. (1997). Crustal velocity structure of southern Guatemala using refracted and Sp converted waves. *GEOFISICA INTERNACIONAL-MEXICO-*, *36*, 9-20.

Honshu

Hasemi, A., & Horiuchi, S. (2010). Seismic reflector alignment along the volcanic front in northeastern Honshu, Japan. *Journal of Geophysical Research: Solid Earth (1978–2012)*, *115*(B7).

Izu

Takahashi, N., Suyehiro, K., & Shinohara, M. (1998). Implications from the seismic crustal structure of the northern Izu–Bonin arc. *Island arc*, *7*(3), 383-394.

Java/Bali

Luehr, B. G., Koulakov, I., Rabbel, W., Zschau, J., Ratdomopurbo, A., Brotopuspito, K. S., ... & Sahara, D. P. (2013). Fluid ascent and magma storage beneath Gunung Merapi revealed by multi-scale seismic imaging.*Journal of Volcanology and Geothermal Research*, *261*, 7-19.

Kamchatka

Levin, V., Park, J., Brandon, M., Lees, J., Peyton, V., Gordeev, E., & Ozerov, A. (2002). Crust and upper mantle of Kamchatka from teleseismic receiver functions. *Tectonophysics*, *358*(1), 233-265.

Kuriles

Levin, V., Park, J., Brandon, M., Lees, J., Peyton, V., Gordeev, E., & Ozerov, A. (2002). Crust and upper mantle of Kamchatka from teleseismic receiver functions. *Tectonophysics*, *358*(1), 233-265.

Bagatikov, O. A. (Ed.). (2000). *Magmatism and Geodynamics: Terrestrail Magmatism Throughout the Earth's History*. CRC Press. P. 37

Nakanishi, A., Kurashimo, E., Tatsumi, Y., Yamaguchi, H., Miura, S., Kodaira, S., ... & Hirata, N. (2009). Crustal evolution of the southwestern Kuril Arc, Hokkaido Japan, deduced from seismic velocity and geochemical structure.*Tectonophysics*, *472*(1), 105-123.

Lesser Antilles

Christeson, G. L., Mann, P., Escalona, A., & Aitken, T. J. (2008). Crustal structure of the Caribbean–northeastern South America arc-continent collision zone. *Journal of Geophysical Research: Solid Earth (1978–2012)*, *113*(B8).

Marianas

Calvert, A. J., Klemperer, S. L., Takahashi, N., & Kerr, B. C. (2008). Three-dimensional crustal structure of the Mariana island arc from seismic tomography. *Journal of Geophysical Research: Solid Earth (1978–2012)*,*113*(B1).

Mexico

Iglesias, A., Clayton, R. W., Pérez-Campos, X., Singh, S. K., Pacheco, J. F., García, D., & Valdés-González, C. (2010). S wave velocity structure below central Mexico using high-resolution surface wave tomography. *Journal of Geophysical Research: Solid Earth (1978–2012)*, *115*(B6).

Pérez-Campos, X., Kim, Y., Husker, A., Davis, P. M., Clayton, R. W., Iglesias, A., ... & Gurnis, M. (2008). Horizontal subduction and truncation of the Cocos Plate beneath central Mexico. *Geophysical Research Letters*, *35*(18).

New Britain

Estimated from: Reguzzoni, M., & Sampietro, D. (2014). GEMMA: An Earth crustal model based on GOCE satellite data. *International Journal of Applied Earth Observation and Geoinformation*.

Ryukyu

Nakamura, M., & Umedu, N. (2009). Crustal thickness beneath the Ryukyu arc from travel-time inversion. *Earth Planets Space*, *61*(10), 1191-1195.

South Sandwich

Larter, R. D., Vanneste, L. E., Morris, P., & Smythe, D. K. (2003). Structure and tectonic evolution of the South Sandwich arc. *Geological Society, London, Special Publications*, *219*(1), 255-284.

Tonga

Contreras-Reyes, E., Grevemeyer, I., Watts, A. B., Flueh, E. R., Peirce, C., Moeller, S., & Papenberg, C. (2011). Deep seismic structure of the Tonga subduction zone: Implications for mantle hydration, tectonic erosion, and arc magmatism. *Journal of Geophysical Research: Solid Earth (1978–2012)*,*116*(B10).

Appendix A2.3 Are compositional differences between thick and thin arcs produced by a buoyancy filter?

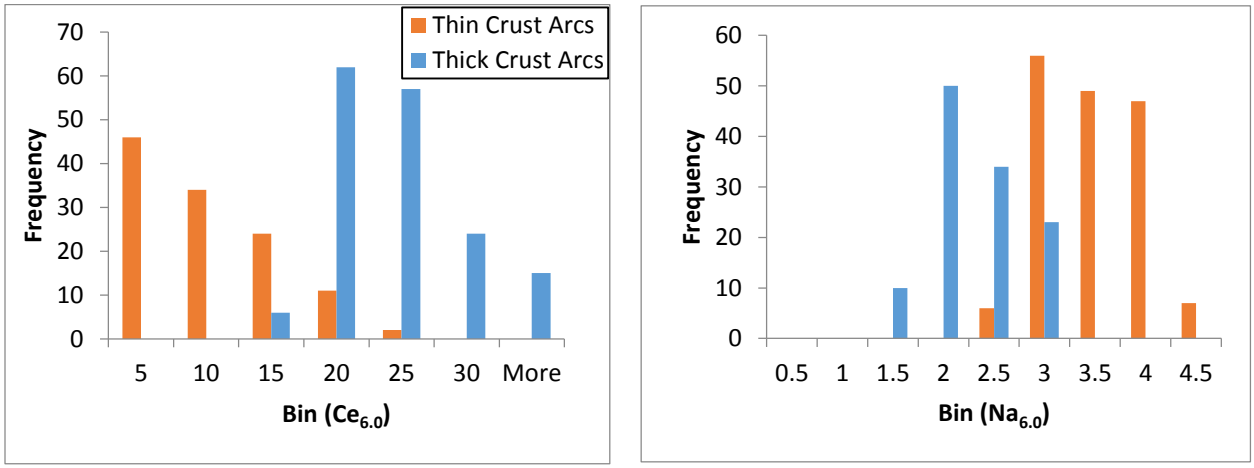

Figure A2.1. Histograms of $Ce_{6.0}$ and $Na_{6.0}$ for arcs with thick crust (47 km>CT>37 km) and thin crust (CT<27 km) demonstrating that the majority of 6-value samples from these regions do not overlap at all.

It is possible that all arcs generate the same range of primary magmas, and that the compositional differences between magmas erupted through thick crust and magmas erupted through thin crust exist because thick overlying crust prevents certain magmas from rising to the surface. Sisson et al. (1996), for example, suggest that only particularly buoyant mafic magmas are transported to upper crustal levels in the Sierra Nevada Batholith. That study proposes that mafic Sierran intrusions owe their low density to high H_2O contents. If the primary H_2O contents of arc magmas are related to the compositional differences noted in section 2.3, it may be the case that a crustal buoyancy filter is largely responsible for the correlations between magma chemistry and crustal thickness.

While some type of buoyancy filter may be responsible for limiting the compositions of mafic intrusions in the Sierra Nevada Batholith, this process does not appear to be responsible for the compositional differences between thick and thin crusted arc front stratovolcano lavas worldwide. If the range of magmas erupted at thick crusted arcs is primarily the result of filtration, thick crusted arc magma compositions should be a subset of thin crusted arc magma compositions, but this is not the case. The enriched magmas erupted at thick crusted arcs are more enriched than *any* magmas erupted through thin crust. As can be seen in Figure A2.1, 59% of all lavas erupted through thick crust (arc with crustal thickness between 37 and 47 km) have $Ce_{6.0}$>20 ppm. Within the thin crusted (arcs with crustal thickness less than 27 km) group, only two unusual lavas from Nicaragua have $Ce_{6.0}$ between 20 and 25 ppm, and no sampled lavas have $Ce_{6.0}$ above 25 ppm. The contrast is even starker for Na. Approximately 63% of 6-value samples from thick crusted arcs have $Na_{6.0}$ contents greater than 3 wt. %, while 33% have $Na_{6.0}$ contents greater than 3.5 wt. %. In thin crusted arcs, not a single sample has $Na_{6.0}$ greater than 3 wt. %. The compositional differences between thick crusted and thin crusted arcs cannot be due to a crustal buoyancy filter, because a significant proportion of magmas erupted through thick crust have compositions that are completely absent in thin crusted settings. If compositional differences between thin crusted and thick crusted arcs are the result of some filtration process, a complementary filtration process must also be removing enriched samples from thin crusted arcs, but such a mechanism is implausible.

Appendix A2.4 Additional plots of Na_2O vs Mg#

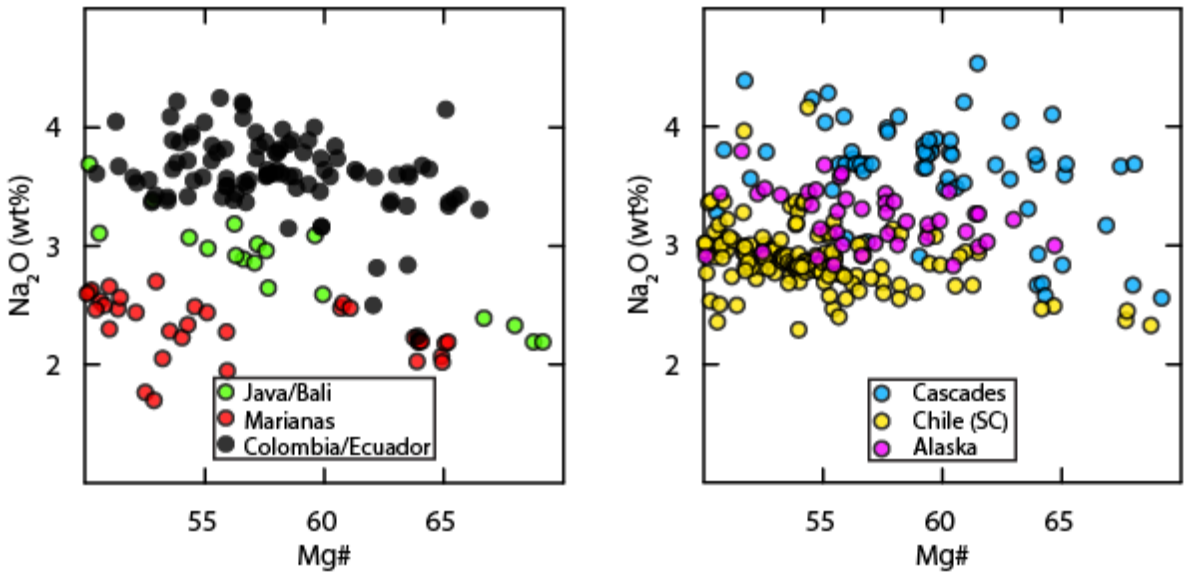

Figure A2.2. This figure serves as a complement to Figure 2.9 in the main text, where samples from all applicable volcanic arcs could not be plotted due to space constraints. As with the arcs in Figure 2.9, the samples from each arc occupy distinct ranges of Na_2O ranging from Mg#=50 all the way to primitive compositions, precluding fractional crystallization as the origin for the offsets between different arcs. Two arcs, Kamchatka and the Aegean, are not pictured here, also have constant, but more dispersed ranges of Na_2O across the full range of Mg#s. These two arcs have variations in Na_2O along the arc front that are consistent with regional variations in crustal thickness.

Appendix A2.5: Mixing end-members plotted on Figure 2.10

Table A2.1: Model end member compositions

	Na2O	P2O5	Sr	Zr	Sm
Enriched End-Member	6.01	0.43	1165	235	6.90
Depleted End-Member	1.34	0.04	160	7	1.00
50% Mix	3.67	0.23	663	121	3.95

Appendix A3.1: Model details

Non-modal mantle melting model description

Our calculation of partition coefficients used for mantle melting is based on a set of four independent parameterizations:

1) Subsolidus mantle modes are extrapolated for each model pressure. At pressures <2GPa, we use the parameterization found in Tenner et al. (2009). At pressures greater than 2 GPa, model clinopyroxene (cpx), modal orthopyroxene (opx) and modal garnet (gt) are extrapolated linearly based on 17% cpx and 30% opx at 1.8 GPa, 1.5% gt at 2 GPa, and 30% cpx, 12% opx, and 2.5% gt at 3 GPa, consistent with the results of Walter (1998), Baker and Stolper (1994), and Baker et al. (1995). Subsolidus olivine is held constant at 53%, following Tenner et al. (2009).

2) The extent of mantle melting is calculated using the equations of Katz et al. (2003) taking into account an enthalpy of fusions of 180 cal/g, as described in the main text.

3) Resulting mantle modes after melting are calculated by extrapolating logarithmically from the experiments of Walter et al. (1995) between 1.7 and 3.5 GPa. If garnet is present, reaction coefficients for cpx, opx, and ol are reduced to accommodate a reaction coefficient for garnet of -0.115. This value is somewhat lower than the garnet reaction coefficient determined by Walter (1998), but is instead likely more consistent with melting of a hydrated mantle wedge, as shown by Hall (unpublished thesis, 1999). If cpx is exhausted, melting proceeds using reaction coefficients of -0.03 for olivine, and -0.97 for opx, following Walter (1998).

4) Partition coefficients for each mode are calculated based on pressure from a variety of literature sources (see Supplementary Dataset A3.2), and then bulk partition coefficients are calculated using the results of step 3).

Slab melting model description

Calculation of slab melt compositions was based on the experimental work of Hermann and Rubatto (2009) and Kessel et al. (2005). The process described below is automated using MATLAB scripts that are available in Supplementary Dataset A3.3. The partition coefficients for elements between slab sources and slab melts, if not mentioned explicitly below, are determined by direct linear extrapolation from partition coefficients from experiments C-2446 (750 °C), C-1848 (800 °C), C-1578 (900 °C), and C-1868 (1050 °C) from Hermann and Rubatto (2009) for sediment melting, and the 4 GPa experiments from Kessel et al. (2005) for AOC melting.

For the LREE, in order to ensure smooth, consistent behavior across a range of temperatures, the D value for Nd was extrapolated exponentially from D=3 at 800 °C to D=1.5 at 1000 °C, which produces the formula [DNd=8E9*T-3.244]. Because LREE may become saturated beyond a certain concentration in sediment melts, maximum concentrations of Nd in melts were also extrapolated from 13 ppm at 800 C to 45 ppm at 1000 °C. Remaining LREE concentrations in slab melts were calculated using starting sediment and AOC compositions, as described in the main text, and average $(D^{(s/l)}LREE)/(D^{(s/l)}Nd)$ values calculated from Hermann and Rubatto (2009), we were held constant. These

values were 0.73, 0.71, 1.6 for La, Ce, and Sm, respectively. The D value for Sr was held at 0.15 for all calculations. Slab melt H_2O contents are extrapolated from 6% H_2O at 980 °C to 25% H_2O at 800 °C.

The hot slab melt contains 6% H_2O while the cold slab melt contains 25% H_2O, values close to the minimum and maximum H_2O contents of experiments. REE concentrations in slab melts were calculated based on both partition coefficients and maximum solubilities, following the results of Hermann and Rubatto (2009). For Nd, D(s/l) was parameterized via exponential extrapolation, from D=3 at 800 °C to D=1.5 at 1000 °C. Maximum solubilities of Nd in sediment melts were extrapolated in the same way, extending from 13 ppm at 800 °C to 45 ppm at 1000 °C. The concentrations of the remaining LREE were calculated using average MORB concentrations from Gale et al. (2013) and the median sediment composition of Plank et al. (2013) along with (D(s/l)LREE)/(D(s/l)Nd) values from Hermann and Rubatto (2009), which are assumed to be constant. Remaining partition coefficients for slab melting were directly extrapolated from Hermann and Rubatto (2009) for sediment melts, and Kessel et al. (2005) for melts of AOC.

References:

Baker, M., Hirschmann, M., Ghiorso, M., Stolper, E., 1995. Compositions of near-solidus peridotite melts from experiments and thermodynamic calculations. Nature 375, 308-311.

Baker, M.B., Stolper, E.M., 1994. Determining the composition of high-pressure mantle melts using diamond aggregates. Geochimica et Cosmochimica Acta 58, 2811-2827.

Hermann, J., Rubatto, D., 2009. Accessory phase control on the trace element signature of sediment melts in subduction zones. Chemical Geology 265, 512-526.

Katz, R.F., Spiegelman, M., Langmuir, C.H., 2003. A new parameterization of hydrous mantle melting. Geochemistry, Geophysics, Geosystems 4.

Kessel, R., Schmidt, M.W., Ulmer, P., Pettke, T., 2005. Trace element signature of subduction-zone fluids, melts and supercritical liquids at 120–180 km depth. Nature 437, 724-727.

Tenner, T.J., Hirschmann, M.M., Withers, A.C., Hervig, R.L., 2009. Hydrogen partitioning between nominally anhydrous upper mantle minerals and melt between 3 and 5 GPa and applications to hydrous peridotite partial melting. Chemical Geology 262, 42-56.

Walter, M.J., 1998. Melting of garnet peridotite and the origin of komatiite and depleted lithosphere. Journal of Petrology 39, 29-60.

Appendix A4.1: Details of data filtration

As described in the main text, and shown in Figure A4.1, for most volcanoes from the SVZ, plots of incompatible elements vs. MgO result in a "wedge" shape, in which the diversity of magma compositions increases as MgO decreases. This wedge shape indicates that a variety of processes are affecting the magma compositions at individual volcanoes, even when MgO contents are greater than 4 wt. %. On Figure A4.1, the green squares indicate samples that were removed during data filtration, as described in the main text, while the red squares are the samples used in the final dataset. For Tolhuaca and Villarrica, no samples with 5.5<wt. % MgO<6.5 pass the filters, but filtered samples are available on each side of this range. Therefore, for these volcanoes, the 6-values were calculated using linear extrapolation of the filtered sample set to 6 wt. % MgO.

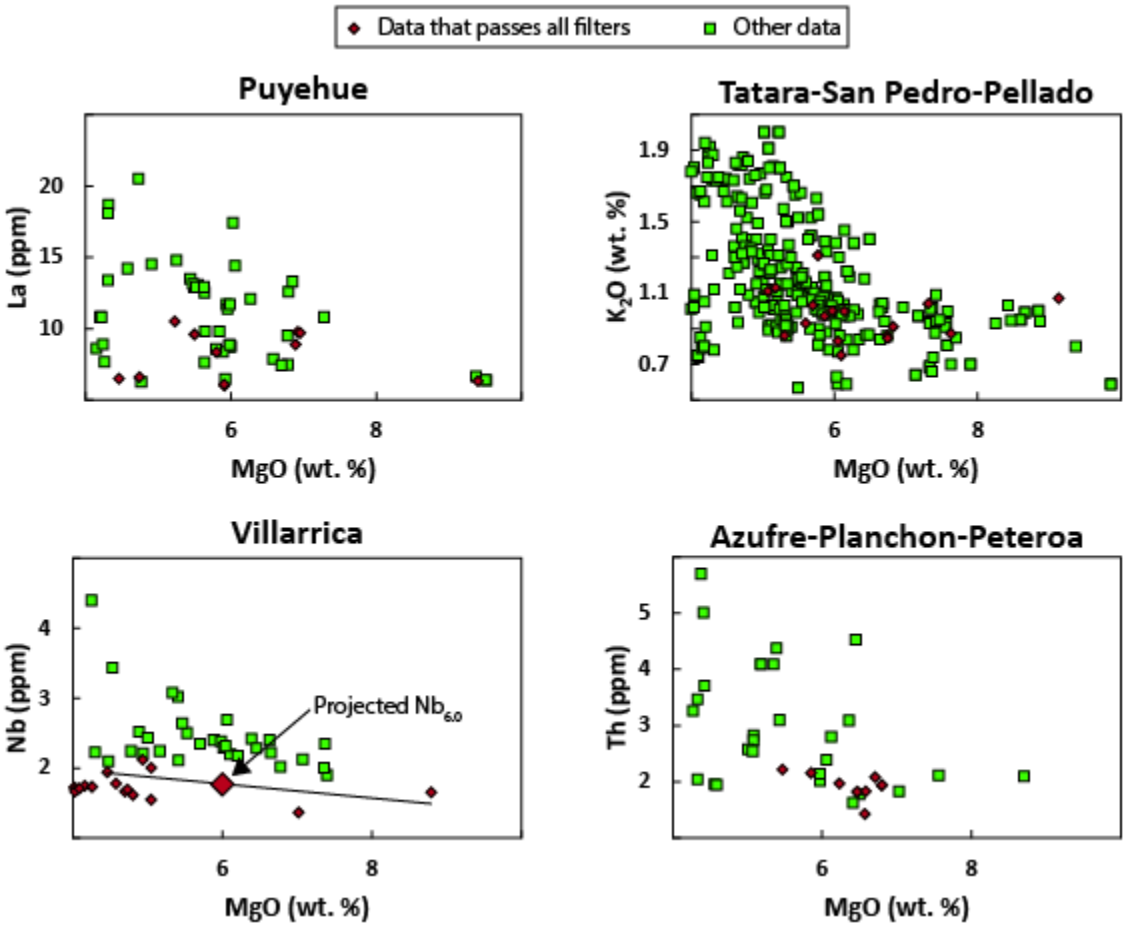

Figure A4.1. This figure demonstrates the "wedge" shape imprint of crustal processing on plots of MgO vs. various incompatible elements, using data from various SVZ volcanoes, as indicated by the individual figure titles. For Villarrica, no filtered samples fall within the range of MgO contents used for 6-values, and so the 6-values are calculated by a linear regression through the filtered data. A normal LLD for crystal fractionation produces a very shallow slope on these plots, and most of the data plotting above the filtered "baseline" values are the result of magma mixing or crustal assimilation.

Because each of the volcanoes exhibit unique behavior, a single set of data filters are not appropriate at every volcano. In general, we included only data with between 5 and 7 wt. % MgO, and between .9 and 1 Eu/Eu*. As described in the main text, there is evidence of crustal contamination as well, for several volcanoes. For these volcanoes, in which the Rb/K ratio or the Rb/Y ratio varied to a large extent, additional filters were applied. Volcanoes with modified data filters, or additional data filters, can be found in Table A4.1 below.

Table A4.1: Data filters applied to each volcanic center

Volcano	Rb/K Cutoff	Additional details
Don Casimiro	>450	
Azufre Planchón Peteroa	>450	
Descabezado Grande	>400	
Tatara-San Pedro-Pellado	>500	
Longaví		Because of kinks in data, the MgO cut off was shifted to 5.5 wt. %
Antuco	Rb/Y>1	Assimilation at Antuco is more easily spotted using the Rb/Y ratio
Tolhuaca		Projected 6-value
Llaima	>450	
Villarrica		Projected 6-value
Mocho-Choshuenco	>450	
Puyehue	>500	
Antillanca		Because of kinks in data, the MgO cut off was shifted to 5.5 wt. %

Appendix A4.2: Inverting for the Gough source

As described in the main text, the Gough Island Basalts are alkaline basalts and therefore are likely the products of low extent of melting. The lavas from the Gough suite comprise a very large range of compositions, but there is evidence they all are derived by melting of a common mantle source. The large range of La concentrations in the Gough basalts do not correlate well with the MgO contents (Figure A4.2), and so cannot be the product of crystal fractionation alone. If only Gough basalts with >6 wt. % MgO are considered, there is an excellent correlation between La and La/Sm. The factor of 2 variation in La can be produced by a factor of 2 variation in F, but in order to simultaneously produce the large variation in La/Sm, F must be very small. To determine the correct range in F to reproduce the Gough source, a hypothetical source composition was calculated for the sample with the median La contents, and then the F value was varied until the slope of La vs. La/Sm produced a match. The best match was produced for the range of F between 0.006 and 0.012, as shown in Figure A4.2. The partition coefficients used in the inversion were the 3 GPa coefficients from the study of Salters and Stracke (2004) with assumed mantle modes of 57% Olivine, 26% Opx, 15% Cpx and 0.2% Garnet.

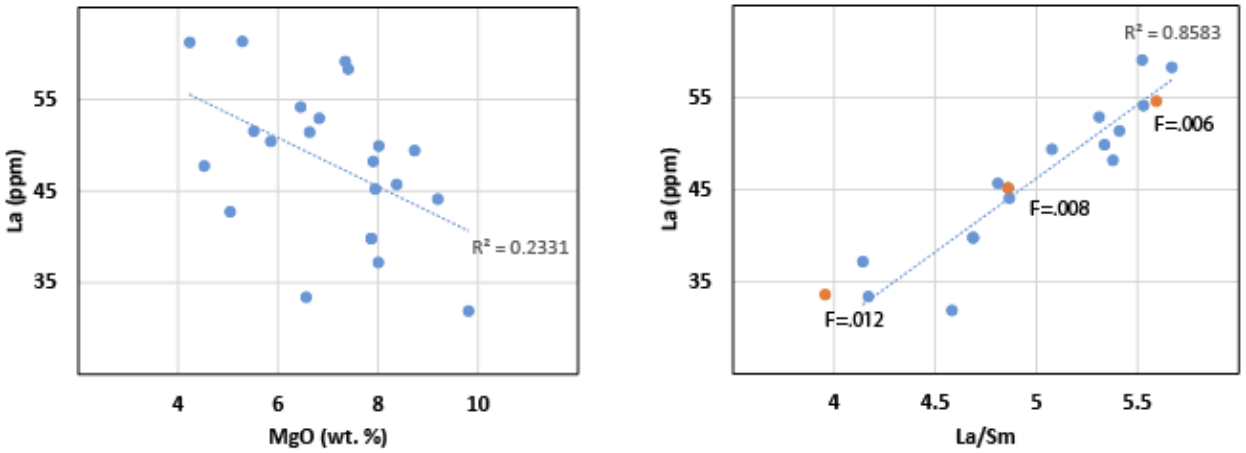

Figure A4.2. The La contents of Gough basalts do not correlate well with MgO and so are not produced by crystal fractionation. The correlation between La and La/Sm (among samples with wt. % MgO>6, as plotted) is suggestive of variation due to a range of extents of melting. The large variation of La/Sm is best produced over a range in extents of melting from F=.006 to F=.012.

Appendix A4.3: Isotope compositions of model components

Table A4.2: Isotope compositions of model components

	$^{143}Nd/^{144}Nd$	$^{87}Sr/^{86}Sr$	$^{176}Hf/^{177}Hf$
Sediment	0.51265	0.705	0.28305
AOC	0.51305	0.7035	0.28324
More depleted source	0.51293	0.7033	0.28305
GIB Source	0.51253	0.7052	0.28271